

METAL OXIDE NANOPARTICLES: EXAMINATION OF GROWTH PROCESSES TO  
GAIN NANOSCALE STRUCTURAL CONTROL

by

LEE KENYON PLUMMER

A DISSERTATION

Presented to the Department of Chemistry and Biochemistry  
and the Graduate School of the University of Oregon  
in partial fulfillment of the requirements  
for the degree of  
Doctor of Philosophy

December 2019

## DISSERTATION APPROVAL PAGE

Student: Lee Kenyon Plummer

Title: Metal Oxide Nanoparticles: Examination of Growth Processes to Gain Nanoscale Structural Control

This dissertation has been accepted and approved in partial fulfillment of the requirements for the Doctor of Philosophy degree in the Department of Chemistry and Biochemistry by:

Catherine J. Page	Chairperson
James E. Hutchison	Advisor
Shannon W. Boettcher	Core Member
Benjamín J. Alemán	Institutional Representative

and

Kate Mondloch	Interim Vice Provost and Dean of the Graduate School
---------------	--

Original approval signatures are on file with the University of Oregon Graduate School.

Degree awarded December 2019

© 2019 Lee Kenyon Plummer

## DISSERTATION ABSTRACT

Lee Kenyon Plummer

Doctor of Philosophy

Department of Chemistry and Biochemistry

December 2019

Title: Metal Oxide Nanoparticles: Examination of Growth Processes to Gain Nanoscale Structural Control

Metal oxide nanoparticles can enable a wide variety of impactful applications due to their structure-dependent properties, tailorabile features, and processability. The nanoparticle core is usually the nanoparticle component that lends a functional property to a particular application. Syntheses are required that reliably produce the nanoparticle core with the appropriate structural characteristics (size, shape, crystal phase, crystallinity, etc.) to yield the specific properties demanded by applications. In order to command control over nanoparticle core structure, we must understand the growth processes that lead to the structure. This dissertation examines growth processes by exploiting a unique metal oxide nanoparticle synthesis method. In this method, the synthetic attributes are analogous to living polymerization reactions implying that nanoparticle core structure can be manipulated with the same degree of control that transformed polymer chemistry.

Leveraging the merits of the living nanoparticle synthesis, the impact of monomer flux, synthesis temperature, and precursor speciation are investigated. In the indium oxide system, it was found that high flux causes the growth of single-crystal, branched

morphologies while low flux results in uniform, faceted morphologies. With increasing synthesis temperature, higher monomer fluxes are required before branched structures are observed. A model is proposed wherein surface diffusion of reactive species plays a key role in dictating nanoparticle morphology. In the iron oxide system, an Fe (III) oleate precursor containing acetylacetone induces multiple twin defects in magnetite/maghemite nanoparticles. We hypothesize that twinning results from insufficient Fe (II) to grow the magnetite crystal. Synthesis with a mixture of Fe (II) and Fe (III) in the precursor affords well-controlled crystal growth that exhibits living characteristics and results in nanoparticles that are nearly free of defects.

Towards building structure-property relationships, the size-dependent magnetic properties of small (< 10 nm) iron oxide nanoparticles were investigated. The nanoparticles exhibited relatively high saturation magnetizations as a result of all but the very surface iron atoms of the nanoparticles contributing to their magnetism. Overall, this research demonstrates the sensitivity of the nanoparticle growth and structure on synthetic variables, and strategies to achieve highly magnetic nanoparticle cores are suggested.

This dissertation includes previously published and unpublished co-authored material.

## CURRICULUM VITAE

NAME OF AUTHOR: Lee Kenyon Plummer

### GRADUATE AND UNDERGRADUATE SCHOOLS ATTENDED:

University of Oregon, Eugene  
Hendrix College, Conway, Arkansas

### DEGREES AWARDED:

Doctor of Philosophy, Chemistry, 2019, University of Oregon  
Master of Science, Chemistry, 2014, University of Oregon  
Bachelor of Arts, Chemistry, 2012, Hendrix College

### AREAS OF SPECIAL INTEREST:

Nanoparticle synthesis  
Nanoparticle growth  
Nanomaterial characterization  
Small Angle X-ray Scattering  
Transmission Electron Microscopy  
Magnetic nanoparticles

### PROFESSIONAL EXPERIENCE:

Graduate Research Assistant, Department of Chemistry and Biochemistry,  
University of Oregon, 2014-2019

Graduate Teaching Assistant, Department of Chemistry and Biochemistry,  
University of Oregon, 2014-2015

Research Assistant, UO/SONY, Eugene, OR, 2014

Research Intern, Oak Ridge National Laboratory, Oak Ridge, TN, 2012-2013

Undergraduate Researcher, Hendrix College, Conway, AR, 2010-2012

## GRANTS, AWARDS, AND HONORS:

CRC Press Chemistry Achievement Award, Hendrix College, 2009

## PUBLICATIONS:

Plummer, L. K.; Crockett, B. M.; Pennel, M. L.; Jansons, A. W.; Koskela, K. M.; Hutchison, J. E. Influence of Monomer Flux and Temperature on Morphology of Indium Oxide Nanocrystals during a Continuous Growth Synthesis. *Chem. Mater.* **2019**, *18*, 7638–7649.

Masood, K.; Zaikova, T.; Plummer, L. K.; Allen, T.; Stasiak, J.; Hutchison, J. E.; Jander, A.; Dhagat, P. Design and Digital Fabrication of Magneto-dielectric Composites for Additive Manufacturing of Gradient Index RF Lenses. *Printing for Fabrication 2019 Conference Proceedings*.

Goodwin, T. E.; Desrochers, L. P.; Fuller, D. A.; Chen, C. J.; Plummer, L. K.; Weddell, M. E.; Marvin, C. C. Learning Organic Chemistry from Bark Beetle Pheromone Biosynthesis. *The Chemical Educator* **2019**, *24*, 87–90.

Lenox, P.; Plummer, L. K.; Paul, P.; Hutchison, J. E.; Jander, A.; Dhagat, P. High-Frequency and High-Field Hysteresis Loop Tracer for Magnetic Nanoparticle Characterization. *IEEE Magnetics Letters* **2018**, *9*, 1–5.

Cooper, S. R.; Plummer, L. K.; Cosby, A. G.; Lenox, P.; Jander, A.; Dhagat, P.; Hutchison, J. E. Insights into the Magnetic Properties of Sub-10 Nm Iron Oxide Nanocrystals through the Use of a Continuous Growth Synthesis. *Chemistry of Materials* **2018**, *30*, 6053–6062.

Jansons, A. W.; Plummer, L. K.; Hutchison, J. E. Living Nanocrystals. *Chemistry of Materials* **2017**, *29*, 5415–5425.

Yan, Y.; Plummer, L. K; Ray, H.; Cook, T., & Bilheux, H. Ductility Evaluation of As-Hydrided and Hydride Reoriented Zircaloy-4 Cladding under Simulated Dry-Storage Condition. *MRS Proceedings*, *1645*, **2014**, Mrsf13-1645-ee01-03.

Yan, Y., Qian, S., Littrell, K., Parish, C., Bell, G., & Plummer, L. K. (2014). Nondestructive Evaluation on Hydrided LWR Fuel Cladding by Small Angle Incoherent Neutron Scattering of Hydrogen. *MRS Proceedings*, *1653*, **2014**, Mrsf13-1653-mm03-07.

## ACKNOWLEDGMENTS

I would like to sincerely thank my committee—Dr. Cathy Page, Dr. Shannon Boettcher, Dr. Benjamín Alemán, and Dr. Jim Hutchison—for their support and guidance throughout my graduate career. I would especially like to thank my advisor, Jim, for allowing me to do research in his lab and imparting his knowledge about the scientific process and problem-solving.

A number of teachers and mentors encouraged me, pushed me, and taught me valuable lessons, and I would not have made it to this point without them. I would like to express my gratitude here for: my father, Dr. Dan Plummer, who instilled in me a desire to understand the world around me; my mother, Sherri Plummer, who taught me that there is no replacement for hard work; Mr. Sickman, whose high demands made me a better student; Steven Richard who taught me tenacity; Dr. Liz Gron, Dr. Tom Goodwin, and Linda Desrochers who saw potential in me that I couldn't; Patrick McDonald who valued my individuality; Dr. Yong Yan who showed me the importance of organization in a project; Dr. Ryuichiro Maruyama, Moto Honda, and Dr. Tatiana Zaikova who all taught me how friendship can make work more meaningful; and Dr. Julie Haack who showed me the value in visual communication and how open conversations can lead to new insights.

I would like to thank fellow students I've met and worked with along the way: Dr. Adam Jansons, whose kind and open attitude opened me to collaborative research; Dr. Susan Cooper, who always had unique and thoughtful insights—whether about research or otherwise—was a wonderful collaborator and friend; Dr. Brandon Crockett who always had insightful ways to think about the chemistry explored in this dissertation;

Makenna Pennel was a wonderful student to mentor and taught me new ways to communicate science; Kiana Kawamura who helped with research on iron oxide; undergraduates Kris Koskela, Alexia Cosby, and Randal Candler who all aided in important synthetic work. In addition to those mentioned above, fellow Hutchison lab members taught me so much: Dr. Bev Smith, Dr. Ed Elliott, Dr. Zack Kennedy, Dr. Brantly Fulton, Dr. Meredith Sharps, Dr. Sam Young, Dr. Aurora Ginzburg, Dr. Brandi Baldock, Raina Krivina, and Nils Johnson. In particular, I would like to give a special thanks to my friend and colleague Tawney Knecht who was a huge source of support.

I would also like to thank the collaborators, staff, and funding sources that enabled this research. The expertise and feedback from our collaborators at OSU—Dr. Pallavi Dhagat, Dr. Albrecht Jander, Philip Lenox, and Colby Whitaker—enabled the work in Chapters IV and V. The staff of CAMCOR, Josh Razink in particular, provided excellent research support and expertise. I am very appreciative of our helpful department office staff, and I would like to acknowledge NSF grants CHE-1610675, ECCS-1310657, and 1609679 for funding the research in this dissertation.

Finally, I would like to acknowledge friends and family: fellow LGBT+ in STEM cofounders—Dr. Erik Hadland, Dr. Lisa Eytel, and Dr. Annie Greenaway; my always-supportive sister, Meghan; Dr. Dan Seidenkrantz, Dr. Keenan Woods, Dr. Lisa Enman, Dr. Conerd Fredrickson, Dr. Loni Kringle, Dr. Mike Nellist, and Dr. Matt Kast for their support and friendship. I would like to thank my friends Dr. Winn Haynes, Dr. Laura McDonald, Emily Uhar, Christian Harrison, Kim Phelps, Allison Moseley, Rachel Jacobs-Strain, and Jace Rohacik. Last and certainly not least, I would like to thank my partner, Mackenzie Rich, for her understanding, unwavering support, and love.

Dedicated to my parents, Dan and Sherri Plummer

## TABLE OF CONTENTS

Chapter	Page
I. INTRODUCTION .....	1
Overview of Nanoparticles .....	1
A Small History of Nanotechnology.....	5
Nanotechnology from Science Fiction to Reality .....	5
Advances and Shortcomings in Nanotechnology .....	7
Metal Oxide Nanoparticles .....	11
Classical Nucleation Theory .....	12
Heat-up Methods: Thermal Decomposition and Ester-Elimination	
Chemistries .....	14
Slow Addition Methods .....	16
Combining Ester-Elimination Chemistry with Slow Addition Approach .....	17
Dissertation Overview .....	19
II. LIVING NANOCRYSTALS .....	24
Introduction.....	24
Living Synthetic Approaches to Macromolecules, including Nanocrystals .....	26
The Hunt for Living Growth Methods.....	30
Leveraging Living Methods to Achieve Advanced Structural Control .....	35
Increasing Doping Efficiency .....	35
Intentionally Modifying the Radial Position of Dopant Atoms within	
Nanocrystals.....	38
Implications of Living Synthetic Methods for Core/Shell Nanocrystal	
Growth .....	41
Outlook .....	44
Bridge to Chapter III .....	48

Chapter	Page
<b>III. INFLUENCE OF MONOMER FLUX AND TEMPERATURE ON MORPHOLOGY OF INDIUM OXIDE NANOCRYSTALS DURING A CONTINUOUS GROWTH SYNTHESIS .....</b>	<b>49</b>
Introduction.....	49
Results and Discussion .....	54
Influence of Precursor Addition Rate on Morphology .....	54
Examining the Impact of Precursor Addition Rates on the Mechanism of Growth .....	59
Determining How Temperature Affects the Influence of Monomer Flux on Morphology.....	67
Utilizing Variable Flux to Transform Morphology .....	72
Conclusions.....	75
Materials and Methods.....	77
Materials .....	77
Continuous Growth Syntheses of Indium Oxide Nanocrystals .....	77
Nanocrystal Characterization.....	79
Bridge to Chapter IV.....	80
<b>IV. ACETYLACETONATE IN AN IRON (III) RICH PRECURSOR INDUCES TWINNING DEFECTS IN IRON OXIDE NANOPARTICLES .....</b>	<b>81</b>
Introduction.....	81
Research and Discussion.....	85
Conclusions.....	102
Experimental .....	104
Materials .....	104
Synthesis of Precursor.....	104

Chapter	Page
Characterization of Precursors .....	104
Synthesis of Nanoparticles.....	105
Characterization of Nanoparticles.....	106
Bridge to Chapter V .....	107
<b>V. INSIGHTS INTO THE MAGNETIC PROPERTIES OF SUB-10 NM IRON OXIDE NANOCRYSTALS THROUGH THE USE OF A CONTINUOUS GROWTH SYNTHESIS .....</b>	<b>108</b>
Introduction.....	108
Results and Discussion .....	112
Synthesis and Characterization of NCs.....	112
Magnetic Properties .....	117
Conclusions.....	125
Materials and Methods.....	127
Materials .....	127
Synthesis .....	127
Physical Characterization.....	128
Magnetic Characterization.....	129
Bridge to Chapter VI.....	130
<b>VI. DESIGN AND DIGITAL FABRICATION OF MAGNETO-DIELECTRIC COMPOSITES FOR ADDITIVE MANUFACTURING OF GRADIENT INDEX RF LENSES.....</b>	<b>131</b>
Introduction.....	131
Additive Manufacturing Methods.....	133
Polymer Particle Bed Infiltration and Fusing .....	134

Chapter	Page
Inkjet Printing of Polymerizable Nanocomposite Ink .....	137
Results.....	140
Conclusion .....	145
VII. CONCLUSION .....	146
Concluding Remarks.....	146
Implications.....	147
Future directions .....	148
APPENDICES .....	150
A. SUPPORTING INFORMATION FOR CHAPTER III: INFLUENCE OF MONOMER FLUX AND TEMPERATURE ON MORPHOLOGY OF INDIUM OXIDE NANOCRYSTALS DURING A CONTINUOUS GROWTH SYNTHESIS .....	150
B. SUPPORTING INFORMATION FOR CHAPTER IV: ACETYLACETONATE IN AN IRON (III) RICH PRECURSOR INDUCES TWINNING DEFECTS IN IRON OXIDE NANOPARTICLES .....	159
C. SUPPORTING INFORMATION FOR CHAPTER V: INSIGHTS INTO THE MAGNETIC PROPERTIES OF SUB-10 NM IRON OXIDE NANOCRYSTALS THROUGH THE USE OF A CONTINUOUS GROWTH SYNTHESIS .....	165
D. SUPPORTING INFORMATION FOR CHAPTER VI: DESIGN AND DIGITAL FABRICATION OF MAGNETO-DIELECTRIC COMPOSITES FOR ADDITIVE MANUFACTURING OF GRADIENT INDEX RF LENSES .....	175
REFERENCES CITED.....	184

## LIST OF FIGURES

Figure	Page
1.1. A timeline of nanoparticles on Earth .....	2
1.2. General architecture of a nanoparticle .....	3
1.3. Structural features of a nanoparticle core that can influence properties.....	10
1.4. Nanoparticle nucleation and growth according to classical nucleation theory.....	12
2.1. Reaction cycle showing the general steps of a living process either for polymerization or nanocrystal growth .....	27
2.2. Schematic representation of our living growth synthesis of metal oxide nanocrystals.....	34
2.3. Doped oxide nanocrystals that have been purified and suspended in hexanes.....	38
2.4. Using a living approach, the radial position of dopants can be controlled intuitively through the addition of doped or undoped precursor, represented by the top reaction schemes .....	42
3.1. Illustration of continuous growth synthesis of indium oxide nanocrystals.....	55
3.2. TEM images illustrating the dependence of nanocrystal morphology on the precursor addition rate .....	57
3.3. Distribution plots of the nanocrystal P/D values extracted from TEM images .....	58
3.4. HRTEM of a branched nanocrystal synthesized at a fast precursor addition .....	60
3.5. Comparison of fast addition, slow addition, and intermittent addition to test shape relaxation hypothesis. ....	64
3.6. Depicts the reaction steps leading to either faceted or branched nanocrystals .....	66

Figure	Page
3.7. Dependence of nanocrystal morphology on monomer flux at different temperatures .....	69
3.8. Nanocrystal growth curves plotted as nanocrystal volume vs. precursor added. ....	72
3.9. TEM images of nanocrystals grown at 290 °C to examine the influence of low flux growth on branched nanocrystals .....	74
4.1. Comparison of nanoparticles by TEM resulting from identical synthesis conditions but using an Fe (III) oleate precursor or an Fe (II) oleate precursor .....	85
4.2. FTIR and optical characterization of Fe (II) rich and Fe (III) rich precursors .....	86
4.3. Phase characterization of nanoparticles by XRD and optical absorbance .....	89
4.4. HRTEM of nanoparticles produced from standard Fe (III) rich precursor.....	92
4.5. FTIR and absorbance of initially Fe (II) rich precursor as it oxidized over time and TEM characterization of nanoparticles resulting from synthesis.....	95
4.6. FTIR characterization of Fe (II) rich oleate with added acetylacetone used as precursor and TEM and HRTEM images of the resulting NPs .....	97
4.7. FTIR characterization of the mixed precursor .....	100
4.8. Growth curve of mixed precursor and TEM images of highly twinned nanoparticles. ....	101
5.1. Size analysis of NCs by SAXS throughout a slow injection reaction .....	114
5.2. TEM and HRTEM micrographs demonstrating morphology and crystallinity of NCs .....	115
5.3. Structure and phase analysis of NCs throughout a slow injection reaction .....	117
5.4. Plot of normalized magnetization as a function of applied field .....	119

Figure	Page
5.5. $M_s$ plotted as a function of NC diameter up to 10 nm for this study and other studies .....	120
5.6. The effective magnetic size plotted as a function of physical size .....	124
6.1. Electromagnetic wave simulation of a gradient index RF lens designed by transformation optics .....	133
6.2. Schematic illustration of the printing system used to fabricate the dielectric polymer nanocomposite samples .....	136
6.3. Micrographs of cross-sections through the dielectric samples at four different BaTiO <sub>3</sub> volume fractions in the PA12 matrix.....	136
6.4. X-ray diffraction pattern of the synthesized barium hexaferrite nanoparticles .....	137
6.5. Example images of cast and printed nanocomposite samples .....	140
6.6. SEM images of surfaces of 3D printed nanocomposites .....	140
6.7. Frequency dependent dielectric properties of samples manufactured by polymer bed infusion, parametric in the BaTiO <sub>3</sub> volume fraction.....	141
6.8. The effective dielectric constant of a BaTiO <sub>3</sub> polymer nanocomposite sample at 1 kHz versus nanoparticle volume fraction .....	143
6.9. Dielectric permittivity versus frequency of samples with different BaTiO <sub>3</sub> nanoparticles loading in DEGDA .....	143
6.10. Dielectric permittivity at 100 MHz versus BaTiO <sub>3</sub> nanoparticle.....	144
6.11. Magnetic permeability versus frequency for a cast sample containing barium hexaferrite nanoparticles in DEGDA with 50 % volume fraction. ....	144
A.1. Histograms of D <sub>eff</sub> for samples featured in Figure 3.2 and 3.3 .....	150
A.2. Histograms of D <sub>eff</sub> for samples featured in Figure 3.5 .....	150

Figure	Page
A.3. Histograms of $D_{eff}$ of samples featured in the TEM images in Figure 3.7 .....	151
A.4. Histograms of $D_{eff}$ of the samples featured in Figure 3.9 .....	151
A.5. Determination of the P/D ratio for a circle, square, and an equilateral cross .....	152
A.6. Example of the process to determine P/D ratio from TEM images .....	152
A.7. Stacked XRD patterns of branched and faceted nanocrystals both exhibit cubic bixbyite structure .....	153
A.8. High resolution TEM images of nanocrystals synthesized at 230 °C, 260 °C, and 290 °C at fast injection rates .....	154
A.9. TEM images demonstrating growth of branched nanocrystals.....	154
A.10. TEM images and analysis to evaluate the possibility of oriented attachment .....	155
A.11. Nanocrystal growth curve plotted for a 260 °C synthesis.....	156
A.12. Number of nanocrystals calculated from three growth experiments at each temperature. ....	158
B.1. Size analysis results of nanoparticles produced with the standard Fe (III) rich precursor (A), and the Fe (II) rich precursor (B). ....	159
B.2. Isothermal TGA run of $Fe(acac)_3$ carried out at 150°C .....	159
B.3. Optical absorbance of iron precursors.....	160
B.4. FTIR of precursor prepared from $Fe(NO_3)_3$ and TEM of nanoparticles resulting from synthesis with the precursor .....	160
B.5. TEM Nanoparticles produced during the preparation of precursor using $Fe(OH)(acetate)_2$ starting material.....	161

Figure	Page
B.6. Size analysis from TEM images of nanoparticles produced with the oxidized precursor .....	161
B.7. HRTEM of nanoparticles produced from the oxidized precursor with corresponding FFT patterns .....	162
B.8. Optical absorbance demonstrating presence of acetylacetone ligands in the standard Fe (III) precursor .....	162
B.9. FTIR spectrum of Fe (II) acetylacetone .....	163
B.10. HRTEM and corresponding FFT patterns of nanoparticles produced from the Fe (II) rich oleate precursor with added acetylacetone .....	163
B.11. TEM images of nanoparticles resulting from synthesis with mixed precursor containing additional acetylacetone .....	164
B.12. Picture taken of reaction flask during synthesis to demonstrate set-up. ....	164
C.1. Growth of nanocrystals as a function of amount of precursor added for three different syntheses .....	166
C.2. SAXS patterns are shown for a growth curve with sizes from 4-10 nm.....	167
C.3. Indexing of HRTEM single particle electron diffraction .....	168
C.4. Powder XRD pattern of the 5 nm NC sample, fit using Rietveld refinement.....	169
C.5. Powder XRD pattern of a 6 nm NC sample fit using Rietveld refinement.....	170
C.6. Powder XRD pattern of a 9 nm NC sample, fit using Rietveld refinement.....	171
C.7. Room temperature magnetization curves of a size series of nanocrystals .....	172
C.8. TEM images of all NC samples that were magnetically characterized.....	173

Figure	Page
C.9. Collection of $M_s$ values reported in the literature plotted versus nanoparticle size .....	173
C.10. The effective magnetic size using two different values for $M_D$ from Langevin function fit plotted as a function of physical size measured by SAXS.....	174
D.1. Structures of Di(ethylene glycol) diacrylate, Irgacure 184, and acrylic acid .....	176
D.2. XRD pattern of ball milled starting materials annealed at 1080°C in air for 2 h with comparisons to Y- and M -type hexaferrite phases. ....	178
D.3. XRD pattern following annealing at 1330°C in air for 4 hours compared to W-type hexaferrite. ....	179
D.4. XRD pattern following annealing at 1230°C in air for 4 hours compared to Z-type, Y-type, and W-type hexaferrite phases.....	179
D.5. XRD pattern of hexaferrite sample annealed at 1230°C after ball milling compared with Z-type, Y-type, and W-type hexaferrite phases .....	180
D.6. TEM image of 1230°C annealed hexaferrite sample after ball milling. ....	180
D.7. XRD pattern of sample produced via slow injection method with the cubic spinel phase for comparison.....	181
D.8. Images of printed composites with low-loading and high loading. ....	183

## LIST OF TABLES

Table	Page
2.1. Analogous concepts and terminology between polymers and nanoparticles.....	29
2.2. Connection between prerequisites, synthetic attributes and outcomes for living growth nanocrystal synthesis.....	32
A.1. Metrics determined from TEM analysis of starting materials for and results from oriented attachment control experiment.....	156
C.1. NC diameter and dispersity determined by SAXS of NC samples .....	165
C.2. Refined parameters using Rietveld refinement of the 5 nm NC sample (measured by SAXS). Spacegroup <i>Fd-3m</i> . .....	170
C.3. Refined parameters using Rietveld refinement of a 6 nm NC sample (measured by SAXS). Spacegroup <i>Fd-3m</i> . .....	171
C.4. Refined parameters using Rietveld refinement of a 9 nm NC sample (measured by SAXS). Spacegroup <i>Fd-3m</i> . .....	172
C.5. Physical diameter, magnetic diameter, percent maghemite, and the saturation magnetization.....	172

# CHAPTER I

## INTRODUCTION

### Overview of nanoparticles

Nanoparticles today have a reputation of being high tech and only in the most advanced products and applications. They've been presented as the material that will enable everything that is difficult: curing cancer,<sup>1</sup> imaging inside the body with better resolution than ever before,<sup>2</sup> purifying water,<sup>3</sup> harvesting solar energy,<sup>4</sup> storing energy from renewable sources,<sup>5</sup> and making industrial chemical reactions easier<sup>6</sup>.

Nanoparticles are particulates of matter—be it carbon-based, a metal, metal oxide, or metal chalcogenide—that are between 1 and 100 nm in diameter, which is very small. To put it in perspective, a particle 10 nm across is to a penny what a beach ball is to the planet Earth. Just because we've only recently been able to “see” nanoparticles, however, doesn't mean that they haven't been around.

Nanoparticles, in fact, have been around for a very long time<sup>7,8</sup>—likely since the beginning of the earth (Figure 1.1). Nanoparticles are created naturally from ocean spray and carbonaceous materials from fires and volcanoes. They are produced by certain bacteria<sup>9</sup> and geochemical processes in bodies of water<sup>10</sup>. Arguably, humans have been incidentally creating nanoparticles since we first built fires, and we certainly began producing them in the form of pollution from industrial processes such as burning fossil fuels and mining.<sup>8</sup> Thousands of years ago, as people developed a taste for art, we began

intentionally but unknowingly producing nanoparticles in the glazes of pottery and embedded in stained glass windows and ornamental vessels to form striking colors.<sup>7</sup> The incredible potential of nanoparticles, however, was recognized only recently in the 20<sup>th</sup> century. The year 1985 marked the start of our foray into intentional, precision synthesis of nanomaterials: soccer ball-like structures of carbon were synthesized by a group at Rice University, and quantum dots (nanoparticles made from semiconducting material) were synthesized at Bell labs.<sup>11</sup>

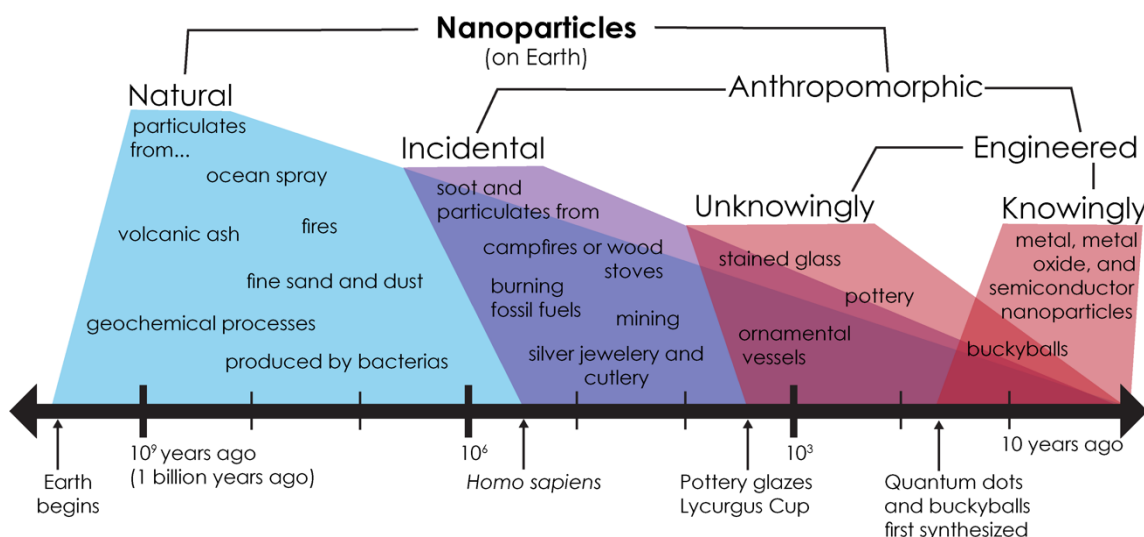


**Figure 1.1.** A timeline of nanoparticles on Earth. The timeline is a log plot in years ago from today (2019).

The architecture of nanoparticles synthesized today for research and applications (and for the purposes of this dissertation) can generally be described as comprising a core and a ligand shell as depicted in Figure 1.2. The core material, typically an inorganic material, imparts some desired property. The core is covered with ligands, that is,

molecules that attach to the surface, to form the ligand shell. The ligand shell enables processability and it can also provide additional functionalities.

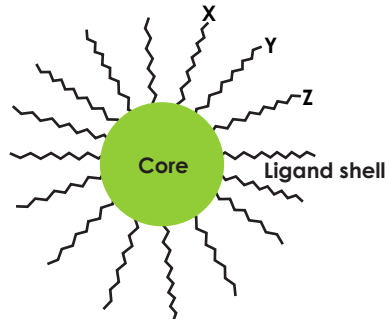


**Figure 1.2.** General architecture of a nanoparticle consisting of a core (green) and ligand shell that can have different chemical functionalities (represented as X, Y, and Z).

A huge attraction of nanoparticles is the core material's size-dependent properties. Michael Faraday first suspected metal particulates of having different properties than bulk material when he was studying thin films of gold in the 1850s.<sup>12</sup> Faraday washed his films with a solution and noticed the solution was faintly pink, and, when shining light through the solution, he observed a well-defined cone of the light beam. He figured this scattering of light (now known as the Faraday-Tyndall effect) was a result of particulates of gold too small to see.<sup>12</sup> It would later become apparent that the color was also a result of the small size.

Size-dependent properties are a result of the confined nature of nanoparticle core. These properties include optical and electronic properties such as the electronic band gap with size resulting in changes in fluorescence color in quantum dots.<sup>13</sup> Localized surface plasmon resonance (LSPR) in which electrons in conductive nanoparticles oscillate with incoming light of a particular wavelength resulting in absorbance of that wavelength is another example.<sup>14</sup> This phenomenon accounts for their color (like the pink solutions

Faraday observed). Magnetic behavior also changes. At small enough sizes, a magnetic material will possess only a single magnetic domain instead of many as in the bulk and lose its ability to magnetize in the absence of an applied magnetic field. The smaller the particle, the greater the field that must be applied to magnetize it.<sup>15</sup> The high surface to volume ratio is another source of emerging properties at the nanoscale. With small nanoparticles, surface atoms constitute a significant percentage of the total atoms that make up the particle (~50 % for a 4 nm diameter nanoparticle),<sup>16</sup> which can result in differing electronic structure and chemical reactivities.<sup>17</sup>

The ligand shell is the other important structural feature of nanoparticles. The ligand shell provides stability to the core preventing it from aggregating or fusing with other nanoparticles.<sup>18</sup> Without it, the nanoparticle core properties would not be retained. The nature of the ligands will determine whether the nanoparticle disperses in polar media (such as water or ethanol) or nonpolar media (such as an oil or hexanes). Dispersing the nanoparticle will enable the nanoparticle to be delivered where needed such as into an organism or applied as a coating or film. The ligand shell can also impart additional, more complex functionalities. Chemical groups at the ends of ligands can be utilized to attach nanoparticles to a surface<sup>19</sup> or to perform some other function. For example, a fluorescent molecule could be linked to the nanoparticle in order to track where the nanoparticle travels once inside a living organism.<sup>20</sup> Together the core properties combined with attributes of the ligand shell can enable a multitude of capabilities.

The nanoparticle architecture just described is highly complex compared to the particulate matter that came from natural sources and even the unknowingly human-

engineered nanoparticles. How did we progress from natural and unintentional nanoparticles to the level of sophistication achievable today? Many scientific developments in the area of nanotechnology were necessary to reach this point.

### **A small history of nanotechnology**

Nanotechnology, as defined in the National Nanotechnology Initiative Report in the year 2000, is “the ability to work at the molecular level, atom by atom, to create large structures with fundamentally new molecular organization.” It goes on to say “nanotechnology is concerned with materials and systems whose structures and components exhibit novel and significantly improved physical, chemical, and biological properties, phenomena, and processes due to their nanoscale size. The aim is to exploit these properties by gaining control of structures and devices at atomic, molecular, and supramolecular levels...”.<sup>21</sup> Today, the idea of harnessing the potential of nanoscale structures seems ubiquitous, but it wasn’t always so.

#### *Nanotechnology from science fiction to reality*

The concept of nanotechnology captured the imagination of the western world in the mid and late 20<sup>th</sup> century. Many pinpoint Richard Feynman’s famous lecture “There’s plenty of room at the bottom” in December of 1959 as the birth of nanotechnology as a field of study. In this lecture, he implored the audience to imagine a world where the encyclopedia Britannica could be written on the head of a pin.<sup>22</sup> He referenced DNA as the epitome of writing small. He highlighted the ability of biological components to function at small scales. He talked about miniaturizing the computer.<sup>22</sup> Decades before this famous talk, however, science fiction novels and short stories had already exposed

these topics as science historian Colin Milburn points out. These works included among others: *The Girl in the Golden Atom* by Ray Cummings, “Microcosmic God” by Theodore Sturgeon, “Waldo” by Robert Heinlein, “Hobbyist” by Frank Russel, *Needle* by Hal Clement.<sup>23</sup> They described ideas such as top-down construction of infinitesimally small materials and atom by atom assembly. Feynman’s standing as a well-renowned physicist lent credence to the concepts and ideas of writing and constructing on small scales. Furthermore, he rallied the science community to develop technologies to “see” what we are doing on the atomic scale, to consider these “small” ideas, and even proposed a high school competition towards the goal of writing small.<sup>22</sup>

In the following decades nanotechnology caught hold. In 1974, Tokyo University of Science Professor Norio Taniguchi first used the term “nano-technology” in a conference proceedings paper.<sup>24</sup> Physicist Eric Drexler wrote the futuristic novel *Engines of Creation: The Coming Era of Nanotechnology* in 1986. Imaging techniques were invented and developed that enabled the characterization and manipulation of material on the nanoscale. The transmission electron microscope (TEM) and scanning electron microscopes (SEM) first invented in the 1930s<sup>25</sup> were gradually advanced to achieve better magnifying and resolving power. Today, TEMs can reach sub nanometer resolutions<sup>26</sup> while also performing physical characterization such as crystal phase analysis, elemental analysis, and much more.<sup>27</sup> Following initial developments of TEM and SEM, the scanning tunneling microscope (STM) and the atomic force microscope created in the 1980s<sup>28</sup> could image and also manipulate atoms and molecules.

On top of enabling technologies, funding took off in the year 2000 when the Clinton administration began the National Nanotechnology Initiative pouring millions of

dollars into funding opportunities.<sup>21</sup> Academic journals emerged for nanoscale research specifically (*Nanotechnology* (1990), *Nano Letters* (2001), *Small* (2005), *Nature Nanotechnology* (2006), *ACS Nano* (2007), *Nanoscale* (2009), etc.). Key discoveries and experiments now mark the milestones in the progression of nanotechnology. Smalley et al. first synthesized buckminsterfullerene (the soccer ball-like carbon structure) in 1985, which attracted the 1996 Nobel prize in chemistry.<sup>11</sup> In 1991, Iijima discovered carbon nanotubes,<sup>29</sup> and in 1993, IBM's Almaden Research Center created a “quantum corral”—a circle of 48 iron adatoms nudged into a circle on a copper surface—using an STM.<sup>30</sup> In the area of inorganic nanoparticle synthesis, the highly effective method known as the hot-injection technique to create semiconductor nanoparticles with low size dispersity was published by Bawendi et al. in 1993.<sup>31</sup>

Today, academic articles motivate nuanced research with exceptionally sophisticated applications. Many of these applications demand very specific nanoparticle properties that result from the nanoparticles possessing specific size and structure. For example, magnetic nanoparticle imaging in living organisms that utilizes the superparamagnetic behavior of iron oxide nanoparticles.<sup>32,33</sup> Similarly, tumor destruction by heating of magnetic nanoparticles with alternating magnetic fields (known as hyperthermia),<sup>34</sup> or using quantum dots as bright and robust fluorescent cell labelling.<sup>35</sup>

### *Advances and shortcomings in nanotechnology*

Yet, a look at currently available products leave a lot to be desired. The latest Consumer Product Inventory (CPI) put out by the Project on Emerging Nanotechnologies in 2015, demonstrated a chasm between the highly sophisticated nanomaterials and applications extolled in the academic literature and nanotechnology that is actually

available on the market. Less than 2,000 products could be identified that contain some sort of nanotechnology.<sup>36</sup> In these products, nanoparticles typically provided passive and simple functions.<sup>36</sup> For example, the largest category of nanotech products belonged to “health and fitness” mainly in the form of functionalized textiles or equipment to impart anti-microbial or protective coatings, and also included a rather disconcerting number of ingestible supplements.<sup>36</sup> Why is there such a large discrepancy between the literature and the real world?

There are several likely reasons. One possible source of the discrepancy has to do with marketed visibility or, rather, invisibility. Public perception of risk around nanoparticles is higher than that of academics or government officers.<sup>37</sup> This fear is reflected in media references. In the animated series *Futurama*, “nanobots” (that resemble tiny army tanks and originally intended to purify water) fabricated by the character Professor Farnsworth learn to self-replicate and take over a planet.<sup>38</sup> Similarly, in the graphic novel *Singularity 7*, “nanites” gain the ability to self-replicate and then breakdown all living things that.<sup>39</sup> These concepts stem from Drexler’s rather unfortunate forewarnings about nanomachines from his 1986 book *Engines of Creation*.<sup>23</sup> Other concerns from the public stem from unintended consequences in other realms of chemical technologies such as the persistence of DDT in the environment,<sup>40</sup> fluorocarbons that eat away at our atmosphere,<sup>41</sup> and asbestos that causes lung damage and cancer.<sup>42</sup> With this in mind, there is not much impetus for products containing nanotechnology to strongly advertise that fact.

In some areas of nanotechnology, there may not be such a large discrepancy between high expectations and real products. The authors of a report on the CPI noted

that the electronic category (laptop computers, tablets, and game consoles, for example) was notably small but also may be underrepresented as a result of intellectual property. The electronics category included many computer components, such as computer processors and memory, that enable a wide variety of personal electronics. It is arguable that nanotechnology is, in fact, ubiquitous and has already changed our world dramatically. In the words of LANL director of center for integrated nanotechnologies Terry Michalske, “We can do things we can’t imagine right now”.<sup>23</sup>

It seems that the products and applications that have progressed and excelled (i.e. those in the electronic category) are those that utilize top-down manufacturing methods. Top-down productions involve manipulations to existing material with various techniques that directly operate on a material. For example, transistor devices created from photolithography and selective etching or direct electron beam lithography of a resist film to create nanoscale features.

The products and applications lagging in the sophistication that was promised in the literature are relegated to bottom-up manufacturing. Bottom-up methods involve controlled synthetic approaches to develop the nanoscale architecture from molecular or atomic components. Nanoparticle synthesis is a prime example of a bottom-up procedure. A nanoparticle synthesis produces an ensemble of particles from the reaction of molecular components. If the reactions involved are not well-controlled, then the nanoparticle product will not be well-controlled. The sophisticated applications that take advantage of attributes like size-dependent properties require syntheses with excellent command over nanoparticle size.

However, size isn't the only important feature. The nanoparticle core comprises many different structural characteristics (Figure 1.3) each of which can influence properties. The core could have any of a variety of shapes such as spherical, plate-like, rod-like, branched, or some type of faceted polyhedron. If the nanoparticle is being used in a catalytic role, the specific shape could impact its performance.<sup>43</sup> The crystal phase in the nanoparticle can influence properties such as magnetism<sup>44</sup> as can defects in the crystal.<sup>45</sup> Some defects are desired, such as oxygen vacancies in Sn-doped indium oxide to increase conductivity for example.<sup>46</sup> If there is a mix or a broad dispersion of one of these characteristics in a nanoparticle ensemble, then the properties of the ensemble will also vary.

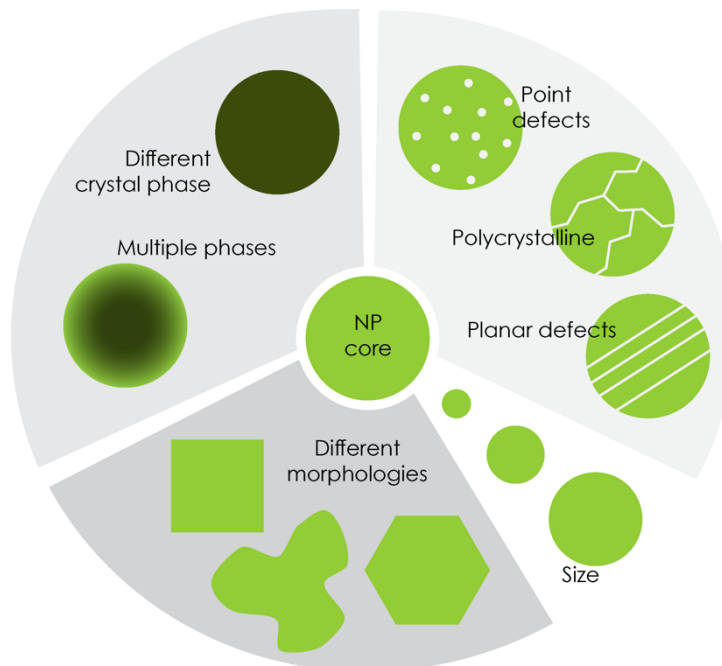


**Figure 1.3.** Structural features of a nanoparticle core that can influence properties.

A successful nanocrystal synthesis must reproducibly yield the desired nanocrystal size, shape, crystallinity, and phase. This is a difficult task considering the

large and nuanced parameter space affecting particle formation and growth. The nanoparticle crystal structure is sensitive to synthesis conditions such as the nanoparticle growth rate, synthesis temperature, or speciation of starting materials. For this reason, it is important to build an understanding of the molecular level processes of nanoparticle formation and growth.

## Metal oxide nanoparticles

It is well-worth the effort to develop synthetic methods for metal oxide nanoparticles specifically. Metal oxides tend to be abundant on Earth and, consequently, are inexpensive.<sup>47</sup> There is a vast number of current and potential applications for metal oxide nanomaterials that range from the pigments and cosmetics to environmental remediation and energy harvesting. Nanostructured metal oxides can be used in sensing applications,<sup>48</sup> as photocatalysts,<sup>49</sup> in the biomedical field,<sup>50</sup> and in environmental remediation<sup>51</sup>. Currently, nanostructured TiO<sub>2</sub> is used in self-cleaning coatings, ZnO is used as pigments in paints,<sup>51</sup> and CeO<sub>2</sub> is widely used in catalytic converters<sup>52</sup>. Many of the previously mentioned nanoparticle applications utilize metal oxide nanoparticles (for example, magnetic particle imaging and hyperthermia).

Because interest in nanoparticles came largely out of size-dependent properties, and, therefore, size-tunable properties, the size control was and continues to be the focus of nanoparticle synthesis methods. A generalized understanding of nanoparticle synthesis, known as classical nucleation theory, has been put forward time and again in the literature to describe nucleation and growth of nanoparticles. It stems from work by LaMer and et al. on their study of sulfur sols.<sup>53</sup>

## *Classical nucleation theory*

Classical nucleation theory describes how a fast and brief nucleation event can result in a uniform size distribution of nanoparticles. To summarize the theory, a precursor molecule (P in Figure 1.3) converts to some monomer (M in Figure 1.3) species. The concentration of monomer builds up to saturate the solution before finally nucleating because of a relatively large energy barrier to nucleation. This energy barrier is estimated by considering the difference between the (favorable) volume free-energy and (unfavorable) surface energy. When monomer concentration surpasses some critical concentration ( $[M]_{\text{crit}}$  in Figure 1.4), nucleation of nanoparticles occurs. The radius at which particle formation becomes favorable is called the critical radius. The critical radius and nucleation barrier can be used to estimate a nucleation rate. Generally, nucleation rate will increase with increases in temperature and supersaturation level but will decrease with surface energy.<sup>54</sup> Assuming the temperature and the surface energy are constant, rapid decrease in monomer concentration as it converts to nucleated particles is relied upon to cease the nucleation period.

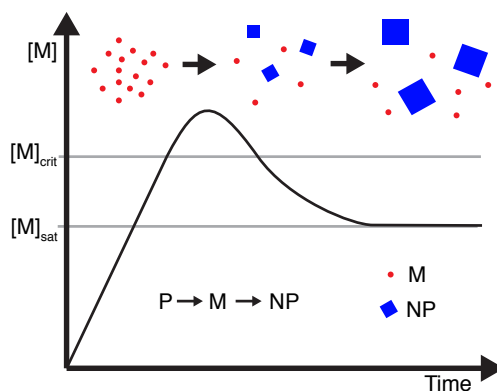


**Figure 1.4.** Nanoparticle nucleation and growth according to classical nucleation theory. Plot of monomer,  $[M]$ , as a function of time. The generic reaction equation shows precursor (P) converting to M (red dots) which forms nanoparticles (NP, blue squares).

Growth ensues thereafter from the reservoir of monomer solution that is no longer saturated enough to nucleate new particles. Thus, addition of monomer onto the existing nuclei occurs. Nanoparticle growth will occur up until the concentration of monomer drops to the saturation of the solvent ( $[M]_{sat}$ ). If monomer concentration drops too low, then dissolution from the surface of nanoparticles back to monomer will occur. Specifically, smaller particles that are less favorable because of their higher surface energy will tend to dissolve. The excess monomer may then grow onto larger particles. This process of small particles shrinking and larger particles growing is called Ostwald Ripening.<sup>55</sup>

Together the concepts of nucleation and growth from classical nucleation theory can help us understand the nanoparticle size achieved from syntheses. The number of nuclei formed is the main factor dictating the final size of the nanoparticles. If relatively few nuclei form, each one will consume more monomer from the left-over reservoir and be larger compared to the case when many nuclei form.

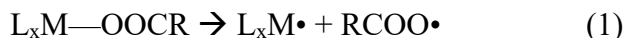
Classical nucleation theory has recently come under scrutiny (more discussion on this in Chapter VII), but it put forth useful concepts that apply to most nanoparticle syntheses. First is the idea that an intermediate species (monomer) forms from precursor, which is language commonly used in the literature and will be used in the remainder of the dissertation. Second is the idea of separating nucleation from growth in order to produce nanoparticles with narrow size dispersions. If nanoparticles are forming throughout the entire nanoparticle synthesis then nanoparticles formed early will be much

larger than ones formed towards the end, and the nanoparticle ensemble will have a broad size distribution.

#### *Heat-up methods: thermal decomposition and ester elimination chemistries*

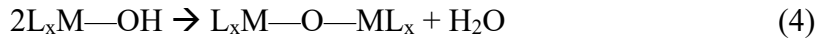
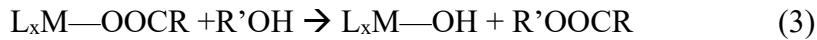
The most common type of metal oxide nanoparticle synthesis in the literature is the heat-up method. In the heat-up method, starting materials such as metal precursor, stabilizing ligands, and solvent, are put in a reaction flask together and heated at a controlled rate to high temperatures. Several factors can influence the approximate nanoparticle size achieved: the temperature ramp rate,<sup>56</sup> the reflux temperature,<sup>57,58</sup> and the ligand concentration<sup>59</sup> among other things. There are two main reaction chemistry scaffolds that produce narrow size dispersions of metal oxides in the literature: thermal decomposition syntheses and ester-elimination (or amide-elimination) syntheses.

In thermal decomposition procedures, metal precursor (typically a metal oleate) and excess ligand (typically oleic acid) are heated to reflux temperatures (typically 290 °C or greater) in high boiling point solvents such as octadecene. At these high temperatures, bond homolysis of metal carboxylates occurs yielding radical species:<sup>60</sup>



Radical species then react with one another or other precursor to begin forming metal oxide bonds of the nanoparticle.

In ester or amide-elimination syntheses, metal carboxylates react with alcohol or amine to produce an ester or amide and a metal hydroxide species (equation 3) followed by condensation of the metal hydroxide species to form metal oxide bonds (equation 4).<sup>61,62</sup>



In these types of syntheses, the temperature doesn't have to be as high as for thermal decomposition syntheses and is typically well below 300 °C.

While thermal decomposition syntheses have resulted in impressively narrow size dispersions of nanoparticles, they suffer from significant drawbacks. The monomers are radical species which react rapidly and indiscriminately with each other, precursor molecules, and likely solvent. The high temperatures employed in inert environments create a reducing atmosphere as a result of solvent decomposition<sup>63</sup> or as a result of metal precursor break down.<sup>60</sup> The highly reductive environments can affect the metal oxide phase even producing metal particles in some cases.<sup>64</sup> Furthermore, reactions involving the solvent can affect the nanoparticle formation and growth in unanticipated ways.<sup>65,66</sup>

Studying the thermal decomposition literature of iron oxide nanoparticles demonstrates that size isn't the only important structural feature. In 2004, Hyeon et al. demonstrated size dispersions of less than 5% (that is, one standard deviation divided by the average size) in iron oxide nanoparticles in a highly cited article in *Nature*.<sup>57</sup> Using this synthesis method resulted in researchers reporting magnetic properties of what they thought were magnetite (the ferrimagnetic phase) iron oxide nanoparticles when the nanoparticles were, in fact, contaminated with the more reduced paramagnetic wüstite phase.<sup>67</sup> Studies to explore the source of the unusual magnetic properties of wüstite-contaminated nanoparticles ensued.<sup>68</sup>

Ester or amide-elimination routes, on the other hand, can be carried out in milder conditions alleviating issues observed in thermal decomposition methods. Reactive metal

hydroxides form and produce nanoparticles at relatively low temperatures (< 260 °C) that thermal decomposition cannot access.<sup>69</sup> Undesired reduction of metal oxides can be avoided and well-defined chemical routes lead to more predictable syntheses.<sup>70,71</sup>

#### *Slow addition methods*

Chemistry aside, slow addition methods are an alternative to the heat-up methods and provide their own set of values. In slow addition methods, metal precursor is added (usually with a syringe pump) at a slow, controlled rate into a reaction flask containing solvent at elevated temperatures. One advantage that slow addition methods offer is eliminating the fate of final nanoparticle size on the nanoparticle formation event. In a heat-up method, the number of nanoparticles that form will dictate the resulting nanoparticle size. As the nanoparticle formation event is highly sensitive to reaction parameters such as, temperature, concentration of monomer, surfactants present,<sup>54</sup> and nuances of precursor preparation,<sup>72</sup> it can be difficult to reliably produce a specific desired nanoparticle size. In a slow addition synthesis, the number of nanoparticles formed is still sensitive to reaction conditions, but the final nanoparticle size can be dictated by the amount of precursor added.

Additional advantages come from the ability to study the nanoparticles throughout the synthesis. Because nanoparticle growth occurs over the time of the precursor addition, samples of reaction solution can be taken and analyzed offering snapshots at different stages of the synthesis.<sup>73</sup> The precursor addition rate can be adjusted as well, which can enable the study of how different growth rates and temperatures affect the nanoparticles.

### *Combining ester-elimination chemistry with the slow addition approach*

The Hutchison lab has developed a metal oxide nanoparticle synthesis that combines the merits of the slow addition method with ester-elimination chemistry. Slow addition of a metal oleate precursor into hot oleyl alcohol (typically 230 to 290°C) leads to the continuous, controlled growth of nanoparticles. Oleyl alcohol serves as both a solvent and a reagent. Because alcohol is present in a large excess compared to the metal oleate precursor, esterification (and, therefore, metal hydroxide formation) reaction kinetics are pseudo first order thereby simplifying the variable space. Normally, water formed as a byproduct of metal hydroxide condensation would be an issue at these temperatures—causing rapid evaporation and bumping—but under these circumstances, water formation is slow due to the slow addition of precursor.

The slow addition approach makes the synthesis adaptable to different reaction conditions and metals, which the Hutchison lab has exploited. This adaptability is possible because the precursor addition rate limits nanoparticle growth rather than the reactant concentrations and reactivities. Thus, addition rates can be tuned as needed to fit different reaction conditions and materials. We have developed the indium and iron systems to have excellent control over nanoparticle growth (as will be demonstrated in later chapters) because of this attribute of the slow addition synthesis. In doped indium oxide syntheses, dopant incorporation efficiency is high and leads to an even distribution of dopant throughout the nanoparticle<sup>74,75</sup> since the incorporation of dopant metals and matrix metals is not dictated by the variable reactivities of the metal precursors. Adjustment of the precursor addition rate also allows controlled nanoparticle growth at different temperatures under similar reaction chemistry, which may sound

straightforward but isn't. In heat-up methods, the synthesis temperature is set by the solvent boiling point. Using different solvents leads to the introduction of another influencing synthetic variable since solvents can affect the precursor reactivity and the redox environment.<sup>65</sup> The slow addition methods can be carried out with the same solvent at different temperatures because the addition rate of the precursor can be adjusted to accommodate the slower (at lower temperatures) or faster (at higher temperatures) precursor to monomer conversion.

Characteristics of the reaction chemistry compliment the slow addition approach. The large excess of alcohol available drives esterification forward to create the reactive metal hydroxides, which readily condense at the temperatures used for synthesis (above 200 °C). As a result, the synthesis has high reaction yields (typically above 90%). Additionally, esterification and condensation chemistry are irreversible, so etching or dissolution from the surface of the nanoparticle is typically not observed. There is little opportunity for bond hydrolysis since water generated during condensation is quickly driven off. Excess ligand, which may have the ability to etch nanoparticles, is not readily available since it is consumed by esterification. The stability of the nanoparticles after growth processes also contributes to the high reaction yields.

Together, the slow addition rate and high reaction yield enable a unique and powerful way to analyze the nanoparticle synthesis. By removing and characterizing aliquots of the reaction liquid throughout a synthesis, a plot of nanoparticle size as a function of precursor consumed can be constructed. The nanoparticle size in an aliquot removed at a particular time is correlated to an amount of precursor added to the reaction. The amount of precursor added can be assumed to be the amount of precursor consumed

since the reaction yield is high (due to the esterification/condensation chemistry) and nanoparticle growth is being limited by the slow addition. A plot of size, specifically the nanoparticle volume, versus precursor consumed enables evaluation of the synthesis. This concept is explored in Chapters II and III. If the number of nanoparticles growing during synthesis is stable, then the plot can be used in a predictive manner. One could calculate how much precursor to add in order to grow a desired nanoparticle size.

While size control is important, so are other qualities of the nanoparticle core structure (as highlighted in Figure 1.3 and above discussions). Previous work in the Hutchison lab has explored and demonstrated excellent composition control. Much of this dissertation leverages the unique attributes of the slow addition synthesis to study morphology and defect control by examining growth processes.

## Dissertation overview

This dissertation will explore nanoparticle growth, structure property relationships, and the utilization of nanoparticles in nanocomposites. Chapter II introduces a new way to consider and classify nanoparticle synthesis methods highlighting the slow addition synthesis developed in the Hutchison lab. Chapters III and IV leverage the advantages of the slow addition synthesis to study nanoparticle growth of indium oxide and iron oxide nanoparticles. Chapter V examines size-dependent magnetization by utilizing the well-controlled growth of small spinel iron oxide nanoparticle. Chapter VI is an attempt to bring nanoparticles closer to real-world communications applications by developing high permittivity and high permeability nanocomposite inks and 3D printing techniques.

Chapter II highlights the similarities between certain types of nanocrystals syntheses and living polymerization chemistry. This chapter defines attributes of living nanocrystal syntheses and classifies syntheses put forth in the literature with respect to these attributes. It goes on to discuss the implications for structural control over nanocrystal growth and the progress that's been made in the Hutchison lab with the slow addition synthesis which embodies the concept of living growth. This work was written by Adam Jansons and myself with the guidance of Jim Hutchison.

Chapter III explores how nanocrystal growth is influenced by the flux of monomer species and the synthesis temperature in indium oxide system. The living growth attributes highlighted in chapter II are leveraged to study the aspects of nanocrystal growth that are not possible to examine directly in other types of syntheses. In particular, we explored the effect of monomer flux to the nanoparticle surface and synthesis temperature. Going beyond just control of nanocrystal structure, we develop an understanding of the molecular mechanisms at play during growth to yield particular nanocrystal structures. Towards this end, we developed a metric, the perimeter to diameter (P/D) ratio in order to assess nanoparticle morphologies. We found that at any particular synthesis temperature, increasing monomer flux increased the degree of branching. However, the higher the temperature, the less sensitive nanocrystal morphology was to the monomer flux. We propose this is due to the ability of monomer species to migrate on the nanocrystal surface. The results and our conclusions have implications for heat-up and hot-injection syntheses where monomer concentrations gradually diminish towards the end of nanocrystal growth period and contribute to faceting. This synthetic work and characterization were carried out by myself, Brandon

Crockett, and Makenna Pennel with concepts of the work informed by Kris Koskela and Adam Jansons. Brandon Crockett, Makenna Pennel, and myself wrote the manuscript with guidance from James Hutchison.

Chapter IV examines the effect of ligation and iron oxidation state in the iron precursor on the production of twin defects in iron oxide nanoparticles. Iron oxide nanoparticle syntheses are highly studied because of their promise for a wealth of applications but also complicated owing largely to the variable oxidation state of iron under common synthesis conditions. The continuous/slow addition synthesis using an Fe (III) oleate precursor yielded magnetite nanoparticles with a variety of morphologies, which was a result of twinning defects formed early in nanoparticle formation and growth. Based on the studies in this chapter and structural analyses in the literature on twin defects, Fe (III) acetylacetonate species appear to be more difficult to reduce compared to pure Fe (III) oleate. We believe this redox behavior leads to twin defect formation. This discovery was utilized to demonstrate continuous, living growth when a mixed oxidation state precursor is used and highly twinned nanoparticles when a greater degree of acetylacetonate is ligated to the Fe (III) precursor. This synthetic work in this chapter was carried out by myself and Kiana Kawamura. It was written by myself with the guidance of Jim Hutchison and is intended to be submitted for publication.

Chapter V utilizes the well-controlled synthesis of small (< 10 nm) iron oxide nanocrystals with the Fe (II) rich oleate precursor to examine size-dependent magnetic properties. The nanoparticles were highly crystalline, possessed the spinel crystal structure, and were primarily the maghemite crystal phase. The magnetic properties were exemplary, exhibiting higher saturation magnetizations than most similarly sized

nanocrystals. When modelling the magnetization curves using the Langevin function, the effective magnetic size is nearly commensurate with the physical size. By our estimations, a non-magnetic surface layer exists that is less than 0.2 nm thick, which is much thinner than the literature reported previously. These results suggest that attributes of the synthesis—namely, slow growth with well-defined chemical route—are responsible for the high degree of magnetism. This chapter was written by myself, Susan Cooper, and Pallavi Dhagat with direction and assistance with Jim Hutchison and Pallavi Dhagat. Synthetic work and physical characterization were carried out by myself, Susan Cooper, and Alexia Cosby. Magnetic characterization was carried out by Philip Lenox, Albrecht Jander, and Pallavi Dhagat.

In Chapter VI, nanoparticles are bridged towards communications applications by producing nanocomposite plastics via 3D printing techniques with the aim of tuning dielectric permittivity and magnetic permeability in the composite. Two approaches were taken towards producing the nanocomposite: 1) by polymer particle bed infiltration and fusing; 2) by inkjet printing a polymerizable nanocomposite ink. To develop inks, BaTiO<sub>3</sub> nanoparticles and synthesized hexaferrite nanoparticles were surface functionalized with acrylic acid and disperse in diethylene glycol diacrylate monomer. The nanocomposite ink was alternately printed and cured with UV light layer by layer to produce a nanocomposite film using a Dimatix 3D materials printer. Nanoparticle loadings up to 20 % by weight were achieved with the inkjet printing. To achieve higher loadings, cured samples were prepared by hand for the purposes of measurements. Increasing BaTiO<sub>3</sub> loading increased permittivity of the composite. Hexaferrite composite showed only limited permeability. The difference between the composites and

matrix alone was not high, so future work should aim to increase nanoparticle loadings by inkjet printing as well as identify and synthesize more appropriate materials. Jim Hutchison, Pallavi Dhagat, and Albrecht Jander conceptualized this work. Khalid Masood performed simulations. Tatiana Zaikova and I performed synthetic work for the inkjet printing of polymerizable nanocomposite ink approach while Jim Stasiak, Paul Harmon, and Thomas Allen performed work for particle bed infiltration and fusing approach. This work was written by all listed.

## CHAPTER II

### LIVING NANOCRYSTALS

This chapter was previously published as Jansons, A. W.; Plummer, L. K.; and Hutchison, J. E. Living Nanocrystals. *Chem. Mater.* **2017**, *29*, 5415–5425.

#### **Introduction**

Nanoparticles and nanocrystals hold promise as breakthrough materials for many exciting new applications because of their unique size-dependent properties. During the last several decades, new applications have been reported across nearly every technological sector, including human health,<sup>1</sup> electronics,<sup>2,3</sup> optics,<sup>4,5</sup> energy storage and production,<sup>6</sup> chemical catalysis,<sup>7</sup> and sensing.<sup>8</sup> New synthetic methods have been developed to gain access to nanomaterials needed for these applications, facilitating broader adoption.<sup>9–17</sup> Each new generation of applications demands higher performance nanomaterials, requiring more precise control over the structural features that dictate properties and performance – core size, composition, and surface chemistry. In many cases the pioneering synthetic methods used to discover new materials and applications don't offer the required level of precision. Thus, new applications drive the need for synthetic approaches that offer greater control of the atomic-scale structure and composition of the nanoparticle building blocks.

Some of the most transformative approaches to material synthesis are those that permit atomic level control over composition and structure. For example, vapor-phase

synthetic methods, e.g., atomic layer deposition and molecular beam epitaxy, achieve such resolution in the case of inorganic thin films.<sup>18,19</sup> Advances in vapor phase synthetic methods have afforded access to kinetically-stable compounds, in addition to traditional thermodynamically stable products, and greatly increased the number of structures and properties that can be obtained with a specific stoichiometry.<sup>20,21</sup> Such synthetic methods offer an invaluable approach to control the properties of solid-state materials for demanding applications. The same level of control in liquid phase colloids has been much slower to develop. Perhaps the two best liquid-phase examples from materials chemistry are biomineralization mechanisms<sup>22</sup> and polymerization reactions.<sup>23</sup>

There have been many advances in nanocrystal and nanoparticle synthesis during the last decade; however, most of the commonly employed synthetic methods offer far less structural control than the well-honed reactions employed for small molecule or polymer synthesis. Developing methods to synthesize nanomaterials with uniform core sizes and specific composition with intentionality and reproducibility will enable research on the interplay of size, composition, and structure, as well as facilitate the translation to commercial application. The challenge in gaining such control with colloidal nanocrystal syntheses is understandable and expected – a nanocrystal synthesis must manage the complexities of nucleation and growth in solution,<sup>24</sup> and is further burdened by size- and structure-dependent surface energies. One approach to addressing these challenges is to take inspiration from macromolecular strategies where precise synthetic methods have provided dramatically improved structural control.

Our group recently discovered a new synthetic method to produce metal oxide nanocrystals that is analogous to, and inspired by, living polymerization methods. It

allows unprecedented control over nanocrystal composition and structure. In this perspective, we discuss the synthetic challenges that can be overcome by adopting synthetic approaches to nanocrystals that leverage the attributes of living polymerization methods, with an emphasis on the production of metal oxide materials. We first discuss how commonly employed synthetic methods fit within the definition of a living growth synthesis. We highlight the fine control that is possible with living growth, namely, nanocrystal core size, nanocrystal dopant composition, and the radial position of dopants within a host material. We discuss the implications for the production of core/shell nanocrystals using this approach, and finally note future opportunities to discover, understand and develop living growth methods.

### **Living Synthetic Approaches to Macromolecules, including Nanocrystals**

The discovery and development of living polymerization made it possible to control polymer structure and molecular weight and to understand how each of these influences physical properties, including viscosity, glass transition temperature, and osmotic pressure of polymer solutions.<sup>23,25</sup> Understanding these properties led to, among other things, the development of thermoplastics, non-leaking battery solvents, and an understanding of important biological phenomena.<sup>25</sup> Living growth approaches forever changed polymer science.<sup>25,26</sup>

In living polymerizations, the same number of polymer chains remain present during propagation (growth) steps, chains propagate at the same rate, and chains do not self-terminate (stay living), which allows for the simple production of advanced structures through the addition of a chemically different reactive monomer.<sup>27</sup> Irreversible chain addition reactions, which prevent monomers from detaching from existing chains,

and reactive sites that prevent random chain termination are also key features of living polymerization.<sup>25</sup> An important hallmark of a living process is a linear correlation between the molecular weight of a polymer and the extent of monomer conversion; a phenomenon that allows predictable control of molecular weight with very fine resolution (Figure 2.1). Furthermore, monomer consumption is often near 100%, which contributes to the high level of predictability and control.

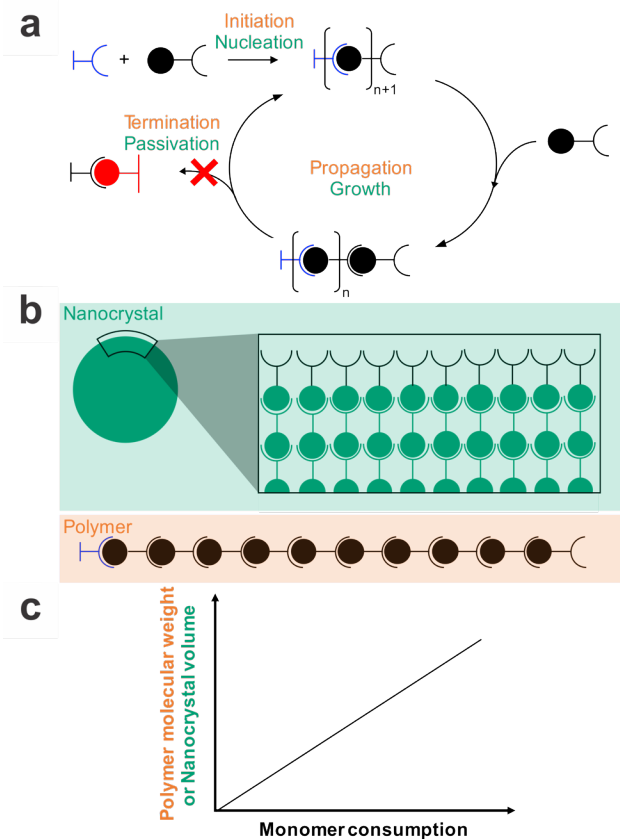


**Figure 2.1.** a) The reaction cycle shows the general steps of a living process either for polymerization (orange lettering) or nanocrystal growth (green lettering). Starting materials initiate (or nucleate) to form species with a reactive site. Addition of monomer to this reactive site results in the generation of another reactive site (referred to as propagation or growth). In a living system, growth is indefinite, and proceeds without termination or passivation. b) Examples of a nanocrystal (green) or polymer (orange) that would result from the general scheme in a. c) A growth curve for a polymer or nanocrystal. Living growth is characterized by a linear correlation between monomer consumption and polymer molecular weight (for polymers), or a linear correlation between monomer consumption and nanocrystal volume (for nanocrystals).

Analogies between polymers and nanocrystals have been described.<sup>14,28,29</sup> Indeed, synthetic polymers and nanoparticles share many characteristics: not only do the properties of both materials depend on their size (or molecular weight) and composition, they are also characterized and described in much the same way - by type, average size, and polydispersity. The terminology of polymer chemistry and nanoparticle chemistry has many parallels (Table 1). A *living* approach to nanocrystal synthesis might possess attributes similar to living polymerization; it could produce product with low size dispersions, support further growth with additional monomer (i.e. not be limited in size), and result in high yields (i.e. precursor/monomer should be nearly completely consumed). Growth could be controlled precisely (e.g., layer-by-layer) in an intuitive manner involving living growth on the surface rather than undesirable processes, such as new nucleation, ripening or coalescence, that (often) lead to a loss of synthetic control. Such living growth processes would offer a deliberate approach to assembling complex nanoscale structures.

Despite the analogies between polymers and nanocrystals, an important difference is the organic/inorganic interface. In the inorganic systems, surface chemistry will play an important role in any living growth process. Most nanocrystals are stabilized by surfactants (or ligands) during the growth process. If the ligands are too weakly bound, the nanocrystal will be prone to coalescence, whereas ligands bound too strongly will impede growth. Having proper surface reactivity, with labile surfactants and maintenance of reactive (living) sites for monomer addition, allows propagation of growth on the particle surface. Alternatively, a surface that is too stable, with strongly bound surfactants

and/or the absence of reactive sites will not be conducive to epitaxial growth. As a result of a more stabilized surface, any growth will result in polycrystalline nanoparticles and/or monomer will accumulate in solution, ultimately leading to new nucleation events and a dispersion of sizes.

**Table 2.1.**Analogous concepts and terminology between polymers and nanoparticles.

	<b>Polymer synthesis</b>	<b>Nanoparticle synthesis</b>
<b>Analogous Terminology</b>	Chain	Particle
	Initiation	Nucleation
	Propagation	Growth
	Chain termination	Particle passivation
	Block copolymer	Core/shell particle
	Random copolymer	Doped particle
<b>Similar Terminology</b>	Size	
	Dispersity	

Given the transformative nature of living polymerization methods, and the striking similarities between nanocrystals and polymers, obvious questions arise; do nanocrystal synthetic methods exist today that share the important attributes of living polymerization? How can one identify existing synthetic methods as living, or develop living synthetic methods for nanocrystals? If living approaches exist, to what degree can they be leveraged for improved composition and structural control? Below we analyze

common methods of nanocrystal synthesis with a lens towards identifying living processes, and defining their synthetic prerequisites, behaviors, and outcomes.

### *The hunt for living growth methods*

Currently many liquid-phase synthetic methods exist for the production of nanocrystals, including (but not limited to) aqueous reduction, aqueous sol-gel, non-aqueous sol-gel, hydrothermal/solvothermal, thermal decomposition, and hot-injection.<sup>9,13,30–32</sup> Of those commonly employed for the production of monodisperse oxide nanocrystals, methods that take place in high-boiling organic solvents, including heat-up and hot-injection methods, are utilized the most.<sup>33</sup> Under these conditions, the key requirements for the production of uniform nanoparticles are thought to be the separation between nucleation and growth phases as outlined by LaMer<sup>24</sup> and the management of aggregation or Ostwald ripening (or “defocusing” events).<sup>34</sup>

At first glance, seeded growth methods mirror living growth processes.<sup>14,35–41</sup> Seeded growth techniques are applicable for a wide variety of semiconducting and metallic structures and have been successfully utilized to tune nanocrystal size for decades, sometimes with fine resolution.<sup>35</sup> In these methods, growth might take place through either heterogeneous nucleation on the particle surface or through discrete monomer addition to surface reactive sites, but the details are typically unknown. If a seeded growth synthesis is “living”, one would expect the addition of more monomer to result in a *predictable* increase in core size (i.e. proceed with no aggregation, ripening, or new nucleation). In the majority of seeded growth literature, the number of particles present during the growth stage(s) or the expected size increase with precursor addition is not reported (with few exceptions<sup>36,42</sup>). Living syntheses should produce single crystal,

homoepitaxial nanocrystals, which suggests monomer adds to a reactive surface instead of heterogeneous nucleation on the particle surface. It is often unclear in the seeded growth literature whether particles are single crystals. A recent study on the magnetic properties of iron oxide found that nanocrystals obtained from seeded growth methods produced strained regions in the nanocrystal, leading to anomalous magnetic properties.<sup>43</sup> Finally, in living growth, monomer addition onto a crystal is an irreversible reaction, thus the rate of dissolution of monomer from the crystal surface should be negligible. As a result, no change in particle size or dispersion is expected upon annealing. Table 2.1 outlines the prerequisites, synthetic attributes, and outcomes of living nanocrystal syntheses.

*Slow addition of reagent to preformed seeds can result in monodisperse nanocrystals of metals, oxides and semiconductors.*<sup>42,44-47</sup> Some of these may be living growth processes, although it is difficult to know because predictions about expected nanocrystal sizes are not typically given, and size sorting processes (like size selective precipitation) are frequently utilized. The need for size selection implies that new nucleation has occurred during the growth process.

The Huber group found that size of iron oxide nanoparticles could be controlled predictably with sub-nanometer precision through the slow addition (3 mL/hr) of iron carboxylate into hot docosane and oleic acid.<sup>44</sup> Using small-angle X-ray scattering analysis (SAXS) they showed a linear correlation between nanocrystal volume and precursor addition (expected for living processes, Figure 2.1), and were able to grow nanocrystals to “arbitrarily large sizes.” The reaction presumably proceeds through a type of thermal decomposition mechanism given that the reaction temperature (350°C) is

well above the thermal decomposition point of the iron oleate precursor (onset ~200–240°C).<sup>48</sup> The study is a tremendous advance in the synthesis and size control of iron oxide nanocrystals. However, there is still much to learn about this growth process: Is new monomer being incorporated by surface reaction(s), or is heterogeneous nucleation the cause for the observed growth behavior? Further, is there particle ripening upon annealing?

**Table 2.2.** Connection between prerequisites, synthetic attributes and outcomes for living growth nanocrystal synthesis.

Prerequisites	Synthetic attributes	Outcomes
<ul style="list-style-type: none"> <li>Maintenance of reactive surface (no surface passivation)</li> <li>Constant number of growing species</li> <li>Non-reversible monomer addition</li> </ul>	<ul style="list-style-type: none"> <li>Predictable, linear growth of core molecular weight (volume) with monomer consumed</li> <li>Addition of more monomer results in further growth</li> <li>No ripening upon annealing</li> <li>High yield</li> </ul>	<ul style="list-style-type: none"> <li>Highly tunable size with narrow dispersity</li> <li>High level of control over structure &amp; composition</li> <li>Single crystal particles</li> </ul>

Our group recently discovered a synthetic route that embodies the attributes of a living growth process outlined in Table 2.1. Slow addition of metal carboxylates into oleyl alcohol at temperatures below the thermal decomposition point of the precursor affords a large variety of metal oxide nanocrystals (including In<sub>2</sub>O<sub>3</sub>, γ-Fe<sub>2</sub>O<sub>3</sub>, Mn<sub>3</sub>O<sub>4</sub>, CoO, and ZnO).<sup>49</sup> The reaction proceeds via the esterification of metal oleates to produce metal hydroxides, which then condense onto the particle surface (Figure 2.2). We were initially surprised by several aspects of this synthesis. It seemed particularly unusual that the *slow* addition of reagents produced single crystalline, monodisperse nanocrystals in

very high yield (often >90%). One would normally expect the addition of more metal precursor to result in the new nucleation of nanocrystals, which would significantly increase the size distribution. Because the method produces monodisperse nanocrystals, we sought to understand the growth mechanism.

Using  $\text{In}_2\text{O}_3$  as a model system, and a combination of transmission electron microscopy (TEM) and small-angle X-ray scattering analysis (SAXS), we investigated how nanocrystal size, size dispersion and shape evolved as a function of metal precursor addition. With SAXS, we could also investigate the number of nanocrystals present in solution. We found that nanocrystal volume grows linearly with the amount of precursor added (Figure 2.2) and the number of nanocrystals present during this time is constant. These findings suggest that growth proceeds through a living process.<sup>50</sup> Even more extraordinary, the nanocrystals can be left in reaction solution at elevated temperatures for hours without a change in the average size or size dispersion, and are susceptible to further predictable growth upon addition of monomer after this “annealing” period. Since the publication of this finding we have reliably made nanocrystals from three to more than 30 nm in diameter in gram quantities and have yet to find a maximum size that can be produced. We believe this growth mechanism is sustained by hydroxyls continually present on the nanocrystal surface, and reactive hydroxyls produced via the esterification of metal oleates with oleyl alcohol (Figure 2.2).

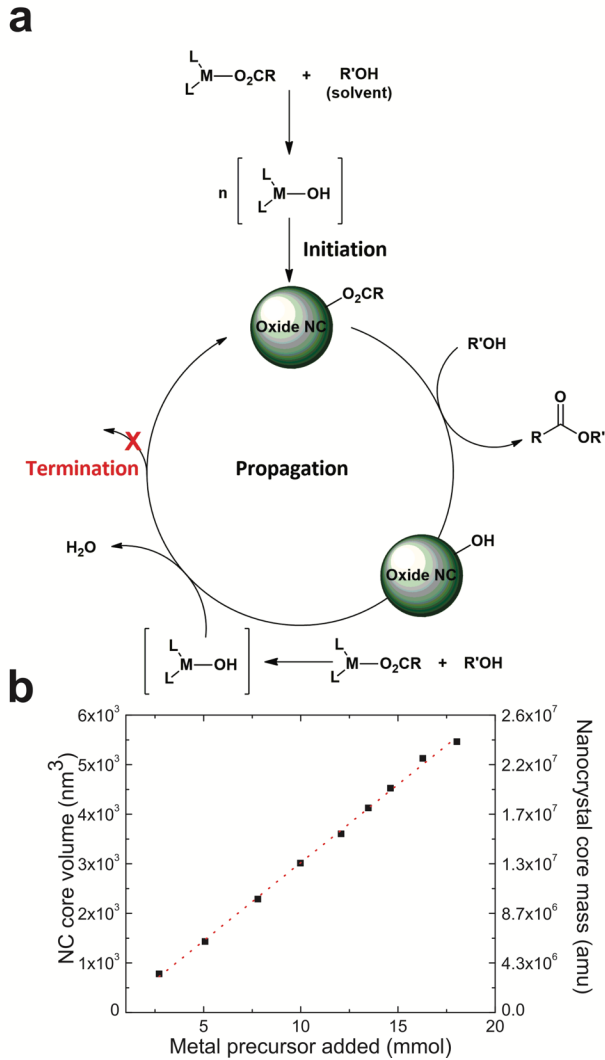


**Figure 2.2.** **a)** Schematic representation of our living growth synthesis of metal oxide nanocrystals. Slow addition of metal oleate promotes metal hydroxide formation leading to initiation of nanocrystal growth. Nanocrystals continue to grow during propagation as additional monomer is added. Metal hydroxyls on the nanocrystal surface support a living growth mechanism. **(b)** SAXS data taken during the synthesis of  $\text{In}_2\text{O}_3$  nanocrystals. We found a linear correlation ( $R^2 = 0.998$ ) between the nanocrystal core volume (e.g. core molecular mass) and the amount of metal precursor added to the reaction flask. Analogous to a living polymerization reactions, this synthetic method allows access to particle sizes with sub-nanometer precision, as well as the logical preparation of more complex structures and compositions, including doped and core/shell nanocrystals. Adapted with permission from reference 47. Copyright 2016 American Chemical Society.

Our findings from these initial studies pointed towards a growth mechanism for metal oxide nanocrystals that we believe has unmatched potential. Drawing analogies to polymer chemistry (Table 1), we sought to apply these ideas to living nanocrystal growth and harness the attributes of living growth to produce structures and compositions previously impossible to synthesize. In the following sections, we describe three tests of the potential of our living growth system, highlighting the advantages and significance of this new approach.

### **Leveraging Living Methods to Achieve Advanced Structural Control**

#### *Increasing doping efficiency*

Doping, or the intentional introduction of extrinsic defects, is a common way to impart new electronic, optical, or magnetic properties within inorganic materials and is critical for the development of high-performance applications of these materials. Doping bulk materials, via diffusion or ion implantation, is now commonplace and essential to the electronics industry. Doping methods for colloidal nanocrystals, however, are much less developed. Excellent, recent reviews on the subject can be found in the literature.<sup>51-53</sup> Not surprisingly, because of the high energy required to substitute dopant atoms within the host framework of a nanocrystal, dopants are often excluded to the surface, form new clusters or secondary phases, or are not incorporated into the crystal at all.<sup>54</sup> Because of the inherently small number of atoms in a nanocrystal, small changes in the number of dopant atoms can result in the drastic alteration of properties. As a result, it is imperative that the concentrations of dopants be predictably controlled within a material. Living

growth methods for nanocrystal synthesis should enhance the extent of structural control one can gain over nanocrystal composition and structure, particularly dopant distribution.

A key prerequisite to effective doping in nanocrystal synthesis is matching host and dopant precursor reaction rates in order to successfully incorporate and substitute dopant atoms into a host lattice.<sup>51</sup> Reliable incorporation of dopant atoms can be extremely challenging using traditional approaches. In thermal decomposition reactions for instance, precursor reactivity must be considered and estimated in order to achieve even modest doping efficiencies. As an extreme example, the synthesis of Mn-doped ZnS nanorods at 1.6 atomic % required a 20 molar % Mn<sup>2+</sup> precursor solution (an incorporation efficiency of only 8%).<sup>55</sup> While such low efficiency could be improved greatly by altering the choice of the reagents, finding the appropriate precursor given the synthetic conditions can be a challenge. An improvement in dopant incorporation efficiency seems to have emerged thanks to the recent utilization of so called “nonaqueous sol-gel” routes to produce doped nanocrystals.<sup>32,56–60</sup> These mechanisms rely on defined molecular transformations, rather than thermal decomposition, to arrive at the final doped product. In general, utilization of predictable chemistries to produce metal-oxygen bond formation, facilitated by ester, amide, or ether formation, can simplify the choices of appropriate metal precursors, and allow for higher doping efficiency. However, just as in thermal decomposition reactions, if both dopant and host precursor do not catalyze bond formation at the same rate, then the desired doped product may not be formed.<sup>56,60</sup>

We hypothesized that utilization of our *slow* injection, living growth method<sup>49</sup> would allow for more effective dopant incorporation, as any small differences in metal-

catalyzed esterification rate would be overcome by the slow nature of precursor addition. Additionally, rather than carefully selecting metal precursors based on perceived reactivity, we chose to simply use metal oleates in desired molar ratios. We doped  $\text{In}_2\text{O}_3$  with  $\text{Mn}^{2+}$ ,  $\text{Fe}^{3+}$ ,  $\text{Co}^{2+}$ ,  $\text{Cu}^{2+}$ , and  $\text{Zn}^{2+}$  ions, each with nominal concentrations of 5, 10, and 20 molar % dopant (Figure 2.3). The dopant incorporation in  $\text{Cu}^{2+}$ :  $\text{In}_2\text{O}_3$  nanocrystals matched that of the precursor with ~70% efficiency, while the incorporation in  $\text{Mn}^{2+}$ ,  $\text{Fe}^{3+}$ ,  $\text{Co}^{2+}$ , and  $\text{Zn}^{2+}$ :  $\text{In}_2\text{O}_3$  nanocrystals doped with an impressive >90% efficiency, as measured my inductively coupled plasma optical emission spectroscopy (ICP-OES). Powder X-ray diffraction (XRD) confirm that the nanocrystals are bcc- $\text{In}_2\text{O}_3$  (Figure 2.3), and by using Reitveld analysis can confirm the decrease in lattice constant with increasing dopant concentration, as expected when smaller dopant cations replace larger  $\text{In}^{3+}$  cations. The nanocrystals are formed with small size dispersions, and the mean size of the nanocrystal can be altered with same level of precision as undoped nanocrystals (Figure 2.2).<sup>50</sup> We find agreement in dopant concentration of the entire sample (using ICP-OES) to the nanocrystal surface dopant concentration (using X-ray photoelectron spectroscopy, XPS). This indicates that the dopants are not surface segregated, and distributed homogeneously throughout the sample. While host and dopant cation size will invariably play a role into incorporation efficiencies, we demonstrate that higher incorporation is possible if synthetic methods operate with living attributes. We anticipate this discovery should pave the way for further studies utilizing doped nanocrystals, including co-doped systems.

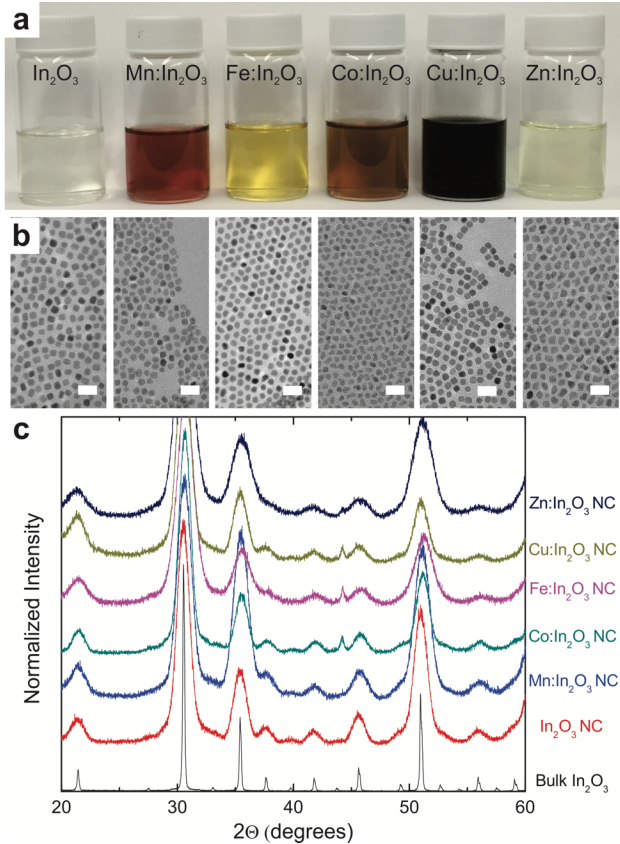


**Figure 2.3.** **a)** Doped oxide nanocrystals that have been purified and suspended in hexanes. The vials, from the left to right, correspond to undoped  $\text{In}_2\text{O}_3$ ,  $\text{Mn}^{2+}:\text{In}_2\text{O}_3$ ,  $\text{Co}^{2+}:\text{In}_2\text{O}_3$ ,  $\text{Fe}^{3+}:\text{In}_2\text{O}_3$ ,  $\text{Cu}^{2+}:\text{In}_2\text{O}_3$ , and  $\text{Zn}^{2+}:\text{In}_2\text{O}_3$  all doped at 10 atomic %. Corresponding TEM images of samples from each solution are found in **(b)**, directly beneath the vials in **(a)**. Scale bars are 20 nm. Powder X-ray diffractograms from each of the samples is displayed in **(c)**. All diffraction patterns match the bcc- $\text{In}_2\text{O}_3$  crystal structure.

#### *Intentionally modifying the radial position of dopant atoms within nanocrystals*

Unique properties can be harnessed in materials when synthetic methods can alter structure on the atomic scale. An excellent example of this is the drastic difference in properties that arise between doped nanocrystals that have the same composition but different radial placement of dopants within the nanocrystal. One might logically expect this due to the different chemical environments of surface vs. buried inner atoms.

Sometimes these properties can provide useful insight. For instance, different electronic absorption features between tetrahedral surface-bound dopants and tetrahedral substitutional dopants aided in understanding the growth mechanism of doped ZnO.<sup>61</sup> Controlling the specific placement of dopants *with intention*; however, has been difficult, and prevailing colloidal nanocrystal synthetic methods provide very little opportunity to produce structures with deliberate dopant placement. Nanocrystals produced in a living manner on the other hand, with layer-by-layer control over composition, would allow the precise placement of dopant atoms within a nanocrystal, thereby granting the synthetic chemist an enhanced level of mastery over important properties.

One important property that arises in many doped oxide nanocrystals is the near-IR or IR localized surface plasmon resonance absorption (LSPR). LSPRs arise in many heterovalent doped-oxide nanocrystal because extrinsic defects contribute free electrons into the conduction band of the material and oscillate at a particular frequency.<sup>62</sup> These materials have become an area of active research interest because of their potential in chemical sensing, biology, electronics, and energy production.<sup>63–67</sup> Key metrics of LSPRs are quality (LSPR<sub>max</sub> energy divided by the full width at half maximum of the LSPR) and dopant activation (the number of free electrons in the nanocrystal divided by the number of dopant atoms).

It has been found empirically that different synthetic methods for doped oxide nanocrystals lead to differences in the radial position of dopants. Different reactivities of the metal precursors and ligand types presumably influence the extent and timing of dopant incorporation. In a striking example that demonstrates the large influence the radial placement of dopant atoms has on material properties, the Milliron group

investigated two different synthetic methods for Sn-doped indium oxide (ITO) nanocrystals.<sup>68</sup> They found that one method produces homogeneously-doped ITO and the other produces surface-doped ITO. They attributed the large difference in the LSPR response to the radial distribution of dopants. While the synthetic methods utilized for that study produced doped nanocrystals with varying radial distribution of dopants, such distributions were not the intended outcome of the original synthetic methods.<sup>69,70</sup> Furthermore, these synthetic methods do not allow for independent control of dopant concentration, the radial distribution of dopants, and nanocrystal size.

We recently demonstrated that utilizing our slow injection approach,<sup>49,50</sup> one can intentionally tune the optically properties of ITO nanocrystals through precise control over the radial distribution of dopants.<sup>71</sup> We synthesized ITO/In<sub>2</sub>O<sub>3</sub> core/shell (core-localized dopant), In<sub>2</sub>O<sub>3</sub>/ITO core/shell (surface-localized dopant), and homogeneously-doped ITO nanocrystals and investigated the differences in LSPR response (Figure 2.4). Using a combination of elemental analysis by both ICP-OES (that yields composition information about the entire nanocrystal sample) and surface analysis by XPS, we confirmed the radial locations of the dopants in each of the three cases. Because the synthetic method operates with living attributes, production of the nanocrystals was a simple, one-pot reaction that did not require purification in between precursor addition(s) (Figure 2.4).

We followed LSPR response as a function of doped or undoped shell thickness and showed that core-localized doped nanocrystals have significantly higher dopant activations and quality factors. We confirmed that these large differences between the nanocrystals are due to the presence of defects and inactive dopants on the surface of the

nanocrystal. Because small, sub-nanometer shells can be grown onto the core nanocrystal using our approach, we showed that it was possible to activate surface dopants through the addition of a small, sub-nanometer undoped shell to a doped surface.

Using a living approach allows significantly enhanced control over LSPR<sub>max</sub> and quality factor and allows one to rationally sculpt optical properties for specific application. Undoubtedly, the importance of enhanced command over the radial placement of dopant atoms will extend beyond that of ITO. We expect that radial dopant placement will become standard consideration for understanding the many properties of doped nanocrystal systems and anticipate the development of further living syntheses that offer opportunity to control catalytic, magnetic, electronic, and other important physical properties.

#### *Implications of living synthetic methods for core/shell nanocrystal growth*

Core/shell nanoparticles are hybrid nanostructures in which an inorganic core of one material surrounded by a different material.<sup>72</sup> Core/shell particles are generally of interest to impart advantageous properties of the multiple materials it comprises, or improve the existing properties of one or both components. For example, this approach has been invaluable to quantum dot research in which quantum yields and photoluminescent stability of semiconductor nanoparticles are greatly improved by passivating its surface trap states with a different semiconducting material.<sup>73–75</sup> However, current colloidal syntheses for creating the core/shell structure are hampered by several limitations. These limitations include undesirable homogeneous nucleation of shell material, incomplete surface coverage on the core, and non-epitaxial or amorphous growth.<sup>73</sup>

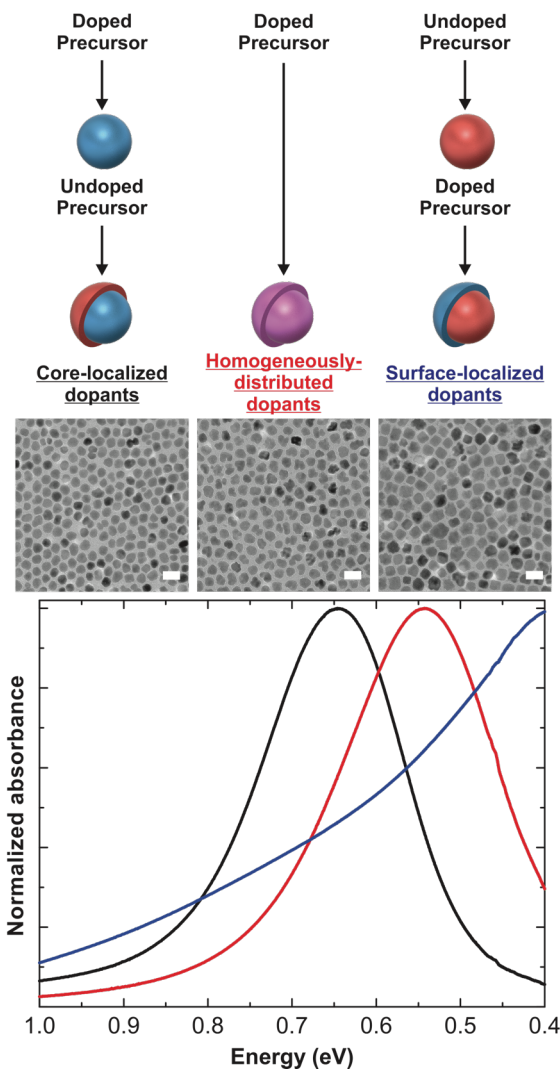


**Figure 2.4.** Using a living approach, the radial position of dopants can be controlled intuitively through the addition of doped or undoped precursor, represented by the top reaction schemes. No purification of the nanocrystals is necessary between precursor additions and particles can be synthesized in one pot. We synthesized ITO nanocrystals with varying radial placement of dopants that were between 10.2-12.8 nm in diameter, containing the same concentration of Sn (within 0.5 atomic %). Below the top scheme are TEM images corresponding to (from left to right) core-localized, homogeneously distributed, and surface-localized dopants. Scale bars are 20 nm. As shown in the bottom plot, core-localized ITO nanocrystals (black trace), ITO with homogeneously distributed dopants (red trace), and surface-localized ITO nanocrystals (blue trace) have drastically different LSPR line shape and maxima. Core-localized dopants have higher quality factors and activations.

Widely used and robust synthetic schemes have been discovered and applied to core-shell synthesis. Two of the most common are the Stöber method used to synthesize silica shells,<sup>75</sup> and adaptations of the successive ion layer adsorption reaction (SILAR) method used to produce quantum dots.<sup>76–79</sup> In the SILAR method, layers of cations and anions are added sequentially to build one atomic layer at a time, typically with purification steps between each. Additionally, careful calculations to determine the amount of anion or cation precursor (often less than one monolayer per addition) are necessary in order to avoid new nucleation events.<sup>76,79</sup> As a result, growing shells is tedious. In the Stöber method, a tetra-alkoxy silane precursor is hydrolyzed then condensed onto existing particles. The method has been adapted for the synthesis of other oxide shell materials, including TiO<sub>2</sub>, ZrO<sub>2</sub> and SnO<sub>2</sub>.<sup>72</sup> In general, the shells are amorphous and often do not fully passivate the core. Though there are some examples of core/shell syntheses comprising different metal oxides,<sup>80–82</sup> there isn't a general, tunable synthetic strategy to do so.

We anticipate that living growth methods will immensely aid in the successful synthesis of a variety of core/shell particles, and produce structures with advantageous magnetic, electronic, catalytic, and optical properties. This is a result of the living nature of the synthesis method; because the core surface remains reactive through the formation of active functional groups on the particle surface and there is high yield in precursor consumption, sequential additions of different metal precursor will suffice in creating an abrupt change from core to shell material. Such a procedure is intuitive and simple, eliminating the need for rigorous purification and quantification of shell precursor. The nature of regenerating a reactive surface holds several advantages to shell

growth. Precursors of different metal salts will favor condensation onto these sites rather than new homogeneous nucleation. Condensation of metal precursor will tend towards epitaxial growth because growth onto cores is not a heterogeneous nucleation event. Furthermore, because we anticipate the growth will not be promoted by heterogeneous nucleation, growth should occur over the entire particle surface rather than creating islets or dimer-like species.

Indeed, our group has published preliminary results of successful core/shell growth. The synthesis of  $\gamma$ -Fe<sub>2</sub>O<sub>3</sub>/MnO and ZnO/ $\beta$ -Ga<sub>2</sub>O<sub>3</sub> core/shell particles with the slow injection synthesis displayed epitaxial and uniform growth of shell material around core.<sup>49</sup> We expect that growing sequential shell materials on one another utilizing a living method will be possible, and will maintain the same level of composition control as described above. Given the amount of precursor added and the size of a particle, it follows that one can calculate the required amount of precursor material to yield a shell of desired thickness.

## Outlook

Herein, we outlined key prerequisites and attributes of living growth methods for nanocrystals. Living growth is possible when the production and maintenance of reactive sites on the surface facilitate growth through the controlled addition of reactive monomers. This type of growth mechanism has several consequences; because growth occurs by monomer addition rather than heterogeneous nucleation, epitaxial growth of single crystal nanoparticles results. Further, continuous growth from “living” reactive sites on the particle surface leads to nanocrystals with low size dispersions. When monomer addition is irreversible, crystals are no longer susceptible to ripening. At the

same time, when crystals are stabilized against core fusion or aggregation by a surface-bound surfactant, a constant number of nanocrystals persists throughout the growth process. When a constant number of crystals is maintained for the entire growth process, addition of more precursor leads to *predictable* growth. Finally, the preservation of reactive species in a controlled, layer-by-layer growth process provides opportunities to introduce new elements, thus altering the composition and structure of the nanocrystal with sub-nanometer precision, affording access to novel doped and core/shell structures.

Discovery and development of new living growth methods for nanocrystals will require greater understanding of key mechanistic aspects of these processes. Perhaps the most important aspect for exploration is understanding the nanocrystal surface chemistry during growth. In order to support a living growth process, there must be a complex interplay of 1) ligand binding to promote particle stability, and 2) appropriately reactive surface promoting epitaxial growth through monomer addition. Although some mechanistic understanding can be inferred from particle growth studies over time, *in situ* and *ex situ* experiments to probe the surface chemistry will be needed. Investigation into the influence of ligand type and concentration, characterization of the structure of metal precursor, and examination of the growth behavior during different addition rates, and at different reaction temperatures, will be needed to advance our understanding of these systems. Direct characterization of the surface chemistry may be more difficult to obtain. Studies should target the chemical makeup of the reactive nanocrystal surface, structure of reactive monomer produced from precursors, and nuclei or clusters formed early in the growth process through detailed, likely *in situ*, chemical analysis.

Many of the answers to these questions will require more advanced analytical tools and rigorous analysis of nanocrystal growth mechanisms. Cutting-edge analytical tools are needed to monitor nucleation and nanocrystal growth, assess atomic-scale compositional and structural changes over time, as well as monitor functional groups participating in living growth processes.<sup>83-85</sup> We have found SAXS an invaluable tool to quickly probe the products of new synthetic routes and monitor nanocrystal growth. Lab-scale SAXS instruments are now more widely available, and offer the capability to quickly obtain size, size dispersion, and concentration measurements. Compared to TEM, SAXS analysis can obtain information from a statistically significant population of nanoparticles in a fraction of the time that image analysis takes, and offers the added benefit of probing nanoparticle size, shape, and structure in solution.<sup>86</sup> Of course, TEM maintains its value in identifying shape, and corroborating SAXS measurements. Furthermore, HRTEM measurements are necessary to characterize crystallinity of synthesized products. Atomic pair distribution function analysis (PDF) is a powerful tool that can probe species at the atomic level, and should provide significant insights regarding reactive monomer formation, nucleation, and growth.<sup>87-89</sup> PDF should be especially useful for probing the structures of very small species (e.g. monomers and nuclei) that are not easily detected and characterized by SAXS or TEM. Towards monitoring key functional groups in monomers and on nanocrystal surfaces, we believe that traditional small-molecule chemical analysis tools, including NMR, IR, and Raman spectroscopy, together with complementary surface chemistry tools, such as XPS or ToF-SIMS, can be used alongside more sophisticated methods to enhance our mechanistic understanding of living growth processes.

Despite the challenges evident in discovering new living growth systems and elucidating the mechanisms, the future of precision nanomaterial production through these approaches is promising and inspiring. It appears that living growth methods are widely applicable across the periodic table, employing single metals or several metals in combination. From what we have seen so far, these mechanisms facilitate the convenient and rapid assembly of new nanostructures with advantageous and appealing properties. At the same time, these intuitive synthetic approaches produce high-performance nanomaterials in fewer steps, in higher yields, and under greener conditions than thermal decomposition methods. Already, the synthesis of an almost-infinite number of binary, doped, co-doped, and core/shell oxide nanocrystal structures is possible by living growth. Products of these syntheses promise increased performance in optical, electronic, and catalytic application, as well as provide avenues for understanding fundamental physical processes. With respect to the compositions and structures that can be produced via these methods, we have only scratched the surface. We expect living approaches will make it possible to produce shape-controlled nanostructures, ternary oxides, and other chalcogenide nanocrystals (not limited to oxides). Some existing approaches to other chalcogenides may in time prove to be living mechanisms.<sup>47</sup> Combining these materials in unique, epitaxial heterostructured compositions will bring about a flurry in discovery-driven science.

### **Bridge to Chapter III**

In Chapter II, the characteristics of a living nanocrystal synthesis were defined, and it was highlighted that the slow addition method developed in the Hutchison lab fall in line with these characteristics. The outlook section suggested, in part, studies

on addition rate and synthesis temperature will advance our knowledge of the living nanocrystal system. Chapter III explores how these two synthetic variables affect nanocrystal morphology. From the data, we develop a model that explains the trends we observe between morphology and addition rate at three different synthesis temperatures.

CHAPTER III

INFLUENCE OF MONOMER FLUX AND TEMPERATURE ON MORPHOLOGY OF  
INDIUM OXIDE NANOCRYSTALS DURING A CONTINUOUS GROWTH  
SYNTHESIS

This chapter was published as Plummer, L. K.; Crockett, B. M.; Pennel, M. L.; Jansons, A. W.; Koskela, K. M.; Hutchison, J. E. Influence of Monomer Flux and Temperature on Morphology of Indium Oxide Nanocrystals during a Continuous Growth Synthesis. *Chem. Mater.* **2019**, *31*, 7638–7649.

### **Introduction**

Crystal growth through the assembly of atoms, molecular fragments or intact molecules into extended regular arrangements is a critical process throughout chemistry, biology, geology, and materials science. The atomic-level to macro-scale structures instilled by the assembly process define, in turn, the properties and function of the extended material. As a consequence, the mechanisms of crystal growth, and the parameters that influence the growth process, have been widely studied for crystals and thin films.<sup>1–7</sup> For nanocrystals, significantly less is known about how growth conditions influence their growth despite the fact that the properties of nanoscale structures are especially sensitive to atomic-scale changes in structure.<sup>8–11</sup> Here, we examine how the growth and structure of metal oxide nanocrystals depend upon the growth conditions, specifically precursor addition rate and temperature.

The crystallinity and morphology of a nanocrystal, as with all crystals, are influenced by a series of steps: diffusion of crystallizing species to the surface, adsorption (and desorption) and surface diffusion of these species, and island growth/formation.<sup>3,12-</sup><sup>15</sup> One of the key parameters that affects each of these processes is the concentration of the crystallizing species, typically a reactive fragment derived from a molecular precursor. This concentration is generally described as a degree of supersaturation, which, in turn, defines the flux of material to the surface of the growing crystal. The role of flux in determining the growth rate and, more importantly, morphology has been widely reported for the growth of organic and inorganic crystals,<sup>6,16-19</sup> formation of snowflakes,<sup>20-25</sup> biomineralization processes,<sup>26,27</sup> and the deposition of thin films (e.g., molecular beam epitaxy and thermal evaporation).<sup>28-31</sup>

Studies of thin film deposition provide insight into how the deposition rate (or flux) to the surface of a growing inorganic material influences crystallinity and morphology. At a given temperature, higher fluxes tend to produce rougher surfaces, smaller crystallite sizes and defects, and amorphous materials.<sup>16,28</sup> Lower fluxes tend to produce atomically smooth, highly crystalline surface morphologies.<sup>12,17,32</sup> These trends have been attributed to the concentration of species delivered to, and adsorbed on, the film surface. At low deposition rates, adsorbed species can diffuse along the film surface to reach, and attach to, an existing island's edge as opposed to nucleating a new island. Such conditions result in the growth of one layer at a time.<sup>12</sup> However, at high deposition rates, the higher concentration of reactive species on the surface induces nucleation and growth on top of already existing islands before the base layer is complete, resulting in uneven, rough topographies. Similar behavior has been observed at high and low

supersaturation levels for crystal growth from solution.<sup>6,17</sup> Collectively, these studies suggest that by controlling the concentration of the crystallizing species, and the flux to the surface, it should be possible to gain control over the crystallinity and morphology of nanoscale particles.

To date, there have been few reports that examine the effects of monomer flux on nanocrystal growth processes. This is likely because flux is difficult to directly control in the common methods used. Most syntheses employ either a heat-up approach,<sup>33</sup> where all starting materials are heated at a controlled rate to the reflux temperature of the solvent, or a hot-injection approach,<sup>34</sup> where a precursor is rapidly injected by hand into the solvent at an elevated temperature.<sup>35</sup> In both cases, the local monomer concentration is highest when nanocrystals are first formed, but rapidly decreases during growth. Flux to the nanocrystal surface is constantly changing throughout these reactions, and it is not possible to directly control or even maintain a constant flux to investigate its influence on the nanocrystal growth processes. Despite the paucity of studies in this area, there are studies that suggest that monomer flux affects the structure and properties of nanocrystals. Weller *et al.* examined the influence of growth rate on the optical properties of II-VI and III-V quantum dots (QDs) produced under fast growth conditions (immediately following fast injection of precursor) and slow growth conditions (during the Ostwald ripening stage of reaction).<sup>36</sup> They found that photoluminescent quantum efficiencies were poor immediately following periods of fast growth compared to QDs grown at relatively slow, steady rates. The authors attributed the diminished performance to surface disorder in the quantum dots that were grown quickly.<sup>36</sup> These results suggest

that it might be possible to achieve enhanced efficiencies if we gain greater control over monomer flux throughout the nanocrystal synthesis.

Recently, continuous addition synthetic methods have been established for nanocrystal growth that make it possible to investigate the influence of flux in greater detail.<sup>37–45</sup> Continuous introduction of precursor material can lead to exquisite size control and produce more uniform nanocrystals. It has also proven effective as a strategy to mitigate Ostwald ripening in quantum dots because maintaining monomer concentration at a constant threshold prevents dissolution of small nanoparticles.<sup>40,41</sup> Well-controlled size tuning has been demonstrated in metal oxides where the amount of precursor added determines the final size in a predictable fashion.<sup>37,39</sup> Our own group has taken advantage of the slow addition, continuous growth method to produce a variety of metal oxide nanocrystals using very similar synthetic conditions,<sup>46</sup> gain precise size control of indium oxide nanocrystals,<sup>37</sup> study size-dependent magnetism in iron oxide nanocrystals,<sup>47</sup> produce core-shell nanocrystal structures,<sup>46</sup> incorporate dopants,<sup>48</sup> and place dopants in specific radial positions to adjust plasmonic properties.<sup>49</sup>

There have been several reports that variations in the rate of addition of precursor can cause morphological changes during nanocrystal syntheses. Alivisatos *et al.* found slower addition yielded anisotropic growth of doped shells on NaLnF<sub>4</sub> cores yielding rod-like morphology while fast addition resulted in nucleation of new nanocrystals which subsequently dissolved and contributed to isotropic growth on the cores yielding spherical morphology.<sup>45</sup> Lai *et al.* attributed different iron oxide nanocrystal morphologies to dissolution and reconstruction of certain facets, resulting from differences in precursor concentration during addition.<sup>43</sup> Similarly, Guo *et al.* attributed

the different faceted shapes of CdS nanocrystals to adjustments of the chemical potential of monomer resulting from different precursor addition rates.<sup>44</sup> So far, only a couple studies have explicitly evaluated how precursor addition rates affect steps of crystal growth and, ultimately, morphology using continuous addition methods. Zhang *et al.* found that growth of bromide-passivated cubic rhodium particles occurred selectively on corners to yield octopods under relatively fast addition, whereas slow addition yielded concave shaped particles.<sup>42</sup> Xia *et al.* observed similar behavior in bromide-capped palladium nanocubes.<sup>38</sup> Both groups explained the observed trends by considering relative rates of surface diffusion and monomer deposition. Translation of these concepts to the growth of metal oxide nanocrystals is not straightforward because of the significant differences between metallic and metal oxide bonding and surface chemistry (for example, compositional variability in metal oxides compared to metals, coordination number differences, localized vs. delocalized electronic properties, etc.<sup>50</sup>).

Herein, we leverage the continuous growth synthesis of metal oxide nanocrystals to investigate the influence of monomer flux on indium oxide nanocrystal growth. Precursor addition rate, which dictates the flux, has a strong influence on nanocrystal morphology, resulting in the growth of either highly branched or compact, faceted nanocrystals, depending upon the flux. Quantitative comparisons between the nanocrystal morphologies produced made it possible to gain mechanistic insight regarding the growth processes involved. The temperature dependence of the relationship between flux and morphology was also analyzed. At higher temperatures, the growth processes were less sensitive to changes in flux. Finally, we used our understanding of the influences of temperature and flux on morphology to produce compact, faceted nanocrystals from

highly branched nanocrystal seeds by regulating the precursor addition rate during growth.

## Results and Discussion

### *Influence of precursor addition rate on morphology*

Slow delivery of precursor (typically 0.1 mmol/min over the course of 10 or more minutes) has been critical to our previously reported work on the continuous growth synthesis of metal oxide nanocrystals.<sup>37,46</sup> Slow addition leads to controlled, layer-by-layer growth, whereas rapid addition leads to the formation of large aggregates. In the slow addition regime, it was unclear what influence the precursor addition rate had on the nanocrystal morphology during growth and why the slower addition promoted such uniform nanocrystal growth. As a first step to investigate the influence of precursor addition rate on nanocrystal growth, four In<sub>2</sub>O<sub>3</sub> nanocrystal samples were synthesized through a slow-injection approach at differing addition rates. The indium oleate precursor solution was prepared by heating a mixture of 1 mmol of indium acetate with a 6 molar excess of oleic acid. The role of the excess oleic acid has discussed in greater detail in prior work.<sup>37,46</sup> Briefly, the excess acid increases the solubility of the indium oleate complex and serves to stabilize the growing nanocrystals, preventing aggregation. The indium oleate precursor was injected into 13 mL of oleyl alcohol held at 260 °C (Figure 3.1) at various addition rates using a syringe pump. From previous work<sup>46</sup> we knew that rapid addition of the precursor by hand resulted in highly polydisperse size populations and rampant bumping, presumably due to the large amount of water produced from

uncontrolled condensation of the precursor and esterification. Thus, for the present investigation, the addition rate was varied from 1.2 mL/min to 0.1 mL/min.

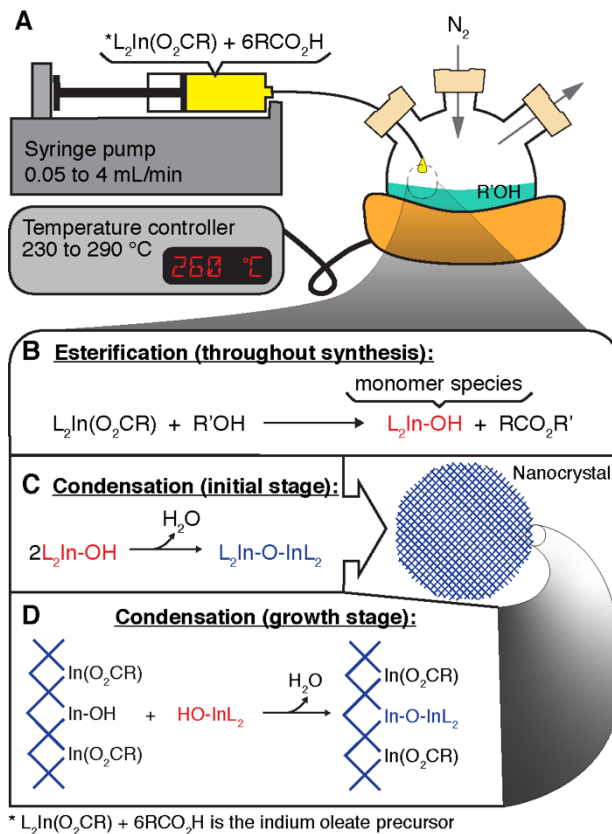


**Figure 3.1.** Continuous growth synthesis of indium oxide nanocrystals. The illustration depicts a typical reaction setup (A). Indium oleate precursor (indium oleate with ~6x excess oleic acid) is added into the round bottom flask containing oleyl alcohol ( $R'OH$ ) at a designated rate *via* the syringe pump. A heating mantle and temperature controller maintain the alcohol at the designated temperature. Throughout the synthesis, precursor is converted to monomer species consisting of an indium hydroxy species (B). Monomer condenses to form nanocrystals (C), and nanocrystals grow *via* the monomer species condensing with hydroxides on the nanocrystal surface (D).

Our decision to vary indium addition rate by varying the addition rate of a precursor of constant indium concentration in oleic acid was made after considering a couple of alternative approaches. We considered adjusting the concentration of indium in the precursor by either varying the amount of oleic acid or adding a solvent while

maintaining a constant addition rate. However, changing the ratio between indium and oleic acid would likely cause changes to morphology,<sup>51</sup> and we did not want to introduce another chemical that may have unintended consequences<sup>52</sup>. Use of solvents can also influence the outcome of the reaction in ways that would complicate the interpretation of the influence of precursor addition rate. More detailed investigation of the role of the indium to oleic acid ratio are currently underway.

X-ray photoelectron spectroscopy (XPS) and x-ray diffraction analysis (XRD) have shown that the nanocrystals produced under these conditions are  $\text{In}_2\text{O}_3$  with the bixbyite crystal structure and XPS and time-of-flight secondary ion mass spectrometry suggest that their ligand shell is primarily oleic acid.<sup>46</sup> Figure 3.2 displays transmission electron microscopy (TEM) images of the  $\text{In}_2\text{O}_3$  nanocrystals produced at the four different precursor addition rates. The nanocrystals formed with faster addition rates (1.2 mL/min, Figure 3.2A) exhibit irregular, branch-like characteristics. As the precursor addition rate is decreased across the series, the nanocrystal morphology loses the branch-like nature, and in the case of the slowest addition (0.1 mL/min, Figure 3.2D) the nanocrystals become cubic and monodisperse. Overall, the nanocrystals produced with faster precursor addition exhibited more branching and greater surface roughness compared to the faceted nanocrystals produced with slower addition.

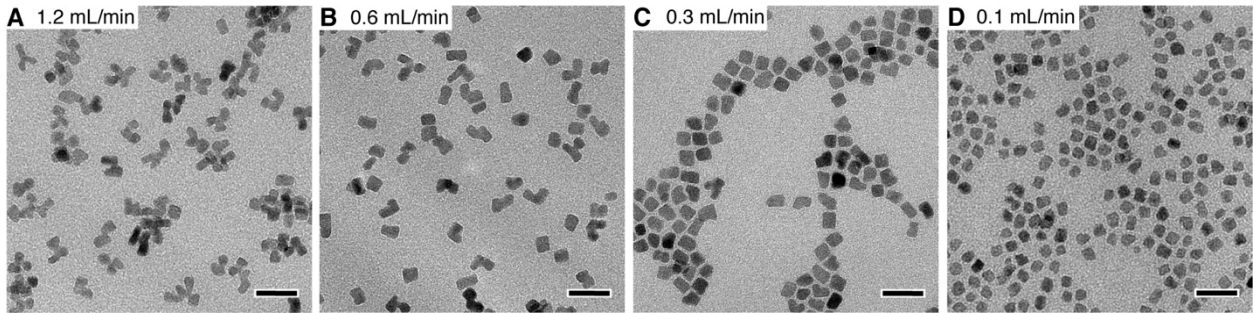


**Figure 3.2.** TEM images illustrating the dependence of nanocrystal morphology on the precursor addition rate. Faster addition produces branched nanocrystals, while slower addition produces faceted nanocrystals. The nanocrystal syntheses were carried out with precursor addition rates of 1.2 mL/min (A), 0.6 mL/min (B), 0.3 mL/min (C), and 0.1 mL/min (D). Scale bars are 20 nm. Size analyses for all TEM images are available in Figure A.1-4.

Although morphological changes are evident across the series by qualitative inspection of the TEM images, we wanted a more objective, quantitative analysis to compare changes in morphology. We considered using Small Angle X-Ray Scattering (SAXS) because this technique is often useful for quantitative size analysis.<sup>37,48,49,53</sup> However, for the highly branched nature of the nanocrystals produced at high addition rates, there is not an appropriate form factor to model the SAXS data. Thus, we sought an approach to extract quantitative information from the TEM data. Because TEM images show the two-dimensional projection of the nanocrystals, we reasoned that measurement of the nanocrystal perimeter, normalized by their effective diameters, would be a good metric to distinguish branched vs. faceted morphologies. The ratio of the perimeter to diameter (P/D ratio) depends on the two-dimensional shape (example calculations are shown in Figure A.5). The lowest possible value is 3.14 for a circle. The P/D of a square is 3.54. As surface roughness and branching increase the P/D ratio can increase indefinitely. Thus, the nanocrystals' perimeters and effective diameters were

extracted from TEM images using image processing software and used to calculate P/D ratios (see Figure A6). Figure 3.3 displays the frequency of P/D ratios for the samples shown in the TEM images in Figure 3.2. The value of the mode of the distribution (P/D ratio measured at the peak maximum) indicates the most represented shape within the sample. The frequency of the mode provides a measure of the homogeneity of morphologies, with higher mode frequencies indicating greater homogeneity. The distribution of frequencies tailing out to high P/D ratios indicates increasing populations of branched shapes.

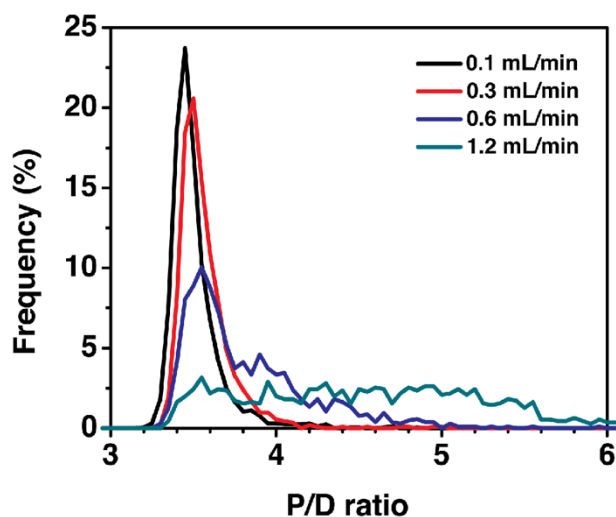


**Figure 3.3.** Distribution plot of the nanocrystal P/D values extracted from TEM images of the samples shown in Figure 3.2. The P/D plots suggest an increase in uniformity as precursor addition rate is decreased.

Figure 3.3 shows that, as the precursor addition rate increases, the value of the mode increases and the frequency of the mode decreases. There is a broad range of P/D ratios for the fastest precursor addition (1.2 mL/min, green trace), indicating a wider distribution of branched structures. These findings are consistent with the qualitative

observations made by examination of the TEM images (Figure 3.2A). The distribution mode centers around 3.5 for the slowest addition (0.1 mL/min, black trace). Given that the P/D of a square is 3.54, this value suggests that the nanocrystals formed with the slowest addition are mostly cubic in shape, consistent with the shapes seen in Figure 3.2D. Taken together, the TEM images and P/D analysis lead to the conclusion that faster addition results in increased branching of the nanocrystals, and slower addition results in faceted, cubic nanocrystals.

#### *Examining the impact of precursor addition rates on the mechanism of growth*

The results displayed in Figures 3.2 and 3.3 demonstrate that slow precursor addition is necessary to promote conditions needed to produce uniform nanocrystals with faceted shapes. As the precursor addition rate increases, branched nanocrystals are produced suggesting a different growth process. Synthesis conditions involving high supersaturation or fast growth often yield branched morphologies,<sup>38,54–58</sup> but the question remains why. One possible cause of branching is polytypism<sup>58</sup> in which a nanocrystal possesses two different crystal phases. Polytypism is common in branched metal chalcogenide nanocrystals but was ruled out in this study because the branched nanocrystals contained only the bixbyite phase (Figure A.7). We considered two alternative hypotheses to explain why fast addition might cause branched morphologies. The branching observed in the nanocrystals in Figure 3.2 could originate from rapid addition of monomer to nanocrystal surfaces resulting in growth at many sites on the surface. Protrusions formed on the surface are more likely to react with additional monomer than the valleys, leading to branched structures.<sup>20,59</sup> Alternatively, given a high

enough precursor addition rate, new nanocrystals could form and react with existing nanocrystals. Then, particle-particle reactions, e.g. coalescence,<sup>60,61</sup> or oriented attachment,<sup>62,63</sup> could occur. To gain insight into the growth mechanism, we examined the structure of branched nanocrystals using high-resolution TEM (HRTEM).

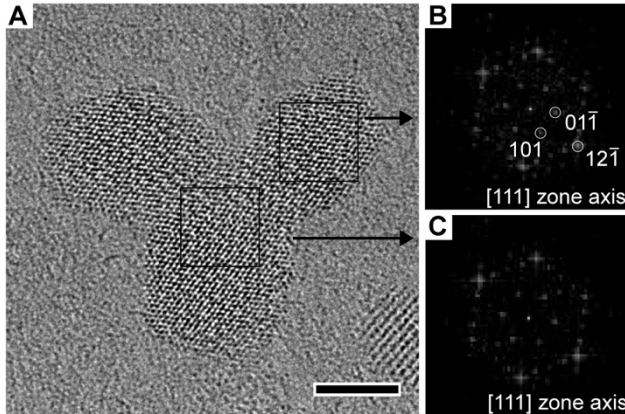


**Figure 3.4.** HRTEM of a branched nanocrystal synthesized at a fast precursor addition, 1.2 mL/min (from the Figure 3.2A sample), indicating that the nanocrystal is free of crystalline defects at the branching sites and throughout the lattice (A). Scale bar is 3 nm. FFT patterns of one of the branches (B) and the central branching area (C) are also shown. Indexing of the FFT patterns (shown in B) revealed the particle is oriented on the [111] zone axis of the bixbyite structure in both locations.

Figure 3.4A shows a representative HRTEM image of a branched nanocrystal from Figure 3.2A grown at the highest precursor addition rate of 1.2 mL/min (additional HRTEM are shown in Figure A.8). Lattice fringes extend throughout the entirety of the nanocrystal without interruption, suggesting that the nanocrystal is free of defects. Figure 3.4B and 3.4C display FFT patterns taken from a branch and the central branch origin respectively from Figure 3.4A. The FFT patterns were both indexed to the [111] zone axis of the bixbyite structure and share the same orientation. The lack of defects and consistent orientation throughout branched nanocrystals suggest they are single crystal,

and, therefore, the branched morphology is not caused by random (non-oriented) particle coalescence during the reaction.

Next, we considered the possibility that the branched structures might occur through oriented attachment. Oriented attachment is a special case of particle coalescence in which primary particles fuse together in a fashion that aligns their crystal lattices resulting in a single crystal nanoparticle after the fusion event. Oriented attachment is typically observed during growth that takes place in the absence of stabilizing ligands.<sup>64–68</sup> Primary particles are usually observable during the growth process, often leading to broad size distributions.<sup>60,69–71</sup> Further, oriented attachment tends to occur on specific facets of nanocrystals leading to a regular pattern of branching.<sup>64,67,72–74</sup> In the present study, a large excess of oleic acid stabilizes the nanocrystals preventing close approach and orientation needed for attachment. In our syntheses, primary nanoparticles (detectable down to 2 nm by TEM) are not observed in the reaction mixtures. Further, our branched nanocrystals, although single crystal have irregular and random branches, as opposed to the regular branching observed in oriented attachment. Taken together, these findings suggest that oriented attachment is not occurring during the formation of branched nanocrystals in our study.

The presence of small, primary particles has been used throughout the literature to distinguish between oriented attachment and growth by monomer addition for single crystal metal oxide nanoparticles with similar branched morphologies as observed in this study. In some cases, growth is determined to occur *via* oriented attachment<sup>71,75–77</sup> while in others it is determined to be a result of monomer addition<sup>78–80</sup>. Studies that concluded oriented attachment was occurring observed the formation of small, primary particles

during synthesis. Studies that determined that growth occurred by atom by atom addition demonstrated that the rate of growth was slower than would be expected for oriented attachment<sup>78</sup> and/or observed no primary particles during growth<sup>80</sup>.

Across all the conditions examined in our growth studies, including those conducted under high flux conditions, we did not observe primary particles as the branched nanocrystals grew larger (see, for example, Figure A.9). Control experiments suggest that nanocrystals as small as 2 nm should be detectable. To examine the stability of smaller nanocrystals in the presence of larger nanocrystals, we mixed reaction mixtures containing relatively small (~6 nm) and large (~10 nm) faceted nanocrystals (each synthesized at 260 °C). These were heated to 260 °C, held at that temperature for one hour followed by further heating at 290 °C for an additional hour. We found that the size populations are nearly identical to the starting mixture (experimental details and TEM results in Figure A.10 and Table A.1).

Based upon these observations, nanocrystal growth appears to occur by monomer addition to nanocrystals and not by particle coalescence events, even in cases of fast addition. The lack of evidence for primary particle formation during growth, plus lack of growth in the absence of precursor leads us to conclude that particle coalescence (including oriented attachment) is an unlikely growth mechanism in this synthesis.

If growth occurs, instead, by monomer attachment to the surface of the growing nanocrystal, then the rate of precursor addition is directly controlling the flux of monomer to nanocrystal surfaces. To explain the branching induced *via* high monomer flux (i.e. fast precursor addition) and the faceted nanocrystals produced *via* low flux (i.e. slow precursor addition), we returned to the monomer addition hypothesis and considered

the local reaction conditions between the monomer and the nanocrystal surface. Based upon what is known from the thin film growth literature, a layer-by-layer mechanism should produce faceted nanocrystals at low flux; however, an alternative hypothesis was that restructuring occurs to achieve the cubic shape. Thus, we considered two probable interaction pathways between the incoming monomer and the nanocrystal surface: 1) monomer adsorbs to the nanocrystal surface, diffuses to a reactive step edge or kink site, reacts with the surface and is immobilized; or 2) monomer reacts with the nanocrystal surface immediately following adsorption, and during the course of growth the nanocrystal surface reorganizes to produce facets.

We designed an experiment to test whether branched structures can reorganize to faceted structures under the reaction conditions. This sort of reorganization, known as shape relaxation (or sometimes as self-integration, self-recrystallization, or shape/surface restructuring), reduces the surface free energy of the nanocrystal by restructuring the surface atoms.<sup>81</sup> Shape relaxation is more commonly observed for metal nanocrystals<sup>82-85</sup> but can also occur in metal oxides.<sup>66</sup> We have shown through previous work with this system that the (100) terminated facets of the cubic nanocrystals are partially hydroxylated,<sup>37,46</sup> and shape relaxation seems plausible with the low surface energy of the (100) facets.<sup>86</sup> Nanocrystals were grown with intermittent periods of fast precursor addition (high monomer flux) and aging (no added precursor). The fast addition periods had the same addition rate that produced the branched nanocrystals in Figure 3.2B. However, taking the aging periods into account, the average addition rate across the growth period was equivalent to the slow addition rate that produced the faceted nanocrystals shown in Figure 3.2D. The fast, slow, and intermittent precursor addition

profiles are shown in Figure 3.5A for comparison. If surface diffusion of monomer prior to condensation with the surface is required to produce faceted nanocrystals, the intermittent addition approach should yield branched nanocrystals because the periods with high flux should provide enough monomer to the surface to cause branched growth. On the other hand, if shape relaxation of the nanocrystals is the cause for the faceted nature, the annealing period should allow for the restructuring to occur and produce faceted nanocrystals in spite of the high monomer flux to the surface during the addition periods.

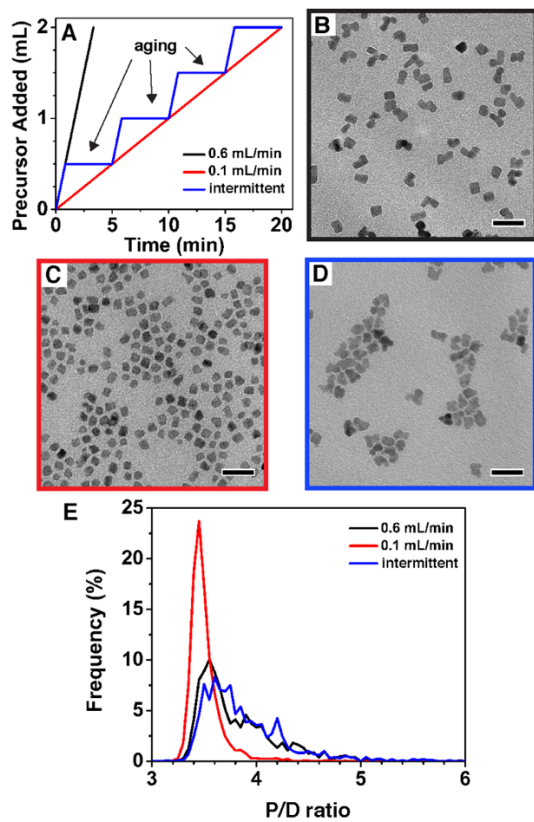


**Figure 3.5.** Comparison of fast addition, slow addition, and intermittent addition (fast addition with aging periods) to test shape relaxation hypothesis. Precursor addition profiles for syntheses carried out at 260 °C (A), where precursor was added at 0.6 mL/min (black trace), 0.1 mL/min (red trace), and intermittent addition/aging (blue trace). Corresponding TEM images of the nanocrystals are shown in (B) (0.6 mL/min), (C) (0.1 mL/min), and (D) (intermittent addition). Scale bars are 20 nm. P/D histograms from the TEM images are shown in (E). Size histograms are available in Figure A.2.

TEM images for nanocrystals synthesized under high monomer flux, low flux, and intermittent high flux/aging conditions are shown in Figure 3.5. The nanocrystal morphology observed from the intermittent aging conditions (Figure 3.5D) closely resembles the morphology observed for the nanocrystals formed at high flux (Figure 3.5B), with both exhibiting irregular morphologies, including branching and/or elongated shapes. The nanocrystals formed with a low flux (Figure 3.5C) exhibit more faceted and homogeneous morphologies. The P/D ratios were analyzed for the three samples and plotted in Figure 3.5E. The intermittently aged nanocrystals exhibit P/D histograms (Figure 3.5E blue trace) almost identical to those observed for the nanocrystals formed at high monomer flux (Figure 3.5E black trace). Both samples exhibit broad distributions having modes of 3.6 and mode frequencies around 10%. In contrast, the nanocrystals formed under low flux conditions (Figure 3.5E red trace) display a much more homogeneous P/D distribution (mode frequency of 24%) and the population is mostly cubic in nature (P/D mode equals 3.5).

These results suggest that shape relaxation does not occur in this system during the timescale of the synthesis. The aging periods did not produce differences in the nanocrystals' morphologies compared with nanocrystals synthesized under high flux conditions with no aging periods. Thus, it appears that once monomers react with the nanocrystal surface, the atoms become kinetically trapped and irregular surfaces cannot be restructured. Thermally induced shape relaxation is observed in metal systems due to the non-directional nature of the metal-metal bonds and mobility of atoms on the nanocrystal surface.<sup>82,83</sup> However, in the case of  $\text{In}_2\text{O}_3$ , the metal oxygen bonds are likely too strong, and thermal energy is insufficient to rearrange at these temperatures. For

example, indium oxide films must reach excess of 500 °C before any structural change is measured.<sup>87</sup> Shape relaxation could also be facilitated by the detachment and reattachment of monomer species,<sup>84,85</sup> yet this mechanism appears to be absent in this system. Likely, the condensation reactions between the monomer and nanocrystal surface are irreversible. In the absence of shape relaxation processes, surface diffusion is the most probable mechanism to produce faceted nanocrystals.

Based on collective observations made from the results shown in Figures 3.2-5 we propose the most probable reaction pathways for the low and high monomer flux regimes, where the addition rate directly influences the concentration of monomer available to react with the nanocrystal surface. Figure 3.6 illustrates growth on a nanocrystal surface during low flux (Figure 3.6A) and high flux (Figure 3.6B).

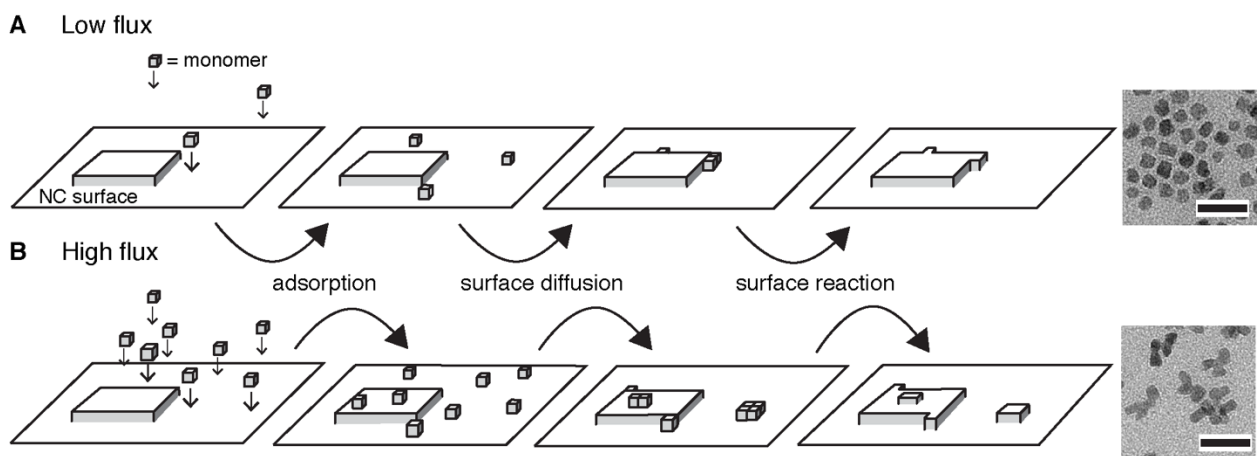


**Figure 3.6.** Depicts the reaction steps leading to either faceted (example in top right) or branched (example in bottom right) nanocrystals in the case of low flux (A) and high flux (B), respectively. Scale bars in the TEM images are 20 nm.

In the case of low flux (Figure 3.6A), indium hydroxy monomers reaching the nanocrystal surface adsorb, likely through hydrogen bonding to hydroxyls on the surface.

The monomer can then diffuse to an edge site where the dwell time of species is longer than on the open planar surfaces,<sup>12</sup> increasing the likelihood of condensation that extends the island's edge. Repetition of this process yields a planar surface, where new monomer can react and the process repeats, much like layer-by-layer epitaxial growth in thin films.<sup>12,88</sup>

Under high monomer flux conditions, there are a couple aspects of the reaction that might shift growth toward the branched growth regime depicted in Figure 3.6B. High flux will lead to higher concentrations of adsorbed monomer on the nanocrystal surface. High surface concentration of the monomer will inhibit surface diffusion through steric hindrance because the monomer species is bulkier than the oleate ligands that would be present otherwise. Additionally, the condensation reaction of monomer with the nanocrystal surface will be increased because the reaction rate is dependent on local monomer concentration. Diminished surface diffusion and faster condensation rates will increase the likelihood of monomer reaction at planar sites, forming new islands rather than contributing to layer-by-layer growth at an edge site. In short, low flux conditions permit adsorbed monomer to diffuse and react with step edge sites to produce faceted nanocrystals, whereas high flux restricts surface diffusion causing monomer to react indiscriminately on the surface to produce the irregular branched structures.

### **Determining how temperature affects the influence of monomer flux on morphology**

The rates of the surface diffusion of monomer depicted in Figure 3.6 and the monomer-surface condensation reaction depicted in Figure 3.1D are both expected to increase with increasing reaction temperature but will exhibit different temperature

dependencies. Thus, the relationship between flux and morphology should be temperature dependent. If the rate of surface diffusion is higher than the monomer-surface reaction rate, then nanocrystal morphologies should become less sensitive to flux at higher temperatures because the monomers will be more surface-mobile and less sterically hindered. On the other hand, if the surface reaction rate predominates compared to the surface diffusion rate, the morphologies should become more sensitive to flux at higher temperatures because there is less time for the surface-adsorbed monomer to diffuse before condensing with the surface. To examine these two scenarios, nanocrystals were synthesized using 1 mmol of precursor at 230 °C, 260 °C, and 290 °C, with varying precursor addition rates. At each temperature, the upper and lower bounds for addition rates were determined experimentally. The lower addition rate was selected to produce the most uniform morphologies, whereas the upper limit was chosen to produce significant branching without inducing secondary nucleation or significantly decreasing the reaction temperature during the addition of precursor.

Figure 3.7 displays TEM images for the nanocrystals synthesized at 230 °C (Figure 3.7A, 3.7B), 260 °C (Figure 3.7D, 3.7E), and 290 °C (Figure 3.7G, 3.7H). Slower precursor addition (low flux) resulted in more faceted nanocrystals (Figure 3.7A, 3.7D, 3.7G), while faster addition (high flux) resulted in significant branching (Figures 3.7B, 3.7E, 3.7H) at all reaction temperatures. As was observed previously for 260 °C, HRTEM again showed that nanocrystals grown at the fastest addition rates for 230 °C and 290 °C syntheses were single crystal (Figure A.8). P/D ratios were extracted from the

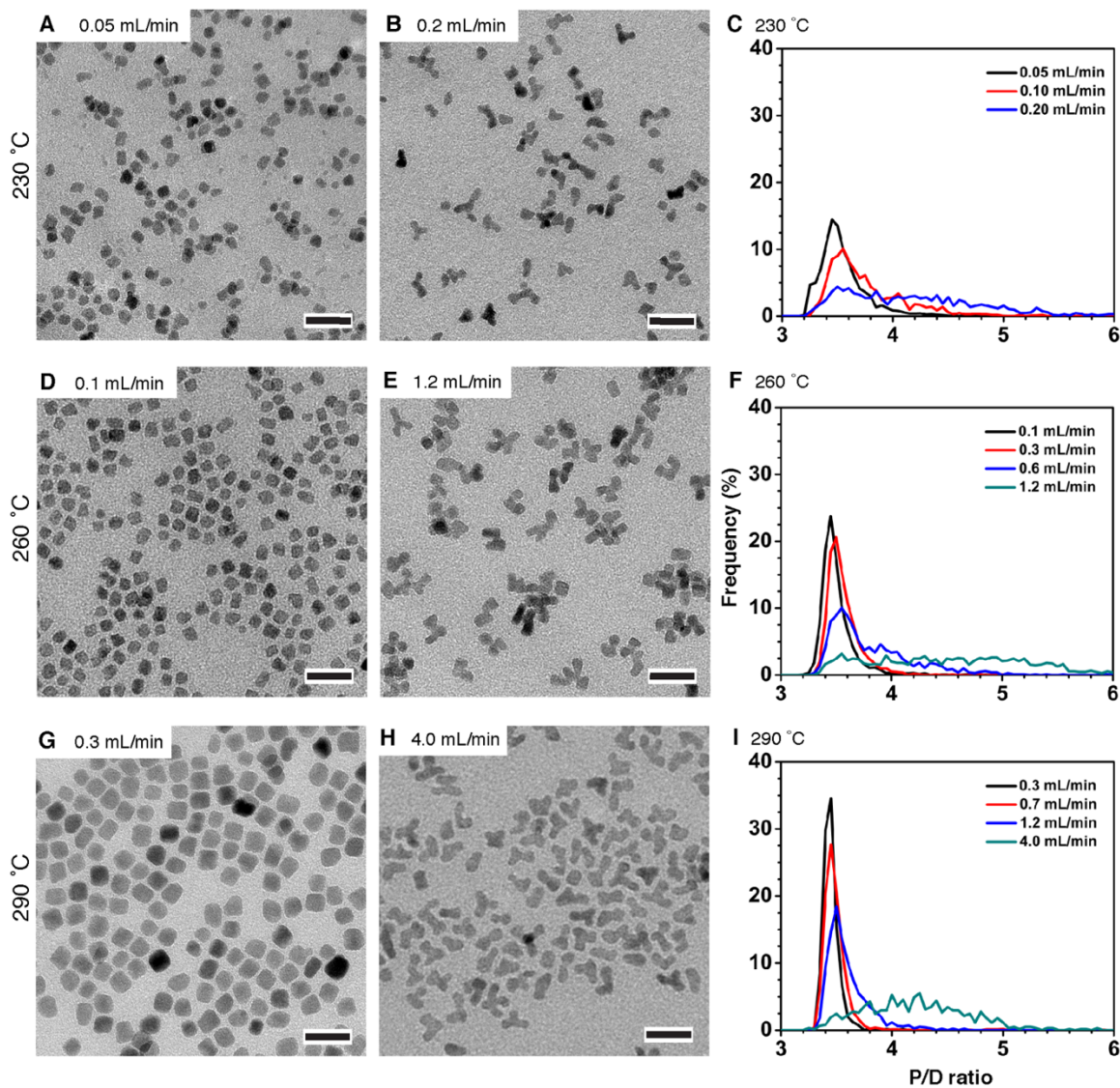


**Figure 3.7.** The dependence of nanocrystal morphology on monomer flux at different temperatures. TEM images of nanocrystals synthesized with 1 mmol of indium at 230 °C (A, B), 260 °C (D, E), and 290 °C (G, H) at the designated addition rate. Overall, the morphologies of the nanocrystals became more faceted as precursor addition rate was decreased for all temperatures. However, as the temperature is increased, much higher addition rates were required to produce branched nanocrystals. Precursor addition rates are noted in the figure insets. Scale bars are 20 nm. The P/D histograms for syntheses at 230 °C (C), 260 °C (F), and 290 °C (I) at various addition rates show that morphology becomes more homogeneous with increasing temperature. Size histograms are available in Figure A.3.

TEM images and the results plotted in Figures 3.7C (230 °C), 3.7F (260 °C), and 3.7I (290 °C). The P/D distributions confirm that a decrease in precursor addition yields more homogeneity in nanocrystal morphology across the temperatures investigated.

Additionally, the nanocrystals are more faceted with increased temperature as evidenced by the mode frequency in the P/D plots increasing from 15% (230 °C) to 24% (260 °C) to a final 35% (290 °C) at the slowest addition for each temperature. The P/D values approach those for a square (3.54) consistent with the cubic shapes observed by TEM.

Interestingly, as temperature is increased, the reaction can sustain much higher addition rates and continue to produce faceted nanocrystals. This can be directly shown in comparing Figure 3.7G (the lowest 290 °C addition rate of 0.3 mL/min) with 7B (the highest 230 °C addition rate of 0.2 mL). While the addition rates are similar, the nanocrystals synthesized at 230 °C are highly branched, whereas the nanocrystals formed at 290 °C are faceted. This comparison highlights the strong influence of temperature on the relationship between monomer flux and morphology. In addition, morphology changes appear to be less sensitive to addition rate at higher temperatures. Overall, nanocrystals synthesized at 290 °C displayed more homogeneous sizes and narrower P/D distributions than could be achieved under any conditions at lower temperatures.

The improvements in morphology (based upon comparisons of P/D ratios in Figure 3.7) observed at elevated temperatures suggest that surface diffusion must have a greater influence on growth behavior than the surface condensation reaction. An increase in surface diffusion affords the monomer the mobility to find a step edge site on the nanocrystal to condense with (Scheme 1A). In addition to increasing mobility across the planar surface, increased surface diffusion also makes it possible for monomer to “step

down” from the top of a terrace to an edge site despite the slightly higher energy barrier involved.<sup>12,89</sup> If surface condensation rates were the greater influence on the nanocrystal growth behavior, there would be more indiscriminate monomer-nanocrystal condensation, leading to a greater number of protrusions, across the nanocrystal as temperature is increased; however, this is not observed.

The isolated nanocrystals shown in Figure 3.7 increase in size with temperature, from 5.7 nm at 230 °C to 9.2 nm at 290 °C. To further examine the growth process under these reaction conditions, growth curves (nanocrystal volume vs. monomer added) were generated by taking aliquots over the course of a 2 or 5 mmol addition. The small size of the nanocrystals formed at 230 °C necessitated addition of 5 mmol of precursor to attain a growth curve spanning a sufficient size range. The nanocrystal volume values were calculated from sizes measured by SAXS, with the volume growth curves plotted in Figure 3.8. The linear growth curves confirm that a continuous growth process occurs under the slow addition conditions studied.<sup>37,90</sup> It is noteworthy that the larger slopes indicate that fewer nanocrystals are formed at higher temperatures (see Figures A.11 and S12). Because there are so few nanocrystals produced at 290 °C, these findings mean that at a particular addition rate, the monomer flux to the individual nanocrystals is even higher than anticipated, yet the nanocrystals are still uniform.

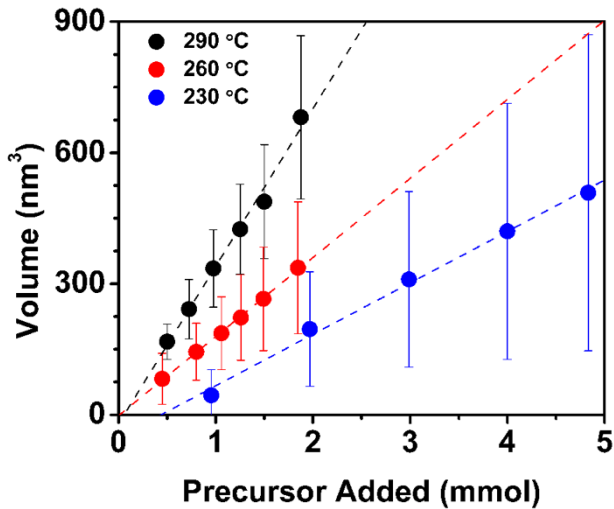


**Figure 3.8.** Nanocrystal growth curves plotted as nanocrystal volume vs. precursor added for 290 °C (black dots), 260 °C (red dots), and 230 °C (blue dots). Error bars reflect one standard deviation of the size dispersion. The dashed lines represent linear fits to the data series. The linear fits indicate that the number of nanocrystals remain constant through the growth period at all temperatures.

### Utilizing variable flux to transform morphology

The preceding sections build a strong case for the influence that flux exerts on nanocrystal morphology. High flux conditions promote surface-diffusion inhibited growth and branched morphology, whereas low flux promotes layer-by-layer growth and faceted morphology. We hypothesized it might be possible to fill in the gaps of branched nanocrystals formed under high flux conditions by continued growth under low flux conditions. Branched nanocrystal cores should contain a high concentration of step edge sites and areas of high energy concave surfaces<sup>66</sup> that, according to the model shown in Scheme 1, should “fill in” if the shell was grown at a low enough flux. To test this hypothesis, nanocrystals were formed at 290 °C using a two-step approach involving rapid precursor addition, followed by a period of slow addition. We chose 290 °C

because, as shown in Figure 3.7, growth at this temperature can produce the most faceted and homogeneous morphologies. Branched nanocrystals were formed by adding 1 mmol of indium precursor at 4 mL/min. Next, 2 mmol of additional precursor was added to these cores at a lower rate (0.17 mL/min). A control sample was synthesized, where the nanocrystals were grown at a constant addition rate of 4 mL/min at 290 °C, with a total precursor addition of 3 mmol to match the amount of precursor used in the two-step process.

TEM images of the initial nanocrystals synthesized with fast addition of precursor (Figure 3.9A) display nanocrystals with the typical branched morphology expected for such conditions, resulting in a broad distribution of P/D values (Figure 3.9D, black trace). A TEM image of the same nanocrystals after continued growth at slow rates is shown in Figure 3.9B. A TEM image of the control, where the nanocrystals were grown with fast addition, continuously is shown in Figure 3.9C. The nanocrystals in Figure 3.9B are essentially free of branching as evidenced by the relatively high frequency (27%) at the mode of their P/D histogram (Figure 3.9D, blue trace). In contrast, the nanocrystals grown under continuous fast addition (Figure 3.9C) present a branched structure similar to those produced by high flux (Figure 3.9A) as shown by their P/D histograms, which nearly trace one another and have maxima around only 7% (Figure 3.9D, red and black traces). These results confirm our surface-diffusion directed growth model wherein low flux caused by slow addition rates promotes attachment of monomers at sites between the branches where there are higher concentrations of reactive step edge sites.

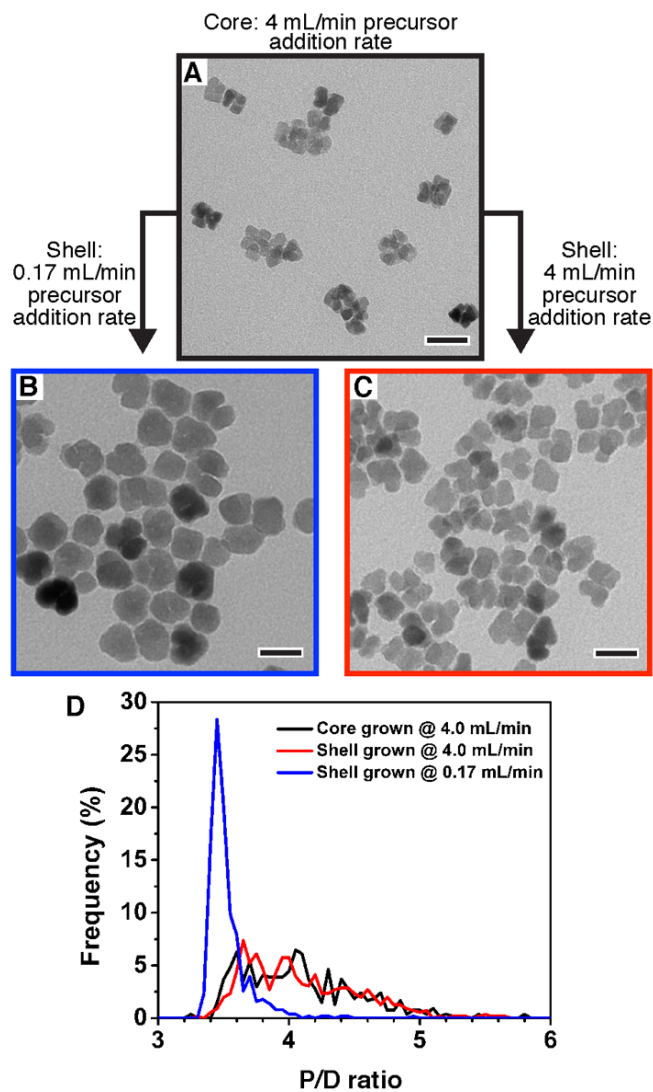


**Figure 3.9.** TEM images of nanocrystals grown at 290 °C to examine the influence of low flux growth on branched nanocrystals. Nanocrystals synthesized by adding 1 mmol of precursor under high flux conditions at 4 mL/min (A), followed by shell growth at a low flux with the addition of 2 mmol of precursor at 0.17 mL/min (B). A control sample was synthesized at a high flux, with 3 mmol precursor added at 4 mL/min (C). Scale bars are 20 nm. The plotted P/D analysis (D) of the samples in A, B, and C indicates that the shell grown at low flux smooths the morphologies of the branched nanocrystal cores (A) while the shell continued to grow at high flux displays similar branched morphology to the cores. Size histograms of samples are available in Figure A.4.

## Conclusions

A continuous growth method, wherein nanocrystal growth can be investigated over a range of precursor addition rates and reaction temperatures, was employed to examine the influence of precursor flux on the growth and morphology of  $\text{In}_2\text{O}_3$  nanocrystals. Under high flux conditions branched morphologies predominate, whereas faceted morphologies result under low flux conditions. Quantitative comparisons of the morphologies were carried out using a new metric that assesses the ratio of the particle's perimeter to its diameter (P/D ratio). This ratio provides a quantitative measure with which to objectively compare the morphologies of nanocrystals produced at different fluxes and temperatures. The branching induced by high flux conditions was shown to be the result of direct reaction of monomers to nanocrystal surfaces, not interparticle reactions (such as coalescence or oriented attachment). Temperature has a profound influence on nanocrystal growth, permitting formation of faceted nanocrystals at high fluxes if the temperature is sufficiently high. Finally, low flux shell growth on highly branched nanocrystal cores fills in the concavities between the branches to produce nanocrystals that are more faceted.

These studies allowed us to gain mechanistic insight into the roles played by flux and temperature on the growth of  $\text{In}_2\text{O}_3$ . The main driver in nanocrystal morphology was found to be surface diffusion of adsorbed monomer, which is indirectly affected by precursor addition rate, i.e., the flux of monomer. Under low flux conditions, where surface monomer concentration is low, adsorbed monomer is able to diffuse to a step edge site and react, promoting layer-by-layer growth and faceted morphology. Conversely, high flux conditions yield a high surface monomer concentration and an

overabundance of adsorbed monomer, sterically hindering surface diffusion and promoting new island formation and branched morphology. Temperature influences the interplay between flux and morphology. Surface diffusion is enhanced at higher temperature (290 °C) and the morphology is less sensitive to flux; this is evidenced by a higher temperature producing the most faceted morphologies and requiring faster precursor addition to yield branched morphologies.

The model developed here for the relationship between monomer flux and nanocrystal morphology may help to explain the uniformity present in many metal oxide nanocrystals synthesized through hot-injection and heat-up approaches. In both synthetic approaches flux steadily decreases as nanocrystal growth progresses, leading to low flux conditions at the end of the reaction. Our results suggest that these conditions at the end of the growth process can produce more uniform nanocrystal morphologies.

Our findings may be applicable to the design of new syntheses to produce nanocrystal morphologies tailored for specific material applications. When uniform, morphologically pure nanocrystals are desired (as for optical, plasmonic, and sensing applications), low flux synthetic conditions are better suited to produce the nanocrystals. However, when higher surface areas or increased surface defect sites are required (as for catalysis and electrochemical applications), high flux conditions for growth are better employed. Additionally, these approaches could potentially be combined to produce novel, hierarchical structures that were previously unattainable, such as the growth of high surface area, branched shells onto a well-defined nanocrystal core to impart dual functionality.

## **Materials and Methods**

### *Materials*

Indium (III) acetate (99.99% trace metals) was purchased from Aldrich. Oleyl alcohol (90%) and oleic acid (80-85%) were purchased from Alfa Aesar. Certified ACS grade acetone and toluene were procured from Fisher Chemical. Chemicals were used as purchased without further purification.

### *Continuous growth syntheses of indium oxide nanocrystals*

Indium precursor was prepared by stirring 1 mmol of indium acetate with 2 mL of oleic acid in a rubber-capped vial and nitrogen gas flowing overhead while submerged in a 150 °C oil bath for a period of one hour. The warm precursor was loaded into a 3 mL syringe (BD plastic) with a 6" 18 G needle attached. Meanwhile, a 50 mL 3-neck round bottom flask was charged with 13.0 mL oleyl alcohol and football-shaped stir bar and necks covered with rubber septa. The alcohol was heated to the desired reaction temperature (230 °C, 260 °C, or 290 °C) using a heating mantle with a DigiTrol II temperature controller from Glas-Col. The alcohol was stirred by magnetic stir plate, and nitrogen was flowed through the overhead space of the reaction flask at a rate of ~120 mL/min, entering through a 16 G needle in the center neck and exiting through a 16G needle in a side neck. Once the desired temperature was reached, indium precursor was added at a specified rate into the oleyl alcohol through a side neck with the aid of a mechanical syringe pump (KD Scientific). The rate of precursor addition was monitored by measuring the volume and duration of each addition. The actual addition rates are reported though they were always very close to the set rate. Typically, the pale yellow

oleyl alcohol became blue and green as precursor was added and the reaction progressed. Following the end of the precursor addition, a small aliquot of the reaction liquid (300  $\mu$ L) was removed and the flask was maintained at the reaction temperature for 20 minutes. The purpose of this heating period was to ensure all precursor would be consumed. Notably, there were no significant changes to the nanocrystal morphology for samples before and after this 20-minute period. Following cooling and exposure to air, an off-white solid is typically observed, and the reaction liquid becomes pale yellow.

The reaction mixture was transferred to centrifuge tubes, rinsing the flask with about 5 mL toluene. Acetone was added (about 4x excess to reaction mix volume) causing formation of a white precipitate. The mixture was centrifuged for 10 minutes at 7000 rpm and the supernatant decanted, leaving behind the nanocrystals as an off-white solid. The nanocrystals were washed twice more by dissolving them in a small amount of toluene and precipitating with acetone, centrifuging, and decanting. Following washing, the nanocrystals were dispersed in toluene, yielding a pale yellow, transparent solution.

To produce growth curves at different temperature syntheses, larger amounts of precursor were prepared – 2 mmol of indium precursor for 260 °C and 290 °C and 5 mmol of indium precursor for 230 °C – with the same ratio of indium to oleic acid (2 mL oleic acid for every 1 mmol of indium precursor). In all cases, the precursor was injected into 13.0 mL oleyl alcohol. The syringe size was adjusted as necessary to accommodate the amount of precursor – a 5 mL syringe for 260 °C and 290 °C syntheses and 10 mL syringe for the 230 °C synthesis. Small aliquots (200 to 300  $\mu$ L) of reaction solution were removed periodically throughout the reaction and washed as described above. The size of the nanocrystals in the aliquots were determined by SAXS.

To produce the core-shell nanocrystals, 3 mmol of indium precursor was prepared. The cores were formed by adding 1 mmol of precursor at a rate of 4.0 mL/min into 290 °C oleyl alcohol. An aliquot was removed. Then the addition was resumed but at a rate of 0.17 mL/min for the remaining 2 mmol of precursor. A control experiment was carried out as well, in which 3 mmol of precursor was all added at 4.0 mL/min.

#### *Nanocrystal characterization*

TEM was carried out using FEI Tecnai G2 Spirit microscope. To prepare grids, carbon-coated copper grids (400 mesh) procured from Ted Pella were briefly dipped into a dilute solution of nanocrystals in toluene (about 0.5 mg nanocrystals/mL) and held vertically until solvent dried (about 20 s). HRTEM imaging was carried out using FEI Titan 300 kV electron microscope on grids prepared in the same manner. Image analysis (size and P/D ratios) was conducted using ImageJ software.<sup>91</sup> After minimal processing, the background was removed by setting a threshold. The remaining particles were analyzed to yield their area and perimeter. For each particle, the area was converted to an effective diameter using the formula for the area of a circle regardless of the actual shape, and the P/D ratio was determined by dividing the particle's perimeter by this diameter. Examples and details for size and P/D analysis are provided Figures A.5 and A.6.

SAXS was carried out using a lab-scale SAXSess mc<sup>2</sup> instrument from Anton Parr (Austria) utilizing a Cu K-alpha X-ray source (operating at 40 kV and 50 mA) and CCD detector (Roper Scientific, Germany). Patterns were modeled to determine size and size distribution using the Irena software package for IGOR (V 6.37).<sup>92</sup> A spherical form factor and gaussian size distribution were used to model nanocrystals from syntheses carried out at 230 °C and 260 °C while a cubic form factor was used to model

nanocrystals from syntheses carried out at 290 °C. XRD patterns were procured with a Rigaku SmartLab diffractometer using Cu K-alpha radiation with Bragg-Brentano geometry, 0.01° 2-theta step size, at a scan rate of about 0.17°/min.

## **Bridge to Chapter IV**

In Chapter III, we studied the effect of monomer flux and synthesis temperature on the growth and resultant morphology of indium oxide nanocrystals. The indium system is a well-behaved and was ideal for use as a model system to examine trends. Because of the great wealth of applications for magnetic iron oxide nanoparticles and the great potential that living growth attributes would bring to controlling iron oxide nanoparticle structure, we wanted to develop the slow addition method for iron oxide nanoparticle growth. Preliminary experiments proved the iron oxide system to be complex and challenging. Reproducibility was an issue. Under some conditions the nanoparticle size distribution was very large. Under other conditions a variety of different shapes were produced. It became apparent that the starting material used to synthesize the iron precursor strongly influenced the growth behavior during nanoparticle synthesis. As such, we carried out a study to examine what about the different precursors was affecting the nanoparticle growth and subsequent morphology.

## CHAPTER IV

### ACETYLACETONATE IN AN IRON (III) RICH PRECURSOR INDUCES TWINNING DEFECTS IN IRON OXIDE NANOPARTICLES

The synthetic work in this chapter was carried out by myself and Kiana Kawamura. It was written by myself with the guidance of Jim Hutchison and is intended to be submitted for publication.

#### **Introduction**

Magnetic iron oxide nanoparticles have vast potential for a wide variety of applications. Because of their magnetic properties and the fact that they are believed to be relatively non-toxic,<sup>1</sup> iron oxide nanoparticles have been explored for a wealth of biomedical applications such as MRI contrast agents,<sup>2–8</sup> magnetic particle imaging,<sup>9–12</sup> thermal treatment for cancer therapy,<sup>13–22</sup> drug delivery,<sup>23</sup> and nanoparticles exhibiting therapeutic and diagnostic attributes have been proposed as “theranostic” tools<sup>24–26</sup>. Their magnetic properties have also made them appealing because they can be magnetically retrieved after performing some other function. These attributes have made them useful as supports for catalysts<sup>27–29</sup> and components in purification and separations strategies<sup>30,31</sup>. As a result of all of this potential, iron oxide nanoparticles are extremely well-studied.

For a majority of applications, the size-dependent magnetism plays an important role. Impressive size control has been demonstrated in the literature<sup>32–36</sup> mainly using

heat-up syntheses involving the thermal decomposition of iron oleate to yield iron oxide nanoparticles. In thermal decomposition syntheses the paramagnetic wüstite ( $\text{FeO}$ ) phase is commonly formed. Unfortunately, for most applications, the desired phases are the ferrimagnetic spinel forms magnetite ( $\text{Fe}_3\text{O}_4$ ) and maghemite ( $\gamma\text{-Fe}_2\text{O}_3$ ). Although it is possible to oxidize wüstite nanoparticles to the spinel forms after they have been synthesized, the magnetic properties fall short of those expected for these structures<sup>36–39</sup> owing to defects introduced in the structure during oxidation. The saturation magnetization values are lower than expected for the spinel phases<sup>36,38,39</sup> and nanoparticles' magnetic size is significantly smaller than their physical size—that is, they behave as though they are smaller nanoparticles<sup>37</sup>.

Much work has been invested in understanding why thermal decomposition syntheses produce wüstite. It's been found that several factors affect the iron oxide crystal phase that results during synthesis, including the Fe (III) precursor itself, the chemistry of the solvent, as well as byproducts of solvent decomposition. It is believed that iron-oxygen bond homolysis that occurs during thermal decomposition reduces iron.<sup>36,40–42</sup> Others have pointed to the reducing ability of long chain alkenes, which are common solvents, at high temperature conditions.<sup>38,43</sup> Byproducts of solvent decomposition such as CO and H<sub>2</sub> have been indicated as another contributor to iron reduction.<sup>40,44,45</sup>

One approach to reduce the number of defects and improve the magnetic properties in iron oxide nanoparticles is to avoid the formation of wüstite and synthesize the spinel form directly. Towards this goal, researchers have introduced oxidants during nanoparticle growth. Krishnan et al. and Rinaldi et al. found that providing a small

amount of gaseous oxygen was sufficient to form spinel iron oxide instead of wüstite.<sup>36,37</sup> Anikeeva et al. discovered that an aromatic ether solvent, such as dibenzyl ether, can behave as an oxidizer when it breaks down thermally, enabling spinel nanocrystals to grow.<sup>38</sup> An alternate strategy, however, would be to avoid the reducing pathways in heat-up syntheses that lead to wüstite. To do this, one must avoid the high temperatures (>300 °C) that lead to thermal breakdown of the organic ligands and/or solvent and the concomitant reduction of the metal.

A suitable synthetic method to test this approach is the lower temperature, continuous growth synthesis developed in our group. Here, a metal oleate precursor is slowly added to hot oleyl alcohol (230 to 290 °C) using a syringe pump. At these lower temperatures, thermal decomposition of metal oleates is very slow. Instead, the metal center behaves as an esterification catalyst between the oleate/oleic acid and oleyl alcohol resulting in the production of metal hydroxide species.<sup>46,47</sup> These metal hydroxide species condense with one another to form and grow the metal oxide nanoparticles. Growth is continuous and the rate can be controlled by the addition rate of precursor, offering excellent control over multiple aspects of nanocrystal structure and composition. A variety of new structures can be prepared with different metal oxide compositions,<sup>46</sup> controlled nanocrystal size<sup>47</sup> and morphology<sup>48</sup>, and dopant distributions within the nanocrystals<sup>49,50</sup>. Because of the successes in other metal oxides, we thought this continuous growth synthesis could provide the same advantages to iron oxide.

It became apparent quickly that the nanoparticle growth with this system was sensitive to the iron precursor used. When an Fe (II) rich oleate, synthesized from Fe(acetate)<sub>2</sub>, was employed, spherical spinel iron oxide nanoparticles with diameters

smaller than 10 nm were formed. These samples possessed low concentrations of crystal defects and high saturation magnetization values compared to similarly sized nanoparticles produced by thermal decomposition methods.<sup>51</sup> However, attempts to grow nanoparticles that were larger than about 10 nm produced samples with broad size dispersity that contained wüstite in their cores. We wondered whether the oxidation state of the precursor might influence the growth of these nanoparticles and turned to a Fe (III) rich oleate precursor synthesized from Fe(acac)<sub>3</sub>. Utilizing this new precursor, it was possible to grow larger nanoparticles (diameters > 10 nm), but a variety of morphologies (Figure 4.1) were produced that we had not observed in any of our other iron oxide nanoparticle syntheses. Furthermore, we hadn't observed similar shapes in the literature. Various ligands<sup>43,52,53</sup> and/or ligand concentrations<sup>54,55</sup> are often employed for directing growth of specific shapes. However, ligands causing these morphologies doesn't seem to be the case here since the Fe (II) rich and Fe (III) rich precursors possess the same ligand (oleic acid) with the same concentration. Because the nanocrystal morphology affects the properties of these materials, we wanted to understand what was causing this phenomenon and learn how to control morphology.

Herein we examine the influence of metal oxidation state and ligation in the precursor on the morphology of nanocrystals produced from different iron oleate precursors. In particular, we investigate the combined effects of iron oxidation state (Fe (II) vs. Fe (III)) and the role of acetylacetone on the nanocrystal morphology, presence or absence of defects, and the crystal phase produced. From this information we show that twinning defects are likely caused by the difficulty in reducing Fe (III) acetylacetone species.

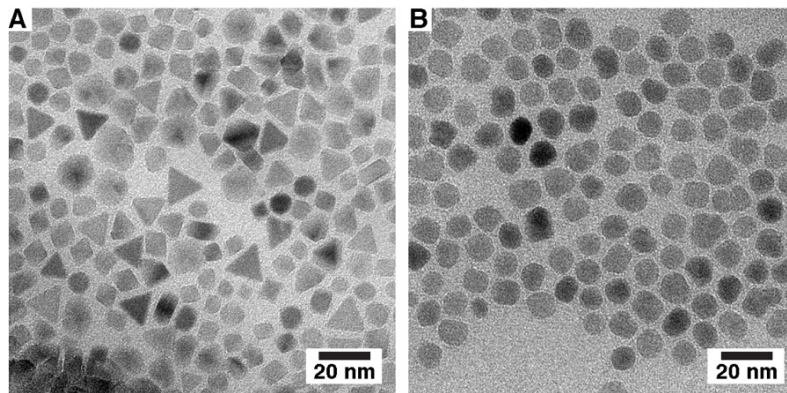


**Figure 4.1.** Comparison of nanoparticles resulting from identical synthesis conditions but using an Fe (III) oleate precursor (A) or an Fe (II) oleate precursor (B). Nanoparticles were synthesized by adding iron oleate precursor into 230 °C oleyl alcohol at a rate of 0.2 mL/min. Size analysis is in Appendix (Figure B.1).

## Research and Discussion

The most common method to produce iron oleate is the salt-exchange method, wherein  $\text{FeCl}_3$  and sodium oleate are refluxed for several hours in a mixture of water, ethanol, and hexane.<sup>34</sup> However, we decided to use an unconventional synthesis method for several reasons. The salt-exchange method exposes the iron oleate complex to ethanol and water which have been shown to coordinate to the iron oleate.<sup>56</sup> Nanoparticle size and size dispersity are highly sensitive to the specific treatment during iron oleate synthesis as a result of the variable binding environment.<sup>36,56,57</sup> Furthermore, remnant sodium and chloride can contaminate growing iron oxide nanoparticles which may affect their shape.<sup>43,58</sup> Starting from an iron salt with a volatile ligand and exchanging with an excess of oleic acid eliminates the need for exposure to water or any other chemical during post synthesis purification.

The Fe (III) rich precursor used throughout most of this study was prepared by mixing  $\text{Fe}(\text{acac})_3$  with approximately six molar excess of oleic acid (2 mL oleic acid for every 1 mmol  $\text{Fe}(\text{acac})_3$ ) for one hour in a 150 °C oil bath with air flowing over head. The period of an hour seemed reasonable based on an isothermal thermogravimetric analysis (TGA) of  $\text{Fe}(\text{acac})_3$  carried out at 150 °C. Ninety percent of the mass loss occurred within 40 minutes of reaching 150 °C (Figure B.2). The same procedure was followed for the preparation of Fe (II) rich precursor except  $\text{Fe}(\text{acetate})_2$  was used instead of  $\text{Fe}(\text{acac})_3$  and  $\text{N}_2$  instead of air was flowed overhead. FTIR analysis of the resulting precursor materials is shown in Figure 4.2.

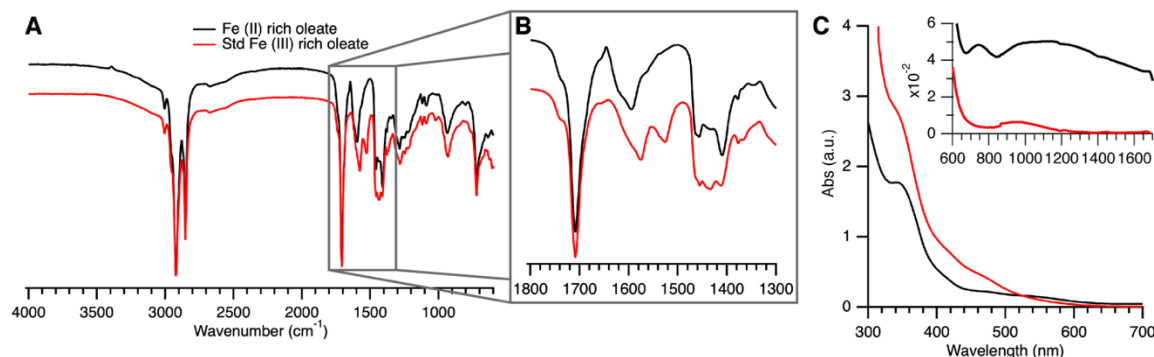


**Figure 4.2.** FTIR and optical characterization of Fe (II) rich and Fe (III) rich precursors. The Fe (III) rich precursor is shown in red and Fe (II) rich precursor black. The full range of acquired FTIR spectrum is shown in (A), and an expanded plot of the region relevant for metal-carboxylate binding is shown in (B). Optical absorbances of precursors in hexanes solutions are shown in (C) with an inset of the NIR region.

The majority of the FTIR spectrum is the same for the two precursors with the exception of the region from ~1350 to 1700  $\text{cm}^{-1}$ , which is the region of interest for carboxylate groups binding to metal cations. Symmetric vibrations of the carboxylate group are exhibited from 1350 to 1500  $\text{cm}^{-1}$  and asymmetric vibration from 1500 to 1700  $\text{cm}^{-1}$ .<sup>59</sup> The symmetric vibration region is similar for both precursors only with

slightly different intensities. In the asymmetric region, however, the Fe (II) rich precursor exhibits primarily one peak while the Fe (III) rich precursor has two. The separation between peaks in the symmetric and asymmetric region, known as  $\Delta$ , can lend information as to the binding mode of the carboxylate group:  $\Delta < 110 \text{ cm}^{-1}$  suggests bidentate,  $140 < \Delta < 200 \text{ cm}^{-1}$  suggests bridging, and  $\Delta > 200 \text{ cm}^{-1}$  suggests unidentate coordination.<sup>56</sup> Thus, the Fe (II) rich precursor (taking the value of 1440 as the symmetric vibration value) has a separation of  $\sim 160 \text{ cm}^{-1}$  indicative of bridging while the Fe (III) rich precursor has separations of  $\sim 160$  and  $\sim 83 \text{ cm}^{-1}$  indicating bridging as well as bidentate binding. The bridging binding mode observed for the Fe (II) rich precursor is consistent with a polymeric structure which is reported for Fe (II) acetate.<sup>60</sup> The Fe (III) rich precursor FTIR spectra is similar to those reported for iron oleate prepared using the salt-exchange method wherein binding modes are bridging and bidentate.<sup>36,56,61</sup>

To understand more about the precursor structures and because we had noticed that the two precursors appeared to be slightly different colors (the Fe (II) precursor was a dark brown-purple while the Fe (III) rich precursor was a dark red-brown), we acquired optical absorbance. Both precursors begin to absorb strongly in the ultraviolet region and exhibit a shoulder peak around 350 nm, while their absorbance in the near-infrared (NIR) region are quite different. The Fe (II) rich precursor has two peaks: one around 745 nm and a very broad peak with a maximum at about 1120 nm. The Fe (III) rich precursor only exhibits one peak in the NIR around 960 nm, which indicates the presence of a tri-iron-oxygen center.<sup>62</sup>

Others have suggested a tri-iron-oxo-cluster with six bridging oleate groups as the structure of Fe (III) oleate synthesized with the salt-exchange method.<sup>36,61</sup> This structure

is consistent with our analysis, since our optical absorbance indicates a tri-iron-oxo core and FTIR spectrum shows bridging carboxylate groups of our Fe (III) rich precursor. However, the FTIR spectrum also indicates the presence of bidentate binding mode. This must mean that either the tri-iron-oxo complex has a mix of bridging and bidentate oleate groups rather than all bridging, or that there is an additional species present in the precursor, possibly a mononuclear complex, that has bidentate carboxylate groups. Regardless, the characterization of our Fe (III) rich precursor is very similar to Fe (III) rich oleate produced by the salt-exchanged method.

From studies employing Fe (III) rich oleate, it appears to be sensitive to reduction by thermal decomposition even at relatively mild temperatures. Feld et al. utilized MALDI-TOF MS to analyze Fe (III) rich oleate during the heating period before nucleation occurs in heat-up syntheses (octadecene solvent) and found that the presence of Fe (II) oleate species increases between the temperatures of 130 and 200 °C.<sup>42</sup> Similarly, Kemp et al. sampled reaction mixtures during the temperature ramping step of heat-up syntheses and determined Fe (II)/Fe (III) content using potassium permanganate titration. They found that Fe (III) reduction was beginning to occur by 180 °C.<sup>36</sup> We wanted to carry out the iron oxide synthesis at relatively low temperatures based on these studies.

Nanoparticles were synthesized with each precursor type using the same procedure. Six milliliters (3 mmol Fe) of the precursor was loaded into a syringe and added to 12.5 mL of 230 °C oleyl alcohol at a rate of 0.2 mL/min (0.1 mmol Fe/min) using a syringe pump. Nitrogen gas was flowed through the reaction vessel at about 110 mL/min. At the end of the precursor addition, the reaction mixture was maintained at

230 °C for 20 minutes to ensure all the starting material had reacted. The resulting nanoparticles were separated by precipitation with acetone and centrifugation. The nanoparticles were washed twice more by dissolving in a small amount of toluene and precipitating with acetone (1:6 ratio of toluene:acetone). Thereafter, nanoparticles were easily dispersed in nonpolar solvents such as hexanes or toluene. The nanoparticles' size and morphology were determined using transmission electron microscopy (TEM) (Figure 4.1, above), their crystal structure was determined using XRD, and their crystal phase (magnetite/maghemite) was determined via optical absorbance (Figure 4.3).

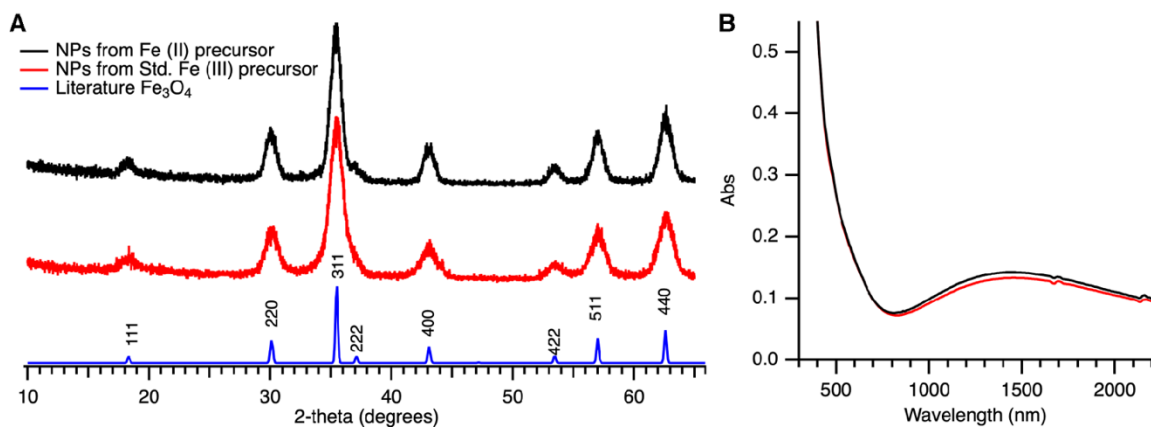


**Figure 4.3.** Phase characterization of nanoparticles by XRD (A) and optical absorbance (B). XRD of nanoparticles produced from standard Fe (III) precursor (center, red trace) and Fe (II) precursor (top, black trace) are compared with a Fe<sub>3</sub>O<sub>4</sub> pattern from the literature (bottom, blue).<sup>63</sup> Optical absorbance nanoparticle solutions normalized to the isosbestic point of magnetite/maghemite (400 nm) produced from standard Fe (III) precursor (red) and Fe (II) precursor (black).

The XRD patterns of both samples of nanoparticles match that of the spinel structure (Figure 4.3). The optical absorbance can lend information about magnetite/maghemite composition as magnetite has broad absorbance in the NIR region while maghemite has no absorbance in this region.<sup>64</sup> Both nanoparticle samples absorb in

the NIR suggesting they contain magnetite. Based on the magnitude of the nanoparticles' absorbance at the magnetite/maghemite isosbestic point (400 nm) and in the NIR, the nanoparticles produced from Fe (III) rich precursor are approximately 55% magnetite, 45% maghemite while the nanoparticles produced from Fe (II) rich precursor are 59% magnetite and 41% maghemite. Oxidation of magnetite to maghemite likely occurs after synthesis because we observed a prominent NIR absorbance immediately following synthesis that decreases over time. The Fe (III) rich precursor yielded nanoparticles that were slightly more oxidized. This may be because the nanoparticle morphologies it produced had higher surface areas compared to the spherical particle produced by the Fe (II) rich precursor, and oxidation must occur at the surface of the nanoparticle. Thus, the higher surface area nanoparticles produced from Fe (III) rich precursor are more oxidized.

TEM images of the nanoparticles produced from the Fe (III) rich precursor were examined to further explore the production of the various morphologies. Many of the shapes appear to be rounded off diamonds and squares which are likely octahedra oriented differently on the TEM grid. Spinel iron oxide nanoparticles are often encapsulated by {111} facets since it is the lowest energy surface, and which results in an octahedral three-dimensional shape.<sup>65,66</sup> Irregular shapes are also exhibited: triangles, elongated rectangles, and larger particles with distinct contrast changes. We suspect that most of the triangle-shaped particles are triangular plates given that they typically don't exhibit dark centers which would be expected for tetrahedral nanoparticles. The TEM shows a few elongated, relatively narrow rectangular shapes, which could be platelet particles oriented on their sides. A few triangle-shaped particles also have darker centers

indicating they are thicker in the center indicating they may be tetrahedra, which, like octahedra, also results from {111} faceting. The round shapes exhibiting contrast changes suggests the presence of polycrystalline nanoparticles. From TEM images it wasn't clear what these various nanoparticle structures had in common.

To understand the crystallinity and facets terminating the nanoparticles, we performed high-resolution TEM (HRTEM) analysis on the (Figure 4.4). Many of the nanoparticles were in fact single crystal based on HRTEM images and fast-Fourier transform (FFT) patterns. In these cases, the HRTEM image showed continuous, uninterrupted array of atomic columns, and the FFT pattern taken from the image corresponded to those expected from diffraction along a particular zone axis (as in Figure 4.4A and B). The triangle particles also exhibited a regular array of atoms (Figure 4.4C), but their FFT patterns were unusual. Spots in the FFT pattern were typical for [111] zone axis, and the prevalence of triangular particles oriented along [111] zone axes suggests that the (111) plane is the basal plane of these particles. However, in addition to expected FFT pattern, there were also unexpected spots (circled in orange in Figure 4.4D). Additionally, the polycrystalline particles also displayed many more spots than expected for a single crystal nanoparticle. They usually appeared to have five crystallites (Figure 4.4E) suggesting they are decahedra, and their FFT pattern likely resulted from the overlap of multiple crystal orientations (Figure 4.4F). Overall, most of the nanoparticles are terminated by (111) planes. The nanoparticles with unusual morphologies, that is, not octahedra, appear to possess defects.

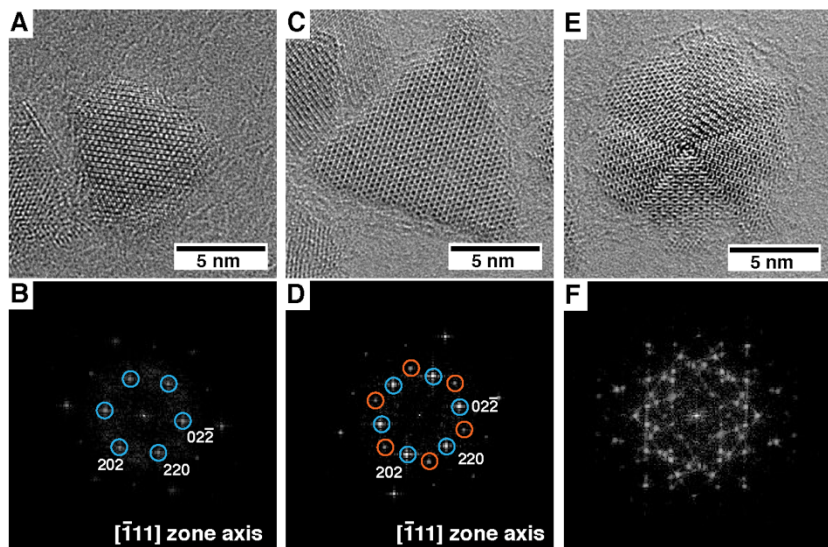


**Figure 4.4.** HRTEM of nanoparticles produced from standard Fe (III) rich precursor demonstrating the variety of nanoparticles produced (A, C, and E) with accompanying FFT patterns (B, D, and F, respectively) to understand crystallinity.

The triangular plates and five-segmented polycrystalline nanoparticles are indicative of twin defects.<sup>67,68</sup> Noble metals with fcc crystal structures often possess twin defects along {111} planes and result in similar-looking nanoparticles.<sup>67</sup> Twinning is somewhat common because it's a low energy defect<sup>68</sup> and also occurs in magnetite which similarly possess fcc crystal structure.<sup>69</sup> Once a twin forms, crystal growth can be propagated along the twinned plane, which results in characteristic morphologies (triangle or hexagonal plates, decahedra, sometimes rods or icosahedra).<sup>68,69</sup> A twin defect is the reversal of atomic stacking sequence along a particular crystal direction. Instead of the typical ABCABC sequence, a twin defect would have ABCBAC sequence.<sup>68</sup> The presence of a twin defect in triangular plate nanoparticles would explain the extra spots in the FFT pattern. Wei et al. observed unexpected spots in FFT patterns of twinned iron oxide nanoplates<sup>70</sup> as did Xiong et al. in the case of twinned palladium

particles<sup>71</sup> apparently due to 1/3 {422} reflection that is usually forbidden for fcc packing. Although a variety of morphologies are produced from the Fe (III) rich precursor, each can be explained by the presence of twin defects.

With a better understanding of the nanoparticles produced by the two different precursors, we assessed how the oxidation state of iron was changing in each case. For the Fe (II) rich precursor, *in situ* PDF studies have suggested that nanoparticles actually grow as wüstite but quickly oxidize to the spinel structure phases when exposed to ambient conditions.<sup>72</sup> In the case of the Fe (III) rich precursor on the other hand, Fe (III) must be partially reduced during the synthesis of nanoparticles. We are not certain of the mechanism of reduction, but a mild thermal decomposition route may be the source based on recent studies on iron oleate discussed earlier.

What about the Fe (III) rich precursor is causing twin defects to form? As a starting point to answering this question, we considered differences between the Fe (II) rich precursor (synthesized from  $\text{Fe}(\text{acetate})_2$ ) and the Fe (III) rich precursor (synthesized from  $\text{Fe}(\text{acac})_3$ ). Differences between the two precursors include the iron oxidation state, of course, and also the ligands. We had reason to believe that the acetylacetonate ligand is difficult to exchange completely because it is a bidentate chelating ligand. Additionally, successful exchange required temperatures no less than  $\sim 150\text{ }^\circ\text{C}$ . Our attempts to lower the exchange temperature (below  $150\text{ }^\circ\text{C}$ ) during iron oleate preparation by applying vacuum were unsuccessful based on the persistence of solid, presumably  $\text{Fe}(\text{acac})_3$ .

One hypothesis for the source of twin-formation is that acetylacetonate ligands aid in the oriented attachment of nanoparticles. In the iron oxide nanoparticle literature,

the source of twinning is often attributed to oriented attachment mechanisms assisted by magnetic attraction between nanoparticles.<sup>13,69</sup> The [111] direction is the easy axis of magnetization and could aid in orienting nanoparticles and facilitating attachment, and potential twin formation, along (111) planes. Since acetylacetone is relatively short, it may allow the close proximity of nanoparticles required for oriented attachment to occur.<sup>73</sup>

A second hypothesis revolves around the iron oxidation state. It appears that twinned planes in the spinel structure could be Fe (II) deficient. Gilks et al. described twinning in magnetite films as missing an octahedral cation plane.<sup>74</sup> Octahedral sites in the magnetite crystal are rich in Fe (II) where the Fe (II) to Fe (III) ratio is one to one (tetrahedral sites are 100% Fe (III)). Furthermore, the local anion packing around a twin defect is hcp instead of ccp (fcc structures have ccp).<sup>68,69,75</sup> Hematite,  $\alpha\text{-Fe}_2\text{O}_3$ , has an hcp oxygen lattice and comprises only Fe (III) cations.<sup>76</sup> Because twin defects appear to be rich in Fe (III) and mimic the hematite lattice, perhaps Fe (II) must be present in order to grow the spinel lattice. When it is deficient, a hematite-like layer may begin to grow, which becomes the twin defect in a spinel lattice. Therefore, if the concentration of Fe (II) is very low, then twin defects are more likely to form and propagate.

Towards testing our first hypothesis related to acetylacetonate ligands, we prepared an Fe (III) rich precursor that was free of acetylacetonate. Devising a synthesis of such a precursor was not straightforward. Extending the  $\text{Fe}(\text{acac})_3/\text{oleic acid}$  exchange longer than an hour, while likely effective to remove more acetylacetone, also began to reduce Fe (III) based on optical absorbance (Figure B.3). The use of  $\text{Fe}(\text{NO}_3)_3$  as starting material for preparing the precursor was also unsuccessful. Oleic acid appeared to be

oxidized by the nitric acid produced *in situ* and use of the precursor in a synthesis resulted in nanoparticles that were highly disperse with respect to size and shape (Figure B.4). We also tried  $\text{Fe(OH)(acetate)}_2$  as an iron source, but it produced nanoparticles during exchange with oleic acid (Figure B.5). Because of these difficulties, we resorted to oxidizing the Fe (II) rich precursor by exposing it to ambient conditions and monitoring its FTIR spectrum and optical absorbance over time (Figure 4.5A, B).

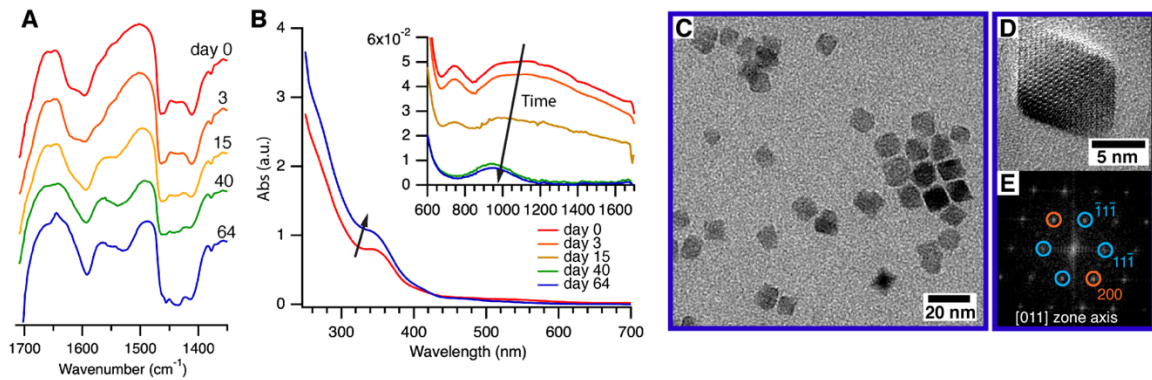


**Figure 4.5.** FTIR (A) and absorbance (B) of initially Fe (II) rich precursor as it oxidized over time and electron microscopy characterization (C, D, and E) of nanoparticles resulting from synthesis. The precursor aged for 64 days was used to synthesize nanoparticles shown in the TEM (C) and HRTEM image (D). An FFT pattern from the HRTEM image is shown in (E). The average nanoparticle size was  $10.6 \pm 1.4$  nm (Figure B.6). Additional HRTEM images in Figure B.7.

Dramatic changes in the FTIR and optical absorbance were observed over time and eventually resembled the standard Fe (III) precursor. As it oxidized, a second peak in the asymmetric carboxylate vibration region of the FTIR spectrum grew in, indicative of bidentate binding—analogous to the standard Fe (III) precursor prepared from  $\text{Fe(acac)}_3$ . Similarly, the initial broad absorbance in the NIR region diminished into a smaller one at 950 nm, indicative of the tri-iron-oxygen-core species and, again, similar to the standard

Fe (III) precursor (Figure 4.5B). Direct comparison of the oxidized precursor to the standard Fe (III) precursor shows only subtle differences in the optical absorbance, and the differences are due to presence of acetylacetone ligands (Figure B.8).

Nanoparticles were synthesized using the oxidized precursor with the same conditions that were used for the previous nanoparticle syntheses (addition of precursor at 0.2 mL/min into 230 °C oleyl alcohol). The projected shapes in TEM images of the resulting nanoparticles were mostly diamonds and squares suggesting morphology was primarily octahedral. Shapes characteristic of twin defects—triangles and decahedra—were notably absent. Spherical particles, like those produced from the Fe (III) rich precursor, were also absent. Further examination with HRTEM (Figure 4.5C, D, and Figure B.7) of the nanoparticles revealed that the majority nanoparticles were single crystal.

The lack of twinning from this oxidized precursor supports our first hypothesis that acetylacetone may aid an oriented attachment events and seems to rule out our second hypothesis that twinning is a result of Fe (II) deficiency. The oxidized precursor appears to show that acetylacetone ligands must be associated with twin defect formation. If acetylacetone ligands are solely responsible for twin defects, then ligating Fe (II) precursor with acetylacetone should yield twin defects as well. Towards this end, we prepared Fe (II) precursor and stirred with acetylacetone for a period of ten minutes. FTIR spectra were acquired before and after (Figure 4.6A). Following the period of stirring, a new peak appeared that was not present in either acetylacetone or Fe (II) rich precursor. The new peak was located at 1525 cm<sup>-1</sup>, which is also present in the

literature reports of Fe(acac)<sub>2</sub> (Figure B.9) suggesting acetylacetone coordinated with iron.

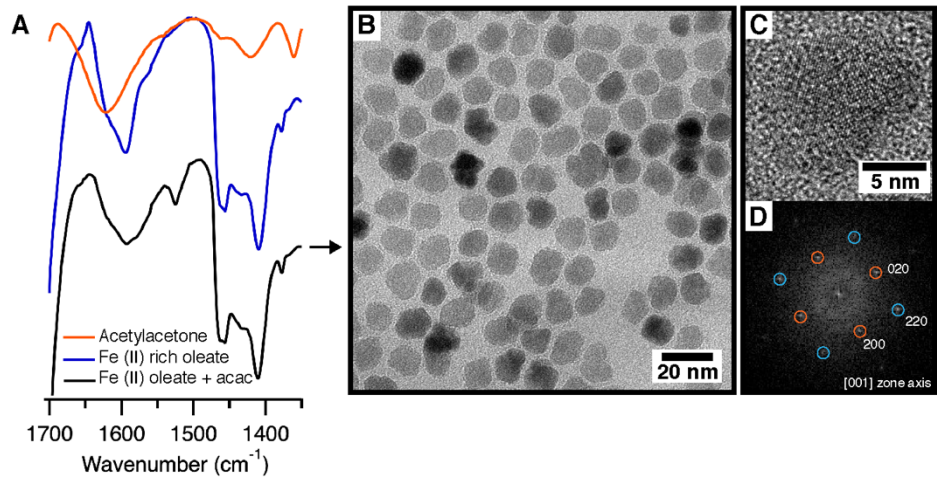


**Figure 4.6.** FTIR characterization of Fe (II) rich oleate with added acetylacetone used as precursor and TEM (B) and HRTEM (C) images of the resulting NPs. Additional HRTEM shown in Appendix Figure B.10.

Synthesis with the Fe (II) rich precursor containing acetylacetone did not induce twin formation. The synthesis was carried out by adding the precursor at the same addition rate of iron as all the previous syntheses. The resulting nanoparticles appear to have rougher surfaces (Figure 4.6B) compared to the previous nanoparticles produced with Fe (II) rich precursor, but HRTEM images did not indicate the presence of twins (Figure 4.6C and D, Figure B.10).

From the results displayed in Figures 4.5 and 4.6, neither Fe (III) oxidation state alone nor acetylacetone ligation alone results in twinned nanoparticles. Instead, it appears that the combination of Fe (III) oxidation state with acetylacetone ligands is responsible for twin defect formation. One possible explanation for the role of

acetylacetone with Fe (III), is that Fe (III) acetylacetone inhibits reduction of Fe (III) to Fe (II), which is required for the production of the spinel structure. From the literature, we know that Fe (III) oleate is susceptible to homolytic cleavage of the iron-carboxylate bond and, therefore, reduction to Fe (II). Perhaps Fe (III) species containing acetylacetone ligands do not undergo the same chemistry as readily.

We reviewed iron oxide thermal decomposition syntheses in the literature to compare those that use Fe (III) oleate starting material and those that use  $\text{Fe}(\text{acac})_3$ —both of which are common. It became evident that, syntheses utilizing  $\text{Fe}(\text{acac})_3$  as a starting material are not as likely to produce reduced phase wüstite compared to iron carboxylate.<sup>32,33</sup> For example, Kim et al. reported the formation of magnetite nanocubes in a heat-up synthesis comprising  $\text{Fe}(\text{acac})_3$ , oleic acid, and benzyl ether solvent.<sup>77</sup> As mentioned in the introduction, benzyl ether may have an oxidizing effect in heat-up syntheses and could also explain the formation of magnetite instead of wüstite. A side-by-side comparison of  $\text{Fe}(\text{acac})_3$  versus an Fe (III) carboxylate starting material is more convincing. Pérez et al. did just that. They measured byproducts of thermal decomposition throughout heat-up syntheses wherein Fe (III) decanoate or  $\text{Fe}(\text{acac})_3$  were used as starting materials.<sup>41</sup> Byproducts of thermal decomposition would indicate a propensity for Fe (III) reduction to Fe (II) since thermal decomposition is the mechanism that reduces iron. In the study, they found that thermal decomposition byproducts were formed at higher temperatures and at lower concentrations when  $\text{Fe}(\text{acac})_3$  was used.<sup>41</sup> This suggested that  $\text{Fe}(\text{acac})_3$  was more difficult to reduce by thermal decomposition compared to the Fe (III) carboxylate starting material.

There's also evidence that Fe(acac)<sub>3</sub> starting material sometimes results in twinned nanoparticles. Erné et al. utilized the synthesis procedure put forth by Sun and Zeng wherein Fe(acac)<sub>3</sub>, oleic acid, oleylamine, and 1,2-hexadecanediol, are heated in phenyl ether to yield spinel iron oxide nanoparticles.<sup>78,79</sup> Seeded growth steps were used to grow larger particles at which time they observed twinned nanoparticles. Wang et al. observed twinned particles following a similar procedure.<sup>80</sup>

If Fe(acac)<sub>3</sub> is more difficult to reduce and thus leads to twinning defects, then providing an Fe (II) source to the standard Fe (III) precursor (which contains acetylacetone ligands) should mitigate twin formation. We tested this by carrying out a nanoparticle synthesis with a mixed precursor consisting of two parts standard Fe (III) precursor and one part Fe (II) precursor—following the ratio of Fe (III) to Fe (II) in stoichiometric magnetite. The FTIR of the mixed precursor reflects the mixture's starting materials (Figure 4.7A) where there is a bridging peak at ~1600 cm<sup>-1</sup> and less intense bidentate peak at ~1540 cm<sup>-1</sup>. The nanoparticle synthesis was performed under the same conditions as previous syntheses (precursor added at 0.2 mL/min into 230 °C oleyl alcohol). TEM images of the resulting particles are shown in Figure 4.7B.

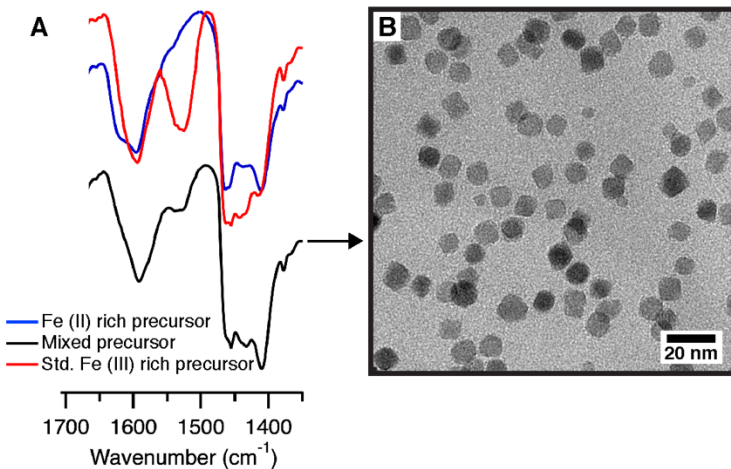


**Figure 4.7.** FTIR (A) characterization of the mixed precursor (lower, black trace) consisting of one part Fe (II) rich precursor (blue trace) and 2 parts standard Fe (III) rich precursor and TEM image of the resultant NPs (B).

The TEM images resulting from the mixed precursor synthesis appear to be free of twinning defects. Nanoparticles are somewhat faceted and rounded off diamonds and square shapes suggesting octahedral morphology. There are not nanoparticles polycrystalline nor triangular shaped nanoparticles that would indicate twin formation. We were concerned, however, that we had simply diluted the acetylacetone ligands to a great enough extent that they could not induce twin-formation. For this reason, we carried out a similar synthesis wherein a mixed precursor with added acetylacetone was used. The results were strikingly similar. The nanoparticles appeared to adopt octahedral morphology and did not exhibit twinning defects (Figure B.11). From these results, then, it appears that Fe (III) acetylacetone's ability to form twin defects is mitigated by the addition of an Fe (II) source.

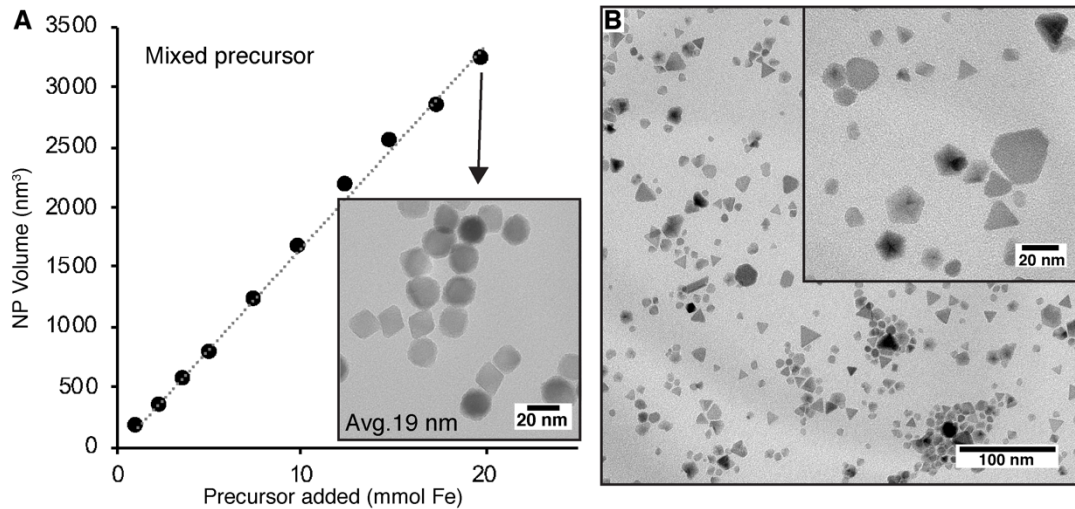


**Figure 4.8.** Growth curve of mixed precursor (A) and TEM images of highly twinned nanoparticles (B). Plot of average nanoparticle volume during the synthesis of 20 mmol of mixed precursor. TEM image of the final nanoparticles (average diameter is 18 nm) is inset. TEM images of nanoparticles produced with Fe (III) rich precursor that was exchanged for only 20 minutes (B).

To demonstrate control over the nanoparticle morphology and growth from what we learned in this study, we synthesized large iron oxide nanoparticles and also highly twinned nanoparticles. Utilizing the mixed oxidation state precursor, 20 mmol was prepared and added into 230 °C oleyl alcohol at 0.2 mL/min. After approximately every 5 mmol added, the addition of precursor was paused, and more oleyl alcohol was slowly added by hand into the flask to replenish what had been consumed by esterification. Small aliquots of the reaction mixture were removed during the synthesis and analyzed by small angle X-ray scattering (SAXS) to determine the nanoparticle size. Plotting the nanoparticle volume as a function of precursor added reveals a linear trend (Figure 4.8A). This implies that all the nanoparticles in the reaction continually grow and no new particle-formation events occur—attributes of a living growth synthesis. The resulting

nanoparticles appeared to be rounded octahedra in shape and were approximately  $18.7 \pm 2.5$  nm in size.

Highly twinned nanoparticles were synthesized by exchanging  $\text{Fe}(\text{acac})_3$  with oleic acid for a period of 20 minutes instead of one hour. Three millimoles of this precursor was added into  $230^\circ\text{C}$  oleyl alcohol at a rate of 0.2 mL/min to yield the nanoparticles displayed in Figure 4.8B. Almost every nanoparticle exhibits morphologies indicative of twin defects. These include triangular plates (some of which are truncated) and well-defined pentagons that, which are decahedral nanoparticles.

## Conclusions

In this study, the effect of iron oleate precursors on the morphology and defect formation of iron oxide nanoparticles was examined in a slow precursor addition synthesis. Iron oleate precursors prepared from different starting materials were characterized using FTIR and optical absorbance to analyze their oxidation states and ligation environment. All syntheses using various precursors were carried out under identical conditions and resulting nanoparticle morphologies and defects were characterized using TEM and HRTEM. A correlation was found between Fe (III) acetylacetone species in the Fe (III) rich precursors and twin defects in the nanoparticles. Twinning was alleviated when an Fe (II) source was provided. Based on the fact that twins in spinel iron oxide seem to have a local deficiency in Fe (II) cations, we believe that twin formation occurs when there is a lack of Fe (II) available. The acetylacetone-ligated Fe (III) rich oleate leads to more twinning because it is more difficult to reduce compared to the Fe (III) precursor possessing only oleate ligands.

With these insights, greater control can be gained in iron oxide nanoparticle with the slow addition synthesis discussed in this chapter as well as in heat-up syntheses. In the slow addition synthesis, using a mixed oxidation state precursor enables the continuous growth of octahedral nanoparticles. If twinned nanoparticles are desired on the other hand, deliberately maintaining acetylacetone ligands in an Fe (III) rich precursor will yield highly twinned nanoparticles. Given the successes achieved with catalysis of other twinned nanoparticles,<sup>81,82</sup> twinned iron oxide nanoparticles may be of interest for study with respect to their catalytic behavior. Beyond the slow addition synthesis, strategies have been put forth in the heat-up synthesis literature towards avoiding over reduction of iron to yield spinel iron oxide phases. Based on our conclusion that iron-acetylacetone species are more difficult to reduce, using Fe(acac)<sub>3</sub> in heat-up syntheses could aid in eliminating over-reduction and wüstite formation.

Beyond spinel iron oxide synthesis, utilizing Fe (III) acetylacetone species may be a strategy for the synthesis of hematite ( $\alpha$ -Fe<sub>2</sub>O<sub>3</sub>) nanoparticles. Currently, hematite nanoparticle syntheses are not well-controlled and have high size and shape dispersions.<sup>83</sup> As twin defects possess local hematite-like packing (hcp), then suppressing Fe (III) reduction completely during synthesis may induce the formation of hematite nanoparticles instead of spinel. If this is possible, then the slow addition method could provide a means to synthesize monodisperse hematite nanoparticles. Furthermore, doping with various metals (Ni, Zn, Co, Ba, etc.) would yield hexaferrite nanoparticles that have high permeabilities and are of interest for a multitude of communications applications and technologies.<sup>84</sup>

## **Experimental**

### *Materials*

Fe(acac)<sub>3</sub> (99.9%), Fe(acetate)<sub>2</sub> (99.99%), and Fe(NO<sub>3</sub>)<sub>3</sub>•9(H<sub>2</sub>O) (99.95%) were purchased from Sigma Aldrich. Oleic acid (85%) and oleyl alcohol (85%) were purchased from Alfa Aesar. Hexanes (99.9%), acetone (99.5%), and toluene (99.9%) were procured from Fisher Chmical. Fe(OH)(acetate)<sub>2</sub> (95%) was obtained from Alfa Chemistry.

### *Synthesis of precursor*

For a typical synthesis of the standard Fe (III) rich precursor, 4 mmol Fe(acac)<sub>3</sub> and 8 mL oleic acid were loaded into a glass vial and suspended in a 150 °C oil bath. The mixture was magnetically stirred for one hour with a gentle flow of air overhead to carry away acetylacetone released by the ligand exchange. Similarly, Fe (II) rich precursor was prepared by mixing 4 mmol Fe(acetate)<sub>2</sub> with 8 mL oleic acid in a 150 °C oil bath but with N<sub>2</sub> flowing overhead instead of air to prevent oxidation. For the acetylacetone Fe (II) precursor, 3 mmol of Fe (II) rich precursor was prepared as described. Then 3 mmol (0.3 mL) of acetylacetone was added and the solution was stirred for 10 minutes at room temperature before use. For the mixed precursor, Fe (III) rich precursor and Fe (II) rich precursor were prepared separately. Then 4 mL Fe (III) rich precursor was mixed with 2 mL Fe (II) rich precursor for about 10 minutes before use.

### *Characterization of precursors*

FTIR characterization of the precursor was carried out with Nicolet 6700 FTIR from Thermo-Fisher. Some spectra were acquired using salt plates, and some were

acquired with diamond ATR accessory. Optical absorbance was carried out with a Perkin-Elmer Lambda-1050 UV/Vis/NIR spectrophotometer. To acquire optical absorbance, precursors were diluted with hexanes. For the UV-Visible region, 5  $\mu$ L of precursor was dissolved in 1 mL hexanes to make a  $\sim$  2.5 mM concentration (Fe basis) solution. For the NIR region, 25  $\mu$ L of precursor was dissolved in 2 mL hexanes to make a  $\sim$  6.3 mM solution. Absorbance spectra were collected from 250 nm to 1800 nm with 5 nm steps of solutions loaded in a quartz cuvette with 2 mm pathlength.

### *Synthesis of nanoparticles*

For synthesis of nanoparticles, 6 mL ( $\sim$  3 mmol Fe) of precursor was loaded in a 10 mL BD plastic syringe and a six-inch 18G needle was attached. Precursor was then added at a rate of 0.2 mL/min into 12.5 mL of 230 °C oleyl alcohol in a 100 mL 3-neck round bottom flask using a KD scientific syringe pump. When precursors with added acetylacetone were used, the addition rate was adjusted to 0.21 mL/min so that the addition rate based on iron (1 mmol/min) was the same as other syntheses. A Glas-Col DigiTrol II temperature controller and heating mantle were used to heat the reaction. The reaction solution was magnetically stirred with a football-shaped stir bar. N<sub>2</sub> gas was flowed through the flask during synthesis. An image of the reaction flask during synthesis is included in Figure B.11. At the end of the precursor addition period, a 1 mL aliquot of the reaction solution was removed, and the remainder was maintained at 230 °C for 20 minutes to ensure all precursor was consumed. After the reaction mixture cooled to room temperature a precipitate could be observed, which were nanoparticles. The nanoparticles were purified by further precipitation with a large excess of acetone (at least 2:1 acetone to reaction mixture) and centrifuged at 7000 rpm for 10 minutes. The dark black-brown

solid was then dispersed in a ~5mL toluene, precipitated with ~ 40 mL acetone, and centrifuged again. This last sequence was repeated once more. Nanoparticles were typically dispersed in toluene for storage.

For the 20 mmol scale synthesis, a 250 mL three neck round bottom flask and an over-headed stirrer with a Teflon paddle were used. We found that magnetic stirring caused issues as the nanoparticles grew larger and would be strongly attracted to the stir-bar. Initially, 12.5 mL oleyl alcohol was heated in the reaction flask to 230 °C and precursor was added at 0.2 mL/min. N<sub>2</sub> was flowed in the overhead space. After adding about 5 mmol (10 mL) of precursor, the addition of precursor was paused and 12 mL of oleyl alcohol was added by hand. Then, the precursor addition was resumed, and the process repeated until approximately 40 mL of precursor had been added. Growing beyond ~19 mL proved to be an issue apparently because of the magnetic attraction between nanoparticles. Nanoparticles appeared to aggregate together, and size dispersity increased.

#### *Characterization of nanoparticles*

For TEM characterization, a dilute dispersion of nanoparticles (~ 0.5 mg/mL) in toluene was prepared, and a TEM grid (TED Pella, 400 mesh carbon-coated copper grid) was dipped into the solution and allowed to dry while being held vertically. Images were acquired on an FEI Tecnai G2 Spirit TEM. High resolution TEM images were acquired Titan 80-300 electron microscope. ImageJ software was used to analyze TEM data. TEM size analysis was performed according to Woehrle et al.<sup>85</sup> For XRD sample preparation, a thick layer of nanoparticles was deposited on (100) Si wafer substrate by drop casting a concentrated dispersion of nanoparticles. XRD was then acquired using a Rigaku

Smartlab diffractometer from 10 to 65 degrees 2-theta with 0.01-degree step size at a rate of 0.17 degrees/min. Cu K $\alpha$  radiation and Bragg-Brentano geometry were used along with a diffracted beam monochromator to eliminate the large fluorescent background from iron. Dilute nanoparticle dispersions in toluene (0.2 mg/mL) were prepared for optical absorbance. Absorbance was collected of solutions loaded in a 2 mm pathlength cuvette from 250 to 2200 nm at step size of 5 nm. For SAXS characterization, aliquots (0.3 mL) of reaction mixture were washed once with acetone (~7 mL) and dispersed in ~ 1 mL toluene. Nanoparticle solutions were loaded in capillary tubes and sealed with epoxy. SAXS patterns were collected with an Anton Paar SAXSess mc<sup>2</sup>, and data was modeled using Irena software package to determine nanoparticle diameter.<sup>86</sup> For the modelling, a spherical form factor and a gaussian distribution were used. The volumes reported in Figure 4.8A were calculated from the resulting average diameters.

## Bridge to Chapter V

Here we analyzed the Fe (II) and Fe (III) rich precursors and the nanoparticle morphology and defects resulting from their use in the synthesis. The following chapter utilizes the Fe (II) rich precursor which exhibits attributes of a living synthesis when used to synthesize relatively small (under 10 nm in diameter) nanoparticles. We leveraged this synthesis behavior to examine the size-dependent magnetic properties of small iron oxide nanoparticles.

CHAPTER V

INSIGHTS INTO THE MAGNETIC PROPERTIES OF SUB-10 NM IRON OXIDE  
NANOCRYSTALS THROUGH THE USE OF A CONTINUOUS GROWTH  
SYNTHESIS

This chapter was previously published as Cooper, S. R., L. Kenyon Plummer, L. K.; Alexia G. Cosby, A. G.; Lenox, P.; Jander, A.; Dhagat, P.; and Hutchison, J. E. *Chem. Mater.* **2018**, *30*, 6053-6062.

## Introduction

The size-dependent magnetic properties of nanocrystals (NCs) such as iron oxide have been widely studied and harnessed for use in technologically important applications.<sup>1-5</sup> Changes in the magnetic properties occur most frequently in samples below 20 nm, where superparamagnetic behavior emerges.<sup>6</sup> For NC systems in general, Auffan *et al.* stated that NC properties are more likely to deviate from bulk when core diameters drop below 15 nm.<sup>7</sup> At the smallest sizes, it has been suggested that the properties of iron oxide NCs are strongly influenced by variations in the local structure of the surface and core in the form of vacancies, structural phase differences, and atomic disorder, in addition to effects solely induced by NC diameter.<sup>8-10</sup> For example, the magnetic properties of iron oxide are influenced by the phase (the spinel phases (magnetite and maghemite) and more reduced forms<sup>11-14</sup>) and surface structure (defects, vacancies, and disorder),<sup>9,15-20</sup> as well as the size<sup>21-24</sup> and shape<sup>25-28</sup> of the core. Each of

these structural features needs to be individually, and independently, tuned to attain optimal performance in applications. For instance, magnetic hyperthermia treatment requires NCs with uniform sizes (narrow dispersity) within the range of 10-20 nm that have high saturation magnetization ( $M_S$ ) and high anisotropy.<sup>29,30</sup> For ideal T1 MRI contrast agents, small NCs (<3 nm) with a large number of unpaired spins and a small magnetic moment are needed.<sup>23</sup> NCs for water purification must be small to have a large increase in surface area to adsorb contaminants as well as having a sufficient magnetic moment for separations.<sup>9,31</sup> In cases where a high saturation magnetization is required, each atomic layer of material added to the NC must contribute as many aligned spins as possible.

The influence of structure on the magnetic properties of iron oxide NCs has been investigated in the past but there are wide disparities in the values of saturation magnetization ( $M_S$ ) reported for different NCs in the sub-10 nm size range. For example,  $M_S$  values reported for 5 nm spinel iron oxide NCs range from 17 Am<sup>2</sup>/kg<sup>15</sup> to 82 Am<sup>2</sup>/kg<sup>32</sup> indicating that diameter is not the only structural feature influencing the values of  $M_S$  for spinel iron oxide NCs. It has been suggested that ligand shell,<sup>16,17</sup> surface roughness,<sup>18</sup> phase (maghemite, magnetite, and wüstite),<sup>24,33,10,34,35</sup> and core structural disorder<sup>12,33,36–38</sup> can also influence the  $M_S$  values. The use of different synthetic methods to access samples with different core sizes further complicates the interpretation of size-dependent  $M_S$  data because different reaction conditions influence the atomic-level core and surface structure in addition to core size.

Most studies conclude that  $M_S$  values for small NCs are lower than the bulk values and decrease with size,<sup>15,16,18,21,23,26,34,39–44</sup> although there are some reports that

suggest bulk values for NCs as small as 5 nm.<sup>17,32,45</sup> The loss of magnetically interacting neighboring atoms, often referred to as broken exchange bonds, at the surface of the material is widely thought to cause the spins at the surface to misalign with the core and no longer contribute to the magnetization of the material.<sup>15,46,47</sup> When the NCs are small, the large surface-to-volume ratio causes these canted spins to be a larger percentage of spins in the NC and therefore reduces the  $M_S$ . For example, the first layer of Fe-O-Fe (~0.3 nm thick) of a 10 nm NCs is 17% of the NCs volume, whereas the same shell thickness would comprise nearly 40% of the volume in a 4 nm NC. The reported values of the thickness of the magnetically disordered layer vary widely in the literature from more than a nanometer thick,<sup>15,47</sup> to some reports suggesting no surface layer at all.<sup>17</sup> Taken together, these large disparities in values of  $M_S$  and differences in the thickness of a magnetically disordered layer, for NCs of same size, suggest that the differences may be due to differences in core or surface structure induced by different synthetic methods.

Reaction conditions have been shown to have significant influence over the magnetic properties for spinel iron oxide NCs. For example, surfactants and ligands can change the ligand shell and therefore the surface structure.<sup>16–18</sup> Roca *et al.* observed  $M_S$  close to bulk values for 6.4 nm diameter NCs with very small canting angles measured by Mössbauer, an effect that they attributed to the oleic acid ligand shell.<sup>17</sup> However, other studies have shown significant decreases in  $M_S$  values for NCs containing oleic acid ligands.<sup>10,21,23,41,42</sup> Reaction solvent can also affect the properties of the NCs. For example, the formation of a reduced wüstite phase that may occur during high temperature syntheses<sup>11,42,48,49</sup> can be mitigated by synthesizing<sup>37</sup> NCs in dibenzyl ether. The use of an oxidizing atmosphere during NC formation can influence the reaction

products by producing spinel instead of a reduced phase.<sup>33</sup> Syntheses conducted at low temperatures, below the thermal decomposition temperature of the precursor, typically report the highest values of  $M_S$  for NCs that show size-dependence below 10 nm diameter, suggesting that low-temperature synthetic conditions may lead to high quality NCs.<sup>16,40</sup> It has been suggested that thermal decomposition reactions produce radical species<sup>10,49–52</sup> that exhibit less selective reactivity. Despite the numerous reports on the magnetic properties of iron oxide NCs, it is difficult to draw conclusions regarding the size-dependence because many reports have very few NCs below 10 nm in diameter to compare.

To understand the influence of NC size on magnetic properties, we need access to a series of sub-10 nm NCs with incremental sizes. We reasoned that a lower temperature, continuous growth synthesis could provide a more selective reaction pathway to produce NCs with sub-nm size increments, employing the same reaction conditions for each size in the series. A lower temperature synthesis would reduce or eliminate the production of highly reactive intermediates and minimize the risk of introducing strain-producing defects. Strain-producing defects include grain boundaries, antiphase boundaries, twin planes and stacking faults. Further, the use of a single, defined reaction pathway will be more likely to result in controlled and uniform NC growth. Given the strong dependence of properties on reaction conditions,<sup>17,18,33,37</sup> each NC in the series should be made under the same synthetic conditions (additives, solvent, atmosphere and temperature).

Herein we report the  $M_S$  and magnetic size of a series of spinel iron oxide NCs produced via a continuous growth method that provides access to small (core diameter <10 nm) NCs with specifically defined diameters. A new, lower temperature (230°C)

method, involving a selective catalytic esterification mechanism, allowed for continuous growth and the production of closely sized increments all synthesized under the same reaction conditions.<sup>53,54</sup> By simply varying the amount of precursor added, the size can be controlled to within a single atomic layer, producing a series of eight distinct size populations evenly distributed between 4 and 10 nm in diameter. Structural characterization suggests that the NCs possess the spinel structure with high maghemite content. The  $M_S$  values for the members of this series show a clear size-dependent trend. Further, the  $M_S$  values are higher than comparably sized NCs produced by other synthesis methods, suggesting that the continuous growth process introduces fewer strain-producing defects, increasing the effective magnetic size of the NCs.

## Results and Discussion

### *Synthesis and Characterization of NCs*

To target the NCs needed for this study, we employed a continuous growth method that our group has established for the synthesis of metal oxides in which a metal oleate precursor is slowly dripped into hot oleyl alcohol.<sup>53,54</sup> We observed previously that the metal center catalyzes the esterification of the oleate with oleyl alcohol at relatively low temperatures developing metal hydroxyl species *in situ* that then condense to form NCs.<sup>53</sup> Given the success of this approach for producing single crystal NCs with controlled composition and structure with near atomic-layer precision in indium oxide,<sup>54,55</sup> we anticipated that it would work well to produce the series of iron oxide NCs needed for this study. We found that as we added iron oleate precursor slowly to the

reaction flask containing hot oleyl alcohol, NCs grow continuously and maintain narrow size dispersion. Since the size is varied by the addition of precursor into the reaction vessel, the temperature, solvent and ligand shell are constant for all synthesized sizes. Addition of precursor also allows for a layer of metal oxide to be added at a time, allowing the synthesis of any diameter NC desired.

Iron oxide NCs were synthesized by adding an iron oleate precursor at a slow injection rate (0.17 ml/min) into oleyl alcohol at 230°C under a constant flow (120 mL/min) of nitrogen. In order to ensure that there was always an excess of oleyl alcohol in the flask, more oleyl alcohol was added to the reaction after every 1 mmol of iron oleate. NCs were sampled for analysis at intervals throughout each synthetic trial by removing aliquots of the reaction mixture and allowing the samples to cool rapidly to room temperature. The sizes of the isolated samples were determined by small angle x-ray scattering (SAXS), as seen in Figure 5.1. Transmission electron microscopy (TEM) was used to determine the morphology of the NCs of a select number of samples (Figure 5.2A-D). High resolution TEM (HRTEM) was used to determine the crystallinity and confirm low defect concentration in the NCs as seen in Figure 5.2E-H. The structure of the NCs was analyzed by powder x-ray diffraction (XRD) and Rietveld refinement as seen in Figure 5.3A and Figure C.4-C.6. The percentage of the magnetite and maghemite phases of the spinel structure in the NCs was determined by near-IR optical absorbance,<sup>56</sup> as seen in Figure 5.3B.

Over the course of the synthesis, SAXS analysis showed that the NCs grew as more iron precursor was added to the reaction (shown in Figure 5.1 and Figures C.1 and C.2). The size of the NCs can be tuned from about 4 to 10 nm by varying the amount of

precursor added to the reaction. During the addition of precursor, the dispersities remained low (below 15%) for all but the smallest sample size (Figure 5.1A and Table C.1). The NC core volume (or molecular mass) exhibited linear growth with respect to the amount of iron precursor added to the reaction flask (Figure 5.1B), suggesting a living growth mechanism.<sup>57</sup> Linear growth enables predictable and reproducible NC diameters from synthesis to synthesis. Reproducibility was verified by completing three separate syntheses which all gave similar NC sizes and dispersities (Figure C.1). Variation in final size and growth rate is a result of different number of nuclei being formed during the nucleation event (see discussion in Appendix C following Figure C.1). In our synthesis size is controlled by the precursor added to the reaction rather than the nucleation event alone (as is the case with one-pot heat up methods) enabling isolation of samples from 4–10 nm from each batch even if nucleation step is different.

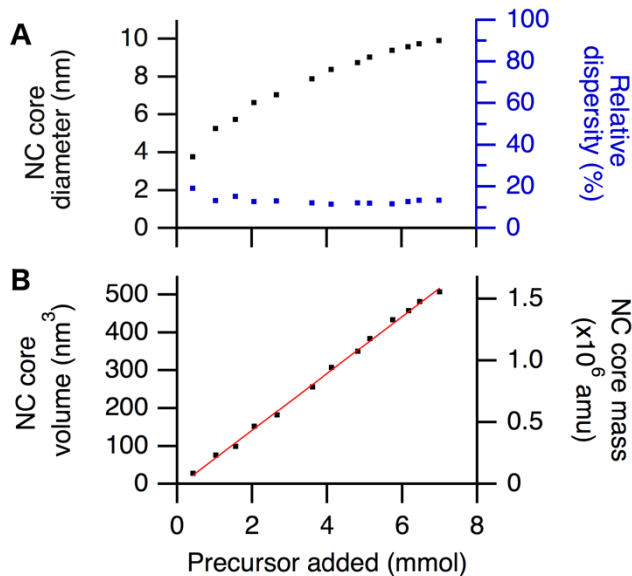


**Figure 5.1.** Size analysis of NCs by SAXS throughout a slow injection reaction showing NC diameter (A), and volume and mass of the NC core (B) plotted as a function of precursor added to the solution. Linear regression analysis of volume vs. precursor resulted in a linear relationship ( $R^2=0.998$ ). In repeated SAXS measurements, the standard deviation of the mean size is less than 0.7 Å.

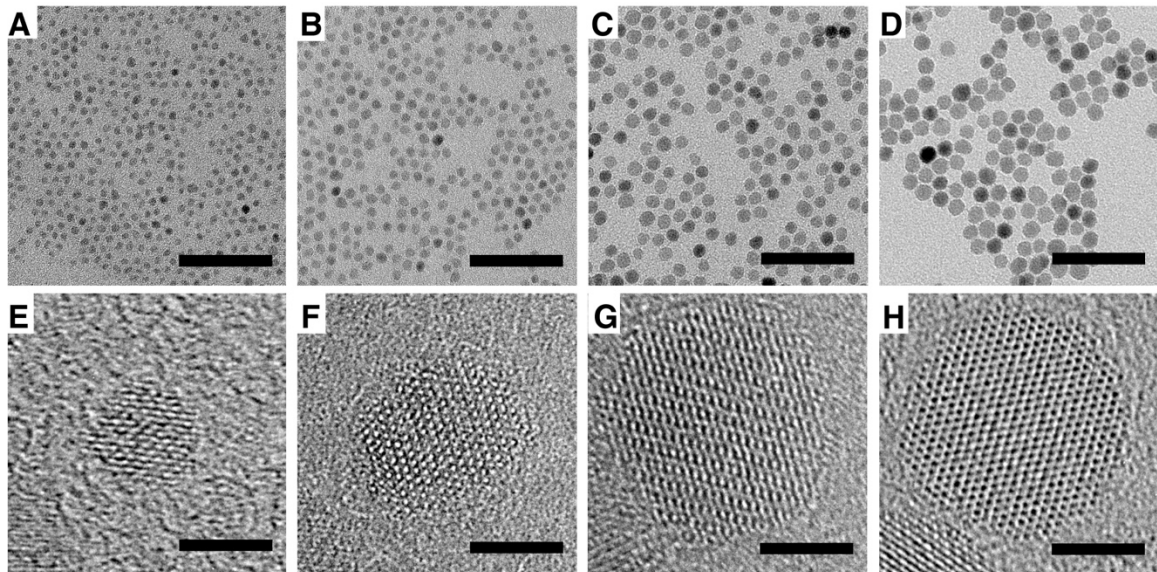


**Figure 5.2.** TEM and HRTEM micrographs demonstrating morphology and crystallinity of NCs with sizes (determined by SAXS) of  $3.9 \pm 0.6$  nm (A, E),  $5.1 \pm 0.7$  nm (B, F),  $6.6 \pm 0.6$  nm (C, G), and  $8.0 \pm 0.8$  nm (D, H). Scale bars are 50 nm for top row and 3 nm for bottom row.

TEM images (Figure 5.2A-D) were analyzed to determine the morphology of the NCs. Figure 5.2 shows a spherical morphology over this size range for all NCs throughout the synthesis. We examined samples across the size range with HRTEM to determine the crystallinity of the NCs throughout their growth. The HRTEM images show lattice fringes that extend through the entirety of the NC, suggesting NCs are single crystal (Figure 5.2E-H). Fast Fourier Transform (FFT) was performed on HRTEM images to further confirm that NCs are single crystalline. Indexed FFT patterns are included in Figure C.3.

XRD patterns for three representative NC samples across the synthesized size range (Figure 5.3A) were analyzed by Rietveld analysis (Table C.2-C.4 and Figure C.4-C.6) to determine the phase of the NCs. Figure 5.3A shows the spinel crystal structure of

iron oxide is present and are free of peaks associated with the wüstite phase. The Rietveld analysis fits and refined parameters are included in the supporting information.

Spinel iron oxide may contain two phases; maghemite ( $\gamma\text{-Fe}_2\text{O}_3$ ) and magnetite ( $\text{Fe}_3\text{O}_4$ ) where the difference in the two phases is the oxidation state of iron in the structure.<sup>58–60</sup> Magnetite contains both  $\text{Fe}^{2+}$  and  $\text{Fe}^{3+}$  cations whereas maghemite contains only  $\text{Fe}^{3+}$  and has some vacancies in sites where  $\text{Fe}^{2+}$  occurs in the octahedrally coordinated sites of the magnetite phase.<sup>59</sup> The maghemite and magnetite phases of the spinel iron oxide structure are hard to elucidate with XRD because there are only subtle differences between the patterns for the two phases and these become less pronounced from the broadening of the peaks in the small NC sizes.<sup>10</sup> We employed near-IR optical absorbance spectroscopy (Figure 5.3B) to determine the percentage of magnetite and maghemite in each NC sample. For samples containing magnetite, there is a strong absorbance from 800-2000 nm due to the charge transfer from  $\text{Fe}^{2+}$  to  $\text{Fe}^{3+}$  that can be used to quantify the amount of magnetite in spinel iron oxide NCs.<sup>56</sup> Spectra were normalized at 400 nm where an isosbestic point for magnetite and maghemite occurs. Using a theoretical absorbance cross section for 10 nm magnetite NCs calculated by Tang *et al.*,<sup>56</sup> a percentage of magnetite is determined from the ratio of the absorbance at 1450 nm to that expected of pure magnetite (0.39 units as scaled in Figure 5.3B). The percentage of magnetite in the NCs increases from 2% to 26% as the core size increases from 3.9 nm to 8 nm (Table S5).

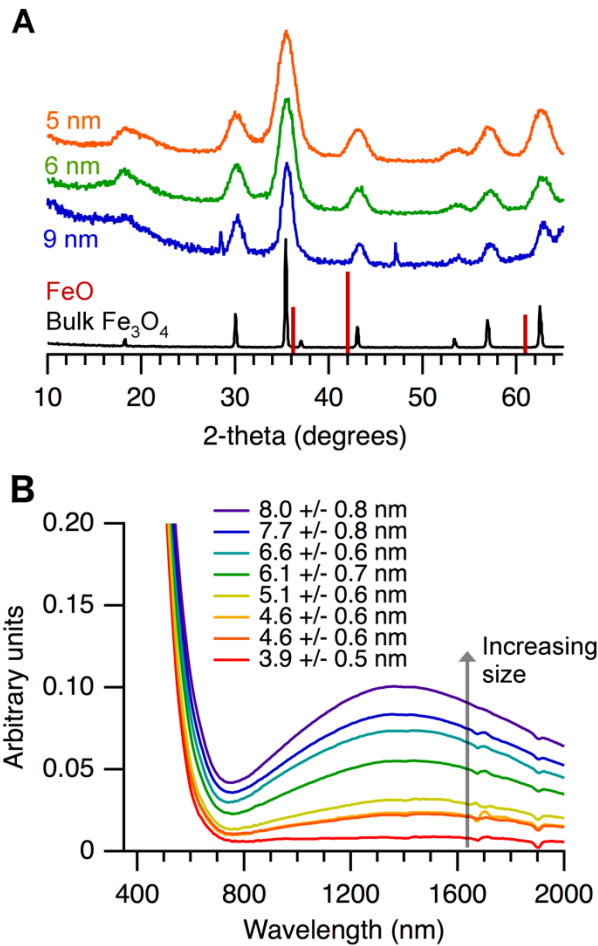


**Figure 5.3.** Structure and phase analysis of NCs throughout a slow injection reaction. Powder XRD patterns (A) of several sizes showing a narrowing of peaks as the NCs increase in size. The peaks at 28° and 47° in the blue pattern (9 nm sample) are due to the substrate. A pattern of bulk magnetite (black) and calculated wüstite (red lines) are shown at bottom of the stack for reference. Normalized optical absorbance spectra (B) of NC solutions were acquired to determine the maghemite/magnetite content. Larger NCs have greater absorption centered at 1450 nm demonstrating greater magnetite content.

## Magnetic properties

Access to this unique series of well-defined NCs all produced by the same synthesis, affords an opportunity for in-depth investigations regarding the size-dependence of the magnetic properties. Magnetization curves were acquired at room

temperature for eight different samples (Figure C.8) with core sizes ranging from 3.9 to 8 nm using a vibrating sample magnetometer (VSM). Samples were dispersed in KBr and pressed into pellets for analysis. The amount of iron oxide in each pellet was quantified using inductively coupled plasma optical emission spectroscopy (ICP-OES). The magnetic response of a pure KBr pellet was subtracted from the magnetization curve obtained for each pellet.

$M_S$  was determined for each sample by fitting the magnetization curves to the Langevin equation (eqn. 1).<sup>33,61</sup>

$$m(B) = V_{ICP} M_S \left[ \coth\left(\frac{mB}{k_B T}\right) - \frac{k_B T}{mB} \right], \quad (1)$$

In equation 1,  $m(B)$  is the moment of the sample measured by VSM at an applied field,  $B$ ;  $V_{ICP}$  is the total volume of iron oxide in the sample determined from ICP-OES measurements;  $M_S$  is the saturation magnetization of the iron oxide in the sample; and  $m$  is the moment of a single NC. The measured magnetization curves were normalized to the  $M_S$  values provided by the fit so that the curves could be readily compared to one another. The individual magnetization curves and the fits to the Langevin equation can be found in Figure C.7.

The normalized magnetization curves are shown in Figure 5.4. Each curve passes through the origin: there is no remanent magnetization at zero field and no hysteresis for any of the samples. The curves suggest that all the NCs exhibit superparamagnetic behavior because they completely demagnetize in the absence of a magnetic field at room temperature. By inspection, it is also clear that the NCs exhibit size-dependent magnetic behavior. The smaller NCs have smaller magnetic moments than the larger NCs and require greater fields to maintain magnetization against thermally-induced

demagnetization. As a result, the magnetic susceptibility (slope of curves through zero field) for smaller NCs is lower than for larger NCs.<sup>61</sup>

The  $M_S$  values for the NCs trend with size across the series (Figure 5.5, Table C.5), with larger NCs having a larger  $M_S$  and smaller NCs having a reduced  $M_S$  as might be expected based upon literature reports.<sup>21,23,43</sup> The value measured for 8.0 nm NCs was 78 Am<sup>2</sup>/kg, decreasing to 55 Am<sup>2</sup>/kg for NCs with a diameter of 3.9 nm. These values are somewhat smaller, but comparable, to the range of values expected for bulk maghemite (60-80 Am<sup>2</sup>/kg).<sup>62</sup>

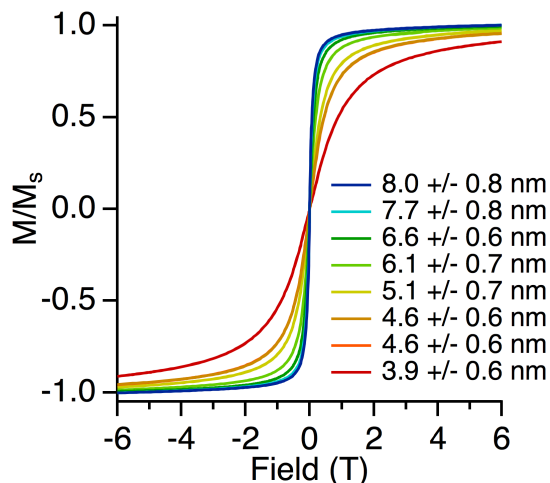


**Figure 5.4.** Normalized magnetization as a function of applied field for the eight distinct NC samples between 4-8 nm in diameter.

Figure 5.5 displays the  $M_S$  values obtained in this study and compares them to those from five published studies<sup>16,21,45,41,40</sup> that are the most comparable to our series of NCs (a more complete collection is included in Figure C.9). As can be seen in the figure, our values are amongst the highest reported in the literature for NCs in this size range and show size-dependent values across this size series. Each of these studies examines iron

oxide NCs with sizes under 10 nm and wherein the size dispersions of each sample are below 20% and are reported to be all spinel structure. All but one of the previously reported studies (Demortière et al.<sup>21</sup>) used the same reaction temperature, solvent, and ligands to synthesize each size in their size series. The  $M_s$  values vary by more than 100% between reports with a 4 nm NC having a reported  $M_s$  between 37 and 83 Am<sup>2</sup>/kg (from Demortiere et al.<sup>21</sup> and Castellanos-Rubio et al.<sup>45</sup>, respectively). Since the size is the same for these materials there must be other variables leading to the differences in  $M_s$ .

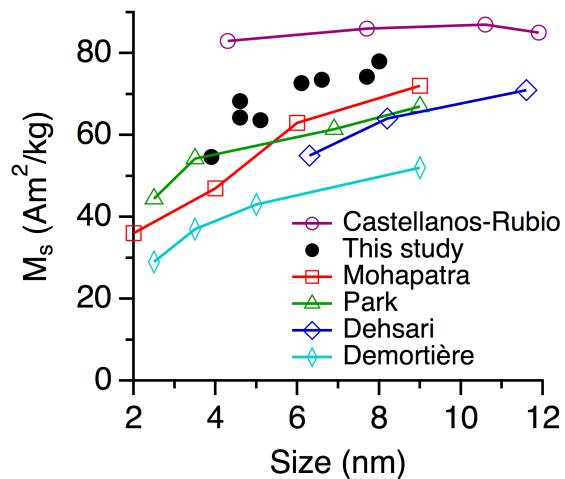


**Figure 5.5.**  $M_s$  plotted as a function of NC diameter up to 10 nm for this study (black circles) and other studies that examined at least three samples under ten nanometers in size with narrow size dispersion. Studies compared are from Castellanos-Rubio *et al.* (purple circles), Mohapatra *et al.*<sup>16</sup> (Red squares), Park *et al.* (green triangles), Dehsari *et al.* (blue diamonds), and Demortière *et al.*<sup>21</sup> (light blue, narrow diamonds). For a representative sample the standard deviation in the method for this measurement was 1.2 Am<sup>2</sup>/kg—the error bars are much smaller than the size of the marker used in the graph for each sample.

The syntheses described above can be grouped into three categories: high temperature syntheses in the presence of an oxidizing agent (air or dibenzyl ether), high

temperature syntheses in the presence of esterification reagents (oleic acid and amine or alcohol) and low temperature syntheses ( $230^{\circ}\text{C}$  and under). The lowest values for size-dependent  $M_S$  in Figure 5.5 were synthesized by thermal decomposition of an iron oleate precursor in air (Demortère *et al.*<sup>21</sup>). Even though these magnetic data were collected at 5K (which yields higher  $M_S$  values than those collected at 300K) they were still among the lowest values. The next highest  $M_S$  values shown in the figure are for NCs synthesized by a high temperature reaction of an iron precursor in the presence of dibenzyl ether and esterification reagents, for example oleic acid, oleylamine and 1,2 hexadecandiol (Dehsari *et al.*<sup>41</sup>). Even higher  $M_S$  values were obtained for NCs synthesized at much lower temperatures: for example at  $200^{\circ}\text{C}$  (Mohapatra *et al.*<sup>16</sup>) and  $95^{\circ}\text{C}$  (Park *et al.*<sup>40</sup>). Castellanos-Rubio *et al.*<sup>45</sup> reported near bulk  $M_S$  values but also showed no size dependence, in contrast to 13 other studies (Figure C.9) in the same size range. The major difference in their study<sup>45</sup> was the use of an  $\text{Fe}^0$  precursor that often produces iron NCs,<sup>63,64</sup> but carried out in the presence of dibenzyl ether. Their results<sup>45</sup> also contrast with Dehsari *et al.*<sup>41</sup> who used dibenzyl ether as a solvent, as well, but with an  $\text{Fe}^{3+}$  precursor, producing NCs that have values well below the bulk  $M_S$  values. Our own results that show higher  $M_S$  values compared to most literature examples were produced using esterification reactions and lower reaction temperatures.

The trend in the size-dependent  $M_S$  values shown in Figure 5.5 suggests that differences in reaction conditions might be the cause of the variations in properties of the resulting NCs. Given that the NCs represented here have comparable sizes, similarly narrow size distributions, and uniform morphologies, the differences in magnetic properties are likely the result of different amounts of strain-producing defects in the NC

cores. Strain-producing defects within the NC structure are known to decrease the effective  $M_S$ ,<sup>12,33,37,65,66</sup> and each of the three categories of synthetic conditions discussed above are expected to influence the number of strain-producing defects in the cores of the NCs to different degrees. Synthesizing NCs in the presence of oxygen<sup>33</sup> or dibenzyl ether<sup>37</sup> prevents the formation of reduced iron oxide that result in strain-producing defects even after oxidation to the spinel structure.<sup>12</sup> The use of starting materials that can potentially undergo esterification and amidification<sup>53,67–70</sup> can facilitate metal oxide formation through defined reaction pathways that prevent the formation of highly reactive species generated in radical reactions (i.e. thermal decomposition) thereby, reducing the number of strain-producing defects. The reactions carried out at lower temperatures, which showed the best magnetic properties in prior studies,<sup>16,40</sup> may produce the fewest strain-producing defects because the approach avoids the highly reactive intermediates and reduced forms of iron oxide produced during thermal decomposition.

Our synthesis likely results in reduced numbers of strain-producing defects because it employs a defined esterification mechanism and is performed at a lower temperature. Furthermore, it involves slow injection of precursor that likely slows NC growth rate compared to the rapid growth found in methods where all precursor is added at once. Rapid growth may trap strain-producing defects within the crystal while relatively slow growth during slow injection may limit the number of strain-producing defects.

The larger values of  $M_S$  found in our NCs prompted us to further analyze the volume of each NC that contributes to the magnetization by determining the effective

magnetic size for the NCs in each sample. The magnetic size can be derived from the Langevin equation and is the portion of the core material within the NC that has an  $M_S$  of the bulk material.<sup>26,30,54,55,61</sup> To obtain the magnetic size, we set  $m = M_D * \frac{\pi}{6}D_c^3$  in Equation 1 where  $M_D$  is the saturation magnetization of bulk maghemite (76 Am<sup>2</sup>/kg or 372 kA/m) and the term  $\frac{\pi}{6}D_c^3$  is the volume of the magnetically active core where  $D_c$  is the diameter. We chose to use the bulk saturation magnetization value of maghemite because our NIR studies showed that the NCs are primarily maghemite. We assumed a lognormal distribution of magnetic diameter.<sup>61</sup> Figure C.10 illustrates the trend obtained if we calculate an  $M_D$  based upon the percentage of each phase measured by near-IR for each NC size. Additional details are provided in the Materials and Methods section.

The magnetic sizes determined by fitting are compared to the physical size measured by SAXS analysis in Figure 5.6. The magnetic sizes are nearly identical to the physical sizes, which implies that nearly all of the core material contributes fully to the magnetic properties of the NC, leading to the higher values of  $M_S$  compared to the literature examples. If we assume that most of the inactive material resides at the surface,<sup>46</sup> our results suggest that there is only a very thin non-magnetic shell. Across the series, there are no significant differences in the thickness of the shell. The slight trend toward larger magnetic sizes at larger physical sizes may be due to small increases in magnetite content at the larger sizes.

The larger magnetically active volume in our NCs suggests that these NCs possess a very thin non-magnetic surface layer and have few strain-producing defects. Our evaluation suggests that the disordered layer is less than 0.2 nm thick which would restrict the magnetic disorder to the iron atoms at the surface of the particle. Reductions

in  $M_S$  from bulk values reported within the NC literature are typically attributed to a magnetically disordered surface layer, and the reported magnetically disordered shell thicknesses is between 0.35-1.0 nm thick.<sup>15,18,21,47,71</sup> The fact that the magnetic size is nearly the physical size within our series suggests that these larger thicknesses may be due to strain-producing defects within the NCs as opposed to larger disordered surface layers. A close examination of our NCs by HRTEM shows single crystal spherical NCs with few NCs exhibiting strain-producing defects. Thus, it seems likely that the increased  $M_S$  values are the result of the fewer strain-producing defects introduced because of the condensation-based reaction mechanism, slower growth rate and lower temperature offered by the slow injection synthesis.

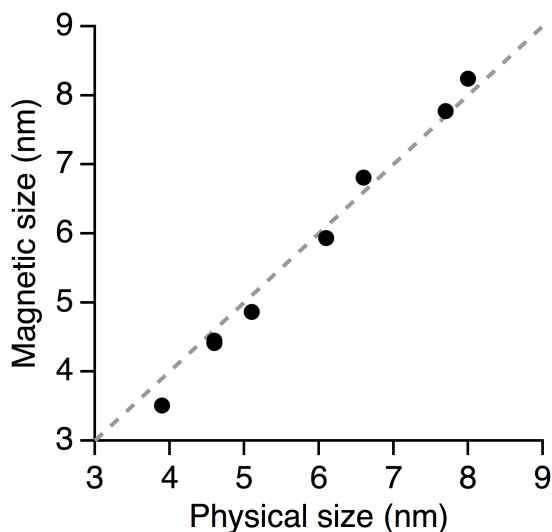


**Figure 5.6.** The effective magnetic size from Langevin function fit plotted as a function of physical size determined by SAXS where the gray dashed line is  $y=x$ .

Comparison of our synthetic method to alternatives reported in the literature offers new insight into how to design syntheses that will produce NCs that are defect free for the study of properties and structure in NCs less than 10 nm in diameter. The

attributes of our synthesis ensure the size and size induced structure are what is being studied, not artifacts introduced as a result of variations in synthetic methods. Lower-temperature and slow growth through a single defined growth mechanism, are likely responsible for the high degree of crystallinity and enhanced magnetic properties of these NCs. Such a mechanism contrasts with thermal decomposition methods that produce NCs that are known to produce a number of byproducts.<sup>49–52</sup> Thermal decomposition reactions produce a variety of organic radicals that have a multitude of competing and accessible reaction pathways resulting in a large number of different products including H<sub>2</sub>, CO, CO<sub>2</sub>, alkenes, ketones, and esters.<sup>49,50,72</sup> It might be expected that there would be an increased incidence of strain-producing defects in NCs produced by lower selectivity shown in thermal decomposition pathways. In fact, the other size series in this size range that have  $M_S$  values approaching ours and size dependence produced NCs at low temperatures<sup>16,40</sup> where radical mechanisms are not likely involved. Based upon these findings taken together, it seems that a reasonable strategy to produce defect-free NCs is to identify and use synthetic methods that avoid radicals or other highly reactive species, have slower growth rates and keep a low temperature. In this way, it may be possible to more effectively tune and tailor the properties of nanomaterials.

## Conclusions

A series of sub-10 nm spinel iron oxide NCs, produced using a continuous growth method, were used to study fundamental questions relating nanoscale structure to size-dependent magnetic properties. This series of NCs is ideal for these studies because size is the only physical characteristic that varies during this continuous growth synthesis. The

NCs show a decrease in  $M_S$  with a decrease in the diameter of the NCs as has been shown in other studies; however, these NCs have higher  $M_S$  values than NCs produced in the same size range by other methods. The magnetic size was approximately the same size as measured by SAXS and TEM indicating a much thinner magnetically dead layer than was previously thought to be present on NCs. This analysis changes our understanding of the nanoscale structure and properties of spinel iron oxide NCs by demonstrating that the magnetically dead layer can, in fact, be much thinner than previously reported and maintain size-dependent magnetic properties across the range. We believe that the high crystallinity, and thus enhanced magnetism, of the NCs measured in this study is due to the attributes of the slow injection synthesis (condensation reaction pathway, slow growth, and relatively low synthesis temperature). Our results further imply that relatively low temperature syntheses may be a strategy to avoid strain-producing defects.

Magnetic and adsorptive properties of small iron oxide NCs have long been of interest to environmental, health, and physics communities, but synthetic approaches to adequately study structure-property relationships have not existed. This slow injection synthesis method is a facile way to produce high quality NCs that can be used by physics, biology, and environmental science fields in order to probe and exploit promising size-dependent properties. For instance, Mössbauer studies using these high quality NCs could be done to examine the origins of these size-dependent magnetic properties. We expect that continuous NC growth will be a useful, transferable strategy to produce other NCs to examine the influence of size on the properties of those materials.

## **Materials and Methods**

### *Materials*

Iron (II) acetate (99.99%), technical grade oleic acid (90%) from Sigma Aldrich was used to make the iron oleate precursor. Magnetite powder from Aldrich (99.99% trace metals basis) used for bulk magnetite XRD trace. Technical grade oleyl alcohol (85%) from Alfa Aesar was used as the solvent in the synthesis of spinel iron oxide NCs.

### *Synthesis*

To make the precursor, 6 mmol of iron (II) acetate (1.04 g) is stirred in a 20 mL vial with a septum with 12 ml of oleic acid under a flow of N<sub>2</sub> heated in an oil bath to 150°C for 1 hour. The oleyl alcohol (12.5 mL) is heated in a 100 mL three neck flask to 230°C under a flow of N<sub>2</sub> of 120 mL/min. The three-neck flask has three septa: one that delivers N<sub>2</sub> through a needle, one holds a larger gauge needle to allow water to escape and the third holds a thermocouple that is connected to a heating controller with a heating mantle. The liquid is magnetically stirred vigorously with a stir bar. One mmol of the precursor is added to the oleyl alcohol at an addition rate of 10 mL/hr with the use of a syringe pump and a 10 mL luer lock plastic syringe with a stainless steel 20-gauge needle. After addition of 2 ml of precursor, 3 ml of oleyl alcohol is added to the reaction. This process is repeated until 6 mmol of iron oleate is added to the reaction. The oleyl alcohol and NC solution is heated at 230°C for an additional 20 minutes after all precursor is added. The reaction is cooled under a flow of N<sub>2</sub> and then was put into a 50 mL centrifuge tube and washed with ethanol in order to precipitate the NCs. The samples are washed with acetone and centrifuged at 7000 rpm for 20 min. The NCs are then

dispersed in toluene and centrifuged once at 3500 rpm for 5 min to remove any remaining insoluble material.

To study the growth of the NCs, a 1 mL gas tight syringe with a 20-gauge stainless steel needle was used to remove 0.3 mL of reaction solution at various points in the addition. The sample was then put into a 15 mL centrifuge tube and allowed to cool to room temperature. These samples were also washed in the same way by centrifugation in acetone and were dispersed finally in toluene and centrifuged.

#### *Physical Characterization*

Transmission electron microscopy images were taken with an FEI Tecnai G2 Spirit microscope. 400 mesh copper TEM grids (Ted Pella) were prepared by dip-coating in dilute solutions of NCs. High resolution TEM was acquired with FEI's Titan 80-300 kV microscope. Diameter was determined from particle area in TEM images using FIJI<sup>73</sup> software to corroborate the NC size with SAXS.

Small angle x-ray scattering patterns (SAXS) were acquired using the SAXSess mc<sup>2</sup> from Anton Paar with work up of SAXS data by Irena software package to determine NC core size, dispersity and volume fraction.<sup>74</sup> Modeling was done using a Gaussian distribution with a spherical form factor and a dilute system structure factor. For samples that were magnetically characterized, a lognormal distribution was used in modeling so that the physical and magnetic sizes could be compared directly. A background was refined in order to account for fluorescence of iron. X-ray diffraction patterns were procured with a Rigaku SmartLab diffractometer using Cu K $\alpha$  radiation and a diffracted beam monochromator to eliminate background iron fluorescence. Near-IR measurements

were performed on dilute ( $\sim$ 1 mg/mL) dispersions of NCs in toluene in 3 mm path length quartz cuvette using PerkinElmer Lambda-1050 UV/Vis/NIR spectrophotometer.

### *Magnetic Characterization*

The magnetic properties of the NCs were measured by room temperature vibrating sample magnetometry (VSM) using the Physical Property Measurement System by Quantum Design, Inc. The magnetic moment was calibrated using a 1 mm diameter Yttrium Iron Garnet Sphere with a mass of 0.0028 mg and a certified magnetization of 27.6 Am<sup>2</sup>/kg at 0.5 T magnetic field (standard reference material 2853 from National Institute of Standards and Technology). Solid pellets consisting of the NCs in KBr, a non-magnetic binder, were prepared for the measurements as follows: The NC dispersion (in toluene) was sonicated for 5 minutes and pipetted into a measured quantity of KBr powder. The fluid and KBr binder were mixed by mortar and pestle for 30 minutes in atmosphere while the toluene solvent was allowed to evaporate. The dry powder mixture was then pressed into pellets. The resulting pellets had a concentration of magnetic NCs of about 0.3% by volume. The actual amounts of iron oxide in pellets were determined after magnetic measurements by ICP-OES.

For iron quantification using ICP-OES, KBr pellets containing magnetically characterized NCs were dissolved in 2 mL concentrated HNO<sub>3</sub> (JT Baker Ultrex ® II ultrapure reagent) over a 48-hour period. Samples were diluted to 2% HNO<sub>3</sub> with nanopure water for analysis. For the calibration curve, ten iron solutions between 100 ppm and 0.01 ppm were prepared from a 1000 ppm Fe standard (ICCA) in 2% HNO<sub>3</sub> matrix. ICP-OES measurements were acquired using a Thermo Scientific X-Series II CCT.

To fit the VSM measurements, the magnetic diameters in the sample were assumed to have a lognormal distribution with a probability density function,

$$P(D_C) = \frac{1}{D_C \sigma \sqrt{2\pi}} \exp\left(\frac{(\ln D_C - \mu)^2}{2\sigma^2}\right) \quad (2)$$

having parameters  $\mu$  and  $\sigma$ . Equations (1) (i.e. the Langevin equation) and (2) were fit by nonlinear regression to the VSM data, with the free parameters  $M_S$ ,  $\mu$ , and  $\sigma$  determined independently for each pellet sample. The effective magnetic size of the NC, or the mean magnetic core diameter,  $\langle D_C \rangle$ , is determined from the parameters of the lognormal distribution according to  $\langle D_C \rangle = \exp(\mu + \frac{\sigma^2}{2})$ .

## Bridge to Chapter VI

Here in Chapter V, a study of size-dependent magnetic properties of spinel structure iron oxide nanoparticles was examined. While the spinel phases (possessing a ccp oxide lattice) of iron oxide are ideal for some applications due to their superparamagnetic behavior, hexagonal ferrites that instead possess an hcp oxide lattice are better suited for other types of applications. Specifically, the high permeability of hexagonal ferrites makes them of interest for device components operating at high frequencies. However, attempts to synthesize hexagonal ferrites with the slow addition method were unsuccessful because it always yielded the spinel structure. As a result, we resorted to top-down methods to synthesize hexagonal ferrite nanoparticles for a collaborative study. In this study, we formulated UV-curable inks containing high permeability and high permittivity nanoparticles for the purpose of 3D printing nanocomposites.

CHAPTER VI

DESIGN AND DIGITAL FABRICATION OF MAGNETO-DIELECTRIC  
COMPOSITES FOR ADDITIVE MANUFACTURING OF GRADIENT INDEX RF  
LENSES

This chapter was published as Masood, K.; Zaikova, T.; Plummer, K.; Allen, T.; Stasiak, J.; Harmon, P.; Hutchison, J.; Jander, A.; Dhagat, P. Design and Digital Fabrication of Magneto-Dielectric Composites for Additive Manufacturing of Gradient Index RF Lenses. In NIP & Digital Fabrication Conference; San Francisco, CA, 2019; Vol. 1, pp 94–99.

## **Introduction**

The future radio wave landscape looks crowded, with personal communications (cell phones, Wi-Fi, Bluetooth), autonomous vehicles (radar, vehicle-to-vehicle and vehicle-to-road communications), and wireless internet-connected devices (the so called “internet of things”) competing for limited radio frequency (RF) spectrum. To conserve the RF spectral resources, as well as the power in mobile devices, each device may require a custom designed antenna beam pattern. This presents an opportunity for digital manufacturing of application-specific gradient index RF lenses to shape and direct the antenna beam.

In this paper, the materials, processing, and characterization techniques required to produce functional gradient index (GRIN) RF lenses using digital and additive

manufacturing methods are discussed. The design of the lenses is based on transformation optics (TO) approaches,<sup>1,2</sup> in which the shape of the input beam and the desired shape of the output beam are used to algorithmically determine the required spatial distribution of refractive index,  $n(x, y, z)$ , for the gradient index lens.<sup>3,4</sup> Existing literature considers varying only the dielectric permittivity,  $\epsilon$ , of the lens material. However, additionally varying the magnetic permeability,  $\mu$ , of the lens material would allow independent control of the wave impedance,  $Z = \sqrt{\frac{\mu}{\epsilon}}$ , as well as the refractive index  $n \approx \sqrt{\mu\epsilon}$ , enabling impedance matching and reduction of unwanted reflections.

An example of a gradient index lens designed by TO methods is shown in Figure 6.1. The electromagnetic wave simulation shows the otherwise hemispherical radiation from a patch antenna being collimated into a beam by use of a graded refractive index cylindrical lens. In this design, the relative permittivity and permeability were constrained to a conservative range of 1 to 5 and 1 to 2.5 respectively. In contrast to an equivalent lens with gradients in permittivity only (requiring values up to 7.5) this lens has lower reflection losses at the lens surface. Additive manufacturing of such a lens will require voxel-by-voxel control of the permittivity and permeability of the material being incorporated into the structure.

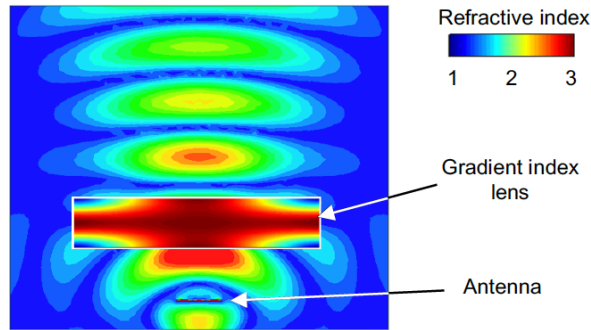


**Figure 6.1.** Electromagnetic wave simulation of a gradient index RF lens designed by transformation optics under the constraint  $\epsilon < 5\epsilon_0$  and  $\mu < 2.5\mu_0$ . The initially radially diverging beam from the antenna (see below the lens). The lens is 25 cm in diameter and 6.25 cm in thickness.

Ultimately, the focusing ability and size reduction of the lens antenna are limited by the range of refractive index (contrast ratio) that can be achieved in the additive manufacturing process. A larger ratio of maximum to minimum refractive index enables more compact lens designs and higher antenna gain to be achieved. Thus, a key goal of our work is not only to fabricate objects with predetermined refractive index gradients, but also to maximize the possible contrast ratio.

### Additive Manufacturing Methods

To ultimately realize small, high gain lenses, the focus of this project has been to develop materials and additive manufacturing processes to incorporate well-controlled fractions of high permittivity and high-permeability nanoparticles into 3D printed objects. We develop two unique additive manufacturing methods for variable permeability/permittivity functional materials:

1. Polymer particle bed infiltration and fusing, in which solutions carrying functional dielectric or magnetic nanoparticles are infiltrated into a polymer powder bed

using inkjet printing. Each layer of powder is fused by heating above the melting temperature of the polymer. The object permeability and permittivity are determined by digitally controlling the amount of solution that is infused in each printed voxel.

2. Inkjet printing of a polymerizable nanocomposite ink, in which suspensions of dielectric or magnetic nanoparticles in a UV-polymerizable matrix solution are printed one layer at a time followed by curing with UV light. The object permeability and permittivity are determined by digitally controlling the ratio of three different “colors” of ink that are jetted into each voxel, i.e. inks containing dielectric nanoparticles, magnetic nanoparticles, or polymer matrix only.

#### *Polymer particle bed infiltration and fusing*

In this technique digital inkjet printing and powder bed fusion processing are integrated to produce functional polymer nanocomposites with predictable and reproducible dielectric properties. Dielectric polymer nanocomposites are fabricated using commercial grade polyamide 12 (PA12) powder (HP 3D High Reusability PA 12).<sup>5</sup> An ink containing a stabilized dispersion of barium titanate ( $\text{BaTiO}_3$ ) nanoparticles was formulated and dispensed into the PA12 powder using a thermal inkjet materials printer. The nanoparticles were synthesized using the mixed-oxide solid-state reaction method.<sup>6</sup> X-ray diffraction measurements confirmed that the nanoparticles had a composition of  $\text{Ba}_1\text{Ti}_{1.1}\text{O}_4$  i.e., near the correct stoichiometry though slightly rich in Ti.

Functionalization of the nanoparticles using ligand-attachment chemistry is used to reduce aggregation of the nanoparticles in the ink solvent.<sup>7</sup> The functionalization process also serves to increase the molecular-scale attachment rates and retention efficiency between the infiltrating nanoparticles and the surfaces of the wetted PA12

particles, resulting in a more homogeneous distribution of nanoparticles within the powder layer.<sup>8,9</sup>

The fabrication system is illustrated in Figure 6.2. In this study, the volume fraction of BaTiO<sub>3</sub> nanoparticles that infiltrated the PA12 powder was controlled using an automated printing program. Following the inkjet printing step, the powder sample was heated above the PA12 melting temperature (~188.5 °C) using radiant heating and then allowed to cool to room temperature. A layer-by-layer approach was used, in which successively a fresh layer of powder (~100 microns thick) was applied, mechanically smoothed, and packed on top of the previously fused layer and then infused with the BaTiO<sub>3</sub> ink. This process was repeated until a ~2 mm thick sample was produced. Using multiple passes to fill the interstitial spaces of the loosely packed powder, a volumetric loading of up to 45% BaTiO<sub>3</sub> could be achieved. After fusing, 1 cm diameter Au electrodes were deposited onto both sides of each sample to facilitate electrical characterization.

Cross-sections through four polymer nanocomposite samples prepared by the powder bed fusion technique are shown in Figure 6.3. Each photograph represents a different volume fraction of BaTiO<sub>3</sub> nanoparticles. In the photographs, clusters of ~100 nm aggregates mixed into the polymer are visible. Although the sample cross sections are still being analyzed, it is likely that clusters are formed by aggregated groups of nanoparticles dispersed into the PA12 polymer host.

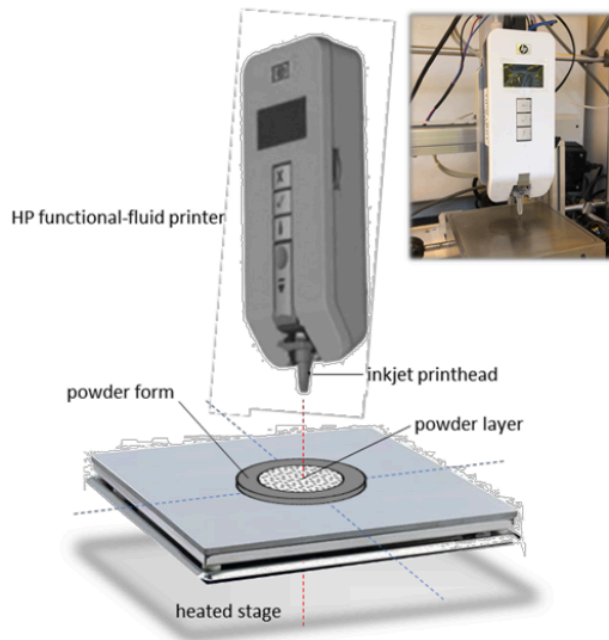


**Figure 6.2.** Schematic illustration of the printing system used to fabricate the dielectric polymer nanocomposite samples. The system includes an experimental printer developed by HP. A photograph of the system is shown in the inset.

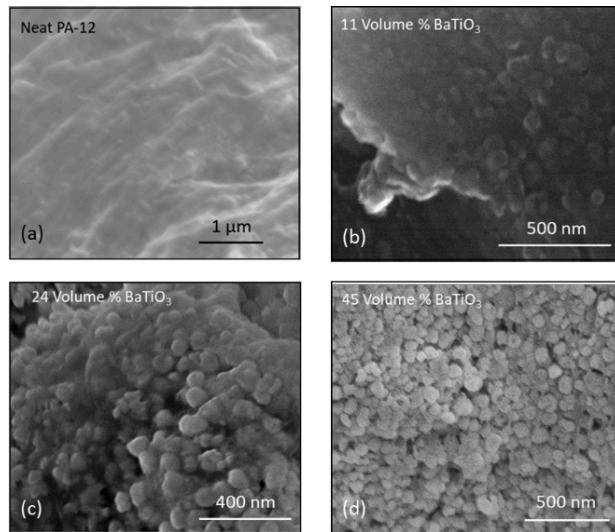


**Figure 6.3.** Micrographs of cross-sections through the dielectric samples at four different BaTiO<sub>3</sub> volume fractions in the PA12 matrix. (a) no fillers, (b) 11%, (c) 24%, and (d) 45%.

### *Inkjet printing of polymerizable nanocomposite ink*

In the second approach, samples were prepared by piezoelectric inkjet printing of dielectric ( $\text{BaTiO}_3$ ) or magnetic (barium hexaferrite) nanoparticles suspended in a UV-cured diethylene glycol diacrylate (DEGDA) matrix.<sup>10</sup> Commercially available nanoparticles were used in the case of  $\text{BaTiO}_3$  (99.95% purity, 50 nm and 100 nm diameters, Inframet Advanced Materials). Barium hexaferrite nanoparticles were synthesized following Temuujin et al.<sup>11</sup> with modifications to target the Co<sub>2</sub>Z phase ( $\text{Ba}_3\text{Co}_2\text{Fe}_{24}\text{O}_{41}$ ), which has the desirable property of high permeability at high frequencies. Briefly, powders of  $\text{BaCO}_3$  (1  $\mu\text{m}$  powder, Alfa Aesar, Cat # 14341),  $\text{Co}_3\text{O}_4$  (50 nm–80 nm powder, Alfa Aesar, Cat # 44661), and  $\alpha\text{-Fe}_2\text{O}_3$  (30 nm–50 nm powder, Alfa Aesar, Cat # 47044) in the molar ratio 3:2/3:12, respectively, were ball milled at 300 rpm for 20 h in ethanol. The resulting powder was annealed for 4 h at 1230 °C in air and subsequently ball milled for 7 h at 500 rpm. The final material is partially Co<sub>2</sub>Z phase as confirmed by x-ray diffraction. The data are shown in Figure 6.4, in comparison to published results by Tachibana et al.<sup>12</sup>

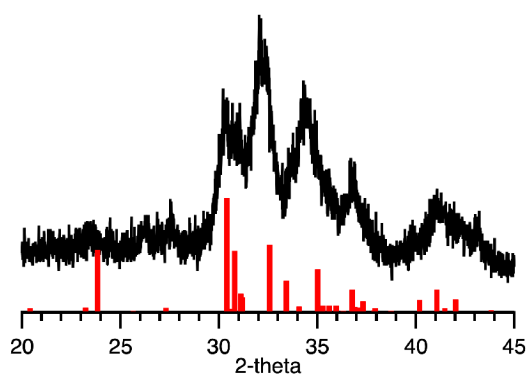


**Figure 6.4.** X-ray diffraction pattern of the synthesized barium hexaferrite nanoparticles (black) with z-phase peak intensities for reference (red).

The inks were prepared by first functionalizing the nanoparticles with acrylic acid. Acrylic acid can effectively integrate the nanoparticles into the matrix material since it can polymerize with the DEGDA and also has a carboxylic acid group capable of binding to the nanoparticle surface. To functionalize, the nanoparticles (1 g) were milled with zirconia balls (~70 g) in a planetary ball-mill (Retsch PM100) for 1 h at 500 rpm with acrylic acid (0.5 mL) and ethanol (15 mL). Thereafter, the mixture was purified by repeated rinsing in ethanol, centrifugation and decanting. Finally, a known volume of ethanol (about 5 mL for every 1 g of nanoparticles) was added to the solid immediately after decanting and sonicated for 1 h. The amount of DEGDA required to achieve the desired nanoparticle concentration was added to the dispersion, and the ethanol was evaporated using a rotary evaporator. The final dispersion of nanoparticles in DEGDA was sonicated daily until casting samples or 3D printing. Immediately prior to use, an initiator (Irgacure 184) was added at 3 wt% (relative to monomer) to the dispersion, which was then sonicated for about 30 minutes.

3D printing was carried out with a Dimatix Materials Printer DMP-2850. Nanoparticle-DEGDA dispersions were loaded into the Dimatix Materials Cartridge consisting of 16 square piezoelectric nozzles spaced 254  $\mu\text{m}$  apart. The nozzles have an effective diameter of 21  $\mu\text{m}$  with drop volumes of about 10 pL. A small spot size UV LED light (365 nm wavelength) attached to the printer head was used for curing by passing over the printed area in a raster pattern. Inks were printed at room temperature in a nitrogen environment onto a piranha-cleaned glass substrate in the pattern of a 3 cm square via a sequence of depositing the ink and curing with UV light. Specifically, two layers of ink were deposited followed by two passes with UV light. This cycle was

repeated in order to build up a thicker sample. Each cycle increased the thickness of the sample by approximately 20  $\mu\text{m}$ .

Inks with high concentration of nanoparticles tend to quickly clog the inkjet print head. Therefore, the key to achieving a high volumetric fraction of nanoparticles in the final object, while still allowing inkjet printing, is to dilute the ink with a solvent (dimethylformamide) that evaporates prior to initiating the polymerization of the DEGDA. Using this approach, a volume fraction as high as 50 % in the printed and cured samples was achieved.

Since the printing process with the experimental inkjet printer is quite slow, additional samples were prepared by casting. Two glass slide coverslips were separated using small strips of double-sided tape.<sup>13</sup> About 150  $\mu\text{L}$  to 250  $\mu\text{L}$  of nanoparticle-DEGDA dispersion was placed on a coverslip between two narrow strips of double-sided tape and the second slide was placed on top (Figure 6.5A). The thickness of the sample could be increased by having multiple layers of tape. This assembly was placed under UV light for about 5 minutes, flipped over, and exposed for another 5 minutes to cure. The cured samples could be removed from the glass slides using a razor blade. Photographs of both cast and printed samples are shown in Figure 6.5. SEM images of the surface of inkjet printed samples are shown in Figure 6.6.

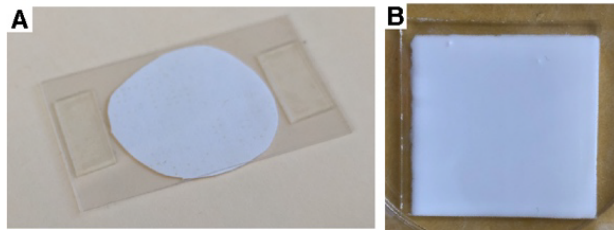


**Figure 6.5.** Example images of cast and printed composite samples. Composite sample is shown in the slide assembly used to cast samples (A). Composite sample is shown on glass substrate after 3D printing (B).

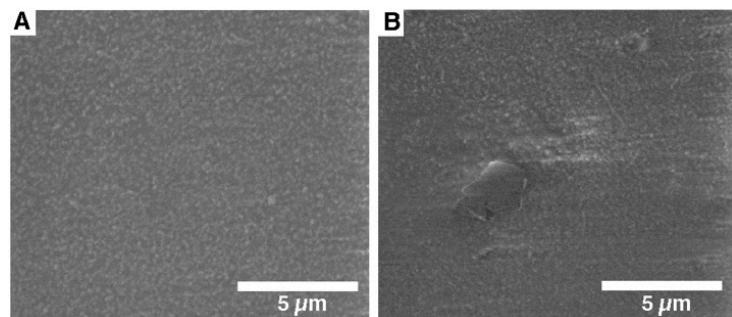


**Figure 6.6.** SEM images of surfaces of 3D printed composites prepared from 50 nm BaTiO<sub>3</sub> nanoparticles at weight fractions of 10 % (A) and 20 % (B).

## Results

The polymer nanocomposite samples were characterized using impedance spectroscopy techniques<sup>14</sup> to determine the complex permittivity  $\varepsilon = \varepsilon' - i\varepsilon''$  as functions of the BaTiO<sub>3</sub> nanoparticle volume fraction. The permittivity is determined from capacitance measurements at frequencies between 100 Hz and 1 GHz. All measurements were made at room temperature.

For the fused powder bed polymer nanocomposites, the dielectric constant  $\varepsilon'$  and the dissipation factor  $\varepsilon''$  as a function of frequency for different volume fraction of BaTiO<sub>3</sub> are plotted in Figure 6.7. A general feature is the systematic decrease of both the

dielectric constants and dissipation factors with increasing frequencies with the slopes becoming steeper with increasing volume fractions. This frequency dependence of both the real  $\epsilon'$  and imaginary  $\epsilon''$  relative permittivity is consistent with the predictions of the Maxwell-Wagner-Sillars (MWS) theory<sup>15,16</sup> describing the dielectric properties of two-phase inhomogeneous media including contributions from the dielectric relaxation of the composite medium, the shapes, sizes, and orientations of the filler particles, and polarization effects at microscopic and macroscopic interfaces.

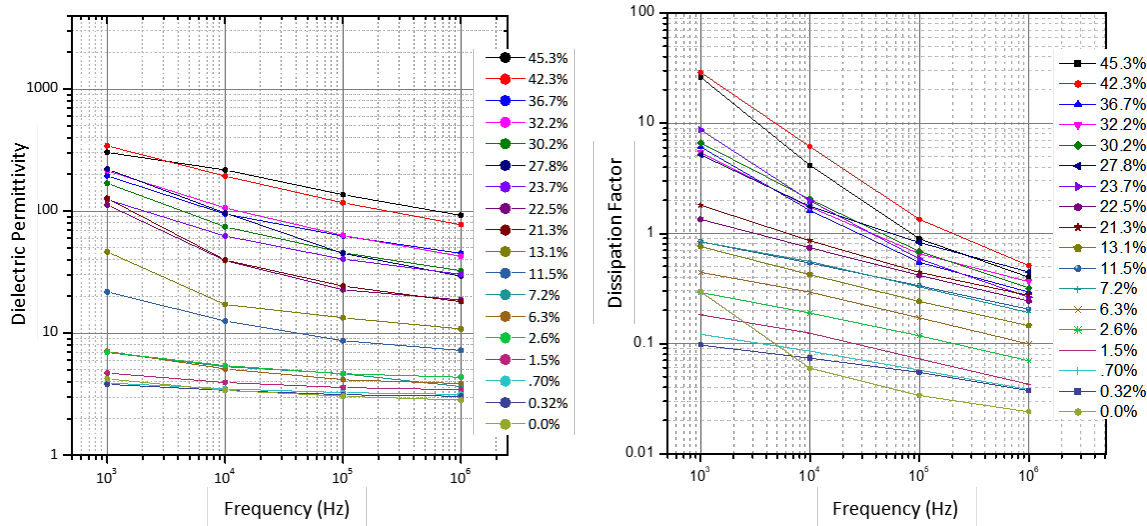


**Figure 6.7.** Frequency dependent dielectric properties of samples manufactured by polymer bed infusion, parametric in the BaTiO<sub>3</sub> volume fraction. (a) the dielectric constant  $\epsilon'$  and (b) the dissipation factor  $\epsilon''$ .

The measured dependence of the dielectric constant on the nanoparticle volume fraction is shown in Figure 6.8. The data are fit using a power-law effective medium “mixing equation” that has been used to model the properties of a wide range of nanocomposite materials<sup>17</sup>:

$$\epsilon_{eff}^{1/\beta} = f \epsilon_i^{1/\beta} + (1-f) \epsilon_e^{1/\beta} \quad (1)$$

in which  $f$  is the volume fraction,  $\varepsilon_{eff}$ ,  $\varepsilon_i$ , and  $\varepsilon_e$  are the effective dielectric constant of the composite, the dielectric constant of the filler, and the dielectric constant medium respectively, and the exponent  $\beta$  can be any integer between 1 and 3. Assuming the dielectric constants for the polymer matrix and the BaTiO<sub>3</sub> nanoparticles to be 3.6 and 500 respectively, there is a good fit of the data ( $R^2 = 0.98$ ) when  $\beta = 3.02$ . With  $\beta = 3$ , the power-law equation corresponds to the well-known Landau-Lifschitz-Looyenga mixing rule.<sup>18</sup>

The goodness of the fit of the data in Figure 6.8 with an established mixing equation suggests that the physical picture of a polymer matrix homogeneously filled with nanoparticles is reasonable and that the procedure used to fabricate polymer nanocomposites with tailored physical properties is promising. Similar mixing rules apply to magnetic composites<sup>19,20</sup> and consequently, it is assumed that this fabrication process can be used to produce magnetodielectric materials with digitally tailored properties.

For the polymer nanocomposite samples prepared by the second technique of printing and UV-curing the ink, representative frequency dependent permittivity is plotted as a function of frequency up to 1 GHz and BaTiO<sub>3</sub> fraction in Figure 6.9. The permittivity, similar to the observation with powder bed samples, decreases with increasing frequency. The relationship between permittivity at 100 MHz and BaTiO<sub>3</sub> fraction for both printed and cast samples is shown in Figure 6.10. At this frequency, a contrast ratio of about 2 (7:3.5) is achieved.

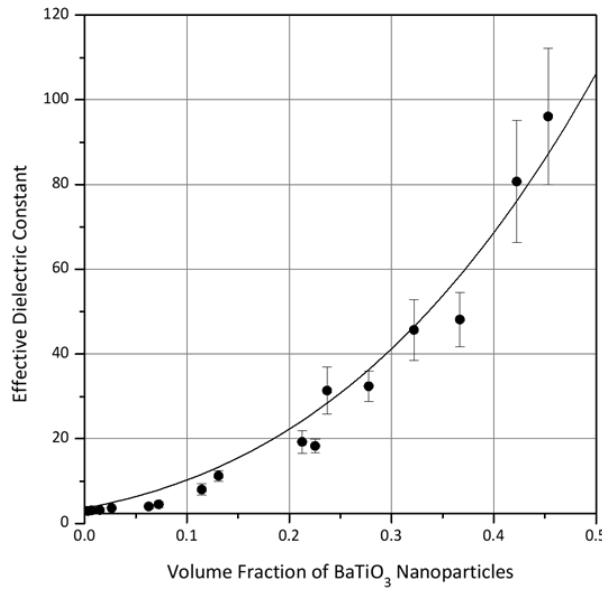


**Figure 6.8.** The effective dielectric constant of a BaTiO<sub>3</sub> polymer nanocomposite sample at 1 kHz versus nanoparticle volume fraction. The data points represent the average of at least 5 measurements and the error bars are  $\pm 1\sigma$ . The solid line is a curve fit using the Looyenga power-law mixing equation.

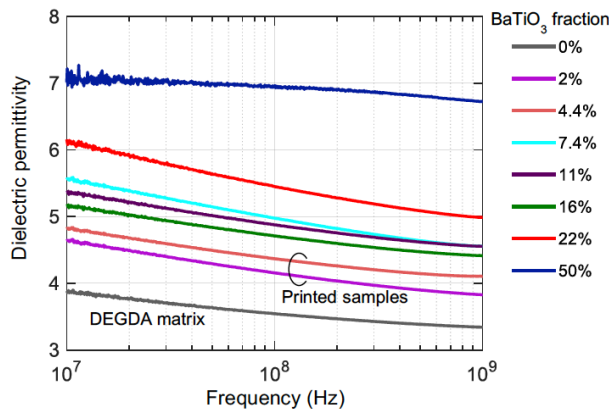


**Figure 6.9.** Dielectric permittivity versus frequency of samples with different BaTiO<sub>3</sub> nanoparticles loading (in volume fraction) in DEGDA. The 2 % and 4.4 % samples were inkjet printed and the remaining were prepared by casting.

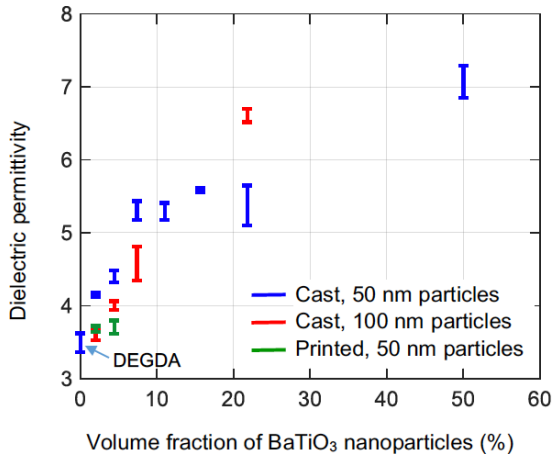


**Figure 6.10.** Dielectric permittivity at 100 MHz versus BaTiO<sub>3</sub> nanoparticle loading (in volume fraction) in DEGDA matrix for composite samples prepared by casting and inkjet printing.

The casting method was also used to prepare a sample containing 50 % volume fraction of barium hexaferrite nanoparticles in DEGDA. The magnetic permeability of this sample as a function of frequency is shown in Figure 6.11. The DEGDA matrix is nonmagnetic (permeability = 1). Thus, the achievable contrast ratio for the magnetic permeability is 1.5 at 100 Hz. This contrast ratio decreases with increasing frequency.

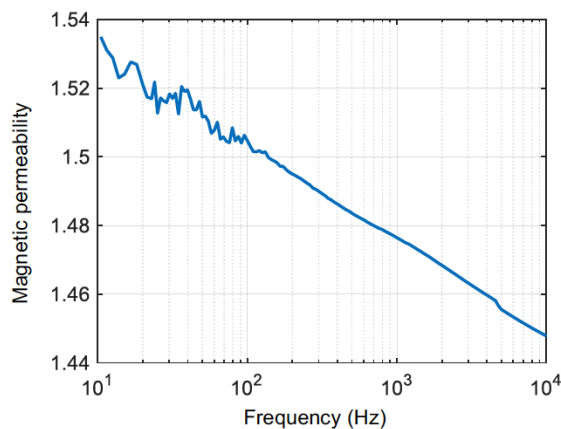


**Figure 6.11.** Magnetic permeability versus frequency for a cast sample containing barium hexaferrite nanoparticles in DEGDA with 50 % volume fraction.

## **Conclusion**

The results from this study demonstrate the possibility of designing and fabricating functional magneto-dielectric composites and 3D devices using digital inkjet printing methods. Two approaches—using particle bed infiltration and fusing and printing polymerizable nanocomposite inks—were explored. The measured dielectric permittivity of the samples was found to be in qualitative agreement between the two techniques. The permittivity increased with higher nanoparticle volume fraction and decreased with increasing frequency. The good agreement of measured values for the fused samples with the established theory for two-phase composites suggests that it will be feasible to design devices with predetermined electromagnetic properties and hence, performance. Spatial control of permittivity and permeability, enabled by these techniques, will permit TO-designed, application-specific gradient index devices to be rapidly prototyped and fabricated for radar and communication technologies. However, despite the promise, significant challenges must be addressed. In particular, achieving high contrast ratio in permittivity and permeability at radio frequencies will be critical.

## CHAPTER VII

### CONCLUSION

#### **Concluding Remarks**

In this body of work, the growth and properties of metal oxide nanoparticles were explored. Considering nanoparticle synthesis as an inorganic polymerization process can be an enlightening way to classify synthesis methods and consider future strategies towards the control of nanoparticle core structure. Indium oxide and iron oxide nanoparticle growth was examined in depth leveraging the unique attributes of the slow addition method developed in the Hutchison lab. In the case of indium oxide growth, it was found that high monomer flux can affect the degree of branching. Higher temperatures deadened the effect of monomer flux, which we believe is due to the increased surface mobility of monomer species. Twin defect formation in iron oxide nanoparticles was sensitive to the ligation and oxidation state of the iron precursor used, which we believe is related to the redox behavior of the iron precursor. Taking advantage of the well-behaved growth of iron oxide nanoparticles with an Fe (II) rich precursor, we carried out a study of size-dependent magnetism in small, spinel iron oxide. It was found that a very thin (~0.2 nm) nonmagnetic surface lead to diminished magnetism as nanoparticle size decreased. However, compared to other similar sized nanoparticles, the slow addition method yielded nanoparticles with high saturation magnetizations. Finally, surface functionalization of BaTiO<sub>3</sub> and hexaferrite nanoparticles was carried-out to create UV-polymerizable nanocomposite inks for the purpose of tuning permeability and permittivity.

## Implications

The main implication from this research is that growth processes dictate nanoparticle core structures. This is important, of course, because the core structure will dictate properties. Chapter III on indium oxide growth demonstrated the sensitivities of nanoparticle growth to synthesis temperature and monomer flux. The studies on iron oxide nanoparticles demonstrated the sensitivity of nanoparticle core structure on the precursor used. The ligation and oxidation state of the iron oleate precursor had profound effects on nanoparticle morphology and crystallinity even though all other growth conditions were identical. Every aspect of the nanoparticle synthesis has an influence on these growth processes.

The sensitivity we observed might make one question proclamations of size-dependent nanoscale structure in nanoparticles. Confining a crystal to small size can lead to difference from the bulk crystal structure,<sup>1</sup> clusters have preferred size-dependent structures based upon what is most stable,<sup>2</sup> and computation studies can tell us the most likely atomic arrangement of a material based on its nanoscale size and energy minimization.<sup>3,4</sup> However, nanoparticle syntheses do not often yield the energy-minimized structure. Though not common, we are not the only ones to recognize that nuances of growth such as monomer flux can affect the nanoparticle structure. A study by Weller et al. (discussed in more detail in Chapter III) found that fast growth in semiconductors lead to atomic disorder near the nanocrystal surfaces.<sup>5</sup> More utility towards property control and prediction may come from studying synthesis dependent structure of nanoparticles.

## **Future directions**

Future work utilizing the slow addition synthesis could go in any number of directions. More complex nanostructures could be synthesized at low temperatures ( $< 230^{\circ}\text{C}$ ) to create branched particles and/or introducing a second metal oxide. Nanoparticles could be directly synthesized with desired ligand functionalities. For example, preparing the precursor with a PEG molecule with a terminal carboxylic acid to create in the end water soluble metal oxides. Reaction parameters could be tuned to try and achieve hematite and hexaferrites (as discussed in Chapter IV). To branch out, the slow addition approach could be applied to other nanoparticle synthesis chemistries such as coprecipitation. However, more impactful work would leverage the ability to use the slow addition method as a tool.

Recently, classical nucleation theory has come under scrutiny questioning the concept of a sudden, rapid nucleation event.<sup>6</sup> The reaction chemistry utilized in this dissertation for metal oxide nanoparticle formations is not in line with the assumptions of classical nucleation theory. The classical nucleation theory put forth by LaMer and coworkers was on the formation of sulfur sols. It describes a precipitation event as a result of saturating the solution with soluble sulfur species. In metal oxide syntheses discussed in this dissertation, particle formation does not come from precipitation but from radical reactions or condensation reactions. Monomer species are highly reactive so it's difficult to imagine achieving high concentrations of before particle formation occurs. It is more likely that particle formation begins to occur at the same time or shortly after monomer formation. This concept is supported by recent research where an iron oxide nanoparticle synthesis was monitored with MALDI-TOF MS (matrix assisted laser

desorption ionization-time of flight mass spectrometry). The authors observed a continuous increase in mass from the metal precursor—no evidence of a burst nucleation to yield some critical size.<sup>7</sup> To build a more accurate understanding of nanoparticle formation, we need to be able to study it.

With the growth curves we can generate, the slow addition approach enables us to estimate the number of nanoparticles growing during synthesis. Trends between the number of nanoparticles formed and various synthetic variables can be assessed. Further insights may be gained into the molecular mechanisms influencing the number of nanoparticles forming because the reaction chemistry is well-defined. NMR, FTIR, and potentially MALDI-TOF MS can be used to monitor the amounts of precursor, ester at any particular time during synthesis. The slow addition of precursor at early stages of reaction may be challenging to measure concentrations of various players. Employing an initial heat-up or hot-injection kind of approach could lend better insights. The slow addition of precursor could be tacked on to the end just as a means to determine the nanoparticle concentration.

APPENDIX A  
 SUPPORTING INFORMATION FOR CHAPTER III:  
 INFLUENCE OF MONOMER FLUX AND TEMPERATURE ON MORPHOLOGY OF  
 INDIUM OXIDE NANOCRYSTALS DURING A CONTINUOUS GROWTH  
 SYNTHESIS

**Effective diameter ( $D_{\text{eff}}$ ) histograms from TEM analysis of samples featured in Figures 3.2, 3.3, 3.5, 3.7, and 3.9 of the manuscript.**

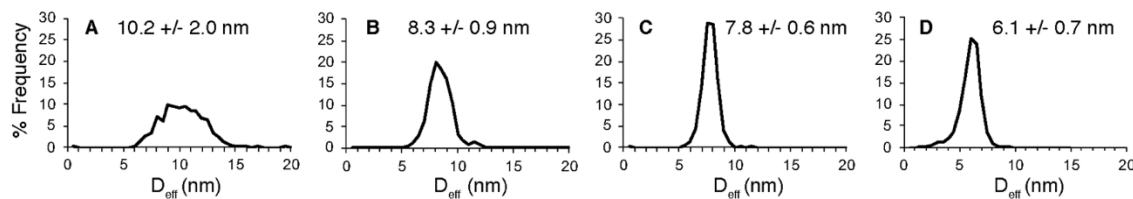


**Figure A.1.** Histograms of  $D_{\text{eff}}$  for samples featured in Figure 3.2 and 3.3. Nanocrystals were synthesized at 260 °C with 1 mmol of indium and precursor addition rates of 1.2 mL/min (A, featured in Figure 3.2A and the teal trace in Figure 3.3), 0.6 mL/min (B, featured in Figure 3.2B and the blue trace in Figure 3.3), 0.3 mL/min (C, featured in Figure 3.2C and the red trace in Figure 3.3), and 0.1 mL/min (D, featured in Figure 3.2D and the black trace in Figure 3.3).

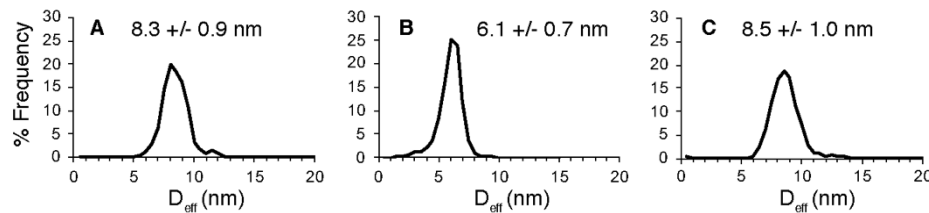


**Figure A.2.** Histograms of  $D_{\text{eff}}$  for samples featured in Figure 3.5. Samples were synthesized at 260 °C by addition of 1 mmol precursor at rates of 0.6 mL/min (A, featured in Figure 3.5B), 0.1 mL/min (B, featured in Figure 3.5C), and 0.6 mL/min with intermittent aging (C, featured in Figure 3.5D).

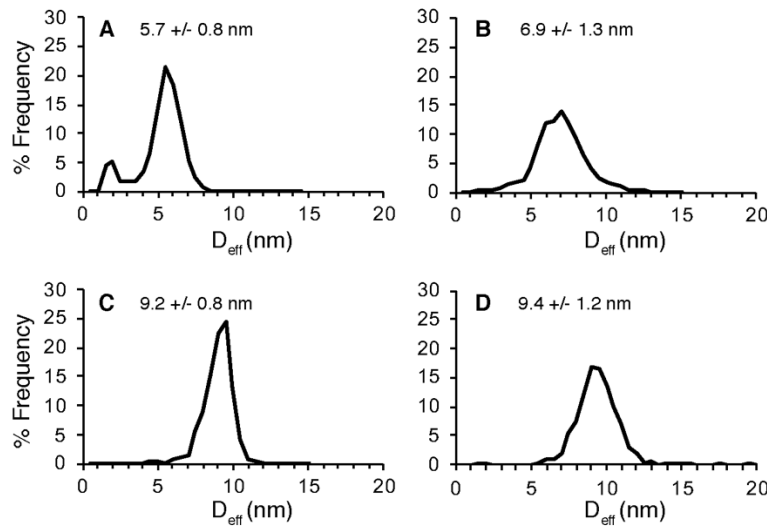


**Figure A.3.** Histograms of  $D_{\text{eff}}$  of samples featured in the TEM images in Figure 3.7. For A and B, the nanocrystals were synthesized at 230 °C with 1 mmol of indium added at 0.05 mL/min (A, featured in Figure 3.7A) and 0.2 mL/min (B, featured in Figure 3.7B). For C and D, the nanocrystals were synthesized at 290 °C with 1 mmol of indium added at 0.3 mL/min (C, featured in Figure 3.7G) and 4.0 mL/min (D, featured in Figure 3.7H).  $D_{\text{eff}}$  histograms for samples featured in Figure 3.7D and 3.7E are already shown in Figure A.1D and A.1A, respectively.

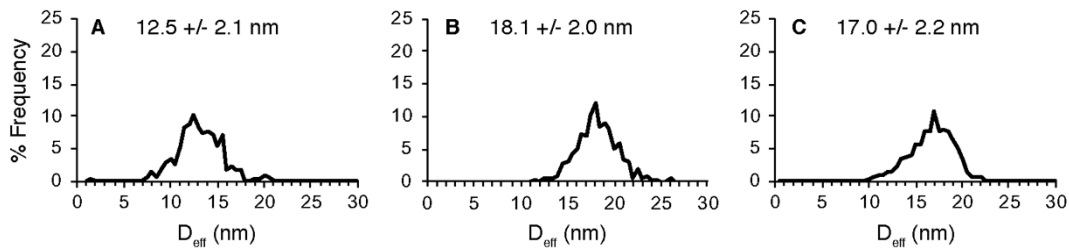


**Figure A.4.** Histograms of  $D_{\text{eff}}$  of the samples featured in Figure 3.9. The nanocrystals were synthesized at 290 °C by adding 1 mmol of precursor at a rate of 4 mL/min (A, featured in Figure 3.9A) followed by 2 additional mmol of precursor at a rate of 0.17 mL/min (B, featured in Figure 3.9B). For comparison, a control sample was synthesized by adding 3 mmol of precursor at 4 mL/min (C, featured in Figure 3.9C).

## Determination of P/D ratios for $\text{In}_2\text{O}_3$ nanocrystals.

Example calculations are provided in Figure A.5. Image processing to determine P/D ratios from TEM images is summarized in Figure A.6.

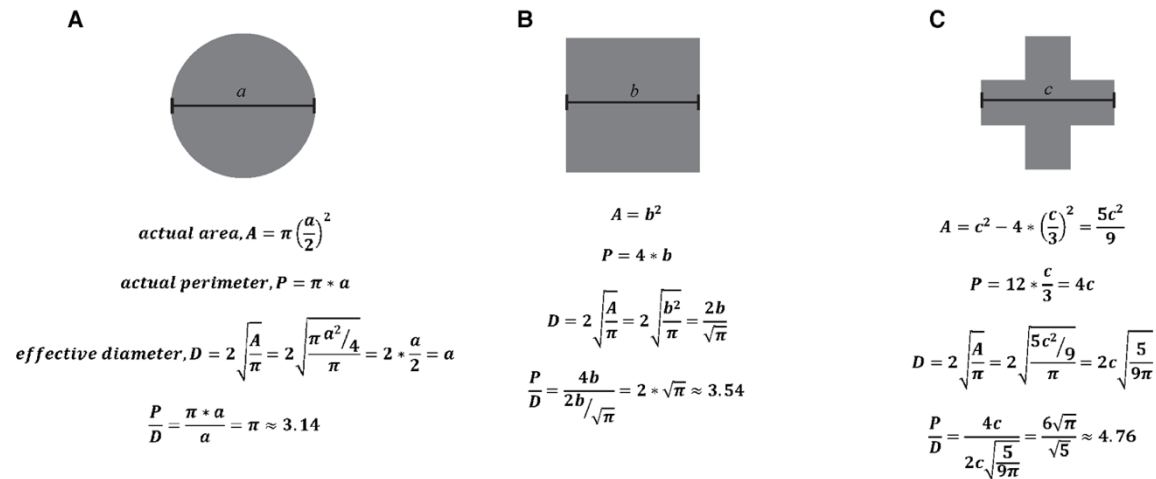


**Figure A.5.** Determination of the P/D ratio for a circle (A), square (B), and an equilateral cross (C). First, the actual area,  $A$ , of the shape is determined. The effective diameter,  $D$ , is determined with the area of a circle equation solved for the diameter regardless of the shape. Then the ratio of the perimeter to the diameter yields a number specific to the shape: approximately 3.14 for a circle, 3.54 for a square, and 4.76 for the cross.

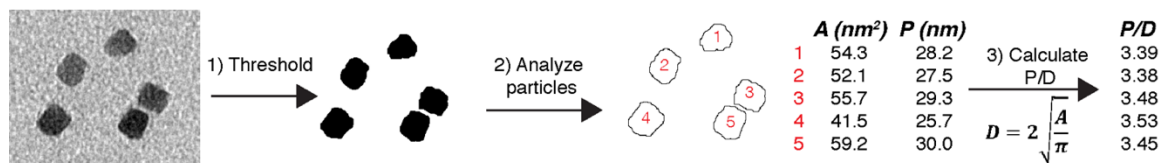


**Figure A.6.** The process to determine P/D ratio from TEM images. The background is removed from the image and the nanocrystals are analyzed to determine their area and perimeter. The effective diameter is determined from the area and the P/D ratio is calculated. In this example, the nanocrystals all appear to be rounded squares/rectangles which is reflected in their P/D ratios which are between a circle and a square.

**X-ray diffraction patterns of faceted and branched nanocrystals.**

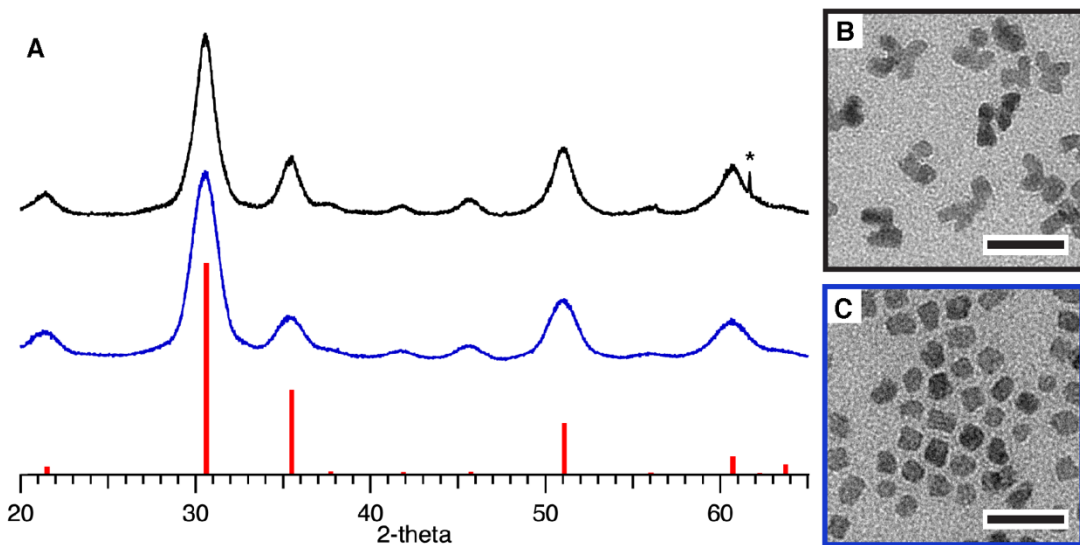


**Figure A.7.** Stacked XRD patterns of branched and faceted nanocrystals both exhibit cubic bixbyite structure. Branched In<sub>2</sub>O<sub>3</sub> nanocrystals synthesized *via* fast precursor addition (1.2 mL/min) at 260 °C are shown in the black trace (\* indicates a substrate peak) while faceted nanocrystals synthesized *via* slow addition (0.1 mL/min) at 260 °C are shown in the blue trace (A). For comparison, literature values for cubic bixbyite are shown as red lines (Marezio, M. Refinement of the Crystal Structure of In<sub>2</sub>O<sub>3</sub> at Two Wavelengths. *Acta Crystallographica* **1966**, *20*, 723–728). TEM images corresponding to the branched (B) and faceted (C) samples characterized are shown at the right. Scale bars are 20 nm.

**Additional high resolution TEM images to supplement Figures 3.4 and 3.7 are provided in Figure A.8.**

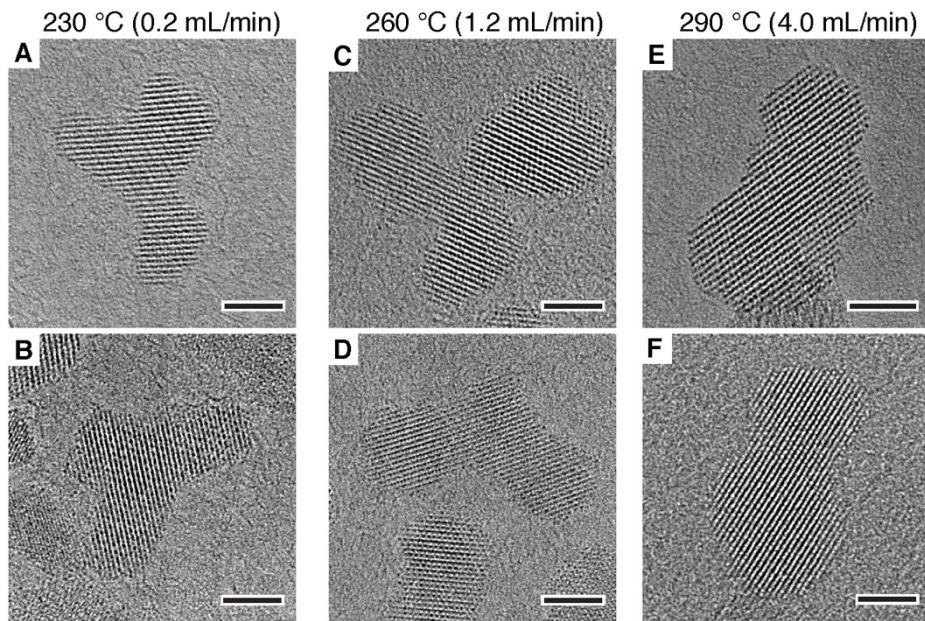


**Figure A.8.** High resolution TEM images of nanocrystals synthesized at 230 °C (A and B), 260 °C (C and D), and 290 °C (E and F) at fast injection rates (0.2, 1.2, and 4 mL/min, respectively). In all cases, lattice fringes extend through the entirety of the nanocrystal suggesting that the nanocrystal is free of defects. Scale bars are 3 nm.

#### Examination of branched nanoparticle growth over time.

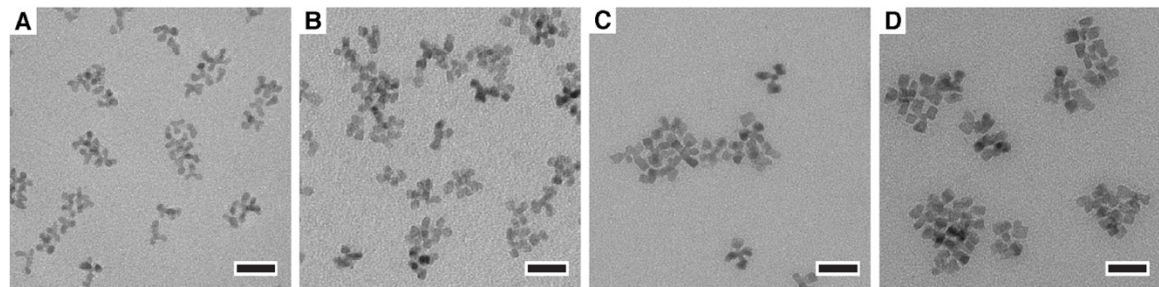


**Figure A.9.** TEM images demonstrating growth of branched nanocrystals. The nanocrystal synthesis was carried out by adding 2 mmol of indium precursor at a rate of 1.2 mL/min into 260 °C oleyl alcohol. Samples were removed after 0.5 mmol (A), 1 mmol (B), 1.5 mmol (C), and 2 mmol (D) of indium precursor had been added. Scale bars are 20 nm.

## Control experiment testing for oriented attachment of nanocrystals during prolonged periods of heating.

Small (~6 nm) and large (~10 nm)  $\text{In}_2\text{O}_3$  nanocrystals were separately synthesized by slowly adding (0.1 mL/min) indium oleate precursor into 13 mL of 260 °C oleyl alcohol. 0.5 mmol of indium was added to produce small nanocrystals while 2 mmol was added to produce large nanocrystals. About 5 mL of each of the reaction mixtures were mixed together and heated to 260 °C. This temperature was maintained for one hour and the temperature increased to 290 °C and held for an additional hour. Small aliquots were taken throughout the experiment to examine the nanocrystals' size and morphology as shown in Figure A.10.

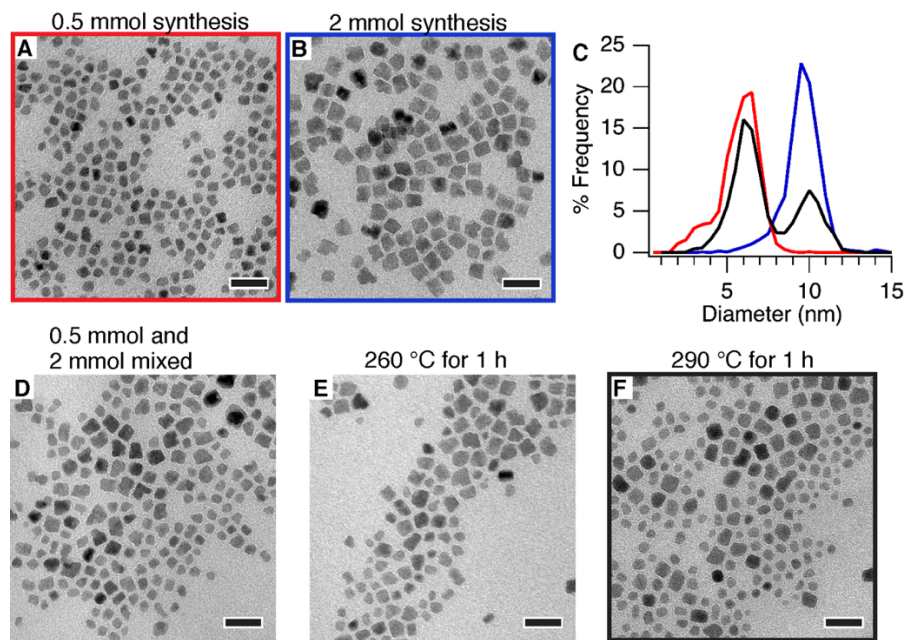


**Figure A.10.** TEM images and analysis to evaluate the possibility of oriented attachment. Small  $\text{In}_2\text{O}_3$  nanocrystals produced *via* slow addition (0.1 mL/min) of 0.5 mmol precursor (A) and larger nanocrystals produced *via* slow addition (0.1 mL/min) of 2 mmol precursor (B) into 260 °C oleyl alcohol. The  $D_{\text{eff}}$  histograms of small and large nanocrystals are shown in the red and blue traces, respectively, of the plot (C). TEM images after mixing small and large nanocrystals (D), after maintaining 260 °C for 1 hour (E), and after subsequently maintaining at 290 °C for 1 hour.

**Table SA.1.** Metrics determined from TEM analysis of starting materials for and results from oriented attachment control experiment.

Starting nanocrystals		After extended heating	
Small NCs	Large NCs	Small population	Large population
Avg. D (nm)	6.0 +/- 0.9	9.7 +/- 1.2	6.2 +/- 0.8
P/D mode, maximum	3.4, 20.4%	3.5, 17.9%	3.4, 24.2%

### Calculation of the number of nanocrystals

Utilized the growth curve shown below in Figure A.11, equations 1-3 demonstrate how we calculated the number of nanocrystals in a synthesis. Results from various temperatures are plotted in Figure A.12.

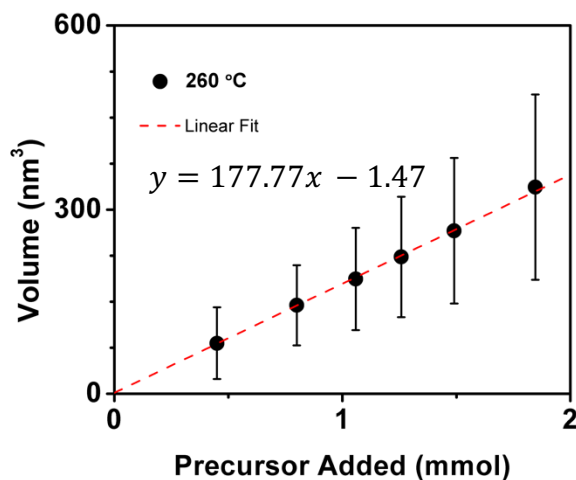


**Figure A.11.** Nanocrystal growth curve plotted as nanocrystal volume versus precursor added for 260 °C. The data shown are replotted from Figure 3.8 in the main text. Error bars reflect one standard deviation of the size dispersion. The dashed lines represent the linear fit to the data series, with equation shown.

The number of nanocrystals ( $NC_{tot}$ ) can be obtained from the linear fits using Equation 1:

Equation 1

$$y = m * x + b$$
$$\frac{nm^3}{NC} = \frac{1}{NC_{tot}} * \frac{Vol}{mmol} * mmol_{inj} + b$$

where  $nm^3/NC$  is the average volume of a single nanocrystal,  $NC_{tot}$  is the total number of nanocrystals in the reaction,  $Vol/mmol$  is the volume of indium oxide per mmol of indium metal ( $2 \times 10^{19} nm^3/mmol$ ), and  $mmol_{inj}$  is the mmol of indium metal precursor injected into the reaction. From Equation 1, the slope of the growth curve is related to  $NC_{tot}$  by Equation 2:

Equation 2:

$$m = \frac{1}{NC_{tot}} * \frac{Vol_{tot}}{mmol}$$

Thus,  $NC_{tot}$  is calculated by Equation 3:

Equation 3:

$$NC_{tot} = \frac{2 * 10^{19}}{m}$$

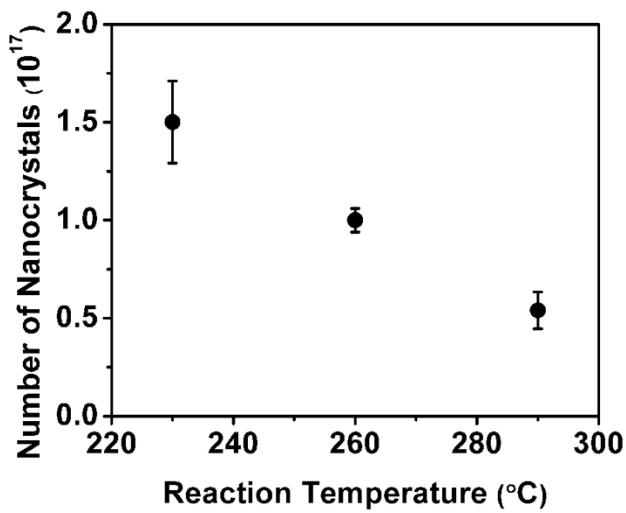


**Figure A.12.** Number of nanocrystals calculated from three growth experiments at each temperature.

APPENDIX B  
 SUPPLEMENTARY INFORMATION FOR CHAPTER IV:  
 ACETYLACETONATE IN AN IRON (III) RICH PRECURSOR INDUCES  
 TWINNING DEFECTS IN IRON OXIDE NANOPARTICLES

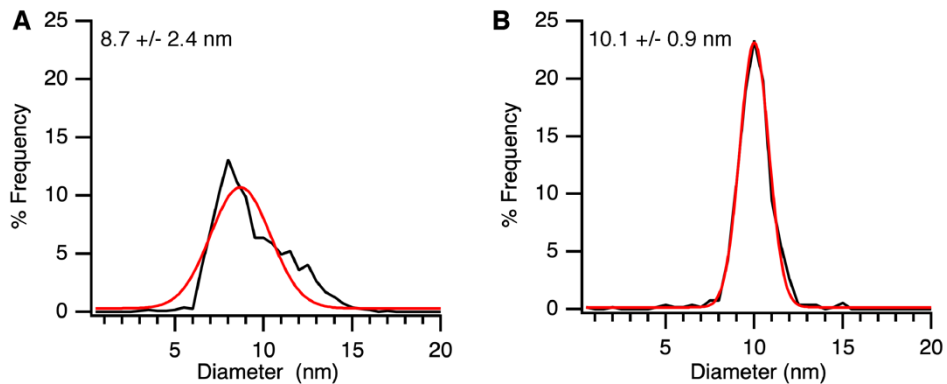


**Figure B.1.** Size analysis results of nanoparticles produced with the standard Fe (III) rich precursor (A), and the Fe (II) rich precursor (B).

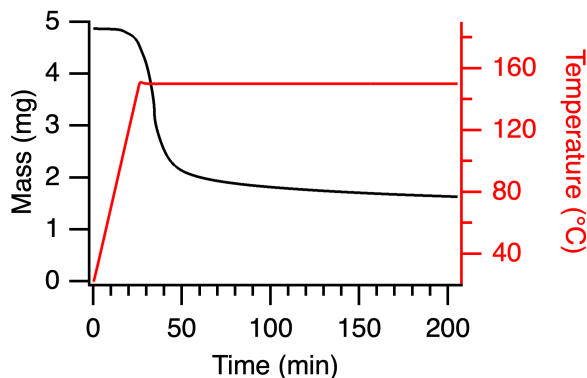


**Figure B.2.** B2 Isothermal TGA run of  $\text{Fe}(\text{acac})_3$  carried out at 150°C. Initial ramp rate was 5 °/min. Overall, there was 67% mass loss. Eighty percent of mass loss occurred within 20 minutes of reaching 150 °C, and 90% occurred within 40 minutes.

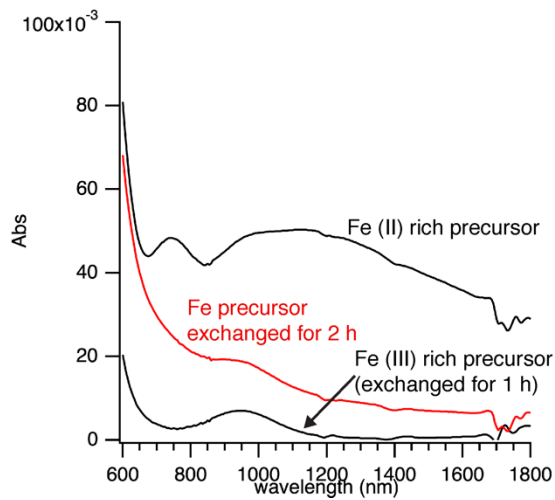


**Figure B.3.** Optical absorbance of iron precursor exchanged for 2 h (from  $\text{Fe}(\text{acac})_3$ ) (red, center) compared to Fe (II) rich precursor (prepared over 1 h from  $\text{Fe}(\text{acetate})_2$ ) and standard Fe (III) rich precursor (prepared for 1 h from  $\text{Fe}(\text{acac})_3$ ).

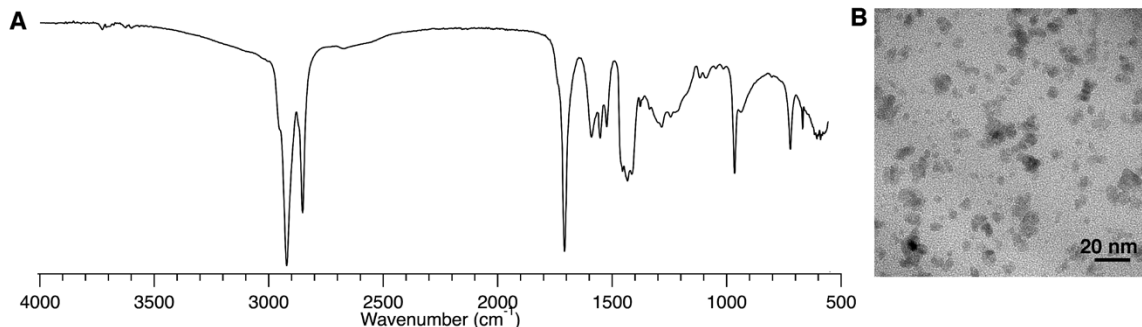


**Figure B.4.** FTIR of precursor prepared from  $\text{Fe}(\text{NO}_3)_3$  (A) and TEM of nanoparticles resulting from synthesis with the precursor (B). The precursor was prepared by stirring 3 mmol  $\text{Fe}(\text{NO}_3)_3$  with 6 mL oleic acid at 150 °C for 1 h. The FTIR spectrum shows a missing C-H stretch due to  $\text{sp}^2$  hybridized carbon-hydrogen bond indicating that the alkene in oleic acid was oxidized. Nanoparticles were synthesized by adding precursor into 12.5 mL 230 °C oleyl alcohol at a rate of 0.2 mL/min.

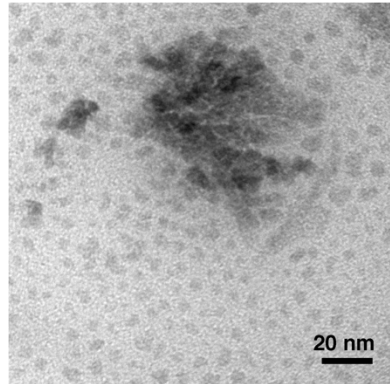


**Figure B.5.** TEM Nanoparticles produced during the preparation of precursor using  $\text{Fe(OH)}(\text{acetate})_2$  starting material. 3 mmol of  $\text{Fe(OH)}(\text{acetate})_2$  was stirred with 6 mL oleic acid in a 150 °C oil bath for a period of one hour. Solid formed, which was unusual. The solid was precipitated with acetone, centrifuged, and dispersed in toluene to form an orange solution.

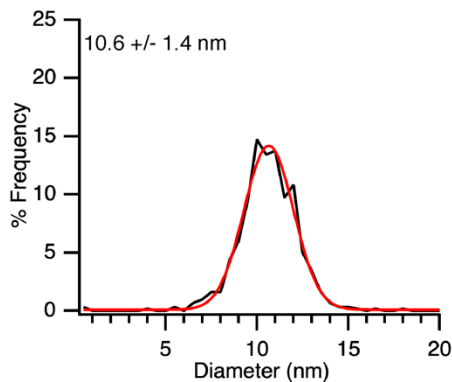


**Figure B.6.** Size analysis from TEM images of nanoparticles produced with the oxidized precursor.

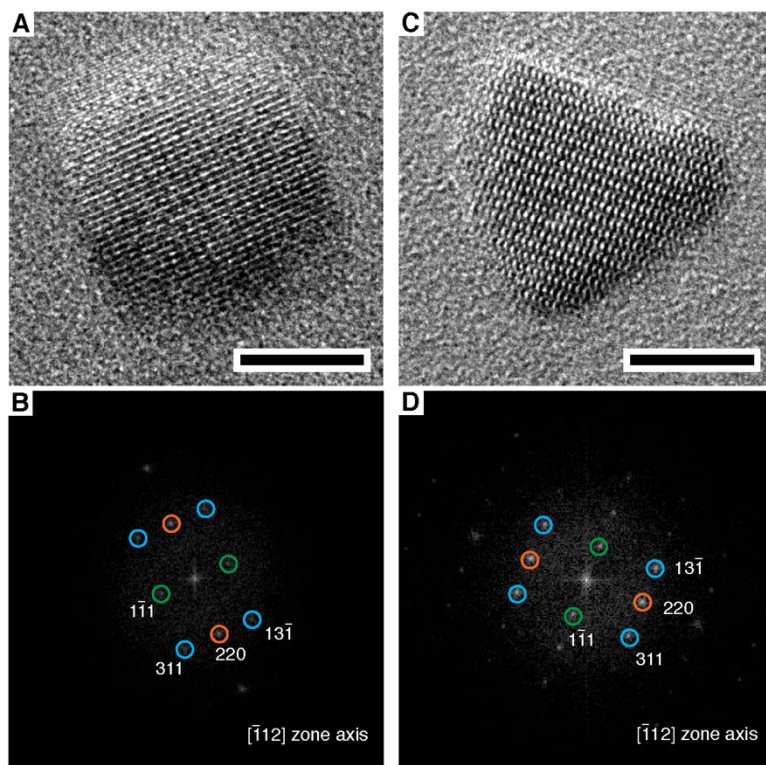


**Figure B.7.** HRTEM (A, C) of nanoparticles produced from the oxidized precursor with corresponding FFT patterns (B, D respectively). Scale bars are 5 nm.

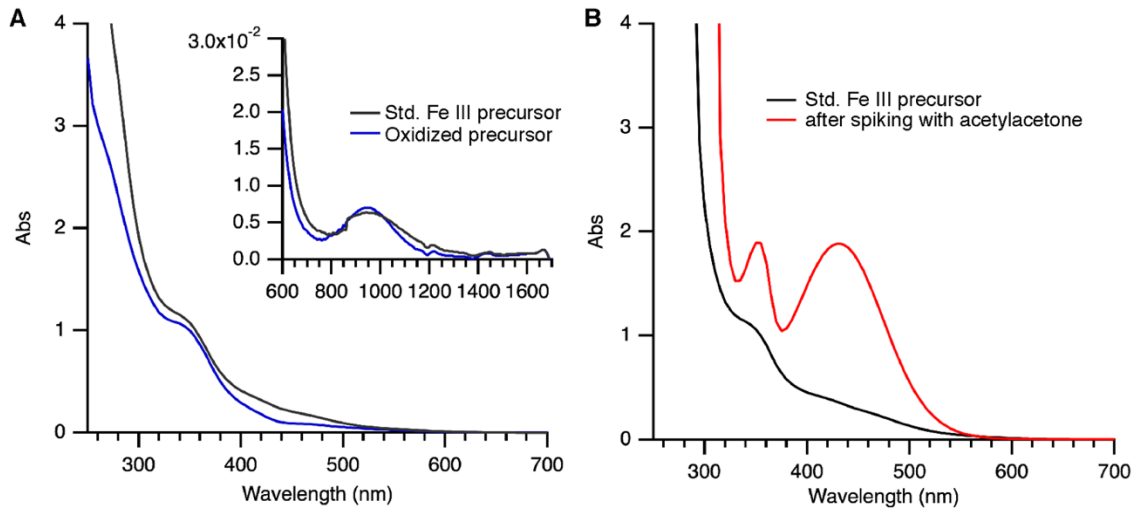


**Figure B.8.** Optical absorbance demonstrating presence of acetylacetone ligands in the standard Fe (III) precursor. The standard Fe (III) precursor and the oxidized precursor in hexanes solutions (same concentration) are plotted (A) showing differences ~430 nm and UV range. The standard Fe (III) precursor was spiked with acetylacetone resulting in increased absorbance at 430 nm and UV wavelengths (B).

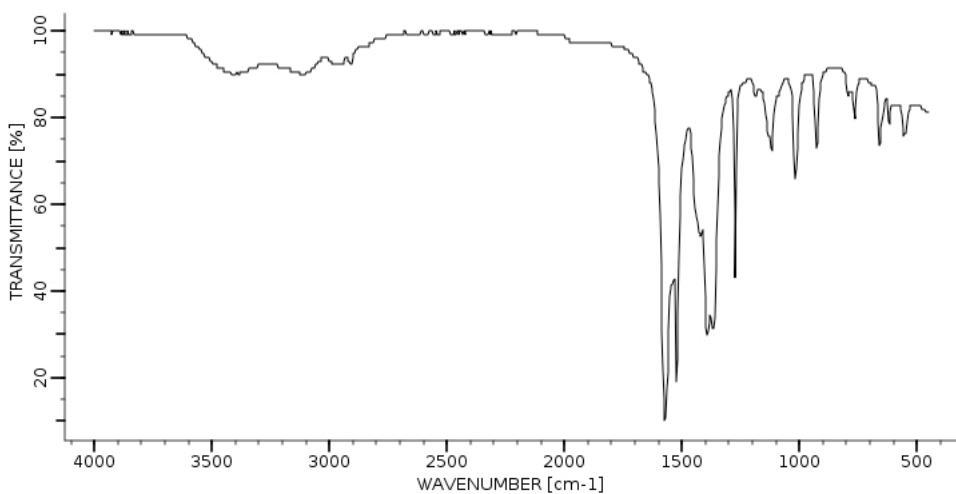


**Figure B.9.** FTIR spectrum of Fe (II) acetylacetone acquired from Bio-Rad/Sadtler IR Data Collection (Bio-Rad Laboratories, Philadelphia, PA (US). Copyright ©Bio-Rad Laboratories).

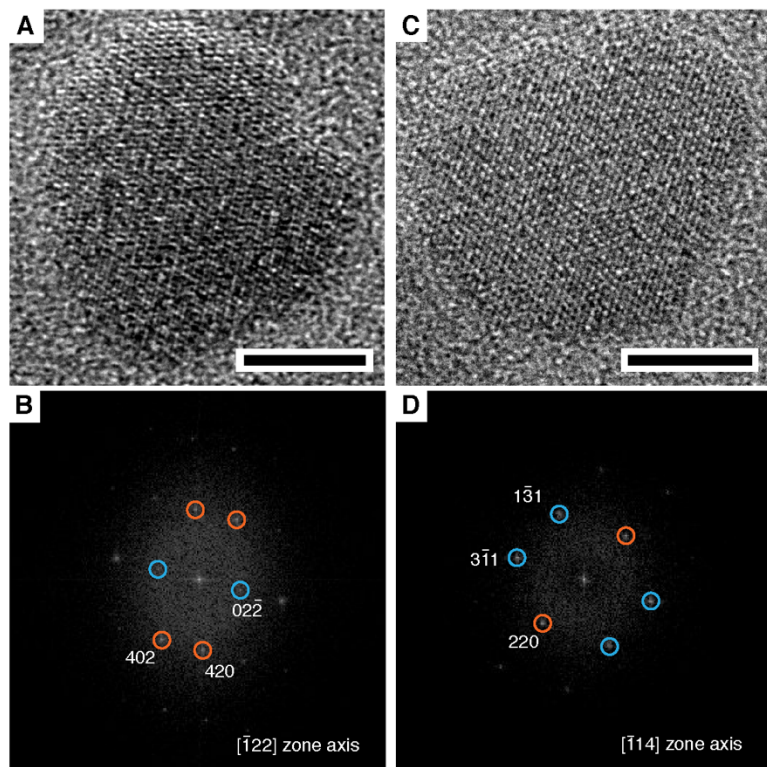


**Figure B.10.** HRTEM (A, C) and corresponding FFT patterns (B, D respectively) of nanoparticles produced from the Fe (II) rich oleate precursor with added acetylacetone. Scale bars are 5 nm.

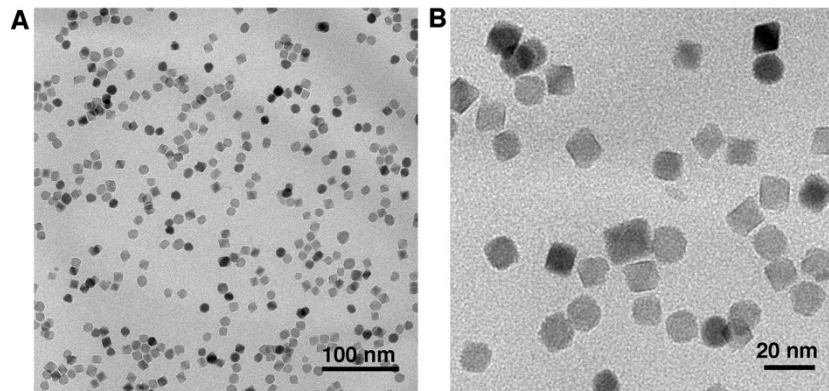


**Figure B.11.** TEM images of nanoparticles resulting from synthesis with mixed precursor containing additional acetylacetone. The mixed precursor was prepared by stirring 4 mL of the standard Fe (III) rich precursor with 2 mL of the Fe (II) rich precursor and 0.3 mL of acetylacetone. Nanoparticles were prepared by adding this precursor into 12.5 mL of 230 °C oleyl alcohol at a rate of 0.21 mL/min (that is, 0.1 mmol Fe/min).

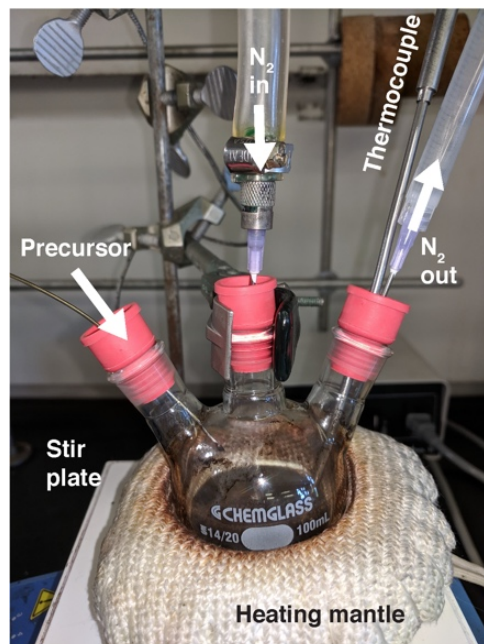


**Figure B.12.** Picture taken of reaction flask during synthesis to demonstrate set-up.

APPENDIX C  
SUPPORTING INFORMATION FOR CHAPTER V:  
INSIGHTS INTO THE MAGNETIC PROPERTIES OF SUB-10 NM IRON OXIDE  
NANOCRYSTALS THROUGH THE USE OF A CONTINUOUS GROWTH  
SYNTHESIS

**Table C.1.** NC diameter and dispersity determined by SAXS of NC samples shown in Figure 5.1A.

NC diameter and dispersity (nm)
3.8 +/- 0.7
5.3 +/- 0.6
5.9 +/- 0.7
6.7 +/- 0.7
7.2 +/- 0.6
8.0 +/- 0.7
8.5 +/- 0.8
8.8 +/- 0.9
9.1 +/- 1.0
9.4 +/- 1.0
9.6 +/- 1.1
9.8 +/- 1.2
10.0 +/- 1.2

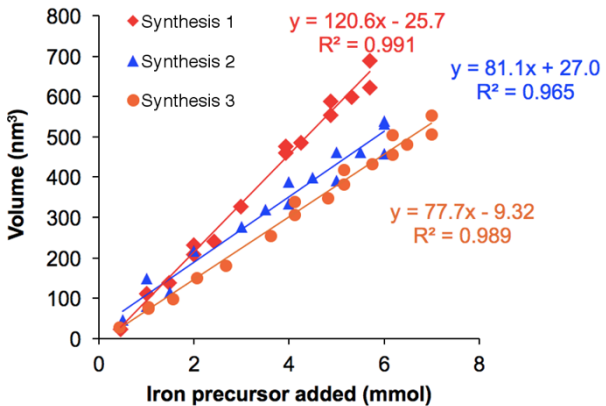


**Figure C.1.** Growth of nanocrystals as a function of amount of precursor added for three different syntheses. Nanocrystal size is displayed in volume calculated from SAXS diameter.

#### Discussion of Figure C.1:

Variation in growth rate is a result of different number of nuclei being formed during the nucleation event. If fewer nuclei form, then each growing particle attains more of the subsequent precursor and grows larger than if more nuclei were formed. The number of nuclei formed depends on the nucleation rate and the period of time over which nucleation occurs. Nucleation is highly sensitive to reaction conditions such as temperature, surface free energy, and supersaturation.<sup>1</sup> There may also be variation in the nucleation period since precursor is added dropwise and the exact volume of the drops in the initial stage of the synthesis could be slightly different from synthesis to synthesis. Nonetheless, the utility of continuous injection syntheses is that the particle size is not determined by the nucleation event alone but by the amount of precursor added to the reaction flask.

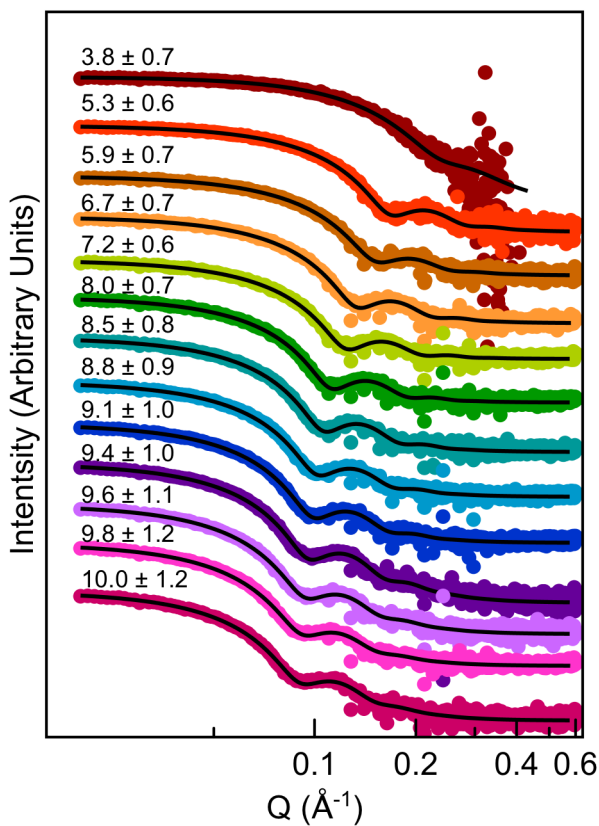


**Figure C.2.** SAXS patterns are shown for a growth curve with sizes from 4-10 nm. The SAXS patterns are stacked from largest (top) to smallest (bottom). Black lines over each SAXS pattern is the fit used to determine size and dispersity of the NCs.

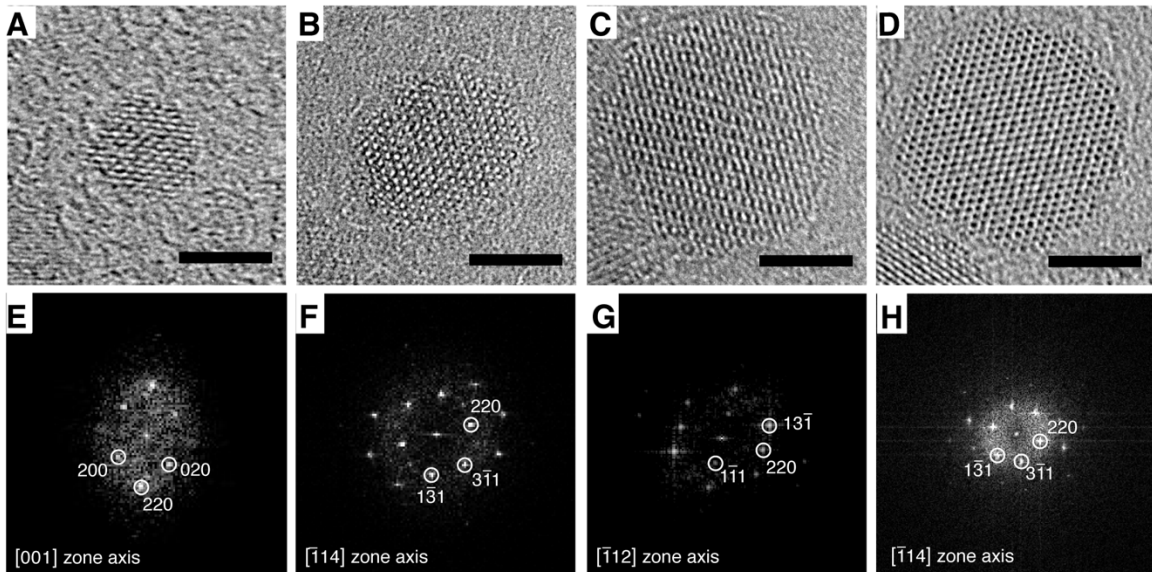


**Figure C.3.** Indexing of HRTEM single particle electron diffraction. HRTEM of four different NC sizes (A-D) with corresponding indexed FFT patterns (E-H) directly below. NCs have sizes (determined by SAXS) of  $3.9 \pm 0.6$  nm (A, E),  $5.1 \pm 0.7$  nm (B, F),  $6.6 \pm 0.6$  nm (C, G), and  $8.0 \pm 0.8$  nm (D, H).

#### Discussion of Figure C.3:

Indexed FFT patterns are included in Figure C.3 to confirm that the particles produced are single crystalline.

#### Rietveld Analysis of Powder Diffraction Data:

Rietveld refinement was performed using the Fullprof suite<sup>2</sup> on acquired Powder XRD data in order to verify the phase. A magnetite crystal structure with spacegroup  $Fd\text{-}3m$  was used to perform the refinement.<sup>3</sup> A standard of crystalline magnetite was refined to determine the instrumental broadening. The background was refined using a 12-term Chebyshev polynomial. For the magnetite phase, the scale factor was refined along with the unit cell parameter, the IG peak shape parameter and the instrumental displacement.

B values of Fe and O fixed at 1 Å<sup>-2</sup> have been used recently in detailed analysis of iron oxide nanocrystals.<sup>4</sup> Further, changing the B value from 0.5 Å<sup>-2</sup> to 2.0 Å<sup>-2</sup> for both Fe and O did not change the refined values for the unit cell parameter or the IG size parameter. The refinements and results are given in Figure C.2-C.4 and Table C.2-C.4.

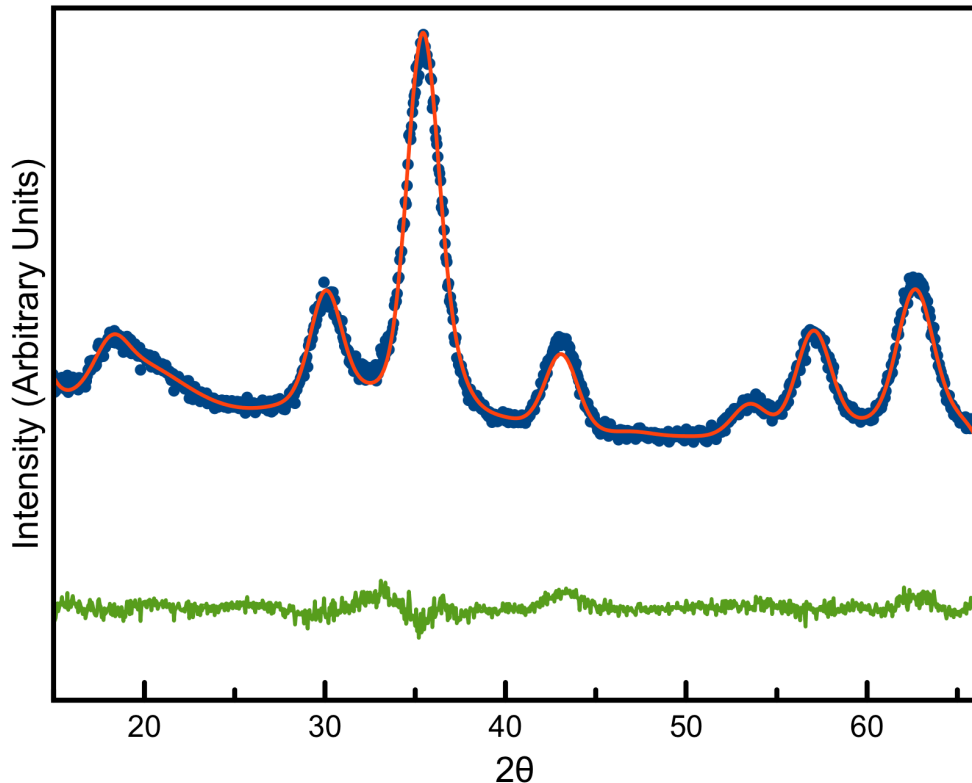


**Figure C.4.** Powder XRD pattern (blue dots) of the 5 nm (measured by SAXS) NC sample, fit using Rietveld refinement (red line) to verify the spinel iron oxide phase and crystallite size. The difference between the data and the model is shown by the green line.

**Table C.2.** Refined parameters using Rietveld refinement of the 5 nm NC sample (measured by SAXS). Spacegroup  $Fd\text{-}3m$ .

Bragg R-factor	3.8 %
R-factor	3.6 %
A	8.372 Å
Instrument Displacement	-0.15
IG	3.60
Crystallite diameter	4.4 nm

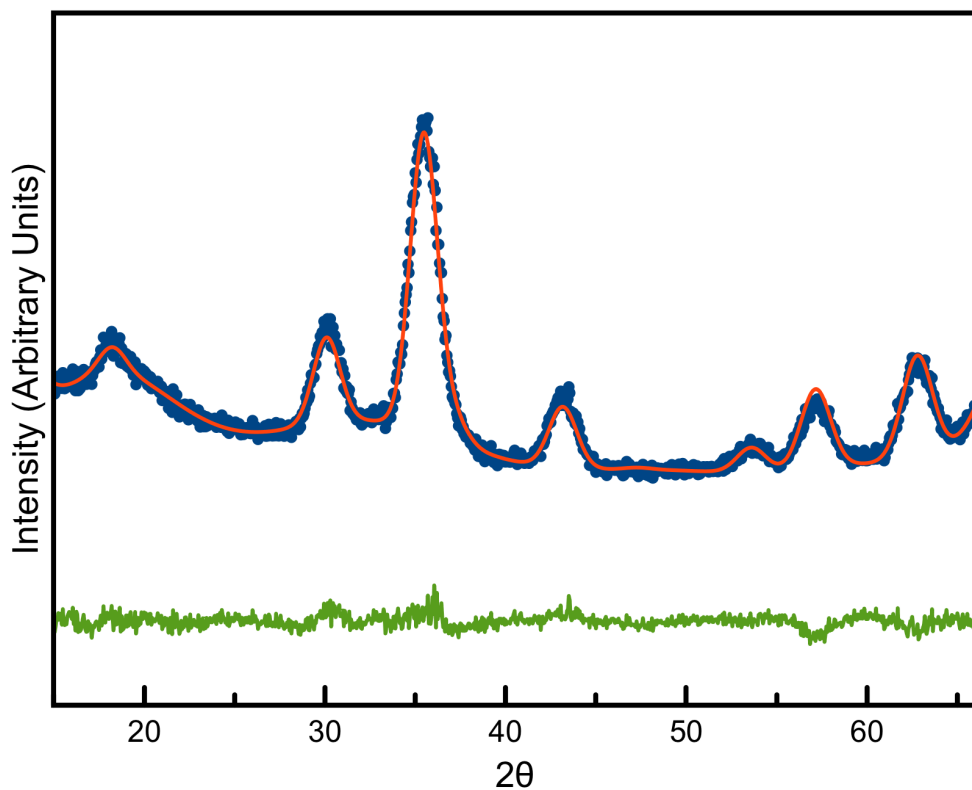


**Figure C.5.** Powder XRD pattern (blue dots) of a 6 nm NC sample (measured by SAXS), fit using Rietveld refinement (red line) to verify the spinel iron oxide phase and crystallite size. The difference between the data and the model is shown by the green line.

**Table C.3.** Refined parameters using Rietveld refinement of a 6 nm NC sample (measured by SAXS). Spacegroup  $Fd\text{-}3m$ .

Bragg R-factor	5.9%
R-factor	5.7%
A	8.353 Å
Instrument Displacement	-0.17
IG	2.73
Crystallite diameter	5.0 nm

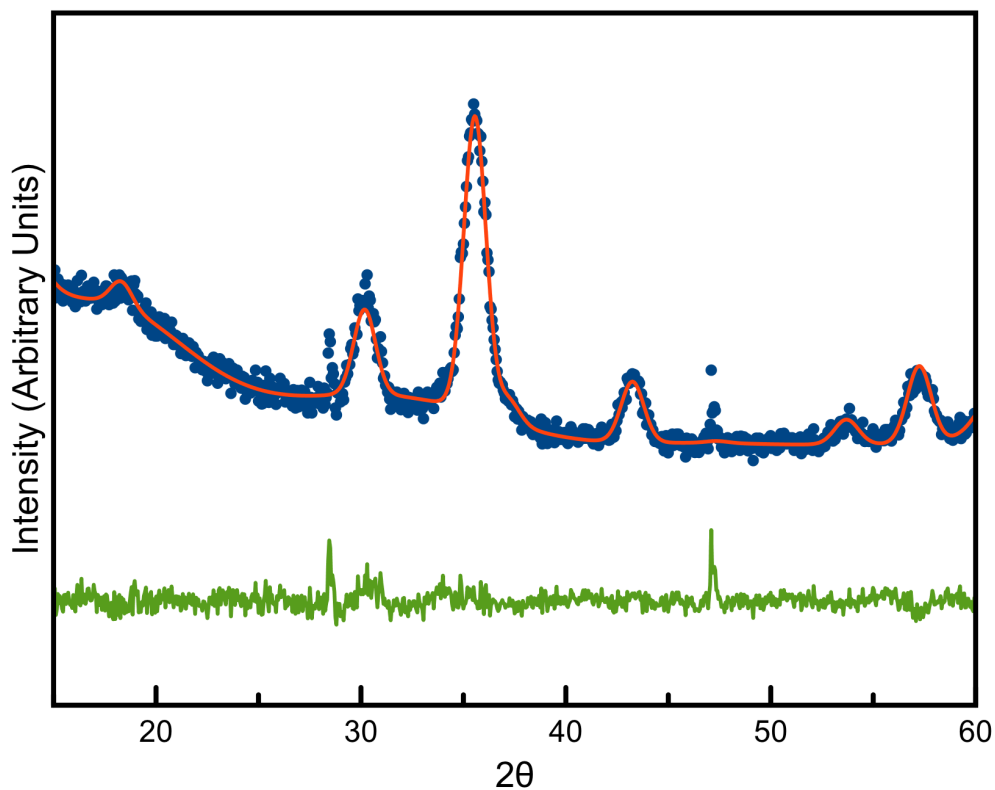


**Figure C.6.** Powder XRD pattern (blue dots) of a 9 nm NC sample (measured by SAXS), fit using Rietveld refinement (red line) to verify the spinel iron oxide phase and crystallite size. The difference between the data and the model is shown by the green line. Peaks at 28° and 47° are from the Si wafer used as a substrate.

**Table C.4.** Refined parameters using Rietveld refinement of a 9 nm NC sample (measured by SAXS). Spacegroup *Fd-3m*.

Bragg R-factor	4.9 %
R-factor	4.0 %
A	8.346 Å
Instrument Displacement	-0.12
IG	1.38
Crystallite diameter	7.1 nm

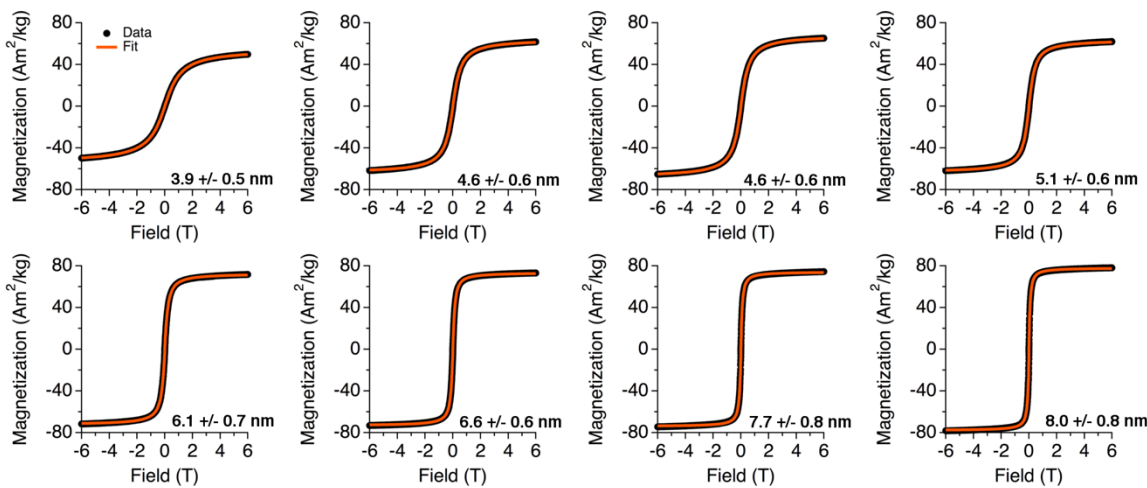


**Figure C.7.** Room temperature magnetization curves of a size series of nanocrystals. Measured data are black while fits to Langevin equation are orange.

**Table C.5.** Physical diameter and standard deviation of size distribution as determined by SAXS, magnetic diameter and standard deviation of distribution as determined by fitting Langevin equation to magnetization curves, percent maghemite as determined by optical absorbance, and the saturation magnetization also determined by fits to magnetization curve.

Physical size (nm)	Magnetic size (nm)	% $\gamma\text{-Fe}_2\text{O}_3$	Saturation Magnetization (Am <sup>2</sup> /kg)
3.9 +/- 0.6	3.5 +/- 0.5	98	54.6 +/- 1.0
4.6 +/- 0.7	4.4 +/- 0.7	94	64.3 +/- 1.1
4.6 +/- 0.7	4.4 +/- 0.8	95	68.3 +/- 1.2
5.1 +/- 0.7	4.8 +/- 0.8	92	63.7 +/- 1.1
6.1 +/- 0.8	5.9 +/- 1.1	86	72.7 +/- 1.3
6.6 +/- 0.7	6.7 +/- 1.0	81	73.5 +/- 1.3
7.7 +/- 0.9	7.6 +/- 1.4	79	74.2 +/- 1.3
8.0 +/- 0.9	8.0 +/- 1.6	74	78.0 +/- 1.4

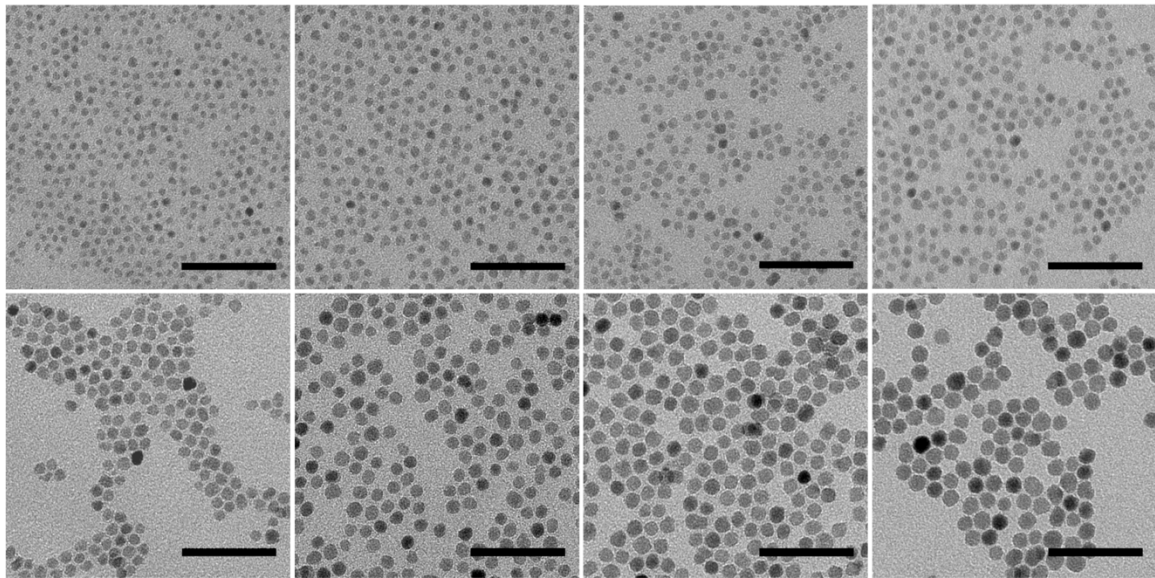


**Figure C.8.** TEM images of all NC samples that were magnetically characterized. Scale bars are 50 nm.

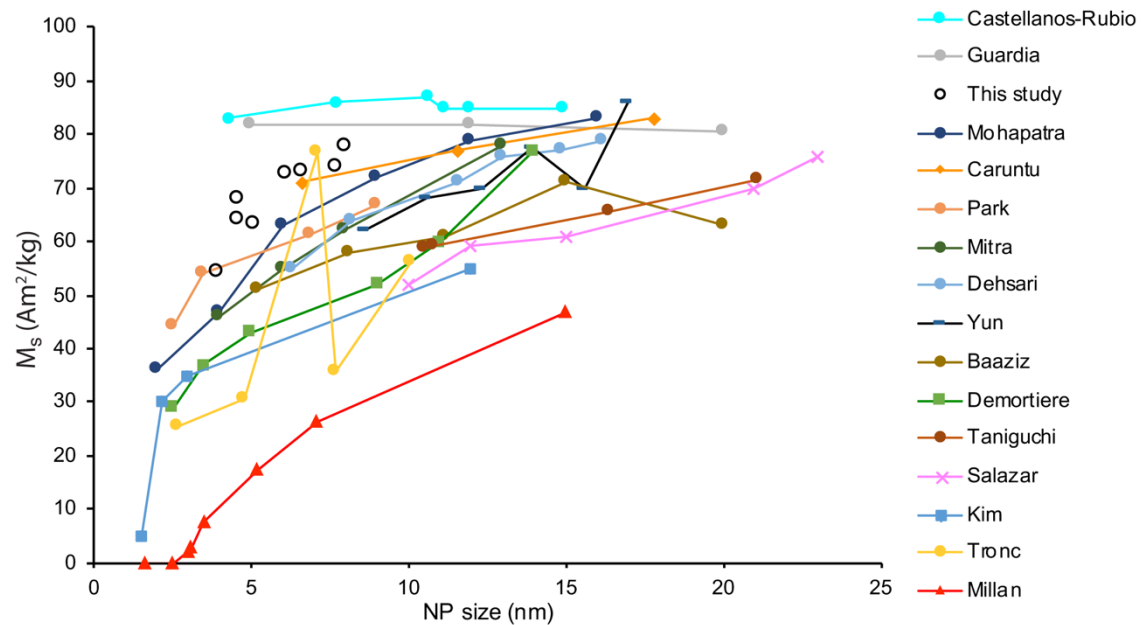


**Figure C.9.** Collection of  $M_s$  values reported in the literature plotted versus nanoparticle size. Includes information from Castellanos-Rubio *et al.*,<sup>5</sup> Guardia *et al.*,<sup>6</sup> Mohapatra *et al.*,<sup>7</sup> Caruntu *et al.*,<sup>8</sup> Park *et al.*,<sup>9</sup> Mitra *et al.*,<sup>10</sup> Dehsari *et al.*,<sup>11</sup> Yun *et al.*,<sup>12</sup> Baaziz *et al.*,<sup>13</sup> Demortière *et al.*,<sup>14</sup> Taniguchi *et al.*,<sup>15</sup> Salazar *et al.*,<sup>16</sup> Kim *et al.*,<sup>17</sup> Tronc *et al.*,<sup>18</sup> Millan *et al.*,<sup>19</sup> and this study. Note that the values reported by Guardia *et al.*, Demortière *et al.*, and Baaziz *et al.* were measured at low temperature (5K), which has the effect of elevating the  $M_s$  compared to room temperature measurements.

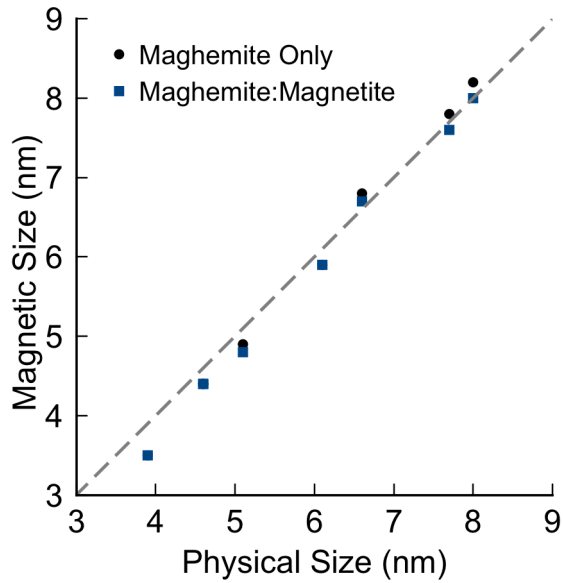


**Figure C.10.** The effective magnetic size using two different values for  $M_D$  from Langevin function fit plotted as a function of physical size measured by SAXS. Black dots are calculated using  $M_D$  commonly used for maghemite of  $76 \text{ Am}^2/\text{kg}$ . Blue squares are calculated using  $M_D$  which reflects the ratio of maghemite:magnetite determined by Near-IR. For the blue squares  $M_D$  used for the maghemite percentage was  $76 \text{ Am}^2/\text{kg}$  and  $M_D$  used for the magnetite percentage was  $92 \text{ Am}^2/\text{kg}$ . The gray dashed line is  $y=x$ .

### Discussion of Figure C.10.

We also calculated the magnetic size using an  $M_D$  equal to the variable percentage of maghemite:magnetite determined by near-IR in Table C.5 in addition to using an  $M_D$  value for maghemite (Figure C.10). We used  $M_D$  values of  $76 \text{ Am}^2/\text{kg}$  for maghemite and  $92 \text{ Am}^2/\text{kg}$  for magnetite to calculate the adjusted  $M_D$  of the NCs. We then used the  $M_D$  for each NC to calculate the magnetic size using  $m = M_D * \frac{\pi}{6} D_C^3$  from Equation 1. Using a variable value of  $M_D$  lowers the magnetic size a bit for larger NCs, as would be expected due to larger magnetite content, so that the magnetic size is not larger than the physical size.

APPENDIX D

SUPPORTING INFORMATION FOR CHAPTER VI:

DESIGN AND DIGITAL FABRICATION OF MAGNETO-DIELECTRIC  
COMPOSITES FOR ADDITIVE MANUFACTURING OF GRADIENT INDEX RF  
LENSES

This appendix was written by T. Zaikova and myself with guidance from J. E. Hutchison. It describes surface functionalization and hexaferrite synthesis utilized in Chapter VI.

**Development of nanoparticle coating and ink formulation**

We developed and produced inks containing dielectric and magnetic nanoparticles for 3D printing. As a nanomaterial with a high dielectric constant, we used barium titanate ( $\text{BaTiO}_3$ ). As magnetic nanomaterial with high permeability, we used  $\text{Co}_2\text{Z}$  (hexagonal barium ferrite composite  $\text{Ba}_3\text{Co}_2\text{Fe}_{24}\text{O}_{41}$ ). All inks were formulated in a di(ethylene glycol) diacrylate (1, Figure D.1, DEGDA) matrix containing the photoinitiator Irgacure 184 (2, Figure D.1). To make particles dispersible in DEGDA for ink jet printing and further photopolymerization, we used small (less than 50 nm in diameter) nanoparticle cores with acrylic acid functional groups (3, Figure D.1) in their outer shell.

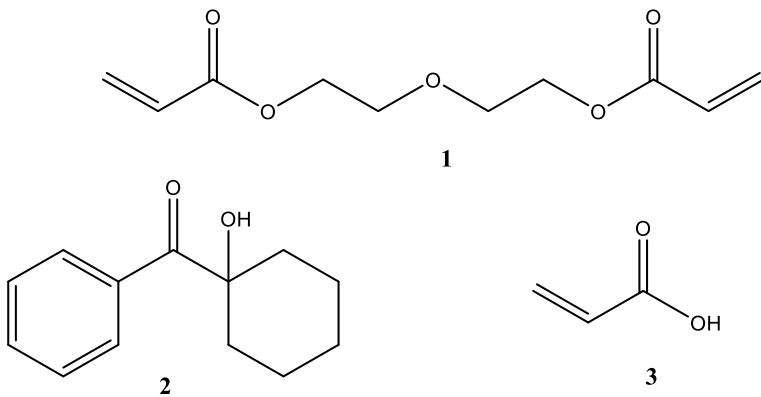


**Figure D.1.** Structures of Di(ethylene glycol) diacrylate (**1**, DEGDA), Irgacure 184 (**2**), and acrylic acid (**3**).

### Synthesis of surface functionalized nanoparticles

#### *Surface functionalization of BaTiO<sub>3</sub> nanoparticles*

Two different procedures were developed to prepare surface modified barium titanate (BaTiO<sub>3</sub>) nanoparticles to be dispersed in polymeric matrix DEGDA. Both procedures required using high energy ball milling as in Atkuri et al.<sup>1</sup>

A RETSCH Planetary Ball Mill PM 100 equipped with a zirconia jar and 3 mm zirconia balls was used. Ball milling experiments have been carried out using 50 nm (Inframat® Advanced Materials™ LLC, Cat # 5622ON-N2) and 500 nm BaTiO<sub>3</sub> (Inframat® Advanced Materials™ LLC, Cat # 5622-ON7) particles as the starting materials.

In the method for large nanoparticles (500 nm), ball milling was carried out in the presence of acrylic acid. Briefly, 1.2 g of 500 nm BaTiO<sub>3</sub> and 500 µL of acrylic acid in 16 mL of ethanol were loaded into the 50 mL zirconium jar followed by loading with 70 g of zirconium balls. The mixture was milled for 7-9 hours at 500 rpm. Acrylic acid was added to prevent aggregation and also serves as a modifying ligand. After ball milling

with acrylic acid mixture was transferred into a 50 mL Corning tube and centrifuged. The supernatant was removed, and solid was washed with twice with 40 mL of ethanol. Ethanol (2-7 mL) was added to solid, and the mixture was sonicated for an hour. It was important to keep nanoparticles in ethanol at all times before use in order to prevent aggregation. Modification of particles surface was confirmed by XPS.

To functionalize small BaTiO<sub>3</sub> (50 nm), 1 g of BaTiO<sub>3</sub> and 500 µL of acrylic acid in 16 mL of ethanol were loaded in a 50 mL jar followed by loading of 70 g of balls. The mixture was milled for 1 hour at 500 rpm. After ball milling with acrylic acid mixture was transferred into 50 mL Corning tube, centrifuged and washed 2x40 mL of ethanol. Desired amount of ethanol (2-7 mL) was added to solid and mixture sonicated for an hour. Particles always should be kept in ethanol before using to prevent aggregation. Modification of particles surface was confirmed by IR spectroscopy. Ball-milling doesn't change particles size as was shown by tunneling electron microscopy (TEM). Synthesized BaTiO<sub>3</sub> nanoparticles were used to prepare ink for 3D printing using the procedure described below.

#### *Synthesis of Co<sub>2</sub>Z nanoparticles*

Two approaches were used to synthesized Co<sub>2</sub>Z hexaferrite. In the first approach we used a well-known solid-state reaction technique<sup>2</sup> with slight modifications. We found that increasing time of ball milling (from 2 h to 22 h) and changing solvent from water to ethanol gave higher percent of desired Co<sub>2</sub>Z phase. Barium carbonate (0.59 g, 2.99 mmol, 1µm powder, Alfa Aesar, Cat #14341), cobalt (II, III) oxide (0.16g, 0.66 mmol, 50-80 nm powder, Alfa Aesar, Cat # 44661), Iron (III) oxide (alpha-phase, 1.92 g, 12 mmol , 30-50 nanopowder) in 16 mL of ethanol were loaded in 50 mL jar followed by 70

g of balls and milled for 20 hours at 300 rpm. Ethanol was evaporated under nitrogen and powder was dried at 104°C for 20 hours.

Various annealing procedures were examined to achieve hexaferrite phases and target the Co<sub>2</sub>Z phase. The phases were characterized qualitatively using X-ray diffraction (XRD). Annealing at 1100°C and below yielded mostly Y-type ( $\text{Ba}_2\text{Co}_2\text{Fe}_{12}\text{O}_{22}$ ) and M-type ( $\text{BaFe}_{12-x}\text{Co}_x\text{O}_{19}$ ) phases of hexaferrite (Figure D.2). Based on Pullar<sup>3</sup>, 1330°C was the ideal temperature to achieve the Z-type (i.e. Co<sub>2</sub>Z) phase, but this resulted in almost exclusively W-type hexaferrite ( $\text{BaCo}_2\text{Fe}_{16}\text{O}_{27}$ ) (Figure D.3). As a result, we lowered the annealing temperature to 1230°C yielding a mix of ferrites that appeared to contain the Z-type phase (Figure D.4).

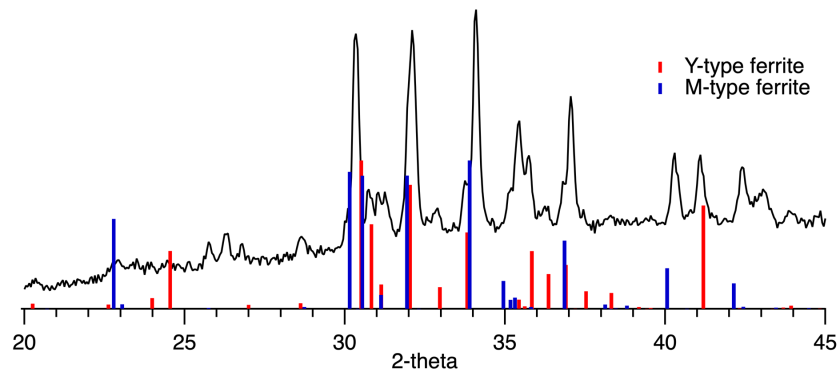


**Figure D.2.** XRD pattern of ball milled starting materials annealed at 1080°C in air for 2 h (black trace) with comparisons to Y (red lines) and M -ype (blue lines) hexaferrite phases.

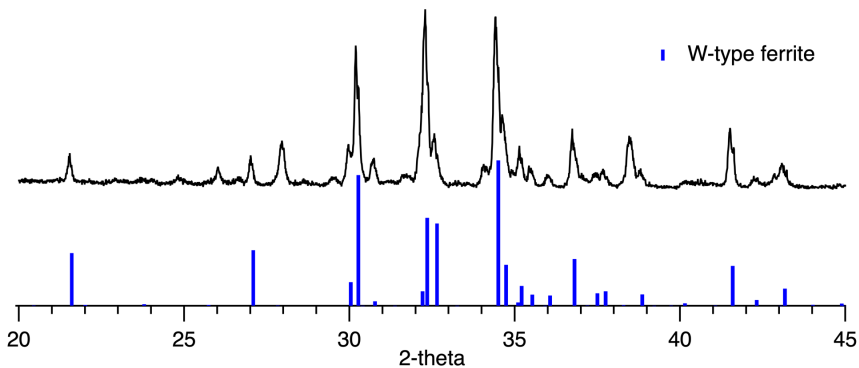


**Figure D.3.** XRD pattern following annealing at 1330°C in air for 4 hours (black trace) with comparison to W-type hexaferrite (blue lines).

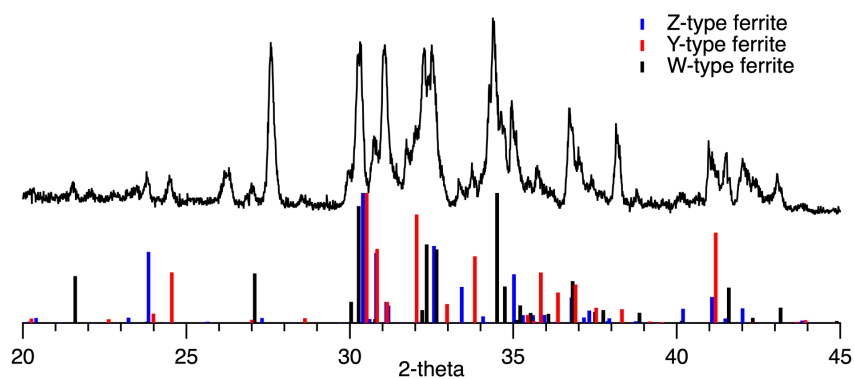


**Figure D.4.** XRD pattern following annealing at 1230°C in air for 4 hours (black trace) with Z-type (blue lines), Y-type (red lines), and W-type (black lines) hexaferrite phases for comparison.

The particle size following the annealing step was too large to produce a dispersion that could pass through nozzles for printing, so we performed another ball milling step. One gram of 1230°C annealed sample was milled with 70 g of balls in 17 mL of ethanol and 450  $\mu$ L of acrylic acid for 7 h at 500 rpm. XRD pattern shows that the sample comprises several hexaferrite phases and has broadened peaks (Figure D.5) compared to the sample prior to ball milling (Figure D.4 black trace). The peaks were broadened due to the small particle size ( $\sim$ 10 nm). The small particle size was confirmed

by transmission electron microscopy (TEM) of the ball milled sample (Figure D.6). The process for preparing the hexaferrite ink for 3D printing is described below.

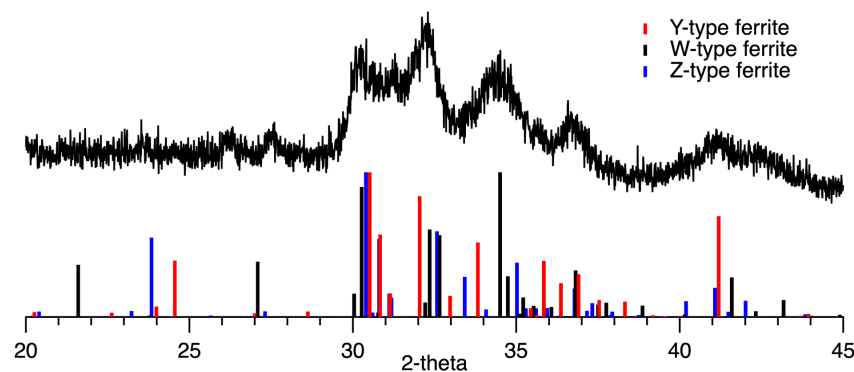


**Figure D.5.** XRD pattern of hexaferrite sample annealed at 1230°C after ball milling (black trace) with Z-type (blue lines), Y-type (red lines), and W-type (black lines) hexaferrite phases for comparison.

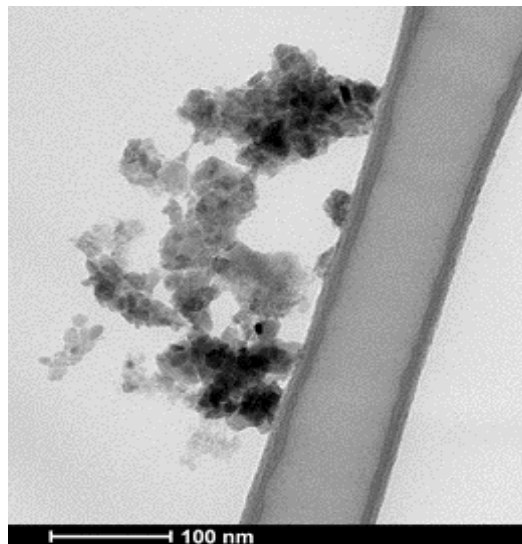


**Figure D.6.** TEM image of 1230°C annealed hexaferrite sample after ball milling.

In the second approach for Co<sub>2</sub>Z nanoparticles synthesis, we used the slow injection method.<sup>4</sup> Barium isopropoxide 0.077 g (0.3 mmol), cobalt (III) acetylacetone 0.071 g (0.2 mmol) and iron (II) acetate 0.42 g (2.4 mmol) were added to 3 mL of oleic acid. The reaction mixture was stirred for 1 h at room temperature. Then, the mixture was heated to 1230°C for 1 h in air. After cooling down to room temperature, the product was collected and washed with ethanol and water. Finally, the product was dried at 60°C for 24 h. The resulting hexaferrite sample was characterized by XRD and TEM. The XRD pattern showed broad peaks characteristic of nanocrystalline materials. The TEM image showed a cluster of dark, irregularly shaped nanoparticles. The size of the nanoparticles was approximately 100 nm.

acid. The mixture was heated for 2 hours at 150°C under nitrogen to produce mixture of barium oleate, cobalt oleate, and iron oleate. The mixed oleates solution obtained was then added dropwise (0.3 mL/min) to 13 mL of oleyl alcohol heated to 230°C. After 20 minutes solution was cooled down to room temperature. The product was precipitated with 30 mL of acetone and solid was collected by centrifugation at 7300 rpm, dissolved in 2 mL of toluene and precipitated with 40 mL of acetone. Precipitated solid was washed with acetone (2x40 mL). The resulting nanoparticles contain Ba, Co, and Fe according to EDX. However, the particles obtained (5-8 nm in size) possess the spinel structure as shown by XRD (Figure D.7). Changing reaction temperature, concentration of starting material, or using iron with higher oxidation state as a starting material didn't lead to desired hexaferrite particles. Further procedure tuning required to obtain desired product.

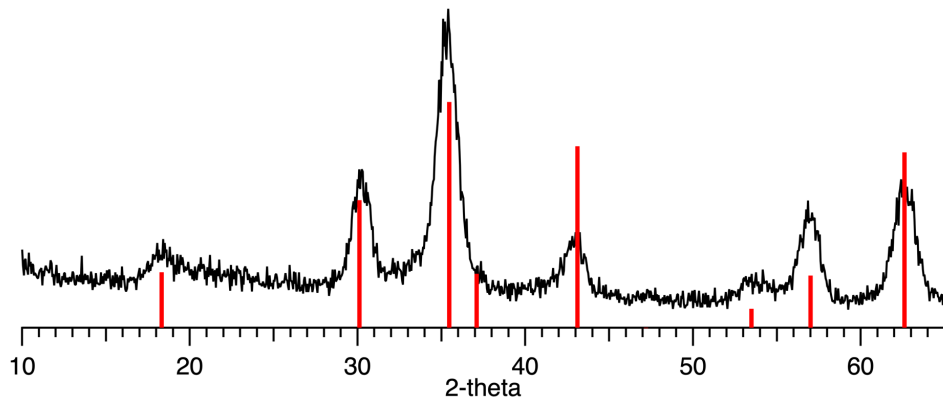


**Figure D.7.** XRD pattern of sample produced via slow injection method (black trace) with the cubic spinel phase (red lines) for comparison.

**General procedure for ink preparation using acrylic acid-modified BaTiO<sub>3</sub> nanoparticles and Co<sub>2</sub>Z hexaferrite nanoparticles**

Acrylic acid-modified nanoparticles (200 mg) were transferred into round-bottom flask as a suspension in ethanol (2 mL) and 2 mL of DEGDA was added to the sample. Ethanol was evaporated using rotary evaporator at 25-30°C. After ethanol evaporation, the sample was sonicated for 20 h. Photoinitiator (Irgacure 184, 60 mg) was added to the mixture, and it was sonicated for an additional hour. The dispersion obtained was used for 3D printing.

#### *Inkjet printing nanoparticle composite inks*

Composite films were formed by inkjet printing in an N<sub>2</sub> atmosphere using published procedure.<sup>5</sup> The printer used was a Dimatix Materials Printer, DMP-2800, manufactured by Fujifilm-Dimatix. The DMP is a laboratory research printer that enables the evaluation of ink jetting technology for new material manufacturing and analytical processes. It is designed for carrying out “proof of concept” and development work with sophisticated capabilities for optimizing process parameters for given application. The DMP is PC-controlled and has a substrate scanning “ink jet” deposition system with a visual drop observation camera, and spot location capability. It prints with user-fillable piezo-based jetting cartridges, each with 16 square nozzles spaced at 254 µm such that ink drop volumes are 10 pl. It is designed specifically for working with organic fluid based “inks” and is equipped with a capability for nozzle and substrate heating up to 70 °C.

In our process, prepared BaTiO<sub>3</sub>/DEGDA or hexaferrite/DEGDA inks were printed onto piranha-cleaned glass substrates to form layers 5-10 µm in thickness and then polymerized to form composites. Composites were multilayered up to 22 layers.

Each layer was polymerized under UV light (365 nm) following deposition and before next layer deposition.

The both BaTiO<sub>3</sub>/DEGDA and hexaferrite/DEGDA inks were easily printed at low loadings (7-10% by weight). Printing samples with 30% loading was challenging. Dispersions were too viscous to pass through the nozzles of the printing cartridges. To overcome that problem, dispersions were diluted with 2 or 3 mL of ethanol. After deposit a layer and before polymerization, ethanol was allowed to evaporate for 5 minutes under nitrogen atmosphere. Examples of high-loading samples are shown in Figure D.8. Printed samples were submitted for dielectric permittivity measurements and magnetic characterization.

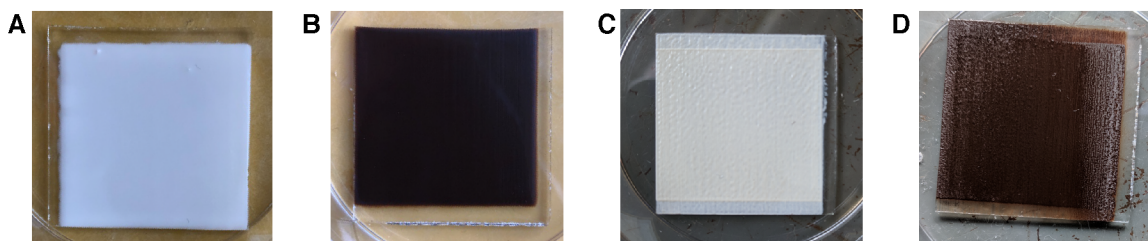


**Figure D.8.** Images of printed composites with low-loading (A and B) and high loading (C and D). White samples are BaTiO<sub>3</sub>/DEGDA composites, and brown samples are hexaferrite/DEGDA composites.

## REFERENCES CITED

### Chapter I

- (1) Awasthi, R.; Roseblade, A.; Hansbro, P. M.; Rathbone, M. J.; Dua, K.; Bebawy, M. Nanoparticles in Cancer Treatment: Opportunities and Obstacles. *Curr. Drug Targets* **2018**, *19*, 1696–1709.
- (2) Han, X.; Xu, K.; Taratula, O.; Farsad, K. Applications of Nanoparticles in Biomedical Imaging. *Nanoscale* **2019**, *11*, 799–819.
- (3) Simeonidis, K.; Mourdikoudis, S.; Kaprara, E.; Mitrakas, M.; Polavarapu, L. Inorganic Engineered Nanoparticles in Drinking Water Treatment: A Critical Review. *Environ. Sci. Water Res. Technol.* **2016**, *2*, 43–70.
- (4) Ma, C.; Yan, J.; Huang, Y.; Wang, C.; Yang, G. The Optical Duality of Tellurium Nanoparticles for Broadband Solar Energy Harvesting and Efficient Photothermal Conversion. *Sci. Adv.* **2018**, *4*, eaas9894.
- (5) Liu, J.; Qiao, S. Z.; Chen, J. S.; Lou, X. W.; Xing, X.; Lu, G. Q. Yolk/Shell Nanoparticles: New Platforms for Nanoreactors, Drug Delivery and Lithium-Ion Batteries. *Chem. Commun.* **2011**, *47*, 12578.
- (6) Shearon, W. H.; Fullem, W. R. Silica-Alumina Petroleum Cracking Catalyst. *Ind. Eng. Chem.* **1959**, *51*, 720–726.
- (7) Heiligttag, F. J. The Fascinating World of Nanoparticle Research. *Mater. Today* **2013**, *16*, 10.
- (8) Lohse, S. Nanoparticles Are All around Us. *Sustainable Nano*, 2013.
- (9) Devouard, B.; Pósfai, M.; Hua, X.; Bazylinski, D. A.; Frankel, R. B.; Buseck, P. R. Magnetite from Magnetotactic Bacteria: Size Distributions and Twinning. *Am. Mineral.* **1998**, *83*, 1387–1398.
- (10) Banfield, J. F.; Zhang, H. Nanoparticles in the Environment. *Rev. Mineral. Geochem.* **2001**, *44*, 1–58.
- (11) The discovery of carbon atoms bound in the form of a ball is rewarded <https://www.nobelprize.org/prizes/chemistry/1996/press-release/>.
- (12) The Royal Institution. Michael Faraday's gold colloids <https://www.rigb.org/our-history/iconic-objects/iconic-objects-list/faraday-gold-colloids> (accessed Oct 16, 2019).

- (13) Alivisatos, A. P. Semiconductor Clusters, Nanocrystals, and Quantum Dots. *Science* **1996**, *271*, 933–937.
- (14) Luther, J. M.; Jain, P. K.; Ewers, T.; Alivisatos, A. P. Localized Surface Plasmon Resonances Arising from Free Carriers in Doped Quantum Dots. *Nat. Mater.* **2011**, *10*, 361–366.
- (15) Kolhatkar, A.; Jamison, A.; Litvinov, D.; Willson, R.; Lee, T. Tuning the Magnetic Properties of Nanoparticles. *Int. J. Mol. Sci.* **2013**, *14*, 15977–16009.
- (16) Grassian, V. H. When Size *Really* Matters: Size-Dependent Properties and Surface Chemistry of Metal and Metal Oxide Nanoparticles in Gas and Liquid Phase Environments. *J. Phys. Chem. C* **2008**, *112*, 18303–18313.
- (17) Van Santen, R. A. Complementary Structure Sensitive and Insensitive Catalytic Relationships. *Acc. Chem. Res.* **2009**, *42*, 57–66.
- (18) Xu, L.; Liang, H.-W.; Yang, Y.; Yu, S.-H. Stability and Reactivity: Positive and Negative Aspects for Nanoparticle Processing. *Chem. Rev.* **2018**, *118*, 3209–3250.
- (19) Kellon, J. E.; Young, S. L.; Hutchison, J. E. Engineering the Nanoparticle–Electrode Interface. *Chem. Mater.* **2019**, *31*, 2685–2701.
- (20) Schladt, T. D.; Schneider, K.; Schild, H.; Tremel, W. Synthesis and Bio-Functionalization of Magnetic Nanoparticles for Medical Diagnosis and Treatment. *Dalton Trans.* **2011**, *40*, 6315.
- (21) Interagency Working Group on Nanoscience, Engineering and Technology. *National Nanotechnology Initiative - Leading to the next industrial revolution*; Washington, D.C., 2000; pp 1–100.
- (22) Feynman, R. P. There's Plenty of Room at the Bottom. *Eng. Sci.* **1960**, *23*, 22–36.
- (23) Milburn, C. *Nanovision: Engineering the Future*; Duke University Press: Durham, NC, 2008.
- (24) Nunes, D.; Pimentel, A.; Santos, L.; Barquinha, P.; Pereira, L.; Fortunato, E.; Martins, R. Introduction. In *Metal Oxide Nanostructures: Synthesis, properties and Applications*; Elsevier: Cambridge, US, 2019.
- (25) McMullan, D. Scanning Electron Microscopy 1928–1965. *Scanning* **2006**, *17*, 175–185.
- (26) Courtland, R. Pushing the Limits: Technological Advances Are Triggering a Revolution in Electron Microscopy. *Nature* **2018**, *563*, 462–464.

- (27) Williams, D. B.; Carter, C. B. *Transmission Electron Microscopy: A Textbook for Materials Science*, 2nd ed.; Springer: New York, 2008.
- (28) Weiss, P. S. *A Conversation with Dr. Heinrich Rohrer: STM Co-Inventor and One of the Founding Fathers of Nanoscience*. *ACS Nano* **2007**, *1*, 3–5.
- (29) Iijima, S. Helical Microtubules of Graphitic Carbon. *Nature* **1991**, *354*, 56–58.
- (30) Crommie, M. F.; Lutz, C. P.; Eigler, D. M. Confinement of Electrons to Quantum Corrals on a Metal Surface. *Science* **1993**, *262*, 218–220.
- (31) Murray, C. B.; Norris, D. J.; Bawendi, M. G. Synthesis and Characterization of Nearly Monodisperse CdE (E = S, Se, Te) Semiconductor Nanocrystallites. *J. Am. Chem. Soc.* **1993**, *115*, 8706–8715.
- (32) Gleich, B.; Weizenecker, J. Tomographic Imaging Using the Nonlinear Response of Magnetic Particles. *Nature* **2005**, *435*, 1214–1217.
- (33) Wu, L. C.; Zhang, Y.; Steinberg, G.; Qu, H.; Huang, S.; Cheng, M.; Bliss, T.; Du, F.; Rao, J.; Song, G.; et al. A Review of Magnetic Particle Imaging and Perspectives on Neuroimaging. *Am. J. Neuroradiol.* **2019**, *40*, 206–212.
- (34) Dutz, S.; Hergt, R. Magnetic Particle Hyperthermia—a Promising Tumour Therapy? *Nanotechnology* **2014**, *25*, 452001.
- (35) Alexson, D.; Chen, H.; Cho, M.; Dutta, M.; Li, Y.; Shi, P.; Raichura, A.; Ramadurai, D.; Parikh, S.; Stroscio, M. A.; et al. Semiconductor Nanostructures in Biological Applications. *J. Phys. Condens. Matter* **2005**, *17*, R637–R656.
- (36) Vance, M. E.; Kuiken, T.; Vejerano, E. P.; McGinnis, S. P.; Hochella, M. F.; Rejeski, D.; Hull, M. S. Nanotechnology in the Real World: Redeveloping the Nanomaterial Consumer Products Inventory. *Beilstein J. Nanotechnol.* **2015**, *6*, 1769–1780.
- (37) Capon, A.; Gillespie, J.; Rolfe, M.; Smith, W. Perceptions of Risk from Nanotechnologies and Trust in Stakeholders: A Cross Sectional Study of Public, Academic, Government and Business Attitudes. *2015*, *13*.
- (38) Carey-Hill, D. *A Clockwork Origin*; Futurama; 2010.
- (39) Templesmith, B. *Singularity 7*; Singularity; IDW Publishing, 2010.
- (40) Olenick, L. The Cautionary Tale of DDT -- Biomagnification, Bioaccumulation, and Research Motivation. *Sustainable Nano*, 2013.

- (41) EPA. Government Ban on Fluorocarbon Gases in Aerosol Products Begins October 15 [1978] <https://archive.epa.gov/epa/aboutepa/government-ban-fluorocarbon-gases-aerosol-products-begins-october-15-1978.html> (accessed Oct 15, 2019).
- (42) OSHA. Asbestos <https://www.osha.gov/SLTC/asbestos/> (accessed Oct 15, 2019).
- (43) Jiji, S. G.; Gopchandran, K. G. Shape Dependent Catalytic Activity of Unsupported Gold Nanostructures for the Fast Reduction of 4-Nitroaniline. *Colloid Interface Sci. Commun.* **2019**, *29*, 9–16.
- (44) Sharma, S. K.; Vargas, J. M.; Pirota, K. R.; Kumar, S.; Lee, C. G.; Knobel, M. Synthesis and Ageing Effect in FeO Nanoparticles: Transformation to Core–Shell FeO/Fe<sub>3</sub>O<sub>4</sub> and Their Magnetic Characterization. *J. Alloys Compd.* **2011**, *509*, 6414–6417.
- (45) Luigjes, B.; Woudenberg, S. M. C.; de Groot, R.; Meeldijk, J. D.; Torres Galvis, H. M.; de Jong, K. P.; Philipse, A. P.; Erné, B. H. Diverging Geometric and Magnetic Size Distributions of Iron Oxide Nanocrystals. *J. Phys. Chem. C* **2011**, *115*, 14598–14605.
- (46) Luo, S. N.; Kono, A.; Nouchi, N.; Shoji, F. Effective Creation of Oxygen Vacancies as an Electron Carrier Source in Tin-Doped Indium Oxide Films by Plasma Sputtering. *J. Appl. Phys.* **2006**, *100*, 113701.
- (47) Haxel, G.; Hedrick, J.; Orris, G. Rare Earth Elements--Critical Resources for High Technology <https://pubs.usgs.gov/fs/2002/fs087-02/> (accessed Oct 10, 2019).
- (48) Viter, R.; Iatsunskyi, I. Metal Oxide Nanostructures in Sensing. In *Nanomaterials Design for Sensing Applications*; Micro and Nano Technologies; Elsevier, 2019; pp 41–91.
- (49) Bajorowicz, B.; Kobylanksi, M.; Malankowska, A.; Mazierski, P.; Nadolna, J.; Pieczynska, A.; Zaleska-Medynska, A. Application of Metal Oxide-Based Photocatalysis. In *Metal Oxide-Based Photocatalysis: Fundamentals and Prospects for Application Metal Oxides*; Elsevier: Amsterdam, Neterlands, 2018.
- (50) Gupta, A. K.; Gupta, M. Synthesis and Surface Engineering of Iron Oxide Nanoparticles for Biomedical Applications. *Biomaterials* **2005**, *26*, 3995–4021.
- (51) Canas-Carrell, J. E.; Li, S.; Parra, A. M.; Shrestha, B. Metal Oxide Nanomaterials: Health and Environmental Effects. In *Health and Environmental Safety of Nanomaterials: Polymer nanocomposites and other materials containing nanoparticles*; Elsevier: Cambridge, UK, 2014; pp 200–221.

- (52) Montini, T.; Melchionna, M.; Monai, M.; Fornasiero, P. Fundamentals and Catalytic Applications of CeO<sub>2</sub> -Based Materials. *Chem. Rev.* **2016**, *116*, 5987–6041.
- (53) LaMer, V. K.; Dinegar, R. H. Theory, Production, and Mechanism of Formation of Monodisperse Hydrosols. *J. Am. Chem. Soc.* **1950**, *72*, 4847–4854.
- (54) van Embden, J.; Chesman, A. S. R.; Jasieniak, J. J. The Heat-Up Synthesis of Colloidal Nanocrystals. *Chem. Mater.* **2015**, *27*, 2246–2285.
- (55) Sugimoto, T. Preparation of Monodispersed Colloidal Particles. *Adv. Colloid Interface Sci.* **1987**, *28*, 65–108.
- (56) Sharifi Dehsari, H.; Heidari, M.; Halda Ribeiro, A.; Tremel, W.; Jakob, G.; Donadio, D.; Potestio, R.; Asadi, K. Combined Experimental and Theoretical Investigation of Heating Rate on Growth of Iron Oxide Nanoparticles. *Chem. Mater.* **2017**, *29*, 9648–9656.
- (57) Park, J.; An, K.; Hwang, Y.; Park, J.-G.; Noh, H.-J.; Kim, J.-Y.; Park, J.-H.; Hwang, N.-M.; Hyeon, T. Ultra-Large-Scale Syntheses of Monodisperse Nanocrystals. *Nat. Mater.* **2004**, *3*, 891–895.
- (58) Lynch, J.; Zhuang, J.; Wang, T.; LaMontagne, D.; Wu, H.; Cao, Y. C. Gas-Bubble Effects on the Formation of Colloidal Iron Oxide Nanocrystals. *J. Am. Chem. Soc.* **2011**, *133*, 12664–12674.
- (59) Yu, W. W.; Falkner, J. C.; Yavuz, C. T.; Colvin, V. L. Synthesis of Monodisperse Iron Oxide Nanocrystals by Thermal Decomposition of Iron Carboxylate Salts. *Chem. Commun.* **2004**, *20*, 2306.
- (60) Kwon, S. G.; Piao, Y.; Park, J.; Angappane, S.; Jo, Y.; Hwang, N.-M.; Park, J.-G.; Hyeon, T. Kinetics of Monodisperse Iron Oxide Nanocrystal Formation by “Heating-Up” Process. *J. Am. Chem. Soc.* **2007**, *129*, 12571–12584.
- (61) Ito, D.; Yokoyama, S.; Zaikova, T.; Masuko, K.; Hutchison, J. E. Synthesis of Ligand-Stabilized Metal Oxide Nanocrystals and Epitaxial Core/Shell Nanocrystals via a Lower-Temperature Esterification Process. *ACS Nano* **2014**, *8*, 64–75.
- (62) Narayanaswamy, A.; Xu, H.; Pradhan, N.; Kim, M.; Peng, X. Formation of Nearly Monodisperse In<sub>2</sub>O<sub>3</sub> Nanodots and Oriented-Attached Nanoflowers: Hydrolysis and Alcoholysis vs Pyrolysis. *J. Am. Chem. Soc.* **2006**, *128*, 10310–10319.
- (63) Hai, H. T.; Kura, H.; Takahashi, M.; Ogawa, T. Phase Transformation of FeO/Fe<sub>3</sub>O<sub>4</sub> Core/Shell Nanocubes and Facile Synthesis of Fe<sub>3</sub>O<sub>4</sub> Nanocubes. *J. Appl. Phys.* **2010**, *107*, 09E301.

- (64) Tancredi, P.; Rojas, P. C. R.; Moscoso-Londoño, O.; Wolff, U.; Neu, V.; Damm, C.; Rellinghaus, B.; Knobel, M.; Socolovsky, L. M. Synthesis Process, Size and Composition Effects of Spherical  $\text{Fe}_3\text{O}_4$  and  $\text{FeO}@\text{Fe}_3\text{O}_4$  Core/Shell Nanoparticles. *New J. Chem.* **2017**, *41*, 15033–15041.
- (65) Chen, R.; Christiansen, M. G.; Sourakov, A.; Mohr, A.; Matsumoto, Y.; Okada, S.; Jasanoff, A.; Anikeeva, P. High-Performance Ferrite Nanoparticles through Nonaqueous Redox Phase Tuning. *Nano Lett.* **2016**, *16*, 1345–1351.
- (66) Qiao, L.; Fu, Z.; Li, J.; Ghosen, J.; Zeng, M.; Stebbins, J.; Prasad, P. N.; Swihart, M. T. Standardizing Size- and Shape-Controlled Synthesis of Monodisperse Magnetite ( $\text{Fe}_3\text{O}_4$ ) Nanocrystals by Identifying and Exploiting Effects of Organic Impurities. *ACS Nano* **2017**, *11*, 6370–6381.
- (67) Kovalenko, M. V.; Bodnarchuk, M. I.; Lechner, R. T.; Hesser, G.; Schäffler, F.; Heiss, W. Fatty Acid Salts as Stabilizers in Size- and Shape-Controlled Nanocrystal Synthesis: The Case of Inverse Spinel Iron Oxide. *J. Am. Chem. Soc.* **2007**, *129*, 6352–6353.
- (68) Estrader, M.; López-Ortega, A.; Golosovsky, I. V.; Estradé, S.; Roca, A. G.; Salazar-Alvarez, G.; López-Conesa, L.; Tobia, D.; Winkler, E.; Ardisson, J. D.; et al. Origin of the Large Dispersion of Magnetic Properties in Nanostructured Oxides:  $\text{Fe}_x\text{O}/\text{Fe}_3\text{O}_4$  Nanoparticles as a Case Study. *Nanoscale* **2015**, *7*, 3002–3015.
- (69) Zhang, Z.; Zhong, X.; Liu, S.; Li, D.; Han, M. Aminolysis Route to Monodisperse Titania Nanorods with Tunable Aspect Ratio. *Angew. Chem. Int. Ed.* **2005**, *44*, 3466–3470.
- (70) Sun, S.; Zeng, H. Size-Controlled Synthesis of Magnetite Nanoparticles. *J. Am. Chem. Soc.* **2002**, *124*, 8204–8205.
- (71) Sun, S.; Zeng, H.; Robinson, D. B.; Raoux, S.; Rice, P. M.; Wang, S. X.; Li, G. Monodisperse  $\text{MFe}_2\text{O}_4$  ( $\text{M} = \text{Fe, Co, Mn}$ ) Nanoparticles. *J. Am. Chem. Soc.* **2004**, *126*, 273–279.
- (72) Balakrishnan, T.; Lee, M.-J.; Dey, J.; Choi, S.-M. Sub-Nanometer Scale Size-Control of Iron Oxide Nanoparticles with Drying Time of Iron Oleate. *CrystEngComm* **2019**, *21*, 4063–4071.
- (73) Vreeland, E. C.; Watt, J.; Schober, G. B.; Hance, B. G.; Austin, M. J.; Price, A. D.; Fellows, B. D.; Monson, T. C.; Hudak, N. S.; Maldonado-Camargo, L.; et al. Enhanced Nanoparticle Size Control by Extending LaMer's Mechanism. *Chem. Mater.* **2015**, *27*, 6059–6066.

- (74) Jansons, A. W.; Koskela, K. M.; Crockett, B. M.; Hutchison, J. E. Transition Metal-Doped Metal Oxide Nanocrystals: Efficient Substitutional Doping through a Continuous Growth Process. *Chem. Mater.* **2017**, *29*, 8167–8176.
- (75) Crockett, B. M.; Jansons, A. W.; Koskela, K. M.; Johnson, D. W.; Hutchison, J. E. Radial Dopant Placement for Tuning Plasmonic Properties in Metal Oxide Nanocrystals. *ACS Nano* **2017**, *11*, 7719–7728.

## Chapter II

- (1) Nakhleh, M. K.; Amal, H.; Jeries, R.; Broza, Y. Y.; Aboud, M.; Gharra, A.; Ivgi, H.; Khatib, S.; Badarneh, S.; Har-Shai, L.; *et al.* Diagnosis and Classification of 17 Diseases from 1404 Subjects via Pattern Analysis of Exhaled Molecules. *ACS Nano* **2017**, *11*, 112–125.
- (2) Choi, J.-H.; Wang, H.; Oh, S. J.; Paik, T.; Sung, P.; Sung, J.; Ye, X.; Zhao, T.; Diroll, B. T.; Murray, C. B.; *et al.* Exploiting the Colloidal Nanocrystal Library to Construct Electronic Devices. *Science* **2016**, *352*, 205–208.
- (3) Talapin, D. V.; Lee, J.-S.; Kovalenko, M. V.; Shevchenko, E. V. Prospects of Colloidal Nanocrystals for Electronic and Optoelectronic Applications. *Chem. Rev.* **2010**, *110*, 389–458.
- (4) Mulvaney, P. Surface Plasmon Spectroscopy of Nanosized Metal Particles. *Langmuir* **1996**, *12*, 788–800.
- (5) Link, S.; El-Sayed, M. A. Spectral Properties and Relaxation Dynamics of Surface Plasmon Electronic Oscillations in Gold and Silver Nanodots and Nanorods. *J. Phys. Chem. B* **1999**, *103*, 8410–8426.
- (6) Chen, X.; Li, C.; Gratzel, M.; Kostecki, R.; Mao, S. S. Nanomaterials for Renewable Energy Production and Storage. *Chem. Soc. Rev.* **2012**, *41*, 7909–7937.
- (7) Astruc, D.; Lu, F.; Aranzaes, J. R. Nanoparticles as Recyclable Catalysts: The Frontier between Homogeneous and Heterogeneous Catalysis. *Angew. Chem. Int. Ed.* **2005**, *44*, 7852–7872.
- (8) Saha, K.; Agasti, S. S.; Kim, C.; Li, X.; Rotello, V. M. Gold Nanoparticles in Chemical and Biological Sensing. *Chem. Rev.* **2012**, *112*, 2739–2779.
- (9) Park, J.; Joo, J.; Kwon, S. G.; Jang, Y.; Hyeon, T. Synthesis of Monodisperse Spherical Nanocrystals. *Angew. Chem. Int. Ed.* **2007**, *46*, 4630–4660.
- (10) Thanh, N. T. K.; Maclean, N.; Mahiddine, S. Mechanisms of Nucleation and Growth of Nanoparticles in Solution. *Chem. Rev.* **2014**, *114*, 7610–7630.

- (11) Hendricks, M. P.; Campos, M. P.; Cleveland, G. T.; Jen-La Plante, I.; Owen, J. S. A Tunable Library of Substituted Thiourea Precursors to Metal Sulfide Nanocrystals. *Science* **2015**, *348*, 1226–1230.
- (12) Campos, M. P.; Hendricks, M. P.; Beecher, A. N.; Walravens, W.; Swain, R. A.; Cleveland, G. T.; Hens, Z.; Sfeir, M. Y.; Owen, J. S. A Library of Selenourea Precursors to PbSe Nanocrystals with Size Distributions near the Homogeneous Limit. *J. Am. Chem. Soc.* **2017**.
- (13) Reiss, P.; Carrière, M.; Lincheneau, C.; Vaure, L.; Tamang, S. Synthesis of Semiconductor Nanocrystals, Focusing on Nontoxic and Earth-Abundant Materials. *Chem. Rev.* **2016**, *116*, 10731–10819.
- (14) Watzky, M. A.; Finke, R. G. Nanocluster Size-Control and “Magic Number” Investigations. Experimental Tests of the “Living-Metal Polymer” Concept and of Mechanism-Based Size-Control Predictions Leading to the Syntheses of Iridium(0) Nanoclusters Centering about Four Sequential Magic Numbers. *Chem. Mater.* **1997**, *9*, 3083–3095.
- (15) van Embden, J.; Chesman, A. S. R.; Jasieniak, J. J. The Heat-Up Synthesis of Colloidal Nanocrystals. *Chem. Mater.* **2015**, *27*, 2246–2285.
- (16) Lee, J.; Zhang, S.; Sun, S. High-Temperature Solution-Phase Syntheses of Metal-Oxide Nanocrystals. *Chem. Mater.* **2013**, *25*, 1293–1304.
- (17) Wang, F.; Richards, V. N.; Shields, S. P.; Buhro, W. E. Kinetics and Mechanisms of Aggregative Nanocrystal Growth. *Chem. Mater.* **2014**, *26*, 5–21.
- (18) Leskelä, M.; Ritala, M. Atomic Layer Deposition Chemistry: Recent Developments and Future Challenges. *Angew. Chem. Int. Ed.* **2003**, *42*, 5548–5554.
- (19) Herman, M. A.; Sitter, H. *Molecular Beam Epitaxy: Fundamentals and Current Status*; Springer Science & Business Media, 2012; Vol. 7.
- (20) Stein, A.; Keller, S. W.; Mallouk, T. E. Turning Down the Heat: Design and Mechanism in Solid-State Synthesis. *Science* **1993**, *259*, 1558–1564.
- (21) Hornbostel, M. D.; Hyer, E. J.; Thiel, J.; Johnson, D. C. Rational Synthesis of Metastable Skutterudite Compounds Using Multilayer Precursors. *J. Am. Chem. Soc.* **1997**, *119*, 2665–2668.
- (22) Mann, S. *Biomineralization: Principles and Concepts in Bioinorganic Materials Chemistry*; Oxford University Press on Demand, 2001; Vol. 5.

- (23) Szwarc, M. Living Polymers. Their Discovery, Characterization, and Properties. *J. Polym. Sci. Part Polym. Chem.* **1998**, *36*, IX–XV.
- (24) LaMer, V. K.; Dinegar, R. H. Theory, Production and Mechanism of Formation of Monodispersed Hydrosols. *J. Am. Chem. Soc.* **1950**, *72*, 4847–4854.
- (25) Patterson, G. Sixty Years of Living Polymers. *Nature* **2016**, *536*, 276–278.
- (26) Szwarc, M. ‘Living’ Polymers. *Nature* **1956**, *178*, 1168–1169.
- (27) Webster, O. W. Living Polymerization Methods. *Science* **1991**, *251*, 887–893.
- (28) Yin, Y.; Alivisatos, A. P. Colloidal Nanocrystal Synthesis and the Organic-Inorganic Interface. *Nature* **2005**, *437*, 664–670.
- (29) Steigerwald, M. L.; Brus, L. E. Semiconductor Crystallites: A Class of Large Molecules. *Acc. Chem. Res.* **1990**, *23*, 183–188.
- (30) Murray, C. B.; Norris, D. J.; Bawendi, M. G. Synthesis and Characterization of Nearly Monodisperse CdE (E = Sulfur, Selenium, Tellurium) Semiconductor Nanocrystallites. *J. Am. Chem. Soc.* **1993**, *115*, 8706–8715.
- (31) Cushing, B. L.; Kolesnichenko, V. L.; O’Connor, C. J. Recent Advances in the Liquid-Phase Syntheses of Inorganic Nanoparticles. *Chem. Rev.* **2004**, *104*, 3893–3946.
- (32) Niederberger, M. Nonaqueous Sol–Gel Routes to Metal Oxide Nanoparticles. *Acc. Chem. Res.* **2007**, *40*, 793–800.
- (33) Kwon, S. G.; Hyeon, T. Formation Mechanisms of Uniform Nanocrystals via Hot-Injection and Heat-Up Methods. *Small* **2011**, *7*, 2685–2702.
- (34) Peng, X.; Wickham, J.; Alivisatos, A. P. Kinetics of II-VI and III-V Colloidal Semiconductor Nanocrystal Growth: “Focusing” of Size Distributions. *J. Am. Chem. Soc.* **1998**, *120*, 5343–5344.
- (35) Park, J.; Lee, E.; Hwang, N.-M.; Kang, M.; Kim, S. C.; Hwang, Y.; Park, J.-G.; Noh, H.-J.; Kim, J.-Y.; Park, J.-H.; *et al.* One-Nanometer-Scale Size-Controlled Synthesis of Monodisperse Magnetic Iron Oxide Nanoparticles. *Angew. Chem. Int. Ed.* **2005**, *44*, 2872–2877.
- (36) Yu, H.; Gibbons, P. C.; Kelton, K. F.; Buhro, W. E. Heterogeneous Seeded Growth: A Potentially General Synthesis of Monodisperse Metallic Nanoparticles. *J. Am. Chem. Soc.* **2001**, *123*, 9198–9199.

- (37) Jana, N. R.; Peng, X. Single-Phase and Gram-Scale Routes toward Nearly Monodisperse Au and Other Noble Metal Nanocrystals. *J. Am. Chem. Soc.* **2003**, *125*, 14280–14281.
- (38) Wilcoxon, J. P.; Provencio, P. P. Heterogeneous Growth of Metal Clusters from Solutions of Seed Nanoparticles. *J. Am. Chem. Soc.* **2004**, *126*, 6402–6408.
- (39) Farrell, D.; Majetich, S. A.; Wilcoxon, J. P. Preparation and Characterization of Monodisperse Fe Nanoparticles. *J. Phys. Chem. B* **2003**, *107*, 11022–11030.
- (40) Sun, S.; Zeng, H.; Robinson, D. B.; Raoux, S.; Rice, P. M.; Wang, S. X.; Li, G. Monodisperse MFe<sub>2</sub>O<sub>4</sub> (M = Fe, Co, Mn) Nanoparticles. *J. Am. Chem. Soc.* **2004**, *126*, 273–279.
- (41) Steigerwald, M. L.; Alivisatos, A. P.; Gibson, J. M.; Harris, T. D.; Kortan, R.; Muller, A. J.; Thayer, A. M.; Duncan, T. M.; Douglass, D. C.; Brus, L. E. Surface Derivatization and Isolation of Semiconductor Cluster Molecules. *J. Am. Chem. Soc.* **1988**, *110*, 3046–3050.
- (42) Jana, N. R.; Gearheart, L.; Murphy, C. J. Evidence for Seed-Mediated Nucleation in the Chemical Reduction of Gold Salts to Gold Nanoparticles. *Chem. Mater.* **2001**, *13*, 2313–2322.
- (43) Levy, M.; Quarta, A.; Espinosa, A.; Figuerola, A.; Wilhelm, C.; García-Hernández, M.; Genovese, A.; Falqui, A.; Alloyeau, D.; Buonsanti, R.; *et al.* Correlating Magneto-Structural Properties to Hyperthermia Performance of Highly Monodisperse Iron Oxide Nanoparticles Prepared by a Seeded-Growth Route. *Chem. Mater.* **2011**, *23*, 4170–4180.
- (44) Vreeland, E. C.; Watt, J.; Schober, G. B.; Hance, B. G.; Austin, M. J.; Price, A. D.; Fellows, B. D.; Monson, T. C.; Hudak, N. S.; Maldonado-Camargo, L.; *et al.* Enhanced Nanoparticle Size Control by Extending LaMer’s Mechanism. *Chem. Mater.* **2015**, *27*, 6059–6066.
- (45) Gordon, T. R.; Cargnello, M.; Paik, T.; Mangolini, F.; Weber, R. T.; Fornasiero, P.; Murray, C. B. Nonaqueous Synthesis of TiO<sub>2</sub> Nanocrystals Using TiF<sub>4</sub> to Engineer Morphology, Oxygen Vacancy Concentration, and Photocatalytic Activity. *J. Am. Chem. Soc.* **2012**, *134*, 6751–6761.
- (46) Buonsanti, R.; Grillo, V.; Carlino, E.; Giannini, C.; Kipp, T.; Cingolani, R.; Cozzoli, P. D. Nonhydrolytic Synthesis of High-Quality Anisotropically Shaped Brookite TiO<sub>2</sub> Nanocrystals. *J. Am. Chem. Soc.* **2008**, *130*, 11223–11233.
- (47) Tamang, S.; Lee, S.; Choi, H.; Jeong, S. Tuning Size and Size Distribution of Colloidal InAs Nanocrystals via Continuous Supply of Prenucleation Clusters on Nanocrystal Seeds. *Chem. Mater.* **2016**, *28*, 8119–8122.

- (48) Bronstein, L. M.; Huang, X.; Retrum, J.; Schmucker, A.; Pink, M.; Stein, B. D.; Dragnea, B. Influence of Iron Oleate Complex Structure on Iron Oxide Nanoparticle Formation. *Chem. Mater.* **2007**, *19*, 3624–3632.
- (49) Ito, D.; Yokoyama, S.; Zaikova, T.; Masuko, K.; Hutchison, J. E. Synthesis of Ligand-Stabilized Metal Oxide Nanocrystals and Epitaxial Core/Shell Nanocrystals via a Lower-Temperature Esterification Process. *ACS Nano* **2014**, *8*, 64–75.
- (50) Jansons, A. W.; Hutchison, J. E. Continuous Growth of Metal Oxide Nanocrystals: Enhanced Control of Nanocrystal Size and Radial Dopant Distribution. *ACS Nano* **2016**, *10*, 6942–6951.
- (51) Buonsanti, R.; Milliron, D. J. Chemistry of Doped Colloidal Nanocrystals. *Chem. Mater.* **2013**, *25*, 1305–1317.
- (52) Bryan, J. D.; Gamelin, D. R. Doped Semiconductor Nanocrystals: Synthesis, Characterization, Physical Properties, and Applications. In *Progress in Inorganic Chemistry*; John Wiley & Sons, Inc., 2005; pp. 47–126.
- (53) Radovanovic, P. V. Defect-Induced Optical and Magnetic Properties of Colloidal Transparent Conducting Oxide Nanocrystals. In *Functional Metal Oxides*; Wiley-VCH Verlag GmbH & Co. KGaA, 2013; pp. 163–194.
- (54) Norris, D. J.; Efros, A. L.; Erwin, S. C. Doped Nanocrystals. *Science* **2008**, *319*, 1776–1779.
- (55) Deng, Z.; Tong, L.; Flores, M.; Lin, S.; Cheng, J.-X.; Yan, H.; Liu, Y. High-Quality Manganese-Doped Zinc Sulfide Quantum Rods with Tunable Dual-Color and Multiphoton Emissions. *J. Am. Chem. Soc.* **2011**, *133*, 5389–5396.
- (56) Buonsanti, R.; Llordes, A.; Aloni, S.; Helms, B. A.; Milliron, D. J. Tunable Infrared Absorption and Visible Transparency of Colloidal Aluminum-Doped Zinc Oxide Nanocrystals. *Nano Lett.* **2011**, *11*, 4706–4710.
- (57) Della Gaspera, E.; Chesman, A. S. R.; van Embden, J.; Jasieniak, J. J. Non-Injection Synthesis of Doped Zinc Oxide Plasmonic Nanocrystals. *ACS Nano* **2014**, *8*, 9154–9163.
- (58) Djerdj, I.; Garnweitner, G.; Arcon, D.; Pregelj, M.; Jaglicic, Z.; Niederberger, M. Diluted Magnetic Semiconductors: Mn/Co-Doped ZnO Nanorods as Case Study. *J. Mater. Chem.* **2008**, *18*, 5208–5217.

- (59) Bilecka, I.; Luo, L.; Djerdj, I.; Rossell, M. D.; Jagodič, M.; Jagličić, Z.; Masubuchi, Y.; Kikkawa, S.; Niederberger, M. Microwave-Assisted Nonaqueous Sol–Gel Chemistry for Highly Concentrated ZnO-Based Magnetic Semiconductor Nanocrystals. *J. Phys. Chem. C* **2011**, *115*, 1484–1495.
- (60) Liang, X.; Ren, Y.; Bai, S.; Zhang, N.; Dai, X.; Wang, X.; He, H.; Jin, C.; Ye, Z.; Chen, Q.; *et al.* Colloidal Indium-Doped Zinc Oxide Nanocrystals with Tunable Work Function: Rational Synthesis and Optoelectronic Applications. *Chem. Mater.* **2014**, *26*, 5169–5178.
- (61) Schwartz, D. A.; Norberg, N. S.; Nguyen, Q. P.; Parker, J. M.; Gamelin, D. R. Magnetic Quantum Dots: Synthesis, Spectroscopy, and Magnetism of Co<sup>2+</sup>- and Ni<sup>2+</sup>-Doped ZnO Nanocrystals. *J. Am. Chem. Soc.* **2003**, *125*, 13205–13218.
- (62) Luther, J. M.; Jain, P. K.; Ewers, T.; Alivisatos, A. P. Localized Surface Plasmon Resonances Arising from Free Carriers in Doped Quantum Dots. *Nat Mater* **2011**, *10*, 361–366.
- (63) Kovalenko, M. V.; Manna, L.; Cabot, A.; Hens, Z.; Talapin, D. V.; Kagan, C. R.; Klimov, V. I.; Rogach, A. L.; Reiss, P.; Milliron, D. J.; *et al.* Prospects of Nanoscience with Nanocrystals. *ACS Nano* **2015**, *9*, 1012–1057.
- (64) Lounis, S. D.; Runnerstrom, E. L.; Llordés, A.; Milliron, D. J. Defect Chemistry and Plasmon Physics of Colloidal Metal Oxide Nanocrystals. *J. Phys. Chem. Lett.* **2014**, *5*, 1564–1574.
- (65) Faucheaux, J. A.; Stanton, A. L. D.; Jain, P. K. Plasmon Resonances of Semiconductor Nanocrystals: Physical Principles and New Opportunities. *J. Phys. Chem. Lett.* **2014**, *5*, 976–985.
- (66) Kriegel, I.; Scognella, F.; Manna, L. Plasmonic Doped Semiconductor Nanocrystals: Properties, Fabrication, Applications and Perspectives. *Phys. Rep.*
- (67) Johns, R. W.; Bechtel, H. A.; Runnerstrom, E. L.; Agrawal, A.; Lounis, S. D.; Milliron, D. J. Direct Observation of Narrow Mid-Infrared Plasmon Linewidths of Single Metal Oxide Nanocrystals. *Nat Commun* **2016**, *7*.
- (68) Lounis, S. D.; Runnerstrom, E. L.; Bergerud, A.; Nordlund, D.; Milliron, D. J. Influence of Dopant Distribution on the Plasmonic Properties of Indium Tin Oxide Nanocrystals. *J. Am. Chem. Soc.* **2014**, *136*, 7110–7116.
- (69) Kanehara, M.; Koike, H.; Yoshinaga, T.; Teranishi, T. Indium Tin Oxide Nanoparticles with Compositionally Tunable Surface Plasmon Resonance Frequencies in the Near-IR Region. *J. Am. Chem. Soc.* **2009**, *131*, 17736–17737.

- (70) Choi, S.-I.; Nam, K. M.; Park, B. K.; Seo, W. S.; Park, J. T. Preparation and Optical Properties of Colloidal, Monodisperse, and Highly Crystalline ITO Nanoparticles. *Chem. Mater.* **2008**, *20*, 2609–2611.
- (71) Crockett, B. M.; Jansons, A. W.; Koskela, K. M.; Johnson, D. W.; Hutchison, J. E. Tuning Localized Surface Plasmon Resonances in Sn-Doped  $\text{In}_2\text{O}_3$  (ITO) Through Radial Distribution of Dopant Atoms. *ACS Nano*. Under review
- (72) Casavola, M.; Buonsanti, R.; Caputo, G.; Cozzoli, P. D. Colloidal Strategies for Preparing Oxide-Based Hybrid Nanocrystals. *Eur. J. Inorg. Chem.* **2008**, *2008*, 837–854.
- (73) van Embden, J.; Jasieniak, J.; Gómez, D. E.; Mulvaney, P.; Giersig, M. Review of the Synthetic Chemistry Involved in the Production of Core/Shell Semiconductor Nanocrystals. *Aust. J. Chem.* **2007**, *60*, 457–471.
- (74) Reiss, P.; Protière, M.; Li, L. Core/Shell Semiconductor Nanocrystals. *Small* **2009**, *5*, 154–168.
- (75) Ghosh Chaudhuri, R.; Paria, S. Core/Shell Nanoparticles: Classes, Properties, Synthesis Mechanisms, Characterization, and Applications. *Chem. Rev.* **2012**, *112*, 2373–2433.
- (76) Li, J. J.; Wang, Y. A.; Guo, W.; Keay, J. C.; Mishima, T. D.; Johnson, M. B.; Peng, X. Large-Scale Synthesis of Nearly Monodisperse CdSe/CdS Core/Shell Nanocrystals Using Air-Stable Reagents via Successive Ion Layer Adsorption and Reaction. *J. Am. Chem. Soc.* **2003**, *125*, 12567–12575.
- (77) Reiss, P.; Bleuse, J.; Pron, A. Highly Luminescent CdSe/ZnSe Core/Shell Nanocrystals of Low Size Dispersion. *Nano Lett.* **2002**, *2*, 781–784.
- (78) Xie, R.; Kolb, U.; Li, J.; Basché, T.; Mews, A. Synthesis and Characterization of Highly Luminescent CdSe–Core CdS/Zn/Cd/S/ZnS Multishell Nanocrystals. *J. Am. Chem. Soc.* **2005**, *127*, 7480–7488.
- (79) Tan, R.; Blom, D. A.; Ma, S.; Greytak, A. B. Probing Surface Saturation Conditions in Alternating Layer Growth of CdSe/CdS Core/Shell Quantum Dots. *Chem. Mater.* **2013**, *25*, 3724–3736.
- (80) Ocana, M.; Hsu, W. P.; Matijevic, E. Preparation and Properties of Uniform-Coated Colloidal Particles. 6. Titania on Zinc Oxide. *Langmuir* **1991**, *7*, 2911–2916.
- (81) He, Q.; Zhang, Z.; Xiong, J.; Xiong, Y.; Xiao, H. A Novel Biomaterial —  $\text{Fe}_3\text{O}_4:\text{TiO}_2$  Core-Shell Nano Particle with Magnetic Performance and High Visible Light Photocatalytic Activity. *Opt. Mater.* **2008**, *31*, 380–384.

- (82) Davar, F.; Majedi, A.; Abbasi, A. Synthesis of Fe<sub>3</sub>O<sub>4</sub>@ZrO<sub>2</sub> Core–shell Nanoparticles through New Approach and Its Solar Light Photocatalyst Application. *J. Mater. Sci. Mater. Electron.* **2017**, *28*, 4871–4878.
- (83) Morris-Cohen, A. J.; Malicki, M.; Peterson, M. D.; Slavin, J. W. J.; Weiss, E. A. Chemical, Structural, and Quantitative Analysis of the Ligand Shells of Colloidal Quantum Dots. *Chem. Mater.* **2013**, *25*, 1155–1165.
- (84) Holmberg, V. C.; Helps, J. R.; Mkhoyan, K. A.; Norris, D. J. Imaging Impurities in Semiconductor Nanostructures. *Chem. Mater.* **2013**, *25*, 1332–1350.
- (85) Sowers, K. L.; Swartz, B.; Krauss, T. D. Chemical Mechanisms of Semiconductor Nanocrystal Synthesis. *Chem. Mater.* **2013**, *25*, 1351–1362.
- (86) Li, T.; Senesi, A. J.; Lee, B. Small Angle X-Ray Scattering for Nanoparticle Research. *Chem. Rev.* **2016**, *116*, 11128–11180.
- (87) Newton, M. A.; Chapman, K. W.; Thompsett, D.; Chupas, P. J. Chasing Changing Nanoparticles with Time-Resolved Pair Distribution Function Methods. *J. Am. Chem. Soc.* **2012**, *134*, 5036–5039.
- (88) Jensen, K. M. Ø.; Christensen, M.; Juhas, P.; Tyrsted, C.; Bøjesen, E. D.; Lock, N.; Billinge, S. J. L.; Iversen, B. B. Revealing the Mechanisms behind SnO<sub>2</sub> Nanoparticle Formation and Growth during Hydrothermal Synthesis: An In Situ Total Scattering Study. *J. Am. Chem. Soc.* **2012**, *134*, 6785–6792.
- (89) Jensen, K. M. Ø.; Andersen, H. L.; Tyrsted, C.; Bøjesen, E. D.; Dippel, A.-C.; Lock, N.; Billinge, S. J. L.; Iversen, B. B.; Christensen, M. Mechanisms for Iron Oxide Formation under Hydrothermal Conditions: An in Situ Total Scattering Study. *ACS Nano* **2014**, *8*, 10704–10714.

### Chapter III

- (1) van Embden, J.; Sader, J. E.; Davidson, M.; Mulvaney, P. Evolution of Colloidal Nanocrystals: Theory and Modeling of Their Nucleation and Growth. *J. Phys. Chem. C* **2009**, *113*, 16342–16355.
- (2) Tromp, R. M.; Hannon, J. B. Thermodynamics of Nucleation and Growth. *Surf. Rev. Lett.* **2002**, *09*, 1565–1593.
- (3) Boistelle, R.; Astier, J. P. Crystallization Mechanisms in Solution. *J. Cryst. Growth* **1988**, *90*, 14–30.

- (4) McPeak, K. M.; Jayanti, S. V.; Kress, S. J. P.; Meyer, S.; Iotti, S.; Rossinelli, A.; Norris, D. J. Plasmonic Films Can Easily Be Better: Rules and Recipes. *ACS Photonics* **2015**, *2*, 326–333.
- (5) Corpinot, M. K.; Bučar, D.-K. A Practical Guide to the Design of Molecular Crystals. *Cryst. Growth Des.* **2019**, *19*, 1426–1453.
- (6) Kim, K.; Kim, K.-J. Quantitative Study on Crystal Defects Using the Relationship between Crystallization Parameters and Thermal Analysis. *Cryst. Growth Des.* **2018**, *18*, 5021–5028.
- (7) Chambers, S. A. Epitaxial Growth and Properties of Doped Transition Metal and Complex Oxide Films. *Adv. Mater.* **2010**, *22*, 219–248.
- (8) Levy, M.; Quarta, A.; Espinosa, A.; Figuerola, A.; Wilhelm, C.; García-Hernández, M.; Genovese, A.; Falqui, A.; Alloyeau, D.; Buonsanti, R.; et al. Correlating Magneto-Structural Properties to Hyperthermia Performance of Highly Monodisperse Iron Oxide Nanoparticles Prepared by a Seeded-Growth Route. *Chem. Mater.* **2011**, *23*, 4170–4180.
- (9) Wetterskog, E.; Tai, C.-W.; Grins, J.; Bergström, L.; Salazar-Alvarez, G. Anomalous Magnetic Properties of Nanoparticles Arising from Defect Structures: Topotaxial Oxidation of  $\text{Fe}_{1-x}\text{O}|\text{Fe}_{3-\delta}\text{O}_4$  Core|Shell Nanocubes to Single-Phase Particles. *ACS Nano* **2013**, *7*, 7132–7144.
- (10) McKenna, K. P.; Hofer, F.; Gilks, D.; Lazarov, V. K.; Chen, C.; Wang, Z.; Ikuhara, Y. Atomic-Scale Structure and Properties of Highly Stable Antiphase Boundary Defects in  $\text{Fe}_3\text{O}_4$ . *Nat. Commun.* **2014**, *5*, 5740-1–5740-8.
- (11) Anderson, N. C.; Hendricks, M. P.; Choi, J. J.; Owen, J. S. Ligand Exchange and the Stoichiometry of Metal Chalcogenide Nanocrystals: Spectroscopic Observation of Facile Metal-Carboxylate Displacement and Binding. *J. Am. Chem. Soc.* **2013**, *135*, 18536–18548.
- (12) Rosenfeld, G.; Poelsema, B.; Comsa, G. Chapter 3 Epitaxial Growth Modes Far from Equilibrium. In *The Chemical Physics of Solid Surfaces*; Elsevier, **1997**; Vol. 8, pp 66–101.
- (13) Oura, K.; Lifshits, V. G.; Saranin, A. A.; Zotov, A. V.; Katayama, M. *Surface Science: An Introduction*; Springer-Verlag, 2003.
- (14) De Yoreo, J. J.; Vekilov, P. G. Principles of Crystal Nucleation and Growth. *Rev. Mineral. Geochem.* **2003**, *54*, 57–93.
- (15) Vekilov, P. G. What Determines the Rate of Growth of Crystals from Solution? *Cryst. Growth Des.* **2007**, *7*, 2796–2810.

- (16) Pantaraks, P.; Flood, A. E. Effect of Growth Rate History on Current Crystal Growth: A Second Look at Surface Effects on Crystal Growth Rates. *Cryst. Growth Des.* **2005**, *5*, 365–371.
- (17) Meza, L. I.; Anderson, M. W.; Agger, J. R.; Cundy, C. S.; Chong, C. B.; Plaisted, R. J. Controlling Relative Fundamental Crystal Growth Rates in Silicalite: AFM Observation. *J. Am. Chem. Soc.* **2007**, *129*, 15192–15201.
- (18) Pantaraks, P.; Matsuoka, M.; Flood, A. E. Effect of Growth Rate History on Current Crystal Growth. 2. Crystal Growth of Sucrose,  $\text{Al}(\text{SO}_4)_2 \cdot 12\text{H}_2\text{O}$ ,  $\text{KH}_2\text{PO}_4$ , and  $\text{K}_2\text{SO}_4$ . *Cryst. Growth Des.* **2007**, *7*, 2635–2642.
- (19) Land, T. A.; De Yoreo, J. J. The Evolution of Growth Modes and Activity of Growth Sources on Canavalin Investigated by in Situ Atomic Force Microscopy. *J. Cryst. Growth* **2000**, *208*, 623–637.
- (20) Frank, F. C. Snow Crystals. *Contemp. Phys.* **1982**, *23*, 3–22.
- (21) Kobayashi, T. The Growth of Snow Crystals at Low Supersaturations. *Philos. Mag.* **1961**, *6*, 1363–1370.
- (22) Hallet, J. How Snow Crystals Grow: The Deceptively Simple Shapes Raise Fundamental Questions about the Growth of Crystals. *Am. Sci.* **1984**, *72*, 582–589.
- (23) Mason, B. J. Snow Crystals, Natural and Man Made. *Contemp. Phys.* **1992**, *33*, 227–243.
- (24) Furukawa, Y.; Wettlaufer, J. S. Snow and Ice Crystals. *Phys. Today* **2007**, *60*, 70–71.
- (25) Shultz, M. J. Crystal Growth in Ice and Snow. *Phys. Today* **2018**, *71*, 34–39.
- (26) Mirabello, G.; Lenders, J. J. M.; Sommerdijk, N. A. J. M. Bioinspired Synthesis of Magnetite Nanoparticles. *Chem. Soc. Rev.* **2016**, *45*, 5085–5106.
- (27) Meldrum, F. C.; Cölfen, H. Controlling Mineral Morphologies and Structures in Biological and Synthetic Systems. *Chem. Rev.* **2008**, *108*, 4332–4432.
- (28) Salehi, A. The Effects of Deposition Rate and Substrate Temperature of ITO Thin Films on Electrical and Optical Properties. *Thin Solid Films* **1998**, *324*, 214–218.
- (29) Amar, J. G.; Family, F. Kinetics of Submonolayer and Multilayer Epitaxial Growth. *Thin Solid Films* **1996**, *272*, 208–222.

- (30) Cai, K.; Müller, M.; Bossert, J.; Rechtenbach, A.; Jandt, K. D. Surface Structure and Composition of Flat Titanium Thin Films as a Function of Film Thickness and Evaporation Rate. *Appl. Surf. Sci.* **2005**, *250*, 252–267.
- (31) Yang, Y. G.; Johnson, R. A.; Wadley, H. N. G. A Monte Carlo Simulation of the Physical Vapor Deposition of Nickel. *Acta Mater.* **1997**, *45*, 1455–1468.
- (32) Frigeri, P.; Servalli, L.; Trevisi, G.; Franchi, S. Molecular Beam Epitaxy: An Overview. In *Comprehensive Semiconductor Science and Technology*; Elsevier B.V., **2011**; Vol. 3, pp 480–522.
- (33) van Embden, J.; Chesman, A. S. R.; Jasieniak, J. J. The Heat-Up Synthesis of Colloidal Nanocrystals. *Chem. Mater.* **2015**, *27*, 2246–2285.
- (34) de Mello Donegá, C.; Liljeroth, P.; Vanmaekelbergh, D. Physicochemical Evaluation of the Hot-Injection Method, a Synthesis Route for Monodisperse Nanocrystals. *Small* **2005**, *1*, 1152–1162.
- (35) Kwon, S. G.; Hyeon, T. Formation Mechanisms of Uniform Nanocrystals via Hot-Injection and Heat-up Methods. *Small* **2011**, *7*, 2685–27015.
- (36) Talapin, D. V.; Rogach, A. L.; Shevchenko, E. V.; Kornowski, A.; Haase, M.; Weller, H. Dynamic Distribution of Growth Rates within the Ensembles of Colloidal II–VI and III–V Semiconductor Nanocrystals as a Factor Governing Their Photoluminescence Efficiency. *J. Am. Chem. Soc.* **2002**, *124*, 5782–5790.
- (37) Jansons, A. W.; Hutchison, J. E. Continuous Growth of Metal Oxide Nanocrystals: Enhanced Control of Nanocrystal Size and Radial Dopant Distribution. *ACS Nano* **2016**, *10*, 6942–6951.
- (38) Xia, X.; Xie, S.; Liu, M.; Peng, H.-C.; Lu, N.; Wang, J.; Kim, M. J.; Xia, Y. On the Role of Surface Diffusion in Determining the Shape or Morphology of Noble-Metal Nanocrystals. *Proc. Natl. Acad. Sci.* **2013**, *110*, 6669–6673.
- (39) Vreeland, E. C.; Watt, J.; Schober, G. B.; Hance, B. G.; Austin, M. J.; Price, A. D.; Fellows, B. D.; Monson, T. C.; Hudak, N. S.; Maldonado-Camargo, L.; et al. Enhanced Nanoparticle Size Control by Extending LaMer’s Mechanism. *Chem. Mater.* **2015**, *27*, 6059–6066.
- (40) Tamang, S.; Lee, S.; Choi, H.; Jeong, S. Tuning Size and Size Distribution of Colloidal InAs Nanocrystals via Continuous Supply of Prenucleation Clusters on Nanocrystal Seeds. *Chem. Mater.* **2016**, *28*, 8119–8122.

- (41) Franke, D.; Harris, D. K.; Chen, O.; Bruns, O. T.; Carr, J. A.; Wilson, M. W. B.; Bawendi, M. G. Continuous Injection Synthesis of Indium Arsenide Quantum Dots Emissive in the Short-Wavelength Infrared. *Nat. Commun.* **2016**, *7*, 12749–1–12749–9.
- (42) Zhang, H.; Li, W.; Jin, M.; Zeng, J.; Yu, T.; Yang, D.; Xia, Y. Controlling the Morphology of Rhodium Nanocrystals by Manipulating the Growth Kinetics with a Syringe Pump. *Nano Lett.* **2011**, *11*, 898–903.
- (43) Ho, C.-H.; Tsai, C.-P.; Chung, C.-C.; Tsai, C.-Y.; Chen, F.-R.; Lin, H.-J.; Lai, C.-H. Shape-Controlled Growth and Shape-Dependent Cation Site Occupancy of Monodisperse Fe<sub>3</sub>O<sub>4</sub> Nanoparticles. *Chem. Mater.* **2011**, *23*, 1753–1760.
- (44) Wang, X.; Liu, M.; Zhou, Z.; Guo, L. Toward Facet Engineering of CdS Nanocrystals and Their Shape-Dependent Photocatalytic Activities. *J. Phys. Chem. C* **2015**, *119*, 20555–20560.
- (45) Fischer, S.; Swabeck, J. K.; Alivisatos, A. P. Controlled Isotropic and Anisotropic Shell Growth in β-NaLnF<sub>4</sub> Nanocrystals Induced by Precursor Injection Rate. *J. Am. Chem. Soc.* **2017**, *139*, 12325–12332.
- (46) Ito, D.; Yokoyama, S.; Zaikova, T.; Masuko, K.; Hutchison, J. E. Synthesis of Ligand-Stabilized Metal Oxide Nanocrystals and Epitaxial Core/Shell Nanocrystals via a Lower-Temperature Esterification Process. *ACS Nano* **2014**, *8*, 64–75.
- (47) Cooper, S. R.; Plummer, L. K.; Cosby, A. G.; Lenox, P.; Jander, A.; Dhagat, P.; Hutchison, J. E. Insights into the Magnetic Properties of Sub-10 nm Iron Oxide Nanocrystals through the Use of a Continuous Growth Synthesis. *Chem. Mater.* **2018**, *30*, 6053–6062.
- (48) Jansons, A. W.; Koskela, K. M.; Crockett, B. M.; Hutchison, J. E. Transition Metal-Doped Metal Oxide Nanocrystals: Efficient Substitutional Doping through a Continuous Growth Process. *Chem. Mater.* **2017**, *29*, 8167–8176.
- (49) Crockett, B. M.; Jansons, A. W.; Koskela, K. M.; Johnson, D. W.; Hutchison, J. E. Radial Dopant Placement for Tuning Plasmonic Properties in Metal Oxide Nanocrystals. *ACS Nano* **2017**, *11*, 7719–7728.
- (50) Idriss, H.; Barreau, M. A. Active Sites on Oxides: From Single Crystals to Catalysts. *Adv. Catal.* **2000**, *45*, 261–331.
- (51) Jun, Y.; Choi, J.; Cheon, J. Shape Control of Semiconductor and Metal Oxide Nanocrystals through Nonhydrolytic Colloidal Routes. *Angew. Chem. Int. Ed.* **2006**, *45*, 3414–3439.

- (52) Qiao, L.; Fu, Z.; Li, J.; Ghosen, J.; Zeng, M.; Stebbins, J.; Prasad, P. N.; Swihart, M. T. Standardizing Size- and Shape-Controlled Synthesis of Monodisperse Magnetite ( $\text{Fe}_3\text{O}_4$ ) Nanocrystals by Identifying and Exploiting Effects of Organic Impurities. *ACS Nano* **2017**, *11*, 6370–6381.
- (53) Crockett, B. M.; Jansons, A. W.; Koskela, K. M.; Sharps, M. C.; Johnson, D. W.; Hutchison, J. E. Influence of Nanocrystal Size on the Optoelectronic Properties of Thin, Solution-Cast Sn-Doped  $\text{In}_2\text{O}_3$  Films. *Chem. Mater.* **2019**, *31*, 3370–3380.
- (54) Watt, J.; Cheong, S.; Toney, M. F.; Ingham, B.; Cookson, J.; Bishop, P. T.; Tilley, R. D. Ultrafast Growth of Highly Branched Palladium Nanostructures for Catalysis. *ACS Nano* **2010**, *4*, 396–402.
- (55) Lou, X. W.; Yuan, C.; Archer, L. A. An Unusual Example of Hyperbranched Metal Nanocrystals and Their Shape Evolution. *Chem. Mater.* **2006**, *18*, 3921–3923.
- (56) Kanaras, A. G.; Sönnichsen, C.; Liu, H.; Alivisatos, A. P. Controlled Synthesis of Hyperbranched Inorganic Nanocrystals with Rich Three-Dimensional Structures. *Nano Lett.* **2005**, *5*, 2164–2167.
- (57) Watt, J.; Young, N.; Haigh, S.; Kirkland, A.; Tilley, R. D. Synthesis and Structural Characterization of Branched Palladium Nanostructures. *Adv. Mater.* **2009**, *21*, 2288–2293.
- (58) Manna, L.; Milliron, D. J.; Meisel, A.; Scher, E. C.; Alivisatos, A. P. Controlled Growth of Tetrapod-Branched Inorganic Nanocrystals. *Nat. Mater.* **2003**, *2*, 382–385.
- (59) Gorshkov, V.; Zavalov, A.; Privman, V. Shape Selection in Diffusive Growth of Colloids and Nanoparticles. *Langmuir* **2009**, *25*, 7940–7953.
- (60) Carcouët, C. C. M. C.; van de Put, M. W. P.; Mezari, B.; Magusin, P. C. M. M.; Laven, J.; Bomans, P. H. H.; Friedrich, H.; Esteves, A. C. C.; Sommerdijk, N. A. J. M.; van Benthem, R. A. T. M.; et al. Nucleation and Growth of Monodisperse Silica Nanoparticles. *Nano Lett.* **2014**, *14*, 1433–1438.
- (61) Baumgartner, J.; Dey, A.; Bomans, P. H. H.; Le Coadou, C.; Fratzl, P.; Sommerdijk, N. A. J. M.; Faivre, D. Nucleation and Growth of Magnetite from Solution. *Nat. Mater.* **2013**, *12*, 310–314.
- (62) De Yoreo, J. J.; Gilbert, P. U. P. A.; Sommerdijk, N. A. J. M.; Penn, R. L.; Whitelam, S.; Joester, D.; Zhang, H.; Rimer, J. D.; Navrotsky, A.; Banfield, J. F.; et al. Crystallization by Particle Attachment in Synthetic, Biogenic, and Geologic Environments. *Science* **2015**, *349*, aaa6760–aaa6760.

- (63) Palchoudhury, S.; Xu, Y.; Rushdi, A.; Holler, R. A.; Bao, Y. Controlled Synthesis of Iron Oxide Nanoplates and Nanoflowers. *Chem. Commun.* **2012**, *48*, 10499–10501.
- (64) Penn, R. L.; Banfield, J. F. Morphology Development and Crystal Growth in Nanocrystalline Aggregates under Hydrothermal Conditions: Insights from Titania. *Geochim. Cosmochim. Acta* **1999**, *63*, 1549–1557.
- (65) Pacholski, C.; Kornowski, A.; Weller, H. Self-Assembly of ZnO: From Nanodots to Nanorods. *Angew. Chem. Int. Ed.* **2002**, *41*, 1188–1191.
- (66) Zhuang, Z.; Zhang, J.; Huang, F.; Wang, Y.; Lin, Z. Pure Multistep Oriented Attachment Growth Kinetics of Surfactant-Free SnO<sub>2</sub> Nanocrystals. *Phys. Chem. Chem. Phys.* **2009**, *11*, 8516–8521.
- (67) Du, N.; Zhang, H.; Chen, B.; Ma, X.; Yang, D. Ligand-Free Self-Assembly of Ceria Nanocrystals into Nanorods by Oriented Attachment at Low Temperature. *J. Phys. Chem. C* **2007**, *111*, 12677–12680.
- (68) Li, D.; Nielsen, M. H.; Lee, J. R. I.; Frandsen, C.; Banfield, J. F.; De Yoreo, J. J. Direction-Specific Interactions Control Crystal Growth by Oriented Attachment. *Science* **2012**, *336*, 1014–1018.
- (69) Zhang, J.; Huang, F.; Lin, Z. Progress of Nanocrystalline Growth Kinetics Based on Oriented Attachment. *Nanoscale* **2010**, *2*, 18–34.
- (70) Lim, B.; Jiang, M.; Yu, T.; Camargo, P. H. C.; Xia, Y. Nucleation and Growth Mechanisms for Pd-Pt Bimetallic Nanodendrites and Their Electrocatalytic Properties. *Nano Res.* **2010**, *3*, 69–80.
- (71) Morgan, D. G.; Boris, B. S.; Kuchkina, N. V.; Yuzik-Klimova, E. Yu.; Sorokina, S. A.; Stein, B. D.; Svergun, D. I.; Spilotros, A.; Kostopoulou, A.; Lappas, A.; et al. Multicore Iron Oxide Mesocrystals Stabilized by a Poly(Phenylenepyridyl) Dendron and Dendrimer: Role of the Dendron/Dendrimer Self-Assembly. *Langmuir* **2014**, *30*, 8543–8550.
- (72) Zhang, Q.; Liu, S.-J.; Yu, S.-H. Recent Advances in Oriented Attachment Growth and Synthesis of Functional Materials: Concept, Evidence, Mechanism, and Future. *J Mater Chem* **2009**, *19*, 191–207.
- (73) Patterson, S.; Arora, P.; Price, P.; Dittmar, J. W.; Das, V. K.; Pink, M.; Stein, B.; Morgan, D. G.; Losovyj, Y.; Koczkur, K. M.; et al. Oriented Attachment Is a Major Control Mechanism To Form Nail-like Mn-Doped ZnO Nanocrystals. *Langmuir* **2017**, *33*, 14709–14717.

- (74) Polleux, J.; Pinna, N.; Antonietti, M.; Niederberger, M. Ligand-Directed Assembly of Preformed Titania Nanocrystals into Highly Anisotropic Nanostructures. *Adv. Mater.* **2004**, *16*, 436–439.
- (75) Narayanaswamy, A.; Xu, H.; Pradhan, N.; Kim, M.; Peng, X. Formation of Nearly Monodisperse  $\text{In}_2\text{O}_3$  Nanodots and Oriented-Attached Nanoflowers: Hydrolysis and Alcoholysis vs Pyrolysis. *J. Am. Chem. Soc.* **2006**, *128*, 10310–10319.
- (76) Lartigue, L.; Hugounenq, P.; Alloyeau, D.; Clarke, S. P.; Lévy, M.; Bacri, J.-C.; Bazzi, R.; Brougham, D. F.; Wilhelm, C.; Gazeau, F. Cooperative Organization in Iron Oxide Multi-Core Nanoparticles Potentiates Their Efficiency as Heating Mediators and MRI Contrast Agents. *ACS Nano* **2012**, *6*, 10935–10949.
- (77) Luo, S.; Feng, J.; Ng, K. M. Large Scale Synthesis of Nearly Monodisperse, Variable-Shaped  $\text{In}_2\text{O}_3$  Nanocrystals via a One-Pot Pyrolysis Reaction. *CrystEngComm* **2014**, *16*, 9236–9244.
- (78) Jun, Y.; Casula, M. F.; Sim, J.-H.; Kim, S. Y.; Cheon, J.; Alivisatos, A. P. Surfactant-Assisted Elimination of a High Energy Facet as a Means of Controlling the Shapes of  $\text{TiO}_2$  Nanocrystals. *J. Am. Chem. Soc.* **2003**, *125*, 15981–15985.
- (79) Ould-Ely, T.; Prieto-Centurion, D.; Rusakova, I.; Whitmire, K. H. Wet Chemical Synthesis and Characterization of Polypodal  $\text{In}_2\text{O}_3$  Nanoparticles. *CrystEngComm* **2013**, *15*, 6918–6922.
- (80) Cozzoli, P. D.; Snoeck, E.; Garcia, M. A.; Giannini, C.; Guagliardi, A.; Cervellino, A.; Gozzo, F.; Hernando, A.; Achterhold, K.; Ciobanu, N.; et al. Colloidal Synthesis and Characterization of Tetrapod-Shaped Magnetic Nanocrystals. *Nano Lett.* **2006**, *6*, 1966–1972.
- (81) Vartanyan, T. A.; Leonov, N. B.; Przhibel'skiĭ, S. G.; Khromov, V. V. Optical Manifestations of Self-Diffusion of Atoms over the Surfaces of Silver Nanoparticles. *Opt. Spectrosc.* **2009**, *106*, 697–700.
- (82) Gilroy, K. D.; Elnabawy, A. O.; Yang, T.-H.; Roling, L. T.; Howe, J.; Mavrikakis, M.; Xia, Y. Thermal Stability of Metal Nanocrystals: An Investigation of the Surface and Bulk Reconstructions of Pd Concave Icosahedra. *Nano Lett.* **2017**, *17*, 3655–3661.
- (83) Young, N. P.; van Huis, M. A.; Zandbergen, H. W.; Xu, H.; Kirkland, A. I. Transformations of Gold Nanoparticles Investigated Using Variable Temperature High-Resolution Transmission Electron Microscopy. *Ultramicroscopy* **2010**, *110*, 506–516.

- (84) Xia, Y.; Xiong, Y.; Lim, B.; Skrabalak, S. E. Shape-Controlled Synthesis of Metal Nanocrystals: Simple Chemistry Meets Complex Physics? *Angew. Chem. Int. Ed.* **2009**, *48*, 60–103.
- (85) Xiong, Y.; Cai, H.; Wiley, B. J.; Wang, J.; Kim, M. J.; Xia, Y. Synthesis and Mechanistic Study of Palladium Nanobars and Nanorods. *J. Am. Chem. Soc.* **2007**, *129*, 3665–3675.
- (86) Agoston, P.; Albe, K. Thermodynamic Stability, Stoichiometry, and Electronic Structure of Bcc-In<sub>2</sub>O<sub>3</sub> Surfaces. *Phys. Rev. B* **2011**, *84*, 045311-1–045311-20.
- (87) Korotcenkov, G.; Brinzari, V.; Ivanov, M.; Cerneavscchi, A.; Rodriguez, J.; Cirera, A.; Cornet, A.; Morante, J. Structural Stability of Indium Oxide Films Deposited by Spray Pyrolysis during Thermal Annealing. *Thin Solid Films* **2005**, *479*, 38–51.
- (88) Kolasinski, K. W. *Surface Science: Foundations of Catalysis and Nanoscience*, Third.; John Wiley & Sons, Ltd, 2012.
- (89) Tersoff, J.; Denier van der Gon, A. W.; Tromp, R. M. Critical Island Size for Layer-by-Layer Growth. *Phys. Rev. Lett.* **1994**, *72*, 266–269.
- (90) Jansons, A. W.; Plummer, L. K.; Hutchison, J. E. Living Nanocrystals. *Chem. Mater.* **2017**, *29*, 5415–5425.
- (91) Woehrle, G. H.; Hutchison, J. E.; Zkar, S. O.; Finke, R. G. Analysis of Nanoparticle Transmission Electron Microscopy Data Using a Public- Domain Image-Processing Program, Image. *Turk. J. Chem.* **2006**, *30*, 1–13.
- (92) Ilavsky, J.; Jemian, P. R. *Irena* : Tool Suite for Modeling and Analysis of Small-Angle Scattering. *J. Appl. Crystallogr.* **2009**, *42*, 347–353.

## Chapter IV

- (1) Lewinski, N.; Colvin, V.; Drezek, R. Cytotoxicity of Nanoparticles. *Small* **2008**, *4*, 26–49.
- (2) Qiao, R.; Yang, C.; Gao, M. Superparamagnetic Iron Oxide Nanoparticles: From Preparations to in Vivo MRI Applications. *J. Mater. Chem.* **2009**, *19*, 6274.
- (3) Corti, M.; Lascialfari, A.; Micotti, E.; Castellano, A.; Donativi, M.; Quarta, A.; Cozzoli, P. D.; Manna, L.; Pellegrino, T.; Sangregorio, C. Magnetic Properties of Novel Superparamagnetic MRI Contrast Agents Based on Colloidal Nanocrystals. *J. Magn. Magn. Mater.* **2008**, *320*, e320–e323.

- (4) Hachani, R.; Lowdell, M.; Birchall, M.; Hervault, A.; Mertz, D.; Begin-Colin, S.; Thanh, N. T. K. Polyol Synthesis, Functionalisation, and Biocompatibility Studies of Superparamagnetic Iron Oxide Nanoparticles as Potential MRI Contrast Agents. *Nanoscale* **2016**, *8*, 3278–3287.
- (5) Kim, B. H.; Lee, N.; Kim, H.; An, K.; Park, Y. I.; Choi, Y.; Shin, K.; Lee, Y.; Kwon, S. G.; Na, H. B.; et al. Large-Scale Synthesis of Uniform and Extremely Small-Sized Iron Oxide Nanoparticles for High-Resolution  $T_1$  Magnetic Resonance Imaging Contrast Agents. *J. Am. Chem. Soc.* **2011**, *133*, 12624–12631.
- (6) Kucheryavy, P.; He, J.; John, V. T.; Maharjan, P.; Spinu, L.; Goloverda, G. Z.; Kolesnichenko, V. L. Superparamagnetic Iron Oxide Nanoparticles with Variable Size and an Iron Oxidation State as Prospective Imaging Agents. *Langmuir* **2013**, *29*, 710–716.
- (7) Lee, J.-H.; Huh, Y.-M.; Jun, Y.; Seo, J.; Jang, J.; Song, H.-T.; Kim, S.; Cho, E.-J.; Yoon, H.-G.; Suh, J.-S.; et al. Artificially Engineered Magnetic Nanoparticles for Ultra-Sensitive Molecular Imaging. *Nat. Med.* **2007**, *13*, 95–99.
- (8) Wan, J.; Cai, W.; Meng, X.; Liu, E. Monodisperse Water-Soluble Magnetite Nanoparticles Prepared by Polyol Process for High-Performance Magnetic Resonance Imaging. *Chem. Commun.* **2007**, No. 47, 5004–5006.
- (9) Ferguson, R. M.; Khandhar, A. P.; Kemp, S. J.; Arami, H.; Saritas, E. U.; Croft, L. R.; Konkle, J.; Goodwill, P. W.; Halkola, A.; Rahmer, J.; et al. Magnetic Particle Imaging With Tailored Iron Oxide Nanoparticle Tracers. *IEEE Trans. Med. Imaging* **2015**, *34*, 1077–1084.
- (10) Gleich, B.; Weizenecker, J. Tomographic Imaging Using the Nonlinear Response of Magnetic Particles. *Nature* **2005**, *435*, 1214–1217.
- (11) Knopp, T.; Buzug, T. M. *Magnetic Particle Imaging*; Springer Berlin Heidelberg: Berlin, Heidelberg, 2012.
- (12) Wu, L. C.; Zhang, Y.; Steinberg, G.; Qu, H.; Huang, S.; Cheng, M.; Bliss, T.; Du, F.; Rao, J.; Song, G.; et al. A Review of Magnetic Particle Imaging and Perspectives on Neuroimaging. *Am. J. Neuroradiol.* **2019**, *40*, 206–212.
- (13) Kolen'ko, Y. V.; Bañobre-López, M.; Rodríguez-Abreu, C.; Carbó-Argibay, E.; Sailsman, A.; Piñeiro-Redondo, Y.; Cerqueira, M. F.; Petrovykh, D. Y.; Kovnir, K.; Lebedev, O. I.; et al. Large-Scale Synthesis of Colloidal  $\text{Fe}_3\text{O}_4$  Nanoparticles Exhibiting High Heating Efficiency in Magnetic Hyperthermia. *J. Phys. Chem. C* **2014**, *118*, 8691–8701.
- (14) Deatsch, A. E.; Evans, B. A. Heating Efficiency in Magnetic Nanoparticle Hyperthermia. *J. Magn. Magn. Mater.* **2014**, *354*, 163–172.

- (15) Dutz, S.; Hergt, R. Magnetic Particle Hyperthermia—a Promising Tumour Therapy? *Nanotechnology* **2014**, *25*, 452001.
- (16) Fortin, J.-P.; Wilhelm, C.; Servais, J.; Ménager, C.; Bacri, J.-C.; Gazeau, F. Size-Sorted Anionic Iron Oxide Nanomagnets as Colloidal Mediators for Magnetic Hyperthermia. *J. Am. Chem. Soc.* **2007**, *129*, 2628–2635.
- (17) Hergt, R.; Dutz, S.; Röder, M. Effects of Size Distribution on Hysteresis Losses of Magnetic Nanoparticles for Hyperthermia. *J. Phys. Condens. Matter* **2008**, *20*, 385214.
- (18) Khandhar, A. P.; Ferguson, R. M.; Simon, J. A.; Krishnan, K. M. Enhancing Cancer Therapeutics Using Size-Optimized Magnetic Fluid Hyperthermia. *J. Appl. Phys.* **2012**, *111*, 07B306-1–3.
- (19) Laurent, S.; Dutz, S.; Häfeli, U. O.; Mahmoudi, M. Magnetic Fluid Hyperthermia: Focus on Superparamagnetic Iron Oxide Nanoparticles. *Adv. Colloid Interface Sci.* **2011**, *166*, 8–23.
- (20) Levy, M.; Quarta, A.; Espinosa, A.; Figuerola, A.; Wilhelm, C.; García-Hernández, M.; Genovese, A.; Falqui, A.; Alloyeau, D.; Buonsanti, R.; et al. Correlating Magneto-Structural Properties to Hyperthermia Performance of Highly Monodisperse Iron Oxide Nanoparticles Prepared by a Seeded-Growth Route. *Chem. Mater.* **2011**, *23*, 4170–4180.
- (21) Lv, Y.; Yang, Y.; Fang, J.; Zhang, H.; Peng, E.; Liu, X.; Xiao, W.; Ding, J. Size Dependent Magnetic Hyperthermia of Octahedral Fe<sub>3</sub>O<sub>4</sub> Nanoparticles. *RSC Adv* **2015**, *5*, 76764–76771.
- (22) Martinez-Boubeta, C.; Simeonidis, K.; Makridis, A.; Angelakeris, M.; Iglesias, O.; Guardia, P.; Cabot, A.; Yedra, L.; Estradé, S.; Peiró, F.; et al. Learning from Nature to Improve the Heat Generation of Iron-Oxide Nanoparticles for Magnetic Hyperthermia Applications. *Sci. Rep.* **2013**, *3*, 1652-1–8.
- (23) Ulbrich, K.; Holá, K.; Šubr, V.; Bakandritsos, A.; Tuček, J.; Zbořil, R. Targeted Drug Delivery with Polymers and Magnetic Nanoparticles: Covalent and Noncovalent Approaches, Release Control, and Clinical Studies. *Chem. Rev.* **2016**, *116*, 5338–5431.
- (24) Kang, T.; Li, F.; Baik, S.; Shao, W.; Ling, D.; Hyeon, T. Surface Design of Magnetic Nanoparticles for Stimuli-Responsive Cancer Imaging and Therapy. *Biomaterials* **2017**, *136*, 98–114.

- (25) Xie, J.; Liu, G.; Eden, H. S.; Ai, H.; Chen, X. Surface-Engineered Magnetic Nanoparticle Platforms for Cancer Imaging and Therapy. *Acc. Chem. Res.* **2011**, *44*, 883–892.
- (26) Espinosa, A.; Di Corato, R.; Kolosnjaj-Tabi, J.; Flaud, P.; Pellegrino, T.; Wilhelm, C. Duality of Iron Oxide Nanoparticles in Cancer Therapy: Amplification of Heating Efficiency by Magnetic Hyperthermia and Photothermal Bimodal Treatment. *ACS Nano* **2016**, *10*, 2436–2446.
- (27) Polshettiwar, V.; Luque, R.; Fihri, A.; Zhu, H.; Bouhrara, M.; Basset, J.-M. Magnetically Recoverable Nanocatalysts. *Chem. Rev.* **2011**, *111*, 3036–3075.
- (28) Sharma, R. K.; Dutta, S.; Sharma, S.; Zboril, R.; Varma, R. S.; Gawande, M. B. Fe<sub>3</sub>O<sub>4</sub> (Iron Oxide)-Supported Nanocatalysts: Synthesis, Characterization and Applications in Coupling Reactions. *Green Chem.* **2016**, *18*, 3184–3209.
- (29) Shylesh, S.; Schünemann, V.; Thiel, W. R. Magnetically Separable Nanocatalysts: Bridges between Homogeneous and Heterogeneous Catalysis. *Angew. Chem. Int. Ed.* **2010**, *49*, 3428–3459.
- (30) Xu, P.; Zeng, G. M.; Huang, D. L.; Feng, C. L.; Hu, S.; Zhao, M. H.; Lai, C.; Wei, Z.; Huang, C.; Xie, G. X.; et al. Use of Iron Oxide Nanomaterials in Wastewater Treatment: A Review. *Sci. Total Environ.* **2012**, *424*, 1–10.
- (31) Tang, S. C. N.; Lo, I. M. C. Magnetic Nanoparticles: Essential Factors for Sustainable Environmental Applications. *Water Res.* **2013**, *47*, 2613–2632.
- (32) Sun, S.; Zeng, H. Size-Controlled Synthesis of Magnetite Nanoparticles. *J. Am. Chem. Soc.* **2002**, *124*, 8204–8205.
- (33) Sun, S.; Zeng, H.; Robinson, D. B.; Raoux, S.; Rice, P. M.; Wang, S. X.; Li, G. Monodisperse MFe<sub>2</sub>O<sub>4</sub> (M = Fe, Co, Mn) Nanoparticles. *J. Am. Chem. Soc.* **2004**, *126*, 273–279.
- (34) Park, J.; An, K.; Hwang, Y.; Park, J.-G.; Noh, H.-J.; Kim, J.-Y.; Park, J.-H.; Hwang, N.-M.; Hyeon, T. Ultra-Large-Scale Syntheses of Monodisperse Nanocrystals. *Nat. Mater.* **2004**, *3*, 891–895.
- (35) Vreeland, E. C.; Watt, J.; Schober, G. B.; Hance, B. G.; Austin, M. J.; Price, A. D.; Fellows, B. D.; Monson, T. C.; Hudak, N. S.; Maldonado-Camargo, L.; et al. Enhanced Nanoparticle Size Control by Extending LaMer's Mechanism. *Chem. Mater.* **2015**, *27*, 6059–6066.
- (36) Kemp, S. J.; Ferguson, R. M.; Khandhar, A. P.; Krishnan, K. M. Monodisperse Magnetite Nanoparticles with Nearly Ideal Saturation Magnetization. *RSC Adv* **2016**, *6*, 77452–77464.

- (37) Unni, M.; Uhl, A. M.; Savliwala, S.; Savitzky, B. H.; Dhavalikar, R.; Garraud, N.; Arnold, D. P.; Kourkoutis, L. F.; Andrew, J. S.; Rinaldi, C. Thermal Decomposition Synthesis of Iron Oxide Nanoparticles with Diminished Magnetic Dead Layer by Controlled Addition of Oxygen. *ACS Nano* **2017**, *11*, 2284–2303.
- (38) Chen, R.; Christiansen, M. G.; Sourakov, A.; Mohr, A.; Matsumoto, Y.; Okada, S.; Jasanoff, A.; Anikeeva, P. High-Performance Ferrite Nanoparticles through Nonaqueous Redox Phase Tuning. *Nano Lett.* **2016**, *16*, 1345–1351.
- (39) Wetterskog, E.; Tai, C.-W.; Grins, J.; Bergström, L.; Salazar-Alvarez, G. Anomalous Magnetic Properties of Nanoparticles Arising from Defect Structures: Topotaxial Oxidation of  $\text{Fe}_{1-x}\text{O}|\text{Fe}_{3-\delta}\text{O}_4$  Core|Shell Nanocubes to Single-Phase Particles. *ACS Nano* **2013**, *7*, 7132–7144.
- (40) Kwon, S. G.; Piao, Y.; Park, J.; Angappane, S.; Jo, Y.; Hwang, N.-M.; Park, J.-G.; Hyeon, T. Kinetics of Monodisperse Iron Oxide Nanocrystal Formation by “Heating-Up” Process. *J. Am. Chem. Soc.* **2007**, *129*, 12571–12584.
- (41) Pérez, N.; López-Calhorra, F.; Labarta, A.; Batlle, X. Reduction of Iron by Decarboxylation in the Formation of Magnetite Nanoparticles. *Phys. Chem. Chem. Phys.* **2011**, *13*, 19485.
- (42) Feld, A.; Weimer, A.; Kornowski, A.; Winckelmans, N.; Merkl, J.-P.; Kloust, H.; Zierold, R.; Schmidke, C.; Schotten, T.; Riedner, M.; et al. Chemistry of Shape-Controlled Iron Oxide Nanocrystal Formation. *ACS Nano* **2019**, *13*, 152–162.
- (43) Shavel, A.; Liz-Marzán, L. Shape Control of Iron Oxide Nanoparticles. *Phys. Chem. Chem. Phys.* **2009**, *11*, 3607.
- (44) Hai, H. T.; Kura, H.; Takahashi, M.; Ogawa, T. Facile Synthesis of  $\text{Fe}_3\text{O}_4$  Nanoparticles by Reduction Phase Transformation from  $\gamma\text{-Fe}_2\text{O}_3$  Nanoparticles in Organic Solvent. *J. Colloid Interface Sci.* **2010**, *341*, 194–199.
- (45) Hai, H. T.; Yang, H. T.; Kura, H.; Hasegawa, D.; Ogata, Y.; Takahashi, M.; Ogawa, T. Size Control and Characterization of Wustite (Core)/Spinel (Shell) Nanocubes Obtained by Decomposition of Iron Oleate Complex. *J. Colloid Interface Sci.* **2010**, *346*, 37–42.
- (46) Ito, D.; Yokoyama, S.; Zaikova, T.; Masuko, K.; Hutchison, J. E. Synthesis of Ligand-Stabilized Metal Oxide Nanocrystals and Epitaxial Core/Shell Nanocrystals via a Lower-Temperature Esterification Process. *ACS Nano* **2014**, *8*, 64–75.

- (47) Jansons, A. W.; Hutchison, J. E. Continuous Growth of Metal Oxide Nanocrystals: Enhanced Control of Nanocrystal Size and Radial Dopant Distribution. *ACS Nano* **2016**, *10*, 6942–6951.
- (48) Plummer, L. K.; Crockett, B. M.; Pennel, M. L.; Jansons, A. W.; Koskela, K. M.; Hutchison, J. E. Influence of Monomer Flux and Temperature on Morphology of Indium Oxide Nanocrystals during a Continuous Growth Synthesis. *Chem. Mater.* **2019**, *31*, 7638–7649.
- (49) Jansons, A. W.; Koskela, K. M.; Crockett, B. M.; Hutchison, J. E. Transition Metal-Doped Metal Oxide Nanocrystals: Efficient Substitutional Doping through a Continuous Growth Process. *Chem. Mater.* **2017**, *29*, 8167–8176.
- (50) Crockett, B. M.; Jansons, A. W.; Koskela, K. M.; Johnson, D. W.; Hutchison, J. E. Radial Dopant Placement for Tuning Plasmonic Properties in Metal Oxide Nanocrystals. *ACS Nano* **2017**, *11*, 7719–7728.
- (51) Cooper, S. R.; Plummer, L. K.; Cosby, A. G.; Lenox, P.; Jander, A.; Dhagat, P.; Hutchison, J. E. Insights into the Magnetic Properties of Sub-10 nm Iron Oxide Nanocrystals through the Use of a Continuous Growth Synthesis. *Chem. Mater.* **2018**, *30*, 6053–6062.
- (52) Shavel, A.; Rodríguez-González, B.; Pacifico, J.; Spasova, M.; Farle, M.; Liz-Marzán, L. M. Shape Control in Iron Oxide Nanocrystal Synthesis, Induced by Trioctylammonium Ions. *Chem. Mater.* **2009**, *21*, 1326–1332.
- (53) Kovalenko, M. V.; Bodnarchuk, M. I.; Lechner, R. T.; Hesser, G.; Schäffler, F.; Heiss, W. Fatty Acid Salts as Stabilizers in Size- and Shape-Controlled Nanocrystal Synthesis: The Case of Inverse Spinel Iron Oxide. *J. Am. Chem. Soc.* **2007**, *129*, 6352–6353.
- (54) Ge, W.; Sato, R.; Wu, H.-L.; Teranishi, T. Simple Surfactant Concentration-Dependent Shape Control of Polyhedral Fe<sub>3</sub>O<sub>4</sub> Nanoparticles and Their Magnetic Properties. *ChemPhysChem* **2015**, *16*, 3200–3205.
- (55) Zhou, Z.; Zhu, X.; Wu, D.; Chen, Q.; Huang, D.; Sun, C.; Xin, J.; Ni, K.; Gao, J. Anisotropic Shaped Iron Oxide Nanostructures: Controlled Synthesis and Proton Relaxation Shortening Effects. *Chem. Mater.* **2015**, *27*, 3505–3515.
- (56) Bronstein, L. M.; Huang, X.; Retrum, J.; Schmucker, A.; Pink, M.; Stein, B. D.; Dragnea, B. Influence of Iron Oleate Complex Structure on Iron Oxide Nanoparticle Formation. *Chem. Mater.* **2007**, *19*, 3624–3632.
- (57) Balakrishnan, T.; Lee, M.-J.; Dey, J.; Choi, S.-M. Sub-Nanometer Scale Size-Control of Iron Oxide Nanoparticles with Drying Time of Iron Oleate. *CrystEngComm* **2019**, *21*, 4063–4071.

- (58) Xu, Z.; Shen, C.; Tian, Y.; Shi, X.; Gao, H.-J. Organic Phase Synthesis of Monodisperse Iron Oxide Nanocrystals Using Iron Chloride as Precursor. *Nanoscale* **2010**, *2*, 1027.
- (59) Sutton, C. C. R.; da Silva, G.; Franks, G. V. Modeling the IR Spectra of Aqueous Metal Carboxylate Complexes: Correlation between Bonding Geometry and Stretching Mode Wavenumber Shifts. *Chem. - Eur. J.* **2015**, *21*, 6801–6805.
- (60) Weber, B.; Betz, R.; Bauer, W.; Schlamp, S. Crystal Structure of Iron (II) Acetate. *Z. Für Anorg. Allg. Chem.* **2011**, *637*, 102–107.
- (61) Chang, H.; Kim, B. H.; Jeong, H. Y.; Moon, J. H.; Park, M.; Shin, K.; Chae, S. I.; Lee, J.; Kang, T.; Choi, B. K.; et al. Molecular-Level Understanding of Continuous Growth from Iron-Oxo Clusters to Iron Oxide Nanoparticles. *J. Am. Chem. Soc.* **2019**, *141*, 7037–7045.
- (62) Long, G. J.; Robinson, W. T.; Tappmeyer, W. P.; Bridges, D. L. The Magnetic, Electronic, and Mössbauer Spectral Properties of Several Trinuclear Iron (III) Carboxylate Complexes. *J. Chem. Soc. Dalton Trans.* **1973**, No. 6, 573–579.
- (63) Fleet, M. E. The Structure of Magnetite. *Acta Crystallogr. B* **1981**, *37*, 917–920.
- (64) Tang, J.; Myers, M.; Bosnick, K. A.; Brus, L. E. Magnetite Fe<sub>3</sub>O<sub>4</sub> Nanocrystals: Spectroscopic Observation of Aqueous Oxidation Kinetics. *J. Phys. Chem. B* **2003**, *107*, 7501–7506.
- (65) Li, L.; Yang, Y.; Ding, J.; Xue, J. Synthesis of Magnetite Nanoctahedra and Their Magnetic Field-Induced Two-/Three-Dimensional Superstructure. *Chem. Mater.* **2010**, *22*, 3183–3191.
- (66) Zhang, L.; Wu, J.; Liao, H.; Hou, Y.; Gao, S. Octahedral Fe<sub>3</sub>O<sub>4</sub> Nanoparticles and Their Assembled Structures. *Chem. Commun.* **2009**, No. 29, 4378.
- (67) Ringe, E.; Van Duyne, R. P.; Marks, L. D. Kinetic and Thermodynamic Modified Wulff Constructions for Twinned Nanoparticles. *J. Phys. Chem. C* **2013**, *117*, 15859–15870.
- (68) Nasilowski, M.; Mahler, B.; Lhuillier, E.; Ithurria, S.; Dubertret, B. Two-Dimensional Colloidal Nanocrystals. *Chem. Rev.* **2016**, *116*, 10934–10982.
- (69) Rečnik, A.; Nyirő-Kósa, I.; Dódony, I.; Pósfa, M. Growth Defects and Epitaxy in Fe<sub>3</sub>O<sub>4</sub> and γ-Fe<sub>2</sub>O<sub>3</sub> Nanocrystals. *CrystEngComm* **2013**, *15*, 7539.

- (70) Wei, R.; Zhou, T.; Sun, C.; Lin, H.; Yang, L.; Ren, B. W.; Chen, Z.; Gao, J. Iron-Oxide-Based Twin Nanoplates with Strong  $T_2$  Relaxation Shortening for Contrast-Enhanced Magnetic Resonance Imaging. *Nanoscale* **2018**, *10*, 18398–18406.
- (71) Xiong, Y.; McLellan, J. M.; Chen, J.; Yin, Y.; Li, Z.-Y.; Xia, Y. Kinetically Controlled Synthesis of Triangular and Hexagonal Nanoplates of Palladium and Their SPR/SERS Properties. *J. Am. Chem. Soc.* **2005**, *127*, 17118–17127.
- (72) Cooper, S. R. Understanding Size-Dependent Structure and Properties of Spinel Iron Oxide Nanocrystals Under 10 nm in Diameter. PhD, University of Oregon, Eugene, OR, 2018.
- (73) Zhang, H.; De Yoreo, J. J.; Banfield, J. F. A Unified Description of Attachment-Based Crystal Growth. *ACS Nano* **2014**, *8*, 6526–6530.
- (74) Gilks, D.; Nedelkoski, Z.; Lari, L.; Kuerbanjiang, B.; Matsuzaki, K.; Susaki, T.; Kepaptsoglou, D.; Ramasse, Q.; Evans, R.; McKenna, K.; et al. Atomic and Electronic Structure of Twin Growth Defects in Magnetite. *Sci. Rep.* **2016**, *6*, 20943.
- (75) Daneu, N.; Rečnik, A.; Yamazaki, T.; Dolenec, T. Structure and Chemistry of (111) Twin Boundaries in MgAl<sub>2</sub>O<sub>4</sub> Spinel Crystals from Mogok. *Phys. Chem. Miner.* **2007**, *34*, 233–247.
- (76) Cornell, R. M.; Schwertmann, U. *The Iron Oxides: Structure, Properties, Reactions, Occurrence and Uses*; VCH Publishers: New York, 1996.
- (77) Kim, D.; Lee, N.; Park, M.; Kim, B. H.; An, K.; Hyeon, T. Synthesis of Uniform Ferrimagnetic Magnetite Nanocubes. *J. Am. Chem. Soc.* **2009**, *131*, 454–455.
- (78) van Rijssel, J.; Kuipers, B. W. M.; Erné, B. H. Non-Regularized Inversion Method from Light Scattering Applied to Ferrofluid Magnetization Curves for Magnetic Size Distribution Analysis. *J. Magn. Magn. Mater.* **2014**, *353*, 110–115.
- (79) van Rijssel, J.; Kuipers, B. W. M.; Erné, B. H. Bimodal Distribution of the Magnetic Dipole Moment in Nanoparticles with a Monomodal Distribution of the Physical Size. *J. Magn. Magn. Mater.* **2015**, *380*, 325–329.
- (80) Wang, H.; Shrestha, T. B.; Basel, M. T.; Pyle, M.; Toledo, Y.; Konecny, A.; Thapa, P.; Ikenberry, M.; Hohn, K. L.; Chikan, V.; et al. Hexagonal Magnetite Nanoprisms: Preparation, Characterization and Cellular Uptake. *J. Mater. Chem. B* **2015**, *3*, 4647–4653.
- (81) Liu, M.; Wang, L.; Lu, G.; Yao, X.; Guo, L. Twins in Cd<sub>1-x</sub>Zn<sub>x</sub>S Solid Solution: Highly Efficient Photocatalyst for Hydrogen Generation from Water. *Energy Environ. Sci.* **2011**, *4*, 1372.

- (82) Kumar, M.; Deka, S. Multiply Twinned AgNi Alloy Nanoparticles as Highly Active Catalyst for Multiple Reduction and Degradation Reactions. *ACS Appl. Mater. Interfaces* **2014**, *6*, 16071–16081.
- (83) Wang, S.-B.; Min, Y.-L.; Yu, S.-H. Synthesis and Magnetic Properties of Uniform Hematite Nanocubes. *J. Phys. Chem. C* **2007**, *111*, 3551–3554.
- (84) Pullar, R. C. Hexagonal Ferrites: A Review of the Synthesis, Properties and Applications of Hexaferrite Ceramics. *Prog. Mater. Sci.* **2012**, *57*, 1191–1334.
- (85) Woehrle, G. H.; Hutchison, J. E.; Zkar, S. O.; Finke, R. G. Analysis of Nanoparticle Transmission Electron Microscopy Data Using a Public- Domain Image-Processing Program, Image. *Turk. J. Chem.* **2006**, *30*, 1–13.
- (86) Ilavsky, J.; Jemian, P. R. *Irena* : Tool Suite for Modeling and Analysis of Small- Angle Scattering. *J. Appl. Crystallogr.* **2009**, *42*, 347–353.

## Chapter V

- (1) Kolhatkar, A.; Jamison, A.; Litvinov, D.; Willson, R.; Lee, T. Tuning the Magnetic Properties of Nanoparticles. *Int. J. Mol. Sci.* **2013**, *14*, 15977–16009.
- (2) Speliotis, D. E. Magnetic Recording beyond the First 100 Years. *J. Magn. Magn. Mater.* **1999**, *193*, 29–35.
- (3) Lim, E.-K.; Kim, T.; Paik, S.; Haam, S.; Huh, Y.-M.; Lee, K. Nanomaterials for Theranostics: Recent Advances and Future Challenges. *Chem. Rev.* **2015**, *115*, 327–394.
- (4) Lee, N.; Yoo, D.; Ling, D.; Cho, M. H.; Hyeon, T.; Cheon, J. Iron Oxide Based Nanoparticles for Multimodal Imaging and Magnetoresponsive Therapy. *Chem. Rev.*, **2015**, *115*, 10637–10689.
- (5) Laurent, S.; Dutz, S.; Häfeli, U. O.; Mahmoudi, M. Magnetic Fluid Hyperthermia: Focus on Superparamagnetic Iron Oxide Nanoparticles. *Adv. Colloid Interface Sci.*, **2011**, *166*, 8–23.
- (6) Krishnan, K. M.; Pakhomov, A. B.; Bao, Y.; Blomqvist, P.; Chun, Y.; Gonzales, M.; Griffin, K.; Ji, X.; Roberts, B. K. Nanomagnetism and Spin Electronics: Materials, Microstructure and Novel Properties. *J. Mater. Sci.* **2006**, *41*, 793–815.
- (7) Auffan, M.; Rose, J.; Bottero, J.-Y.; Lowry, G. V.; Jolivet, J.-P.; Wiesner, M. R. Towards a Definition of Inorganic Nanoparticles from an Environmental, Health and Safety Perspective. *Nat. Nanotechnol.* **2009**, *4*, 634–641.

- (8) Roduner, E. Size Matters : Why Nanomaterials Are Different. *Chem. Soc. Rev.* **2006**, *35*, 583–592.
- (9) Auffan, M.; Rose, J.; Proux, O.; Borschneck, D.; Masion, A.; Chaurand, P.; Hazemann, J.-L.; Chaneac, C.; Jolivet, J.-P.; Wiesner, M. R.; *et al.* Enhanced Adsorption of Arsenic onto Maghemites Nanoparticles: As(III) as a Probe of the Surface Structure and Heterogeneity. *Langmuir* **2008**, *24*, 3215–3222.
- (10) Park, J.; An, K.; Hwang, Y.; Park, J.-G.; Noh, H.-J.; Kim, J.-Y.; Park, J.-H.; Hwang, N.-M.; Hyeon, T. Ultra-Large-Scale Syntheses of Monodisperse Nanocrystals. *Nat. Mater.* **2004**, *3*, 891–895.
- (11) Lak, A.; Kraken, M.; Ludwig, F.; Kornowski, A.; Eberbeck, D.; Sievers, S.; Litterst, F. J.; Weller, H.; Schilling, M. Size Dependent Structural and Magnetic Properties of FeO–Fe<sub>3</sub>O<sub>4</sub> Nanoparticles. *Nanoscale* **2013**, *5*, 12286–12295.
- (12) Wetterskog, E.; Tai, C. W.; Grins, J.; Bergström, L.; Salazar-Alvarez, G. Anomalous Magnetic Properties of Nanoparticles Arising from Defect Structures: Topotaxial Oxidation of Fe<sub>1-x</sub>O|Fe<sub>3-s</sub>O<sub>4</sub> Core|shell Nanocubes to Single-Phase Particles. *ACS Nano* **2013**, *7*, 7132–7144.
- (13) Pichon, B. P.; Gerber, O.; Lefevre, C.; Florea, I.; Fleutot, S.; Baaziz, W.; Pauly, M.; Ohlmann, M.; Ulhaq, C.; Ersen, O.; *et al.* Microstructural and Magnetic Investigations of Wüstite-Spinel Core-Shell Cubic-Shaped Nanoparticles. *Chem. Mater.* **2011**, *23*, 2886–2900.
- (14) Estrader, M.; López-Ortega, A.; Golosovsky, I. V.; Estradé, S.; Roca, A. G.; Salazar-Alvarez, G.; López-Conesa, L.; Tobia, D.; Winkler, E.; Ardisson, J. D.; *et al.* Origin of the Large Dispersion of Magnetic Properties in Nanostructured Oxides: Fe<sub>x</sub>O/Fe<sub>3</sub>O<sub>4</sub> Nanoparticles as a Case Study. *Nanoscale* **2015**, *7*, 3002–3015.
- (15) Millan, A.; Urtizberea, A.; Silva, N. J. O.; Palacio, F.; Amaral, V. S.; Snoeck, E.; Serin, V. Surface Effects in Maghemite Nanoparticles. *J. Magn. Magn. Mater.* **2007**, *312*, L5–L9.
- (16) Mohapatra, J.; Mitra, A.; Bahadur, D.; Aslam, M. Surface Controlled Synthesis of MFe<sub>2</sub>O<sub>4</sub> (M = Mn, Fe, Co, Ni and Zn) Nanoparticles and Their Magnetic Characteristics. *CrystEngComm* **2013**, *15*, 524–532.
- (17) Roca, A. G.; Niznansky, D.; Poltierova-Vejpravova, J.; Bittova, B.; González-Fernández, M. A.; Serna, C. J.; Morales, M. P. Magnetite Nanoparticles with No Surface Spin Canting. *J. Appl. Phys.* **2009**, *105*, 114309.

- (18) Tronc, E.; Ezzir, A.; Cherkaoui, R.; Chanéac, C.; Noguès, M.; Kachkachi, H.; Fiorani, D.; Testa, A. M.; Grenèche, J. M.; Jolivet, J. P. Surface-Related Properties of  $\gamma$ -Fe<sub>2</sub>O<sub>3</sub> Nanoparticles. *J. Magn. Magn. Mater.* **2000**, *221*, 63–79.
- (19) Vestal, C. R.; Zhang, Z. J. Effects of Surface Coordination Chemistry on the Magnetic Properties of MnFe<sub>2</sub>O<sub>4</sub> Spinel Ferrite Nanoparticles. *J. Am. Chem. Soc.* **2003**, *125*, 9828–9833.
- (20) Daou, T. J.; Grenèche, J. M.; Pourroy, G.; Buathong, S.; Derory, A.; Ulhaq-Bouillet, C.; Donnio, B.; Guillon, D.; Begin-Colin, S. Coupling Agent Effect on Magnetic Properties of Functionalized Magnetite-Based Nanoparticles. *Chem. Mater.* **2008**, *20*, 5869–5875.
- (21) Demortière, A.; Panissod, P.; Pichon, B. P.; Pourroy, G.; Guillon, D.; Donnio, B.; Bégin-Colin, S. Size-Dependent Properties of Magnetic Iron Oxidenanocrystals. *Nanoscale* **2011**, *3*, 225–232.
- (22) Lee, J.; Kwon, S. G.; Park, J.-G.; Hyeon, T. Size Dependence of Metal–Insulator Transition in Stoichiometric Fe<sub>3</sub>O<sub>4</sub> Nanocrystals. *Nano Lett.* **2015**, *15*, 4337–4342.
- (23) Kim, B. H.; Lee, N.; Kim, H.; An, K.; Park, Y. I.; Choi, Y.; Shin, K.; Lee, Y.; Kwon, S. G.; Na, H. B.; *et al.* Large-Scale Synthesis of Uniform and Extremely Small-Sized Iron Oxide Nanoparticles for High-Resolution T<sub>1</sub> Magnetic Resonance Imaging Contrast Agents. *J. Am. Chem. Soc.* **2011**, *133*, 12624–12631.
- (24) Martínez-Boubeta, C.; Simeonidis, K.; Angelakeris, M.; Pazos-Pérez, N.; Giersig, M.; Delimitis, A.; Nalbandian, L.; Alexandrakis, V.; Niarchos, D. Critical Radius for Exchange Bias in Naturally Oxidized Fe Nanoparticles. *Phys. Rev. B* **2006**, *74*, 054430.
- (25) Salazar-Alvarez, G.; Qin, J.; Šepelák, V.; Bergmann, I.; Vasilakaki, M.; Trohidou, K. N.; Ardisson, J. D.; Macedo, W. A. A.; Mikhaylova, M.; Muhammed, M.; *et al.* Cubic versus Spherical Magnetic Nanoparticles: The Role of Surface Anisotropy. *J. Am. Chem. Soc.* **2008**, *130*, 13234–13239.
- (26) Mitra, A.; Mohapatra, J.; Meena, S. S.; Tomy, C. V.; Aslam, M. Verwey Transition in Ultrasmall-Sized Octahedral Fe<sub>3</sub>O<sub>4</sub> Nanoparticles. *J. Phys. Chem. C* **2014**, *118*, 19356–19362.
- (27) Zhou, Z.; Zhu, X.; Wu, D.; Chen, Q.; Huang, D.; Sun, C.; Xin, J.; Ni, K.; Gao, J. Anisotropic Shaped Iron Oxide Nanostructures: Controlled Synthesis and Proton Relaxation Shortening Effects. *Chem. Mater.* **2015**, *27*, 3505–3515.
- (28) Ge, W.; Sato, R.; Wu, H.-L.; Teranishi, T. Simple Surfactant Concentration-Dependent Shape Control of Polyhedral Fe<sub>3</sub>O<sub>4</sub> Nanoparticles and Their Magnetic Properties. *ChemPhysChem* **2015**, *16*, 3200–3205.

- (29) Fortin, J. P.; Wilhelm, C.; Servais, J.; Ménager, C.; Bacri, J. C.; Gazeau, F. Size-Sorted Anionic Iron Oxide Nanomagnets as Colloidal Mediators for Magnetic Hyperthermia. *J. Am. Chem. Soc.* **2007**, *129*, 2628–2635.
- (30) Deatsch, A. E.; Evans, B. A. Heating Efficiency in Magnetic Nanoparticle Hyperthermia. *J. Magn. Magn. Mater.* **2014**, *354*, 163–172.
- (31) Yavuz, C. T.; Mayo, J. T.; Yu, W. W.; Prakash, A.; Falkner, J. C.; Yean, S.; Cong, L.; Shipley, H. J.; Kan, A.; Tomson, M.; *et al.* Low-Field Magnetic Separation of Monodisperse  $\text{Fe}_3\text{O}_4$  Nanocrystals. *Science* **2006**, *314*, 964–968.
- (32) Guardia, P.; Pérez, N.; Labarta, A.; Batlle, X. Controlled Synthesis of Iron Oxide Nanoparticles over a Wide Size Range. *Langmuir* **2010**, *26*, 5843–5847.
- (33) Unni, M.; Uhl, A. M.; Savliwala, S.; Savitzky, B. H.; Dhavalikar, R.; Garraud, N.; Arnold, D. P.; Kourkoutis, L. F.; Andrew, J. S.; Rinaldi, C. Thermal Decomposition Synthesis of Iron Oxide Nanoparticles with Diminished Magnetic Dead Layer by Controlled Addition of Oxygen. *ACS Nano* **2017**, *11*, 2284–2303.
- (34) Santoyo Salazar, J.; Perez, L.; de Abril, O.; Truong Phuoc, L.; Ihiawakrim, D.; Vazquez, M.; Gremche, J.-M.; Begin-Colin, S.; Pourroy, G. Magnetic Iron Oxide Nanoparticles in 10–40 Nm Range: Composition in Terms of Magnetite/Maghemite Ratio and Effect on the Magnetic Properties. *Chem. Mater.* **2011**, *23*, 1379–1386.
- (35) Signorini, L.; Pasquini, L.; Savini, L.; Carboni, R.; Boscherini, F.; Bonetti, E.; Giglia, A.; Pedio, M.; Mahne, N.; *et al.* Size-Dependent Oxidation in Iron/iron Oxide Core-Shell Nanoparticles. *Phys. Rev. B* **2003**, *68*, 195423.
- (36) Luigjes, B.; Woudenberg, S. M. C.; de Groot, R.; Meeldijk, J. D.; Torres Galvis, H. M.; de Jong, K. P.; Philipse, A. P.; Erné, B. H. Diverging Geometric and Magnetic Size Distributions of Iron Oxide Nanocrystals. *J. Phys. Chem. C* **2011**, *115*, 14598–14605.
- (37) Chen, R.; Christiansen, M. G.; Sourakov, A.; Mohr, A.; Matsumoto, Y.; Okada, S.; Jasanoff, A.; Anikeeva, P. High-Performance Ferrite Nanoparticles through Nonaqueous Redox Phase Tuning. *Nano Lett.* **2016**, *16*, 1345–1351.
- (38) Vreeland, E. C.; Watt, J.; Schober, G. B.; Hance, B. G.; Austin, M. J.; Price, A. D.; Fellows, B. D.; Monson, T. C.; Hudak, N. S.; Maldonado-Camargo, L.; *et al.* Enhanced Nanoparticle Size Control by Extending LaMer’s Mechanism. *Chem. Mater.* **2015**, *27*, 6059–6066.

- (39) Caruntu, D.; Caruntu, G.; O'Connor, C. J. Magnetic Properties of Variable-Sized  $\text{Fe}_3\text{O}_4$  Nanoparticles Synthesized from Non-Aqueous Homogeneous Solutions of Polyols. *J. Phys. D. Appl. Phys.* **2007**, *40*, 5801–5809.
- (40) Park, B.; Kim, B. H.; Yu, T. Synthesis of Spherical and Cubic Magnetic Iron Oxide Nanocrystals at Low Temperature in Air. *J. Colloid Interface Sci.* **2018**, *518*, 27–33.
- (41) Dehsari, H. S.; Heidari, M.; Ribeiro, A. H.; Tremel, W.; Jakob, G.; Donadio, D.; Potestio, R.; Asadi, K. Combined Experimental and Theoretical Investigation of Heating Rate on Growth of Iron Oxide Nanoparticles. *Chem. Mater.* **2017**, *29*, 9648–9656.
- (42) Yun, H.; Liu, X.; Paik, T.; Palanisamy, D.; Kim, J.; Vogel, W. D.; Viescas, A. J.; Chen, J.; Papaefthymiou, G. C.; Kikkawa, J. M.; *et al.* Size- and Composition-Dependent Radio Frequency Magnetic Permeability of Iron Oxide Nanocrystals. *ACS Nano* **2014**, *8*, 12323–12337.
- (43) Baaziz, W.; Pichon, B. P.; Fleutot, S.; Liu, Y.; Lefevre, C.; Greneche, J.-M.; Toumi, M.; Mhiri, T.; Begin-Colin, S. Magnetic Iron Oxide Nanoparticles: Reproducible Tuning of the Size and Nanosized-Dependent Composition, Defects, and Spin Canting. *J. Phys. Chem. C* **2014**, *118*, 3795–3810.
- (44) Taniguchi, T.; Nakagawa, K.; Watanabe, T.; Matsushita, N.; Yoshimura, M. Hydrothermal Growth of Fatty Acid Stabilized Iron Oxide Nanocrystals. *J. Phys. Chem. C* **2009**, *113*, 839–843.
- (45) Castellanos-Rubio, I.; Insauti, M.; Garaio, E.; Gil de Muro, I.; Plazaola, F.; Rojo, T.; Lezama, L.  $\text{Fe}_3\text{O}_4$  Nanoparticles Prepared by the Seeded-Growth Route for Hyperthermia: Electron Magnetic Resonance as a Key Tool to Evaluate Size Distribution in Magnetic Nanoparticles. *Nanoscale* **2014**, *6*, 7542–7552.
- (46) Coey, J. M. D. Noncollinear Spin Arrangement in Ultrafine Ferrimagnetic Crystallites. *Phys. Rev. Lett.* **1971**, *27*, 1140–1142.
- (47) Dutta, P.; Pal, S.; Seehra, M. S.; Shah, N.; Huffman, G. P. Size Dependence of Magnetic Parameters and Surface Disorder in Magnetite Nanoparticles. *J. Appl. Phys.* **2009**, *105*, 07B501.
- (48) Bronstein, L. M.; Huang, X.; Retrum, J.; Schmucker, A.; Pink, M.; Stein, B. D.; Dragnea, B. Influence of Iron Oleate Complex Structure on Iron Oxide Nanoparticle Formation. *Chem. Mater.* **2007**, *19*, 3624–3632.
- (49) Kemp, S. J.; Ferguson, R. M.; Khandhar, A. P.; Krishnan, K. M. Monodisperse Magnetite Nanoparticles with Nearly Ideal Saturation Magnetization. *RSC Adv.* **2016**, *6*, 77452–77464.

- (50) Pérez, N.; López-Calahorra, F.; Labarta, A.; Batlle, X. Reduction of Iron by Decarboxylation in the Formation of Magnetite Nanoparticles. *Phys. Chem. Chem. Phys.* **2011**, *13*, 19485–19489.
- (51) Kwon, S. G.; Piao, Y.; Park, J.; Angappane, S.; Jo, Y.; Hwang, N.-M.; Park, J.-G.; Hyeon, T. Kinetics of Monodisperse Iron Oxide Nanocrystal Formation by “Heating-Up” Process. *J. Am. Chem. Soc.* **2007**, *129*, 12571–12584.
- (52) Hai, H. T.; Kura, H.; Takahashi, M.; Ogawa, T. Facile Synthesis of Fe<sub>3</sub>O<sub>4</sub> Nanoparticles by Reduction Phase Transformation from γ-Fe<sub>2</sub>O<sub>3</sub> Nanoparticles in Organic Solvent. *J. Colloid Interface Sci.* **2010**, *341*, 194–199.
- (53) Ito, D.; Yokoyama, S.; Zaikova, T.; Masuko, K.; Hutchison, J. E. Synthesis of Ligand-Stabilized Metal Oxide Nanocrystals and Epitaxial Core/Shell Nanocrystals via a Lower-Temperature Esterification Process. *ACS Nano* **2014**, *8*, 64–75.
- (54) Jansons, A. W.; Hutchison, J. E. Continuous Growth of Metal Oxide Nanocrystals: Enhanced Control of Nanocrystal Size and Radial Dopant Distribution. *ACS Nano* **2016**, *10*, 6942–6951.
- (55) Crockett, B. M.; Jansons, A. W.; Koskela, K. M.; Johnson, D. W.; Hutchison, J. E. Radial Dopant Placement for Tuning Plasmonic Properties in Metal Oxide Nanocrystals. *ACS Nano* **2017**, *11*, 7719–7728.
- (56) Tang, J.; Myers, M.; Bosnick, K. A.; Brus, L. E. Magnetite Fe<sub>3</sub>O<sub>4</sub> Nanocrystals: Spectroscopic Observation of Aqueous Oxidation Kinetics. *J. Phys. Chem. B* **2003**, *107*, 7501–7506.
- (57) Jansons, A. W.; Plummer, L. K.; Hutchison, J. E. Living Nanocrystals. *Chem. Mater.* **2017**, *29*, 5415–5425.
- (58) Fleet, M. E. The Structure of Magnetite. *Acta Cryst.* **1981**, *B37*, 917–920.
- (59) Annersten, H.; Hafner, S. S. Vacancy Distribution in Synthetic Spinels of the Series Fe<sub>3</sub>O<sub>4</sub>—γ-Fe<sub>2</sub>O<sub>3</sub>. *Zeitschrift für Krist.* **1973**, *137*, 321–340.
- (60) Grau-Crespo, R.; Al-Baitai, A. Y.; Saadoune, I.; De Leeuw, N. H. Vacancy Ordering and Electronic Structure of γ-Fe<sub>2</sub>O<sub>3</sub> (Maghemite): A Theoretical Investigation. *J. Phys. Condens. Matter* **2010**, *22*, 255401.
- (61) Chantrell, R. W.; Popplewell, J.; Charles, S. W. Measurement of Particle Size Distribution Parameters in Ferrofluids. *IEEE Trans. Magn.* **1978**, *MAG-14*, 975–977.

- (62) Cornell, R. M.; Schwertmann, U. *The Iron Oxides: Structure, Properties, Reactions, Occurrences, and Uses*; 2nd ed.; Wiley-VCH: Weinheim, 2003.
- (63) Huber, D. L. Synthesis, Properties, and Applications of Iron Nanoparticles. *Small* **2005**, *1*, 482–501.
- (64) Hyeon, T. Chemical Synthesis of Magnetic Nanoparticles. *Chem. Commun.* **2003**, 927–934.
- (65) Levy, M.; Quarta, A.; Espinosa, A.; Figuerola, A.; Wilhelm, C.; García-Hernández, M.; Genovese, A.; Falqui, A.; Alloyeau, D.; Buonsanti, R.; *et al.* Correlating Magneto-Structural Properties to Hyperthermia Performance of Highly Monodisperse Iron Oxide Nanoparticles Prepared by a Seeded-Growth Route. *Chem. Mater.* **2011**, *23*, 4170–4180.
- (66) Pacakova, B.; Kubickova, S.; Salas, G.; Mantlikova, A. R.; Marciello, M.; Morales, M. P.; Niznansky, D.; Vejpravova, J. The Internal Structure of Magnetic Nanoparticles Determines the Magnetic Response. *Nanoscale* **2017**, *9*, 5129–5140.
- (67) Gordon, T. R.; Cargnello, M.; Paik, T.; Mangolini, F.; Weber, R. T.; Fornasiero, P.; Murray, C. B. Nonaqueous Synthesis of TiO<sub>2</sub> Nanocrystals Using TiF<sub>4</sub> to Engineer Morphology, Oxygen Vacancy Concentration, and Photocatalytic Activity. *J. Am. Chem. Soc.* **2012**, *134*, 6751–6761.
- (68) Vioux, A. Nonhydrolytic Sol-Gel Routes to Oxides. *Chem. Mater.* **1997**, *9*, 2292–2299.
- (69) Niederberger, M. Nonaqueous Sol–Gel Routes to Metal Oxide Nanoparticles. *Acc. Chem. Res.* **2007**, *40*, 793–800.
- (70) Chen, Y.; Kim, M.; Lian, G.; Johnson, M. B.; Peng, X. Side Reactions in Controlling the Quality, Yield, and Stability of High Quality Colloidal Nanocrystals. *J. Am. Chem. Soc.* **2005**, *127*, 13331–13337.
- (71) Linderoth, S.; Hendriksen, P. V.; Bødker, F.; Wells, S.; Davies, K.; Charles, S. W.; Mørup, S. On Spin-Canting in Maghemite Particles. *J. Appl. Phys.* **1994**, *75*, 6583–6585.
- (72) Nguyen, T.-D. From Formation Mechanisms to Synthetic Methods toward Shape-Controlled Oxide Nanoparticles. *Nanoscale* **2013**, *5*, 9455–9482.
- (73) Schindelin, J.; Arganda-Carreras, I.; Frise, E.; Kaynig, V.; Longair, M.; Pietzsch, T.; Preibisch, S.; Rueden, C.; Saalfeld, S.; Schmid, B.; *et al.* Fiji: An Open-Source Platform for Biological-Image Analysis. *Nat. Methods* **2012**, *9*, 676–682.
- (74) Ilavsky, J.; Jemian, P. R. *Irena*: Tool Suite for Modeling and Analysis of Small-Angle Scattering. *J. Appl. Crystallogr.* **2009**, *42*, 347–353.

## Chapter VI

- (1) Turpin, J. P.; Massoud, A. T.; Jiang, Z. H.; Werner, P. L.; and Werner, D. H. Conformal mappings to achieve simple material parameters for transformation optics devices. *Optics Express*, **2010**, *18*, 244–252.
- (2) Kundtz, N. B.; Smith, D. R.; Pendry, J. B. Electromagnetic design with transformation optics. *Proceedings of the IEEE*, 2011, Vol. 99, pp. 1622–1633.
- (3) Tang, W.; Member, S.; Argyropoulos, C.; Kallos, E. Discrete coordinate transformation for designing all dielectric flat antennas,” *IEEE Transactions on Antennas and Propagation*, **2010**, *58*, 3795–3804.
- (4) Landy, N. I.; Padilla, W. J. Guiding light with conformal transformations. *Optics Express*, **2009**, *17*, 1777–1780.
- (5) Company, H. D. HP 3D High Reusability PA 12. **2017**, 1–2.
- (6) Kim, M.; Schmitt, S.; Choi, J.; Krutty, J.; Gopalan, P. From self-assembled monolayers to coatings: advances in the synthesis and nano bio applications of polymer brushes. *Polymers*, **2015**, *7*, 1346–1378.
- (7) Heinz, H.; Pramanik, C.; Heinz, O.; Ding, Y.; Mishra, R. K.; Marchon, D.; Flatt, R. J.; Estrela-Llopis, I.; Llop, J.; Moya, S.; Ziolo, R. F. Nanoparticle decoration with surfactants: Molecular interactions, assembly, and applications. *Surface Science Reports*, **2017**.
- (8) S. Torkzaban, S. A. Bradford, J. Wan, T. Tokunaga, and A. Masoudih, “Release of quantum dot nanoparticles in porous media: Role of cation exchange and aging time,” *Environmental Science and Technology*, **2013**, *47*, 11528–11536.
- (9) Bradford, S. A.; Torkzaban, S. Determining parameters and mechanisms of colloid retention and release in porous media. *Langmuir*, **2015**, *31*, 12096–12105.
- (10) Check, C.; Chartoff, R.; Chang, S. Inkjet printing of 3D nanocomposites formed by photopolymerization of an acrylate monomer. *Reactive and Functional Polymers*, **2015**, *97*, 116–122.
- (11) Temuujin, J.; Aoyama, M; Senna, M.; Masuko, T.; Ando, C.; Kishi, H. Benefits of mild wet milling of the intermediates for the synthesis of phase-pure Z-type hexaferrite. *Journal of Materials Research*, **2005**, *20*, 1939–1942.

- (12) Tachibana, T.; Nakagawa, T.; Takada, Y.; Izumi, K.; Yamamoto, T.; Shimada, T.; Kawano, S. X-ray and neutron diffraction studies on iron-substituted Z-type hexagonal barium ferrite:  $\text{Ba}_3\text{Co}_{2-x}\text{Fe}_{24+x}\text{O}_{41}$  ( $x = 0 - 0.6$ ). *Journal of Magnetism and Magnetic Materials*, **2003**, 262, 248–257.
- (13) Popielarz, R.; Chiang, C. K.; Nozaki, R.; Obrzut, J. Dielectric properties of polymer/ferroelectric ceramic composites from 100 Hz to 10 GHz. *Macromolecules*, **2001**, 34, 5910–5915.
- (14) Macdonald, J. R.; Johnson, W. B. Fundamentals of Impedance Spectroscopy. In *Impedance Spectroscopy: Theory, Experimental, and Applications*; John Wiley & Sons, Inc.: Hoboken, New Jersey, 2005.
- (15) Van Beek, L. K. H. The Maxwell-Wagner-Sillars effect, describing apparent dielectric loss in inhomogeneous media. *Physica*, **1960**, 26, 66–86.
- (16) Lu, H.; Zhang, X.; Zhang, H. Influence of the relaxation of Maxwell-Wagner-Sillars polarization and dc conductivity on the dielectric behaviors of nylon 1010. *Journal of Applied Physics*, **2006**, 100, 054104.
- (17) Sihvola, A. H. *Electromagnetic Mixing Formulas and Applications*; The Institution of Electrical Engineers: London, 1999.
- (18) Looyenga, H.; Dielectric constants of heterogeneous mixtures. *Physica*, **1965**, 31, 401–406.
- (19) Sharma, H.; Jain, S.; Raj, P. M.; Murali, K. P. Magnetic and dielectric property studies in Fe- and NiFe-based polymer nanocomposites. *Journal of Electronic Materials*, **2015**, 44, 3819–3826.
- (20) Clay, G.; Song, H.; Nielsen, J.; Stasiak, J.; Khavari, M.; Jander, A.; Dhagat, P. 3D Printing Magnetic Material with Arbitrary Anisotropy. In *NIP & Digital Fabrication Conference*; 1; 2015; Vol. 2015, pp 307–310.

## Chapter VII

- (1) Gilbert, B.; Huang, F.; Zhang, H.; Waychunas, G. A.; Banfield, J. F. Nanoparticles: Strained and Stiff. *Science* **2004**, 305, 651–654.
- (2) Lauritsen, J. V.; Kibsgaard, J.; Helveg, S.; Topsøe, H.; Clausen, B. S.; Lægsgaard, E.; Besenbacher, F. Size-Dependent Structure of MoS<sub>2</sub> Nanocrystals. *Nat. Nanotechnol.* **2007**, 2, 53–58.

- (3) Ringe, E.; Van Duyne, R. P.; Marks, L. D. Kinetic and Thermodynamic Modified Wulff Constructions for Twinned Nanoparticles. *J. Phys. Chem. C* **2013**, *117*, 15859–15870.
- (4) Sehgal, R. M.; Maroudas, D. Equilibrium Shape of Colloidal Crystals. *Langmuir* **2015**, *31*, 11428–11437.
- (5) Talapin, D. V.; Rogach, A. L.; Shevchenko, E. V.; Kornowski, A.; Haase, M.; Weller, H. Dynamic Distribution of Growth Rates within the Ensembles of Colloidal II–VI and III–V Semiconductor Nanocrystals as a Factor Governing Their Photoluminescence Efficiency. *J. Am. Chem. Soc.* **2002**, *124*, 5782–5790.
- (6) Whitehead, C. B.; Özkar, S.; Finke, R. G. LaMer’s 1950 Model for Particle Formation of Instantaneous Nucleation and Diffusion-Controlled Growth: A Historical Look at the Model’s Origins, Assumptions, Equations, and Underlying Sulfur Sol Formation Kinetics Data. *Chem. Mater.* **2019**, *31*, 7116–7132.
- (7) Chang, H.; Kim, B. H.; Jeong, H. Y.; Moon, J. H.; Park, M.; Shin, K.; Chae, S. I.; Lee, J.; Kang, T.; Choi, B. K.; et al. Molecular-Level Understanding of Continuous Growth from Iron-Oxo Clusters to Iron Oxide Nanoparticles. *J. Am. Chem. Soc.* **2019**, *141*, 7037–7045.

## Appendix A

- (1) Marezio, M. Refinement of the Crystal Structure of  $\text{In}_2\text{O}_3$  at Two Wavelengths. *Acta Crystallographica* **1966**, *20*, 723–728.

## Appendix C

- (1) Thanh, N. T. K.; Maclean, N.; Mahiddine, S. Mechanisms of Nucleation and Growth of Nanoparticles in Solution. *Chem. Rev.* **2014**, *114*, 7610–7630.
- (2) Rodríguez-Carvajal, J. Recent Advances in Magnetic Structure Determination by Neutron Powder Diffraction. *Phys. B Condens. Matter* **1993**, *192*, 55–69.
- (3) Fleet, M. E. The Structure of Magnetite. *Int. Union Crystallogr.* **1981**, *2549*, 917–920.
- (4) Andersen, H. L.; Jensen, K. M. Ø.; Tyrsted, C.; Bøjesen, E. D.; Christensen, M. Size and Size Distribution Control of  $\gamma\text{-Fe}_2\text{O}_3$  Nanocrystallites: An in Situ Study. *Cryst. Growth Des.* **2014**, *14*, 1307–1313.

- (5) Castellanos-Rubio, I.; Insausti, M.; Garaio, E.; Gil de Muro, I.; Plazaola, F.; Rojo, T.; Lezama, L. Fe<sub>3</sub>O<sub>4</sub> Nanoparticles Prepared by the Seeded-Growth Route for Hyperthermia: Electron Magnetic Resonance as a Key Tool to Evaluate Size Distribution in Magnetic Nanoparticles. *Nanoscale* **2014**, *6*, 7542–7552.
- (6) Guardia, P.; Pérez, N.; Labarta, A.; Batlle, X. Controlled Synthesis of Iron Oxide Nanoparticles over a Wide Size Range. *Langmuir* **2010**, *26*, 5843–5847.
- (7) Mohapatra, J.; Mitra, A.; Bahadur, D.; Aslam, M. Surface Controlled Synthesis of MFe<sub>2</sub>O<sub>4</sub> (M = Mn, Fe, Co, Ni and Zn) Nanoparticles and Their Magnetic Characteristics. *CrystEngComm* **2013**, *15*, 524–532.
- (8) Caruntu, D.; Caruntu, G.; O'Connor, C. J. Magnetic Properties of Variable-Sized Fe<sub>3</sub>O<sub>4</sub> Nanoparticles Synthesized from Non-Aqueous Homogeneous Solutions of Polyols. *J. Phys. D. Appl. Phys.* **2007**, *40*, 5801–5809.
- (9) Park, B.; Kim, B. H.; Yu, T. Synthesis of Spherical and Cubic Magnetic Iron Oxide Nanocrystals at Low Temperature in Air. *J. Colloid Interface Sci.* **2018**, *518*, 27–33.
- (10) Mitra, A.; Mohapatra, J.; Meena, S. S.; Tomy, C. V.; Aslam, M. Verwey Transition in Ultrasmall-Sized Octahedral Fe<sub>3</sub>O<sub>4</sub> Nanoparticles. *J. Phys. Chem. C* **2014**, *118*, 19356–19362.
- (11) Dehsari, H. S.; Heidari, M.; Ribeiro, A. H.; Tremel, W.; Jakob, G.; Donadio, D.; Potestio, R.; Asadi, K. Combined Experimental and Theoretical Investigation of Heating Rate on Growth of Iron Oxide Nanoparticles. *Chem. Mater.* **2017**, *29*, 9648–9656.
- (12) Yun, H.; Liu, X.; Paik, T.; Palanisamy, D.; Kim, J.; Vogel, W. D.; Viescas, A. J.; Chen, J.; Papaefthymiou, G. C.; Kikkawa, J. M.; *et al.* Size- and Composition-Dependent Radio Frequency Magnetic Permeability of Iron Oxide Nanocrystals. *ACS Nano* **2014**, *8*, 12323–12337.
- (13) Baaziz, W.; Pichon, B. P.; Fleutot, S.; Liu, Y.; Lefevre, C.; Greneche, J.-M.; Toumi, M.; Mhiri, T.; Begin-Colin, S. Magnetic Iron Oxide Nanoparticles: Reproducible Tuning of the Size and Nanosized-Dependent Composition, Defects, and Spin Canting. *J. Phys. Chem. C* **2014**, *118*, 3795–3810.
- (14) Demortière, A.; Panissod, P.; Pichon, B. P.; Pourroy, G.; Guillon, D.; Donnio, B.; Bégin-Colin, S. Size-Dependent Properties of Magnetic Iron Oxide Nanocrystals. *Nanoscale* **2011**, *3*, 225–232.
- (15) Taniguchi, T.; Nakagawa, K.; Watanabe, T.; Matsushita, N.; Yoshimura, M. Hydrothermal Growth of Fatty Acid Stabilized Iron Oxide Nanocrystals. *J. Phys. Chem. C* **2009**, *113*, 839–843.

- (16) Santoyo Salazar, J.; Perez, L.; de Abril, O.; Truong Phuoc, L.; Ihiawakrim, D.; Vazquez, M.; Grenache, J.-M.; Begin-Colin, S.; Pourroy, G. Magnetic Iron Oxide Nanoparticles in 10–40 Nm Range: Composition in Terms of Magnetite/Maghemite Ratio and Effect on the Magnetic Properties. *Chem. Mater.* **2011**, *23*, 1379–1386.
- (17) Kim, B. H.; Lee, N.; Kim, H.; An, K.; Park, Y. Il; Choi, Y.; Shin, K.; Lee, Y.; Kwon, S. G.; Na, H. Bin; *et al.* Large-Scale Synthesis of Uniform and Extremely Small-Sized Iron Oxide Nanoparticles for High-Resolution  $T_1$  Magnetic Resonance Imaging Contrast Agents. *J. Am. Chem. Soc.* **2011**, *133*, 12624–12631.
- (18) Tronc, E.; Ezzir, A.; Cherkaoui, R.; Chanéac, C.; Noguès, M.; Kachkachi, H.; Fiorani, D.; Testa, A. M.; Grenèche, J. M.; Jolivet, J. P. Surface-Related Properties of  $\gamma$ -Fe<sub>2</sub>O<sub>3</sub> Nanoparticles. *J. Magn. Magn. Mater.* **2000**, *221*, 63–79.
- (19) Millan, A.; Urtizberea, A.; Silva, N. J. O.; Palacio, F.; Amaral, V. S.; Snoeck, E.; Serin, V. Surface Effects in Maghemite Nanoparticles. *J. Magn. Magn. Mater.* **2007**, *312*, L5–L9.